

**Study of Tunable Optical Properties of  
Lanthanide-Ion-Doped Rare Earth Phosphors and  
their Applications**

**Thesis Submitted to AcSIR For the Award of  
the Degree of  
DOCTOR OF PHILOSOPHY  
In Chemical Sciences**



**By**

Preeti Padhye

Registration Number: 10CC11A26009

**Under the guidance of**

Dr. Pankaj Poddar

Physical and Materials Chemistry Division  
CSIR-National Chemical Laboratory  
Dr. Homi Bhabha Road  
Pune - 411008

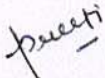
\*\*\*\*\*

*Dedicated to Aai-Baba  
for their endless love and my better half  
Sandip for supporting me all the way*

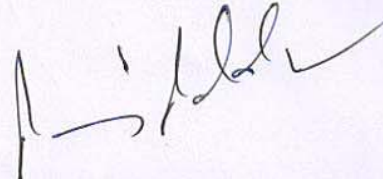
\*\*\*\*\*

## CERTIFICATE

This is to certify that the work incorporated in this Ph.D. thesis entitled "**Study of tunable optical properties of lanthanide-ion-doped rare earth phosphors and their applications**" submitted by Ms. **Preeti Padhye** to Academy of Scientific and Innovative Research (AcSIR) in fulfillment of the requirements for the award of the Degree of **Doctor of Philosophy in Chemical Sciences**, embodies original research work under my supervision/guidance. I further certify that this work has not been submitted to any other University or Institution in part or full for the award of any degree or diploma. Research material obtained from other sources has been duly acknowledged in the thesis. Any text, illustration, table etc., used in the thesis from other sources, have been duly cited and acknowledged.

  
**Preeti Padhye**

**(Student)**

  
**Dr. Pankaj Poddar**

**(Supervisor)**

## DECLARATION

I, hereby declare that the work described in this thesis entitled “**Study of tunable optical properties of lanthanide-ion-doped rare earth phosphors and their applications**” submitted for the degree of **Doctor of Philosophy in Chemical Sciences** has been carried out by me at the Physical and Materials Chemistry Division of the CSIR-National Chemical Laboratory, Pune, India under the supervision of Dr. Pankaj Poddar. Such materials as have been obtained by other sources have been duly acknowledged in this thesis. The work is original and has not been submitted in part or full by me for award of any other degree or diploma in any other University.

**Date:** 17/02/2017

**National Chemical Laboratory**

**Place: Pune**

*Preeti*

**Preeti Padhye**

**(Research Student)**

## **ACKNOWLEDGEMENT**

*First and above all, I praise God, the almighty for providing me this opportunity and granting me the capability to proceed successfully. The journey of this thesis was kept on track and been seen through to completion with the support and encouragement of numerous people, who contributed in many ways to the success of this study and made it an unforgettable experience for me. For me, this thesis is such an important destiny and I am indeed indebted to lot of people for their wishes and blessings for completing this journey. I take this opportunity to acknowledge and extend my sincere gratitude towards all these people who have been involved, directly or indirectly, to make the research work described in this thesis possible.*

*First and foremost, I would like to express my sincere gratitude to my research supervisor Dr. Pankaj Poddar, for giving me an opportunity to pursue my Ph.D. research under his able guidance. It has been a great privilege to work with his dynamic laboratory environment for the past five years. I am really grateful to him for his warm encouragement, thoughtful guidance, constructive critical comments, insights and his tremendous efforts in preparing this dissertation. He has inspired me to become an independent researcher and helped me realize the power of critical reasoning. His constant encouragement helped me to push beyond my limits. His guidance always challenged me intellectually, grafted my scientific skills and knowledge and provided a perfect ambience that I needed to grow as a researcher. I thank him for his endless support filled with patience and enthusiasm during my whole tenure of Ph.D. His advice on both research as well as on my career have been precious.*

*I would also like to thank my doctoral advisory committee members, Dr. Amol Kulkarni, Dr. K. Krishnamoorthy and Dr. Durba Sengupta, Dr. C. Ramesh, for their constructive suggestions, critical comments, guidance and support. I owe a great deal of appreciation and gratitude to my external experts Dr. Santosh Haram and Dr. Raghavendra Kikkeri for evaluating my work. I warmly thank them for their precious*

*advice, analysis, criticism and discussions on my work, I extend my sincere thanks to my collaborators Dr. Samit Chattopadhyay, Dr. Suvankar Gorai, and Aftab for keeping faith on me and helping in advancing my research work, I would also like to thank Dr. Rajmohanan, Kavya from CSIR-NCL, Dr. V. Sudarsan, Dr. Nandi from BARC, Mumbai, Dr. Darshan and Vivek from Star imaging and research center, Joshi hospital, Pune for various important experiments.*

*I extend my sincere thanks to the present Director of CSIR-NCL Dr. Ashwini Kumar Nangia, Dr. Vijaymohanan (former Director), Dr. Sourav Pal (former Director), Head of Physical and Materials Chemistry Division, Dr. P. A. Joy for their kind help and encouragement during the course of this work, I would also extend my gratitude to my former HOD Dr. Anil Kumar for his continuous support, inspiring all the time and making us smile whenever we meet in the corridors with his refreshing conversations. I am also grateful to all the administrative and non-teaching staff of CSIR-NCL for their kind support and their assistance over the years on various occasions.*

*I am grateful to University Grants Commission, New Delhi for the fellowship support.*

*I take an opportunity to thank Suguna Adhyanthaya Madam, my seniors Chandrasekhar, Adhish, Umesh, Imran, Richa, Dheerajji, Raja, Aanchal, Asha, Shubhadip, Priya, Sameer, Anupam, Gayatri, Geeta, although many have moved away from NCL, I will never forget the experiences we've shared and hope to stay in touch. I would like to thank my lovely juniors Monika (my future scope 😊) and Shubhra (bunny) ; Selfie girls, for interesting discussions. Thanks to you darlings for keeping enthusiasm and creating such joyful environment in lab. I thank my closest seniors Subha, and Preeti, friends Mousumi, and Puneet for the motivating discussions, for the restless times we were working together before deadlines, and for all the fun we had in the last five years. These friends have been there for me when the challenges of PhD seemed too huge to overcome.*

*Wholehearted thanks to Mousumi (Shakuni) and Preeti with whom I spent wonderful time. Be it designing the experiments, writing the manuscripts, discussing the problems*

*or attending the conferences. Thank you for understanding me and being with me in my tough times. Thank you for your understanding and encouragement in my many many difficult and stressful moments. Thank you for spending countless hours in the lab explaining and showing me how to do small and big things. Preeti, I must mention that you are one who triggered me in writing my first manuscript, explaining me the things sometime with love and sometime by scolding and then I accelerated further. You have spent hell lot of time in improving my presentations and manuscripts. You build up confidence in me which took me to the next level. Mousumi, we have shared and cherished many difficult and happy times. You have been always there with me whenever needed. Your friendship makes my life a wonderful experience. Thank you darlings for standing with me in all my tough times.*

*I extend my thanks to Rajeev and Ruchita who were always there whenever I needed. In particular, I am grateful to Dr. V. V. Pillai for enlightening me the first glance of research. I would also like to thank my college (M.Sc, M.Phil) teachers and colleagues at University of Mysore, Dr. Devashish bose, Sandeep sir, Ila mam, Prof. G. K. Ananda, Prof. Murthy, Prof. Aravind, Prof. Ponnappa, Prof. Vanishree for always encouraging me in my tough time and motivating me by making me believe in myself.*

*It gives me immense pleasure to thank everyone who helped me write my thesis successfully.*

*I would like to express the heartfelt gratefulness to my Aai and Baba who provided endless love, and unmatched support throughout my life. Thank you for the encouragement and interest in my thesis work. Thank you for believing in me and allowing me to pursue my ambition. I owe my thanks for giving me strength to chase my dreams. Thanks for listening to my problems and providing your perspectives. I would not be who am I today without your efforts and blessings. Thank you Baba for teaching me the value of hard work and education. I would also like to thank my sister Prachi tai for her constant moral support. I would also like to thank Maitreya Jiju, Ujju maushi,*

*Nana, Shama maushi, Ram Kaka and all relatives who all supported me a lot during my PhD days. Their love helped me a lot in achieving my goals.*

*I wholeheartly thank my mother-in-law and brother-in-law, Aai and Somu for their encouragement and continued support over the years and their enthusiasm in my studies. Also for encouraging me whenever I am down and listening to my PhD stories so enthusiastically. Thank you Aai for supporting me in all the ups and downs, for giving me all relaxations from household obligations during my presentations, exams, paper submissions and other important events of my PhD tenure. Above all, I thank them all for trusting me when I most needed it.*

*Finally, I specially acknowledge my husband Sandip for his understanding, support, love, care and for being there with me at all times. Thank you for being with me in my hard times and tolerating my bad temper. Thanks for taking so much interest in my research work and listening all my success and failure stories of my PhD. You have been calm and patient with me when I'm frustrated and annoyed, you celebrate with me when even the littlest things go right, and you are there whenever I need you to just listen. Thank you for sharing my responsibilities and all the things you've done for me like making the early morning tea and dinners during my presentations and whenever I worked late nights. Thank you darling for supporting me in all the ways.*

*I would like to thank all my teachers from school till my PhD for imbibing good values and knowledge in me.*

*How could I forget to thank my niece and nephew, Mishthi and Kanishka, whose unconditional love brings smile on my face in any difficult situation.*

*I could not have completed my research without the support of all these wonderful people!*

*Last but by no means least I thank God for making my life so beautiful.*

***Preeti Padhye...***



## CONTENTS

---

Preface	I-II
List of Abbreviations	III-V
<b>1. Chapter 1: Introduction</b>	<b>1-62</b>
1.1 Lanthanide photophysics	2
1.1.1 Electronic structure of lanthanide ions	2
1.1.2 Lanthanide luminescence	3
1.2 Lanthanide based luminescent materials	7
1.2.1 Lanthanide complexes	8
1.2.2 Ln <sup>3+</sup> -doped glasses, ceramics and polymers	12
1.2.3 Ln <sup>3+</sup> -doped nanoparticles “nanophosphors”	13
1.3 Structure and strategies for enhancing luminescence of rare earth phosphors	15
1.3.1 Host lattice	15
1.3.2 Dopant system	18
1.3.2.1 Activator	20
1.3.2.2 Sensitizer	21
1.4 Classification of rare earth phosphors based on emissive transition pathways	22
1.4.1 Down-conversion	23
1.4.2 Down-shifting	23
1.4.3 Up-conversion	23
1.4.4 Mechanism of down- and up-conversion emission	24
1.5 Various host matrices: “Fluoride Hosts Preferred”	28
1.6 Why $\beta$ -NaYF <sub>4</sub> is so special?	29
1.7 Crystal structure of $\beta$ -NaYF <sub>4</sub> : The reason why is hexagonal phase $\beta$ -NaYF <sub>4</sub> efficient than the cubic $\alpha$ -NaYF <sub>4</sub>	31
1.8 Properties of lanthanide ion-doped nanoparticles	34
1.8.1 Optical properties	34
1.8.1.1 Unique optical features	34
1.8.1.2 Term symbols	38
1.8.1.3 Dieke energy level diagram	40

1.8.2	Magnetic properties	42
1.9	Preparation of rare earth based nanoparticles	44
1.10	Morphology tuning	46
1.11	Hybrids of rare earth phosphors	48
1.11.1	Ln <sup>3+</sup> -doped phosphors-Plasmonic metal hybrids	50
1.11.2	Ln <sup>3+</sup> -doped phosphors-Semiconductor hybrids	51
1.11.3	Ln <sup>3+</sup> -doped phosphor-Magnetic material hybrids	51
1.11.4	Ln <sup>3+</sup> -doped phosphor-Graphene hybrids	52
1.12	Applications	53
2	Thesis outline	54
3	References	57
2.	<b>Chapter 2: Optical and photocatalytic properties of uniform, monodispersed, and highly crystalline up/down-converting, lanthanide ion-doped <math>\beta</math>-NaYF<sub>4</sub> phosphor crystals with controlled multiform morphologies</b>	<b>63-103</b>
2.1	Introduction	65
2.2	Material and methods	68
2.2.1	Materials	68
2.2.2	Synthesis	68
2.2.3	Characterization techniques	69
2.3	Result and Discussion	71
2.3.1	Structural and morphological investigations	71
2.3.1.1	Effect of reaction temperature	72
2.3.1.2	Effect of pH	76
2.3.2	Formation mechanism of multiform structures	79
2.3.3	Optical studies	83
2.3.3.1	UV-visible studies	83
2.3.3.2	Static and dynamic photoluminescence studies	84
2.3.3.2.1	$\beta$ -NaYF <sub>4</sub> :Tb <sup>3+</sup>	84
2.3.3.2.2	$\beta$ -NaYF <sub>4</sub> :Yb <sup>3+</sup> /Er <sup>3+</sup>	88
2.3.3.2.3	$\beta$ -NaYF <sub>4</sub> :Yb <sup>3+</sup> /Tm <sup>3+</sup>	89
2.3.4	Photocatalytic Studies	90
2.3.4.1	Photoselectivity of $\beta$ -NaYF <sub>4</sub> :5 % Tb <sup>3+</sup> phosphors	90

2.3.4.2	Mechanism of MB degradation	94
2.3.4.3	Morphology dependence on photocatalytic properties of $\beta$ -NaYF <sub>4</sub> :5 % Tb <sup>3+</sup> crystals	95
2.4	Conclusion	99
2.5	References	100
3.	<b>Chapter 3: Doxorubicin-conjugated <math>\beta</math>-NaYF<sub>4</sub>:Gd<sup>3+</sup>/Tb<sup>3+</sup> multi-functional phosphor: A multimodal, luminescent-magnetic probe for simultaneous optical, magnetoresonance imaging and an excellent pH-triggered anti-cancer drug delivery nanovehicle</b>	<b>104-156</b>
3.1	Introduction	106
3.2	Materials and methods	110
3.2.1	Materials	110
3.2.2	Synthesis	110
3.2.2.1	Synthesis of amine functionalized $\beta$ -NaYF <sub>4</sub> : Gd <sup>3+</sup> /Tb <sup>3+</sup>	110
3.2.2.2	Synthesis of DOX- conjugated $\beta$ -NaYF <sub>4</sub> : Gd <sup>3+</sup> /Tb <sup>3+</sup>	111
3.2.3	Stability test of $\beta$ -NaYF <sub>4</sub> : Gd <sup>3+</sup> / Tb <sup>3+</sup> nanorods and DOX-conjugated $\beta$ -NaYF <sub>4</sub> :Gd <sup>3+</sup> /Tb <sup>3+</sup>	112
3.2.4	DOX loading and <i>in vitro</i> release of DOX from conjugates	113
3.2.5	<i>In vitro</i> cytotoxicity of DOX-conjugated $\beta$ -NaYF <sub>4</sub> : Gd <sup>3+</sup> /Tb <sup>3+</sup> nanoparticles	114
3.2.5.1	Cell culture	114
3.2.5.2	Proliferation assay	114
3.2.6	Cellular uptake of DOX-conjugated $\beta$ -NaYF <sub>4</sub> : Gd <sup>3+</sup> /Tb <sup>3+</sup> nanorods	115
3.2.7	<i>In vivo</i> toxicity of DOX-conjugated $\beta$ -NaYF <sub>4</sub> : Gd <sup>3+</sup> /Tb <sup>3+</sup>	116
3.2.8	Spin relaxation measurement of $\beta$ -NaYF <sub>4</sub> : Gd <sup>3+</sup> /Tb <sup>3+</sup> nanorods and DOX-conjugated $\beta$ -NaYF <sub>4</sub> : Gd <sup>3+</sup> /Tb <sup>3+</sup> as Magnetic Resonance Imaging Contrast Agents	116
3.2.9	Characterization techniques	117
3.3	Results and Discussion	119

3.3.1	Structural and morphological characterization of $\beta$ -NaYF <sub>4</sub> : Gd <sup>3+</sup> /Tb <sup>3+</sup> and DOX-conjugated $\beta$ -NaYF <sub>4</sub> : Gd <sup>3+</sup> /Tb <sup>3+</sup>	119
3.3.2	Surface properties	123
3.3.3	Optical properties	124
3.3.3.1	UV-visible absorbance studies	124
3.3.3.2	Static photoluminescence studies	125
3.3.3.3	Time-resolved photoluminescence studies	127
3.3.4	<i>In vitro</i> Cytotoxicity	128
3.3.4.1	<i>In vitro</i> cytotoxicity in NIH3T3 fibroblast cell lines	128
3.3.4.2	<i>In vitro</i> cytotoxicity in MCF-7 cancer cell lines	130
3.3.5	Stability assay	131
3.3.6	Controlled DOX release studies of DOX-conjugated $\beta$ -NaYF <sub>4</sub> :Gd <sup>3+</sup> / Tb <sup>3+</sup> nanorods	132
3.3.7	Fluorescence resonance energy transfer (FRET) between $\beta$ -NaYF <sub>4</sub> : Gd <sup>3+</sup> / Tb <sup>3+</sup> nanoparticles and DOX	137
3.3.8	Cellular uptake studies	142
3.3.8.1	Cellular uptake studies by CLSM	142
3.3.8.2	Cellular uptake studies by flow cytometry	146
3.3.9	<i>In vivo</i> studies	147
3.3.10	Magnetic measurements	148
3.3.10.1	Magnetic mass susceptibility	148
3.3.10.2	Longitudinal relaxivity and magnetic resonance imaging	151
3.4	Conclusion	151
3.5	References	153
4.	<b>Chapter 4: A broad spectrum photon responsive, paramagnetic <math>\beta</math>-NaGdF<sub>4</sub>: Yb<sup>3+</sup>, Er<sup>3+</sup> - mesoporous anatase titania nanocomposite</b>	<b>157-221</b>
4.1	Introduction	159
4.2	Materials and methods	165
4.2.1	Materials	165

4.2.2	Synthesis	165
4.2.2.1	Synthesis of $\beta$ -NaGdF <sub>4</sub> : 18 % Yb <sup>3+</sup> , 2 % Er <sup>3+</sup>	165
4.2.2.2	Synthesis of $\beta$ -NaGdF <sub>4</sub> : 18 % Yb <sup>3+</sup> , 2 % Er <sup>3+</sup> / <i>m</i> TiO <sub>2</sub> composite	166
4.2.2.3	Synthesis of <i>m</i> TiO <sub>2</sub>	166
4.2.3	Fabrication of DSSC	166
4.2.4	Spin relaxation measurement of $\beta$ -NaGdF <sub>4</sub> : Yb <sup>3+</sup> , Er <sup>3+</sup> nanorods and $\beta$ -NaGdF <sub>4</sub> : Yb <sup>3+</sup> , Er <sup>3+</sup> / <i>m</i> TiO <sub>2</sub> composite as magnetic resonance imaging (MRI) contrast agents	167
4.2.5	Characterization techniques	168
4.3	Result and Discussion	170
4.3.1	Phase and morphology characterization	170
4.3.2	Surface properties	175
4.3.2.1	Surface functionalization	175
4.3.2.2	Surface area and porosity	177
4.3.2.3	Phonon modes	178
4.3.3	<b>Optical properties</b>	180
4.3.3.1	UV-vis-NIR absorption spectra analysis	180
4.3.3.2	Up-conversion static luminescence properties	182
4.3.3.3	Time resolved luminescence properties	184
4.3.4	Photocatalysis properties	186
4.3.4.1	Photocatalytic activity	186
4.3.4.2	Photocatalytic mineralization of dye by nanocomposite	189
4.3.4.3	Mechanism of photocatalysis by nanocomposite	190
4.3.5	Photovoltaic characteristics	191
4.3.5.1	Photovoltaic measurements	191
4.3.5.2	Mechanism of the DSSC performance based on the nanocomposite	194
4.3.6	Magnetic properties	197
4.3.6.1	Magnetic mass susceptibility	197
4.3.6.2	Longitudinal relaxivity and magnetic resonance imaging	198

4.4	Conclusion	202
4.5	References	204
5.	<b>Chapter 5: Conclusion and future prospective</b>	<b>212-221</b>
5.1	Summary	213
5.2	Scope for future work	217
	<b>List of publications</b>	<b>222</b>

# PREFACE

Lanthanide ion-doped up-/down-converting phosphors are giving an edge over conventional organic fluorescent dyes or quantum dots due to their tailoring, unique and beneficial tunable electronic, optical and magnetic properties that enable potential wide ranging applications in optoelectronics, solid state lasers, security printing, biomedical diagnostics, sensors, solar cells, catalysis and biological imaging. Earlier, the studies and development of phosphors were limited for their lasers and display applications. While, owing to their unique optical properties these also promise for other potential new applications in biological and material sciences. These aspects spark our interest to explore tunable optical properties of trivalent lanthanide ion-doped rare earth fluoride phosphors and their various applications. We have dedicated efforts to deliberate the  $\text{Ln}^{3+}$ -doped rare earth fluoride, specifically  $\text{NaREF}_4$  system and understand the effect of different dopants and dopant combinations, surface cappings, functionalization and their structural and optical properties and investigate various applications. We have also modified the system by conjugation of drug molecules and other entities to make them suitable and efficient for and according to the need of targeted application. This thesis presents detailed work on hexagonal phase  $\text{Ln}^{3+}$ -doped rare earth fluoride ;  $\beta\text{-NaREF}_4\text{:Ln}^{3+}$  systems.

In **chapter 1**, we will discuss about the background of the research work and also addresses the motivation behind studying the lanthanide ion-doped phosphors. We will also talk about the stimulating optical features which make  $\text{Ln}^{3+}$ -doped rare earth phosphors so interesting to study. Towards the end of the chapter, we will discuss the rationale behind choosing the rare earth fluorides and scope of present investigation in the thesis work.

**Chapter 2** will address the fundamental studies on synthesis and optical studies of highly crystalline, uniform and well defined multiform morphologies of  $\beta\text{-NaYF}_4\text{:Tb}^{3+}$  crystals. We will discuss their morphology tuning, effect of capping agents and other reaction parameters. We will also briefly discuss about the possible mechanisms and effect of morphology on the luminescent properties. We will also reveal the photocatalytic properties of  $\beta\text{-NaYF}_4\text{:Tb}^{3+}$  phosphors and their correlation with morphology.

Followed by the fundamental studies on synthesis, structural and optical properties of these  $\beta$ -NaYF<sub>4</sub>:Ln<sup>3+</sup> (Ln<sup>3+</sup> = Tb, Yb/Er and Yb/Tm) crystals, in **chapter 3** we will focus on the design and development of highly crystalline, biocompatible, PEI functionalized  $\beta$ -NaYF<sub>4</sub>:Gd<sup>3+</sup>,Tb<sup>3+</sup> nanorods system as luminescent/magnetic multimodal cell imaging tool. We will further conjugate the anticancer drug doxorubicin to  $\beta$ -NaYF<sub>4</sub>:Gd<sup>3+</sup>,Tb<sup>3+</sup> to enable them as a pH-triggered, site-specific drug delivery nanovehicle. We will further study their structural, optical, magnetic properties, cytotoxicity and cellular uptake mechanisms. We will also explore the pH-triggered drug release properties, and bioimaging and MRI abilities. It is expected that the as developed DOX-conjugated  $\beta$ -NaYF<sub>4</sub>:Gd<sup>3+</sup>/Tb<sup>3+</sup> system combining efficient luminescence, paramagnetic properties, and pH-triggered drug delivery, promises to be a potential multifunctional platform for cancer theranostics, biodetection and imaging.

Further, since the development of multifunctional platforms for broad range of applications has geared tremendous progress towards the design and engineering of such functional materials possessing multiple discrete functions in single composites. Keeping the similar perspective, the objective of **chapter 4** is to develop single multifunctional platform by judicial integration of up-converting luminescent and magnetic  $\beta$ -NaGdF<sub>4</sub>:Yb<sup>3+</sup>,Er<sup>3+</sup> and mesoporous anatase TiO<sub>2</sub> ;  $\beta$ -NaGdF<sub>4</sub>:Yb<sup>3+</sup>,Er<sup>3+</sup>/mTiO<sub>2</sub> nanocomposite system, for enhanced energy and simultaneous biomedical applications. We will study the structural, optical and magnetic properties of respective pristine and  $\beta$ -NaGdF<sub>4</sub>:Yb<sup>3+</sup>,Er<sup>3+</sup>/mTiO<sub>2</sub> nanocomposite systems in detail. We will also explore their potentiality for photocatalysis, solar cell, and MRI applications and will discuss their mechanisms.

Finally, **chapter 5** will describe the conclusion of the overall work presented in this thesis. The future direction of this thesis also presented in this chapter.



## **LIST OF ABBREVIATIONS**

<b>1.</b> Up-conversion	UC
<b>2.</b> Down-conversion	DC
<b>3.</b> Lanthanides	Ln
<b>4.</b> Trivalent lanthanides	Ln <sup>3+</sup>
<b>5.</b> X-ray diffraction	XRD
<b>6.</b> Transmission electron microscope	TEM
<b>7.</b> Scanning electron microscope	SEM
<b>8.</b> Field emission scanning electron microscope	FESEM
<b>9.</b> Selected area electron diffraction	SAED
<b>10.</b> Ultraviolet visible spectroscopy	UV-vis
<b>11.</b> Physical Property Measurement System	PPMS
<b>12.</b> Photoluminescence	PL
<b>13.</b> Nuclear magnetic resonance	NMR
<b>14.</b> Methyl orange	MO
<b>15.</b> Methylene blue	MB
<b>16.</b> Rhodamine B	RhB
<b>17.</b> Malachite green	MG
<b>18.</b> Doxorubicin	DOX
<b>19.</b> Magnetic Resonance Imaging	MRI
<b>20.</b> Sodium rare-earth fluoride	NaREF <sub>4</sub>

<b>21.</b> Sodium yttrium fluoride	NaYF <sub>4</sub>
<b>22.</b> Sodium gadolinium fluoride	NaGdF <sub>4</sub>
<b>23.</b> Excited state absorption	ESA
<b>24.</b> Ligand to Metal charge transfer	LMCT
<b>25.</b> Metal to Ligand charge transfer	MLCT
<b>26.</b> Electric dipole	ED
<b>27.</b> Fluorescence resonance energy transfer	FRET
<b>28.</b> Full width at half maximum	FWHM
<b>29.</b> Valence band	VB
<b>30.</b> Conduction band	CB
<b>31.</b> Metal organic framework	MOF
<b>32.</b> Quantum-dots	QD's
<b>33.</b> Ground state absorption	GSA
<b>34.</b> Energy transfer up-conversion	ETU
<b>35.</b> Photon avalanche	PA
<b>36.</b> Enhanced permeability and retention	EPR
<b>37.</b> Fetal Bovine Serum	FBS
<b>38.</b> Methylthiazole tetrazolium bromide	MTT
<b>39.</b> Confocal laser scanning microscope	CLSM
<b>40.</b> Dye sensitized solar cells	DSSC
<b>41.</b> Reactive oxygen species	ROS
<b>42.</b> Photodynamic therapy	PDT
<b>43.</b> Phosphate buffer saline	PBS
<b>44.</b> Polyethyleneimine	PEI
<b>45.</b> Near infra red	NIR

**46.** Excitation wavelength

$\lambda_{\text{ex}}$

**47.** Emission wavelength

$\lambda_{\text{em}}$

**48.** Nanoparticles

NP's

**49.** Nanocrystals

NC's

# **Chapter 1**

## **Introduction**

### **Outline**

---

This chapter comprises the basic concepts of luminescent properties of lanthanide-ion-doped phosphor materials. The rationale behind focused interest in lanthanide ion-doped down-conversion and up-conversion rare earth fluorides ( $\text{NaREF}_4$ ; RE=Y, Gd) is also discussed in detail. The distinctive electronic, optical and magnetic properties, their structure, classification are described in-depth. The current state of art of these lanthanide ion-doped phosphors is discussed. Various hybrids and applications of phosphors are discussed. Towards the end of this chapter, we have presented the outline of the thesis work.

## 1. Introduction

### 1.1. Lanthanide photophysics

The luminescence from lanthanide ions has been one of the fields of steady growth, due to their fascinating optical properties and potential applications in wide varieties of sciences. The stunning story of lanthanides, also said as rare earths (Sc, Y, La–Lu) started in 1787 when lieutenant Carl Axel Arrhenius from the Royal Swedish Army, an amateur geologist, discovered a curious black stone in a quarry located in the vicinity of Ytterby.<sup>1</sup> Analysis of this heavy stone by mineralogist B. R. Geijer revealed it as a new mineral which was named “ytterbite”. Later in 1894, Johan Gadolin, a professor at the University of Abø, identified and discovered a new element in it by chemical analysis, and named it “yttrium”.<sup>2</sup> Thereafter, these facts initiated a series of investigations which eventually led to the identification of 15 other rare earth elements between 1803 (cerium) and 1907 (lutetium), while the last one (promethium), had being artificially synthesized at the Oak Ridge National Laboratory in 1947.<sup>2</sup>

#### 1.1.1 Electronic structure of lanthanide ions

The lanthanides are unique among the elements, and all lanthanides possess markedly similar properties. Lanthanide ions mostly exists in trivalent state i.e,  $\text{Ln}^{3+}$  ( $\text{Ln}^{\text{III}}$ ) as their most stable oxidation state. The series of these astounding elements commence with lanthanum (atomic number 58) to end with lutetium (atomic number 71), possessing two different types of ground state electronic configuration of Ln atoms:  $[\text{Xe}] 4f^{n-1}5d^1 6s^2$  (for lanthanum, cerium, and gadolinium) and  $[\text{Xe}] 4f^n 5d^0 6s^2$  (for praseodymium, neodymium, promethium, samarium, europium, dysprosium, holmium, erbium, thulium, and ytterbium). Since, lutetium has 14  $4f$  electrons therefore its only possible configuration is  $[\text{Xe}]4f^{14}5d^1 6s^2$ .

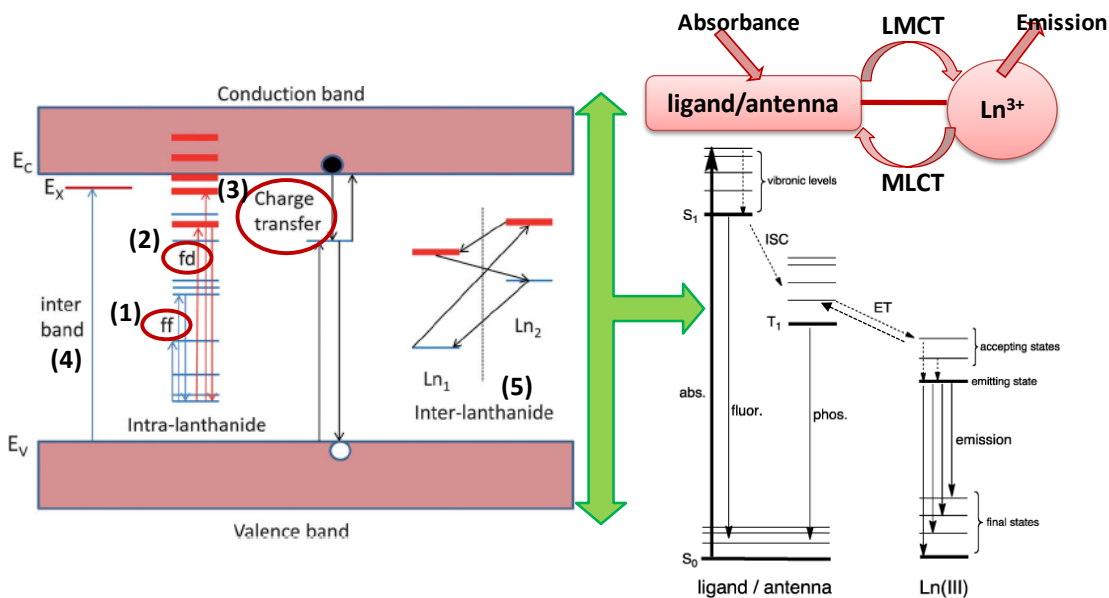
For terbium, the two configurations  $[\text{Xe}]4f^9 6s^2$  and  $[\text{Xe}]4f^8 5d^1 6s^2$  are energetically close to each other so terbium can adopt either one. The electronic configuration for  $\text{Ln}^{\text{III}}$  ions is  $[\text{Xe}] 5d^0 6s^0 4f^n$ ;  $n = 0-14$ . So, one electron goes from  $5d/4f$  and two electrons from the  $6s$  shell. Lanthanide ions correspond to the progressive filling of  $4f$  electron shells.<sup>3</sup> However, this first  $4f$  shell is actually placed inside the fully filled  $5s^2$  and  $5p^6$  and empty  $5d^0$  and  $6s^0$  shells in case of  $\text{Ln}^{\text{III}}$  ions. (Xe electronic configuration:  $1s^2 2s^2 2p^6 3s^2 3p^6 3d^{10} 4s^2 4p^6 4d^{10} 5s^2 5p^6$ ). The lanthanides'  $4f^n$  electronic configurations are split by electronic repulsion and spin-orbit coupling, leading to a rich energy-level pattern. Moreover, the electrons in  $4f$  shell are shielded from the surroundings by the filled  $5s$  and  $5p$  shells and therefore their optical transitions are least influenced by the external environment. The unique combination of these features are the key to their unique spectroscopic properties, subsequently making them very attractive for numerous applications.

### 1.1.2. Lanthanide luminescence

Most of the luminescent organic molecules emit light without change in spin state *i.e.*  $S_1$  to  $S_0$  termed “fluorescence process” (as shown in scheme 1), and thus generally possess relatively small Stokes shift and is typically short-lived (usually several nanoseconds). Alternatively, “phosphorescence process” involves change in spin state *i.e.*  $S_1$  to  $T_1$  by intersystem crossing (ISC) followed by  $T_1$  to  $S_0$ . Since, singlet-triplet processes are spin forbidden, the phosphorescence is long lived (usually in milliseconds).

However, luminescence in trivalent lanthanide ions involve electronic transitions from redistribution of electrons within  $4f$  subshells. Thus, the luminescence from  $\text{Ln}(\text{III})$  ions originates from  $4f-4f$  transitions, which are often sharp in appearance. The intraconfigurational  $4f-4f$  transitions are formally forbidden, and thus possess very low molar

extinction coefficients ( $\epsilon$ ) ( $< 10 \text{ M}^{-1}\text{cm}^{-1}$ , but very often less than  $1 \text{ M}^{-1}\text{cm}^{-1}$ ) which limits the direct excitation.<sup>3,4</sup> Although the electric dipole selection rule forbid  $f$ - $f$  transitions, but can be partially relaxed by several mechanisms as reflected in scheme 1. These involve change in symmetry around the metal ion by coupling with vibrational states. The other important mechanism which cause a breakdown of the selection rules are the mixing with opposite-parity wavefunctions, such as  $5d$  orbitals ( $f$ - $d$  transitions), ligand orbitals or charge transfer states.<sup>5</sup> The coupling between these vibrational and electronic states and the  $4f$  wavefunctions depends on the strength of the interaction between the  $4f$  orbitals and the surrounding ligands; but since the  $4f$  orbitals shielded, the degree of mixing and thus the oscillator strengths of the  $f$ - $f$  transitions remains quite small.<sup>4</sup> As a consequence, the indirect excitation by ligand, antenna or sensitizer is used to yield high luminescence, where ligand absorbs the light and transfers energy to the  $4f$  excited state *via* a mechanism that often involves the triplet ( $T_1$ ) state of the sensitizer (Scheme 1).<sup>6</sup> As a consequence of this mechanism the Stokes shift in lanthanide activated systems is much larger than simpler organic systems. The three main processes of electronic transitions involved in lanthanide ions are  $4f$ - $4f$ ,  $f$ - $d$ , and charge transfer which are denoted as (1), (2) and (3) in scheme 1.<sup>7</sup>



**Scheme 1:** Simplified model for describing a common mechanism for lanthanide luminescence: types of electronic transitions in lanthanide activated compounds ( $4f-4f$  (1),  $f-d$  (2), charge transfer (3), inter-band (4), inter-lanthanide (5); abs: absorbance, fluor: fluorescence, phos: phosphorescence, ET: energy transfer, LMCT: Ligand to Metal charge transfer, MLCT: Metal to Ligand charge transfer).

The other electronic transitions involved in lanthanide activated compounds are inter-band transitions and inter-lanthanide transitions (scheme 1). Inter-band transitions, also said as band to band transitions are the transition that occurs from the valence band (VB) to the conduction band (CB) of the host crystal (detonated as (4) in scheme 1). These transitions overlaps with the  $4f^N-4f^N$  transitions for low band gap hosts, such as oxides or chlorides. An electron is excited from the top of the valence band across the band gap to form an exciton state at energy  $E_x$ . These transitions provide information on the fundamental absorption threshold and the location of the mobility edge or conduction band bottom.



When two lanthanides are simultaneously present an inter-lanthanide electron transfer is possible (denoted as (5) in scheme 1). One lanthanide acts as a donor and the other as an acceptor.<sup>7,8</sup>

Although all the above mentioned transitions are exhibited by lanthanide ions, the luminescence in lanthanide ions is mainly characterized and explained by three types of electronic transitions:

**(1) Intra-configurational 4f–4f transitions**

All the transitions are not permitted and the allowed transitions are described by selection rules. Laporte's parity selection rule implies that the same parity electronic states cannot be connected by electric dipole (ED) transitions; as a consequence *f–f* transitions are forbidden by the ED mechanism. However, when the lanthanide ion is under the influence of a ligand-field, non-centrosymmetric interactions allow the mixing of electronic states of opposite parity into the 4*f* wavefunctions, which somewhat relaxes the selection rules and the transition becomes partially allowed; it is called an induced or forced electric dipole transition. Magnetic dipole transitions are allowed, but their intensity is weak. Intraconfigurational 4*f*–4*f* transitions are sharp and quite narrow as 4*f* shells are shielded from their surroundings by the filled 5*s*<sup>2</sup> and 5*p*<sup>6</sup> orbitals.<sup>5</sup>

**(2) Inter-configurational 4f–5*d* transitions**

These transitions correspond to promotion of a 4*f* electron into the 5*d* sub-shell which is parity allowed. The corresponding transitions are broader than *f–f* transitions because the 5*d* electrons are unshielded and hence greatly influenced by their surroundings. Their energy largely depends upon the metal environment since the 5*d* orbitals can interact directly with the ligand orbitals. The 4*f*–5*d* transitions possess high energy.<sup>3</sup>

### (3) Charge transfer transitions

Ligand to Metal (LMCT) and Metal to Ligand charge transfer (MLCT) both transitions are allowed. The energy of these transitions is very large, and they usually appear in UV region at wavelengths near to 250 nm. These types of transitions are widespread in *d*-transition metal ion. In practical applications, LMCT transitions are mostly used in lamp phosphors for instance to pump energy into  $\text{Eu}^{3+}$  or  $\text{Tb}^{3+}$  ions.

### 1.2. Lanthanide based luminescent materials

Startling interest for lanthanide based luminescence materials is stimulated due to the continuous expansion in the need for luminescent materials meeting the stringent requirements in wealth of applications in wide field of sciences. Lanthanide activated compounds includes lanthanide complexes, metal organic frameworks (MOF's), lanthanide-doped glasses, ceramics, polymers, semiconductors, inorganic materials *etc.* Although, a clear distinction in the classes of lanthanide activated compounds as luminescent materials is not well defined, but some kinds of the lanthanide based compounds are mentioned in Figure 2 and explained briefly.

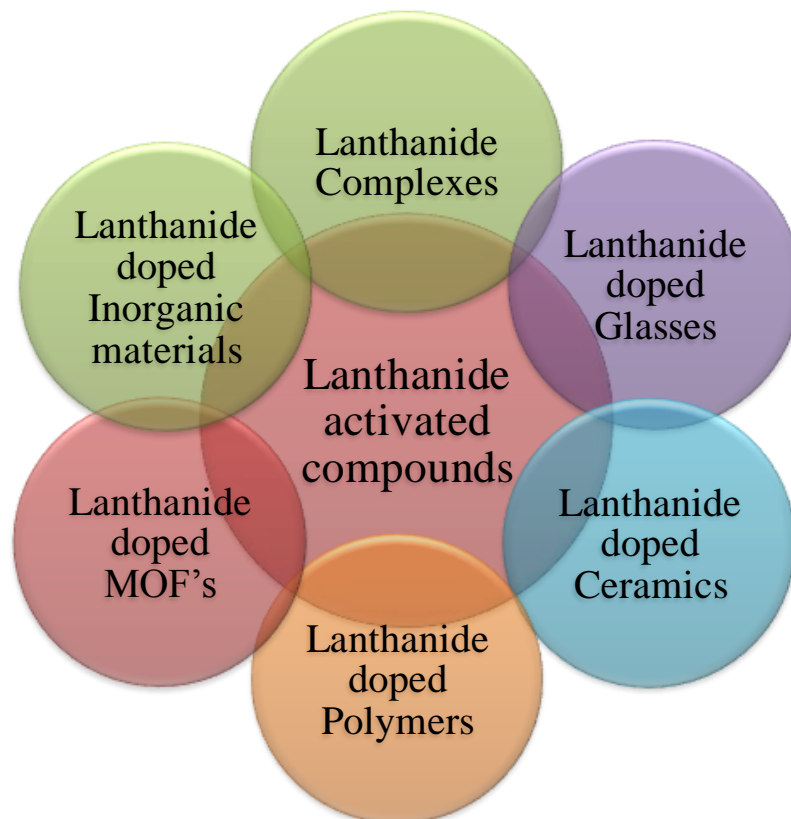


**Figure 2:** Various kind of lanthanide activated compounds.

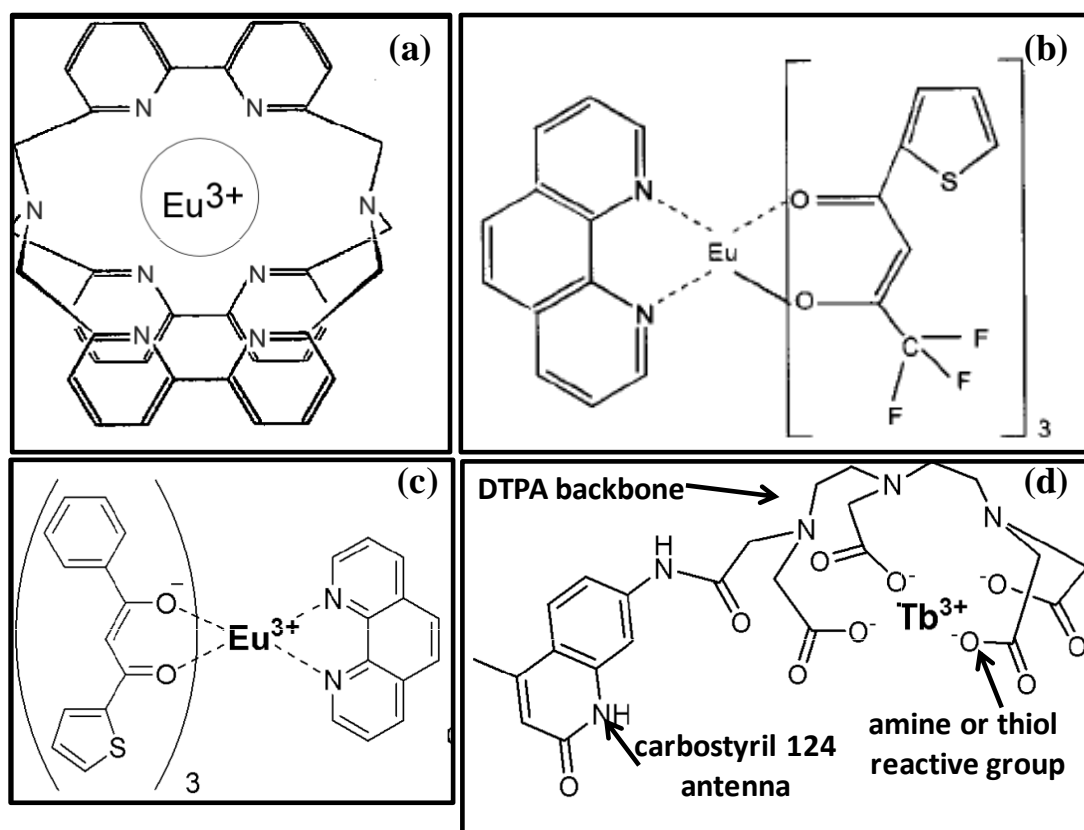
### 1.2.1. Lanthanide complexes:

These are the class of luminescent materials, wherein the complexes of lanthanide ions are formed by coordination of lanthanide ions with organic ligands. The development of luminescent lanthanide complexes were aimed at protecting the lanthanide ions luminescence from non-radiative decay due to presence of quenchers as water molecules, molecular vibrations *etc.*, and thus enable their luminescence in aqueous and biological media. The lanthanide complexes are prepared by introducing the lanthanide ion to the chemically synthesized organic ligand or chromophores and consequent complex formation takes place either readily in the solution itself or upon some activation energy. Since, trivalent lanthanide ions possess large ionic radii and high coordination number *i.e.*, 8-10,<sup>9</sup> thus they strongly

binds to the ligands which also shield and protect the lanthanide ion against quenching and also their coordination chemistry differs from common transition metal complexes. The ligands/organic chromophores also enhances the effective absorption cross-section, consequently first absorbs the incident light and transfers to the lanthanide ion *via* intermolecular energy transfer as explained above in figure 1. The presence of these intensely absorbing chromophores (ligands/antenna) increases overall brightness of the lanthanide complexes by enhancing its extinction coefficient. This metal-centered intense luminescence in lanthanide complexes were discovered by Weissman.<sup>10</sup> He described this phenomenon for the europium (III) complexes of salicylaldehyde, benzoylacetone, dibenzoylmethane, and *meta*-nitrobenzoylacetone. Since, the mechanisms of the energy transfer from the organic ligand to the lanthanide ion were investigated in the early 1960s, many lanthanide complexes were prepared and studied. Lanthanide complexes can be formed by the chelation of lanthanide ions with many different classes of ligands for example cryptates, podands, calixarenes, carboxylic acids, macrocyclic ligands,  $\beta$ -diketones, heterobiaryl ligands, carboxylic acid derivatives, terphenyl ligands, pyridines, proteins, *etc.*<sup>11,12</sup>

In general, there are two types of lanthanide complexes. The first type of complex, is wherein the chelate/ligand backbone itself serves as both the coordination site for the lanthanide ion and also the sensitizer, to absorb light and consequently transfer energy to the bound lanthanide ion. Some of the examples of this type of complex include cryptands,  $\beta$ -diketone, terphenyl-based compounds, pyridine derivatives. In the second type of lanthanide complexes, the chelate that coordinate to the lanthanide ion and the reactive antenna/sensitizer are separate components. Polyaminocarboxylate chelates such as  $\text{Eu}^{3+}$  and  $\text{Tb}^{3+}$  complexes of cs124-DTPA, cs124-DOTA, cs124-TIHA are some of the examples of

this type of lanthanide complex. <sup>13</sup>In these complexes, DTPA or DOTA acts as multidentate chelates to tightly binds to lanthanide ion, shield it from quenching and act as scaffold for attachment of antenna molecule carbostyryl-124 (cs124). The organic chromophore cs-124, serves as an antenna or sensitizer, which absorbs the excitation light and transfers the energy to the lanthanide ion. Structures of some of the lanthanide complexes are shown in Figure 3.



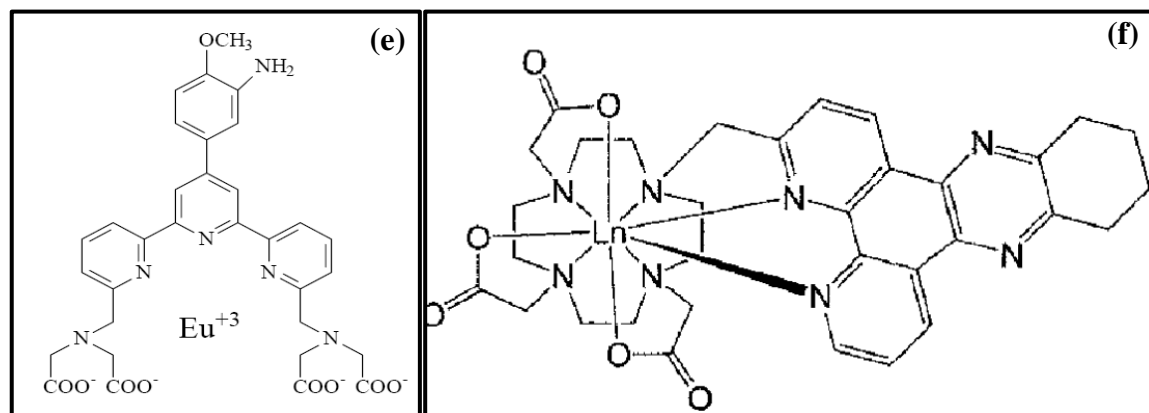


**Figure 3:** Examples of visibly luminescent lanthanide complexes for near-UV excitation. Clockwise starting from top left: (a)  $\text{Eu}^{3+}$  cryptate, (b)  $\text{Eu}$  (1,10-phenanthroline)-tris(4,4,4-trifluoro-1-(2-thienyl)butane-1,3-dionate),  $\text{Eu}(\text{TTA})_3\text{phen}$ , (c)  $\beta$ -diketonate complex, (d) cs124-DTPA-Tb, (e)  $\text{Eu}^{3+}$  Terpyridine and (f) an azatriphenylene-functionalized DOTA complex.

Lanthanide complexes have potential as the active component in chelate lasers, FRET based sensing probes, luminescent probes for cell imaging, organic light emitting diodes (OLED's) *etc.*<sup>14,15</sup> Thus, intense research has been going on in the field of luminescent materials based on molecular lanthanide complexes. However, lanthanide complexes have overcome the drawback of weak light absorption of lanthanide ions, but they are susceptible to photobleaching under intense and continuous excitation, thus suffers from poor photostability. Lanthanide complexes may also exhibit long term toxicity by leaching of  $\text{Ln}^{3+}$  ions and a low labelling ratio of  $\text{Ln}^{3+}$  per biomolecule.

### 1.2.2. Ln<sup>3+</sup>-doped glasses, ceramics and polymers:

For lasers and optical amplifiers applications, such materials are needed that have transparency in spectral region where light generation and amplification takes place. Glasses, ceramics and crystals have potential to meet these requirements. Lanthanide-doped glass-ceramic materials have well interest in the technological point of view due to its versatility regarding the possibility of a wide doping concentration and the narrow lines emission spectra of the lanthanide ions, when compared with transition elements. Since, in lanthanide ions 4*f* electrons are shielded by outer 5*s* and 5*p* orbitals, the positions of the 4*f* energy level are hardly dependent on the host lattice and they remain almost the same as for the free-ion. These properties are interesting for the development of new materials in lighting applications.<sup>16</sup> In such luminescent crystals materials, the “activating” lanthanide ions replace a small fraction of the ions of the host crystals. Glasses are usually fabricated by homogeneously mixing the precursor materials, melting them at high temperatures, cooling the melt to vitrify the material, followed by an annealing step before cutting and polishing. Glasses can be either doped with lanthanide ions, or lanthanide ions can be integral part of the glass forming composition. Fibers can be drawn from glass, and Er<sup>3+</sup>-doped glass fibers have long been used as amplifier units in fiber optic cables for telecommunications, as they can be used to amplify optical signals. The glass system provides a homogeneous host with a high solubility of the optically activated lanthanide ions. Various lanthanide ions (Eu<sup>3+</sup>, Tb<sup>3+</sup>, Yb<sup>3+</sup>, Er<sup>3+</sup>, Tm<sup>3+</sup>, Pr<sup>3+</sup>, Nd<sup>3+</sup>, Sm<sup>3+</sup> *etc.*) can and have been embedded in the different glass matrices such as fluorides, oxide, tellurites, silicates, phosphates, aluminophosphates, halides, and chalcogenide glasses, some of the examples includes; Eu<sup>3+</sup> doped germanotellurite (NZPGT) glasses, Li<sub>2</sub>O–BaO–Al<sub>2</sub>O<sub>3</sub>–La<sub>2</sub>O<sub>3</sub>–P<sub>2</sub>O<sub>5</sub> glasses, Eu<sup>3+</sup>, Dy<sup>3+</sup>: SrAl<sub>2</sub>O<sub>4</sub> glass, Er<sup>3+</sup>-

doped aluminum fluorophosphate glasses, Nd<sup>3+</sup>: Yttrium aluminium garnet (YAG) (Y<sub>3</sub>Al<sub>5</sub>O<sub>12</sub>), Tb: oxynitride (Si-Al-O-N) glass *etc.*<sup>17-21</sup> Similarly, ceramics are also predominantly used in lasers, optical telecommunication applications for example Nd:ThO<sub>2</sub>-Y<sub>2</sub>O<sub>3</sub> ceramics, Nd:YAG ceramics, Eu, Dy: SrAl<sub>2</sub>O<sub>4</sub> glass ceramics, *etc.*<sup>22,23</sup> In the same way lanthanide ions are either coordinated or doped into the polymer matrix, and also lanthanide complexes are doped into the polymers. Such lanthanide activated polymers finds potential applications in optical fibers, lasers and amplifiers. Polymers forms the flexible matrix for lanthanide doped films or fibers. Polymethylmethacrylate (PMMA) is the most common and widespread polymer which easily forms thin films and often used for designing various optical materials. For instance, Yb<sup>3+</sup> ions inserted into PMMA thin films and TPPO (triphenylphosphine oxide) adduct of Er<sup>3+</sup> pentafluorobenzoate co-polymerized with PMMA.<sup>24</sup> Recently, LnMOFs are embedded into the polymer, that can lead to novel transparent organic-inorganic hybrid materials, which can find potential applications in the field of optical devices such as lenses, filters and polarizers.<sup>25</sup> Lanthanide complexes such as Eu tris-(4,4,4,-trifluoro-1-(2 thenoyl)-1,3-butenedione) (Eu(TTFA)<sub>3</sub>) and (Tb(TTFA)<sub>3</sub>) complexes are also doped into the PMMA.<sup>26</sup> Glasses, ceramics and polymers are thermally stable and mechanically strengthened materials for lighting applications.

### 1.2.3. Ln<sup>3+</sup>-doped nanoparticles “nanophosphors”

Inorganic hosts such as glasses and crystals have less effective non-radiative deactivation channels for excited lanthanide ions than do molecular hosts. Ln<sup>3+</sup>-doped NPs are composed of a stable inorganic host and Ln<sup>3+</sup> emitters embedded in the host lattice, thus, are expected to be more photostable. For biological and several new material applications it is important and need to have objects with the luminescent properties of inorganic phosphors



but with sizes of several nanometers and with similar solubility and physicochemical behaviour. Such Ln<sup>3+</sup>-doped “nanophosphors” are currently under active development. As compared to Ln<sup>3+</sup>-chelates, inorganic Ln<sup>3+</sup>-doped nanocrystals (NCs), exhibits many technical advantages such as higher resistance to photobleaching, more luminescent ions in a single NC-label, more flexibility for bioconjugation, and desirable surface modification, simultaneously as preserving the spectroscopic properties of Ln<sup>3+</sup> luminescence.<sup>27,28</sup> Specifically, the rigid inorganic lattice of Ln<sup>3+</sup>-doped NCs is able to protect the dopants from luminescence quenching by high-energy vibrational groups, thus facilitating intense luminescence from almost all the emitting Ln<sup>3+</sup> ions.<sup>29</sup> Moreover, the rigid lattice prevents leaching of Ln<sup>3+</sup> ions rendering the Ln<sup>3+</sup>-doped NCs considerably less toxicity. Another important feature of Ln<sup>3+</sup>-doped NCs is that, by judicious selection of two or more lanthanide dopants (Eu<sup>3+</sup>- red, Tb<sup>3+</sup>/Er<sup>3+</sup>- green, Dy<sup>3+</sup>/Tm<sup>3+</sup>- blue emissions) and host, multicolor labeling and white emission for sensing and white LED's can be achieved. Moreover, via successive photon absorption and energy transfer between Ln<sup>3+</sup> dopants, anti-Stokes upconverting luminescence, a non-linear process can be generated in Ln<sup>3+</sup>-doped NCs. Some of the pioneering researches in field of Ln<sup>3+</sup>-doped rare earth phosphors are mentioned. Earlier, the studies and development of phosphors were limited for their lasers and display applications. In early 1967, yellow emitting Ce<sup>3+</sup>-activated Y<sub>3</sub>Al<sub>5</sub>O<sub>12</sub> phosphor was developed for cathode-ray tubes, especially for color television.<sup>30</sup> Later, in 1989 W.T. Carnall had studied in detail and analysed the optical spectra of lanthanide ions doped into the single crystal LaF<sub>3</sub>.<sup>31</sup> They also established correlations between the experimental transition energies and the computed level structures. Till the end of 1990's, bulk or single crystals of phosphors were studied and majorly used in lighting applications. But, owing to their unique optical

properties these also promise for other new applications, thus research turned toward nanophase synthesis and dispersible phosphors. Most lanthanide ion-doped nanoparticles are made in high-temperature procedures leading to particles without organic groups on the surface and therefore they have no dispersibility in solvents. In 2002, Veggle et al have prepared Ln<sup>3+</sup>-doped LaF<sub>3</sub> nanoparticles with good dispersibility in organic solvents.<sup>32</sup> In 2006, Veggle again developed water soluble amine functionalized luminescent LaF<sub>3</sub>:Ln<sup>3+</sup> nanoparticles for imparting biological activity.<sup>33</sup> Subsequently, many studies progressed towards the synthesis of uniform, monodispersed crystals, their morphology tuning by varying synthesis parameters and studying their optical properties. Yang et al, in 2007 prepared series of NaREF<sub>4</sub> (RE = Y, Pr–Nd, and Sm–Yb) nanocrystals with multiform morphologies and studied shape evolution under varied synthesis parameters.<sup>34</sup> Thereafter, a good deal of Ln<sup>3+</sup>-doped multifunctional hybrids materials were developed for broad range of applications including bioimaging, sensing, biomedical diagnostics, solar cells, security printing *etc.*

### **1.3. Structure and strategies for enhancing luminescence of rare earth phosphors**

In general, the structure of phosphors consists of a suitable host and the lanthanide dopants as activator and sensitizer. The selection of host material and dopant combination is essential to achieve bright luminescence from phosphors.

#### **1.3.1. Host lattice**

The selection of suitable host material is essential in preparation of lanthanide ion-doped phosphors for attaining the favorable optical properties such as high luminescence efficiency and controllable emission profile. The ideal host lattice should exhibit lattice

match, low phonon energy, wide band gap, high refractive index and chemical stability<sup>35</sup> (Figure 5).

**1. Lattice match:** The host materials generally require close lattice match with dopant lanthanide ion. Since, all trivalent rare earth ions possess similar ionic size and chemical properties, thus their inorganic compounds are considered to be ideal host materials for luminescent lanthanide dopant ions. In addition, ions such as  $\text{Ca}^{2+}$ ,  $\text{Na}^+$ ,  $\text{Sr}^{2+}$ , and  $\text{Ba}^{2+}$  also exhibit close ionic size to lanthanide ions that prevents the formation of crystal defects and lattice stress. Therefore, inorganic compounds containing these ions are also frequently used as host materials. Few semiconductor materials such as  $\text{ZnS}$ ,  $\text{CdS}$ ,  $\text{TiO}_2$ ,  $\text{BaTiO}_3$ , *etc* have also been proposed to be a host lattice, but in these host systems it is still debatable that, whether lanthanide ions remains at periphery or embedded homogenously into the lattice due to large lattice mismatch of ionic size between host and dopant ion.<sup>36</sup>

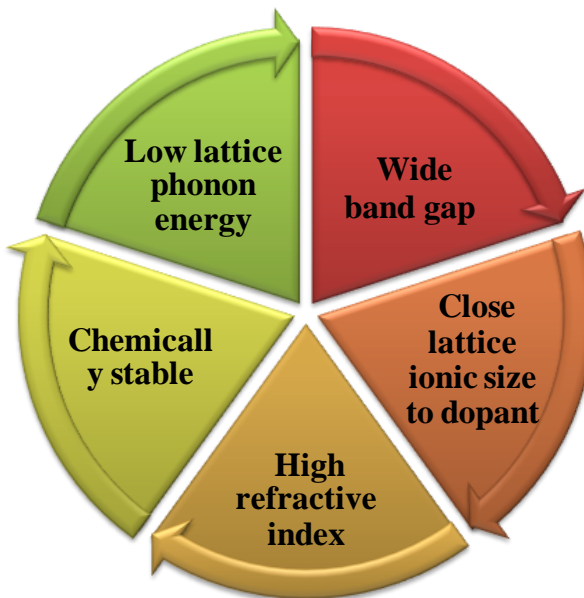


**Figure 5:** Criteria for an ideal host matrix for enhanced luminescence of lanthanide ions.

**2. Low phonon energy and wide band gap:** Low phonon energy of host lattice is required to minimize the non-radiative decay and maximize the radiative emission. The low phonon energy and wide band gap of host lattice enhances the luminescence efficiency of lanthanide dopant ions by reducing the multiphonon non-radiative relaxation process. Multiphonon relaxation can rapidly depopulate the upper excited state and therefore readily quench luminescence.<sup>37</sup> The multiphonon relaxation rate constant  $k_{nr}$  is described as below for  $4f$  levels of lanthanide ions:<sup>38</sup>

$$K_{nr} \propto \exp\left(-\beta \frac{\Delta E}{h\omega_{max}}\right)$$

where,  $\beta$  is an empirical constant of the host,  $\Delta E$  is the energy gap between the populated level and the next lower-lying energy level of a lanthanide ion, and  $h\omega_{max}$  is the highest energy vibrational mode of the host lattice. The energy gap law implies that the multiphonon relaxation rate constant decreases exponentially with increasing energy gap, subsequently enhancing radiative transition and luminescence.<sup>38</sup>

**3. High refractive index and high chemical stability:** The refractive index (R.I) mismatch of the host (phosphor particle) and the surrounding medium should be minimum. The large refractive index mismatch between the host and surrounding medium may lead to high reflectance losses of emitted light at particle-surrounding medium interface, which can result in reduced optical efficiency. Keeping Fresnel reflection law in mind, typically the reflectance loss is supposed to be minimum if refractive index of host is greater the surrounding medium (air/water). If the R.I of host is low, the portion of emitted light that is back reflected is most likely reabsorbed. Even of some portion of the reabsorbed light is re-emitted, another fraction of the reabsorbed portion is lost through non-radiative emissions.

Consequently, the high reflective loss leads to significant reduction of emitted light from the light-emitting phosphor. Similarly, the host is required to be chemically stable to retain the dopant ions without perturbing its emission.

Apart from above mentioned criteria, charge compensation and structure of crystal lattice are important too. Upon incorporation of dopant ion, the host must maintain the charge neutrality to prevent crystal defects. Moreover, the distance between the lanthanide ions in the host lattice should be appropriate to render efficient energy transfer.

### 1.3.2. Dopant system

The lanthanide ion dopants are incorporated into the inorganic host crystals are the localized luminescence emission centers. By doping different lanthanide ions, the phosphors can emit strong down-conversion (DC) or up-conversion (UC) luminescence. Although the luminescence is theoretically expected from all the lanthanide ions, but lanthanide ions such as  $\text{Eu}^{3+}$ ,  $\text{Tb}^{3+}$ ,  $\text{Dy}^{3+}$  are common efficient DC emitters and  $\text{Yb}^{3+}$ :  $\text{Er}^{3+}$ ,  $\text{Tm}^{3+}$ ,  $\text{Ho}^{3+}$  are known to be efficient UC emitters. The two main considerations while choosing dopant ions are:

1. **Ionic size:** The ionic size of dopant ions should be close to the host ions. Different sized dopant ions could dramatically influence the crystal field splitting and coordination environment of lanthanides *via* contraction or expansion of host lattice (Figure 6).<sup>39</sup>

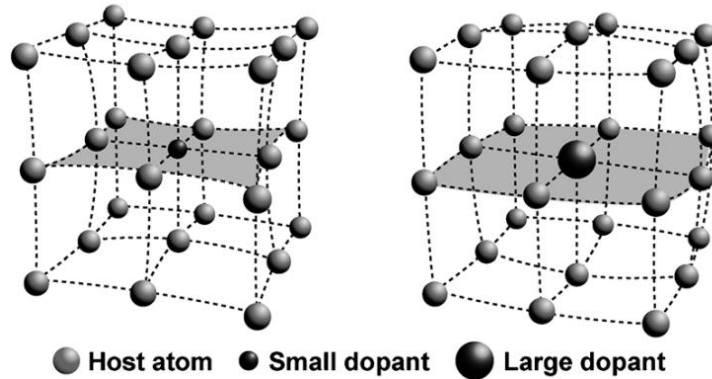


**Figure 6:** Crystal lattice contraction (left) and expansion (right) as a result of the substitution of a host atom with a dopant of varied size.

2. **Dopant concentration:** Lanthanide-ion doping in host lattice is always accompanied by the formation of crystal defects such as interstitial cation and anion occupation and vacancy to maintain the charge neutrality.<sup>39</sup> Thus, to maintain the single crystal phase of the host lattice the dopant concentration has to be controlled strictly. Moreover, the higher concentration of dopant ions leads to clustering and consequent radiationless deactivation and cross-relaxation among the neighbouring dopant ions resulting in luminescence quenching. Thus, lower dopant concentration is favourable to prevent luminescence quenching.

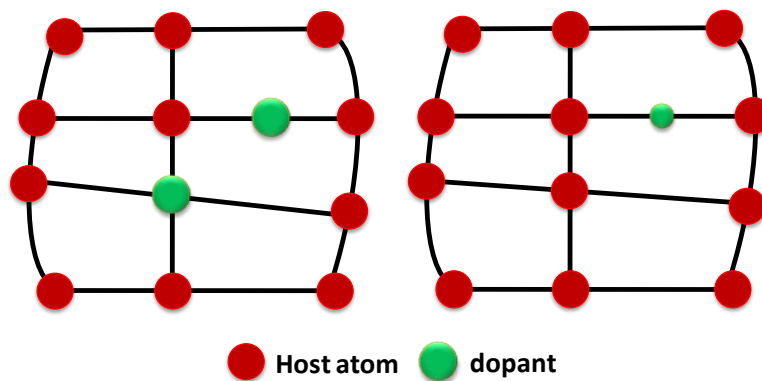


**Figure 7:** Effect of dopant concentration and size on host lattice: interstitial occupation by a small atom (right) and combination of substitution and interstitial occupation (left).

The lanthanide ions can be singly doped or co-doped into the host lattice and resulting luminescence can be achieved by direct excitation (upon single doping) or indirect excitation (co-doping), respectively. The dopant system consists of an activator or combination of activator and sensitizer.<sup>36</sup>

### **1.3.2.1. Activator:**

An activator is a foreign dopant ion which when integrated into a host lattice gives rise to a center which can be excited to luminescence. The lanthanide dopant ion is excited by desirable excitation wavelength, it absorbs and excite from its ground state to the higher excited state and consequently emit radiatively. If within one ion energy gaps between three or more subsequent energy levels are very close enough to facilitate photon absorption and subsequent energy transfer steps, useful emission can be generated. Lanthanide ions such as  $\text{Er}^{3+}$ ,  $\text{Eu}^{3+}$ ,  $\text{Tm}^{3+}$ ,  $\text{Tb}^{3+}$ ,  $\text{Ho}^{3+}$  typically possess ladder like energy levels, are thus frequently used activators.

The below figure 8 shows the schematic representation of a phosphor which contains an activator. The activator creates a center which absorbs excitation energy and converts it into visible radiation.

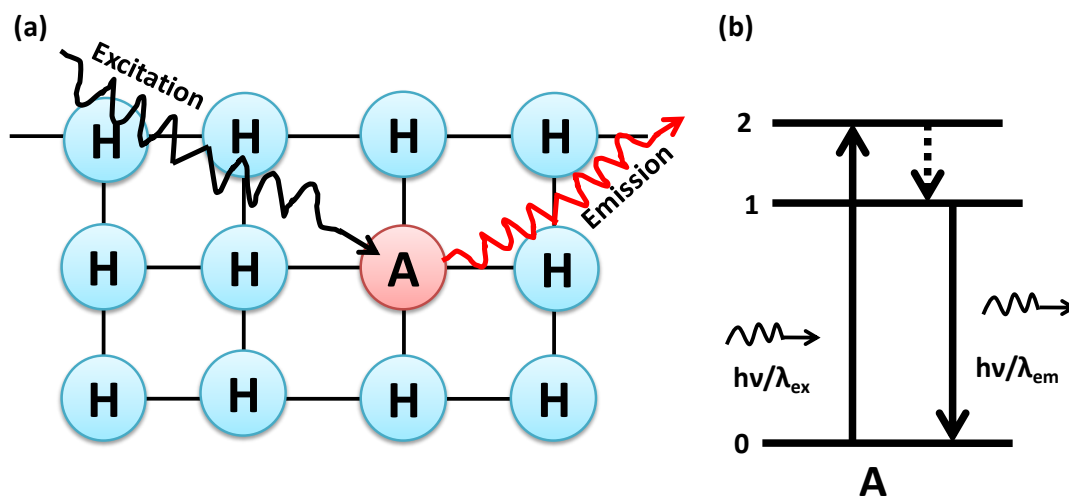


**Figure 8:** Schematic diagram representation of (a) the role in the luminescence process of the activator (A) doped in a host (H) lattice and (b) energy level diagram of the activator A and the emission mechanism of photoluminescence under excitation.

### 1.3.2.2. Sensitizer

The sensitizer is a dopant ion which when incorporated in host lattice is capable of transferring its excitation energy to the neighboring activator dopant ion. In certain instances, the lanthanide activator ion with the desired emission does not exhibit a significant absorption cross-section in the available excitation region. In such circumstances, to increase the absorption of lanthanide-doped phosphors, the materials are often additionally doped with strongly absorbing ions called sensitizers, which absorbs the excitation energy and transfer efficiently non-radiatively to the activator ion, which can emit its characteristics luminescence (Figure 9). In the sensitized luminescence, the dopant ion radiates upon its excitation to a higher energetic state obtained from the non-radiative transfer of the energy from another dopant ion. Thus, the ion that emits the radiation is called an activator, while the



donator of the energy is the sensitizer.  $Ce^{3+}$ ,  $Gd^{3+}$  and  $Yb^{3+}$  are common UV and NIR sensitizers, respectively.<sup>40</sup> The sensitizer content is normally kept high in doubly or triply doped nanocrystals so that to maximally absorb excitation energy and transfer to activator ion, while the activator content is relatively low, to minimize the cross-relaxation energy loss.<sup>35</sup>

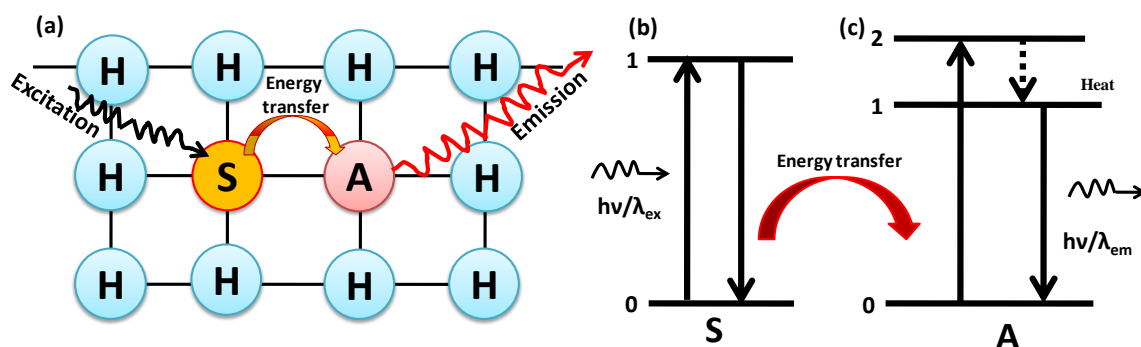


**Figure 9:** Diagrammatic representation of the role in the luminescence process of a sensitizer (S) and its relationship to an activator (A) and the host lattice (H).

#### 1.4. Classification of rare earth phosphors based on emissive transition pathways

The primary forbidden nature of intra- $4f$  transitions in lanthanide ions yields metastable energy levels of lanthanide ions, which favors the occurrence of sequential excitations in excited states of a single lanthanide ion as well as it permits favourable ion-ion interactions in excited states to allow energy transfers between two or more lanthanide ions.<sup>41</sup> According to the involved transition pathways, the luminescence process of  $Ln^{3+}$  ions and their corresponding  $Ln^{3+}$ -doped phosphors are broadly classified into three main categories: 1) Down-conversion, 2) Down-shifting and 3) Up-conversion phosphors.

### 1.4.1. Down-conversion

Down-conversion process is a conventional Stokes type process where one high energy photon is converted to two or more lower energy photons as depicted in Figure 10 (a). Thus, in  $\text{Ln}^{3+}$ -doped down-conversion phosphors, material is excited by high energy photons (shorter wavelength) and emit two or more lower energy photons (longer wavelength).<sup>42</sup>

### 1.4.2. Down-shifting

Downshifting process also feature Stokes emission like down-conversion where excitation with high energy is required, with only an important difference is that only one low energy photon is emitted from absorption of one high energy photon as depicted in Figure 10 (b).<sup>43</sup>

### 1.4.3. Up-conversion

Up-conversion is anti-Stokes emission process, in which two or more low energy excitation photon is converted to one high energy photon through sequential absorption of multiple photons or energy transfer steps as depicted in Figure 10 (c).<sup>44</sup> The  $\text{Ln}^{3+}$ -doped up-conversion phosphors, are the materials where the material is excited by low energy light (longer, usually NIR wavelength), and it emits the high energy light (shorter, usually visible wavelength).

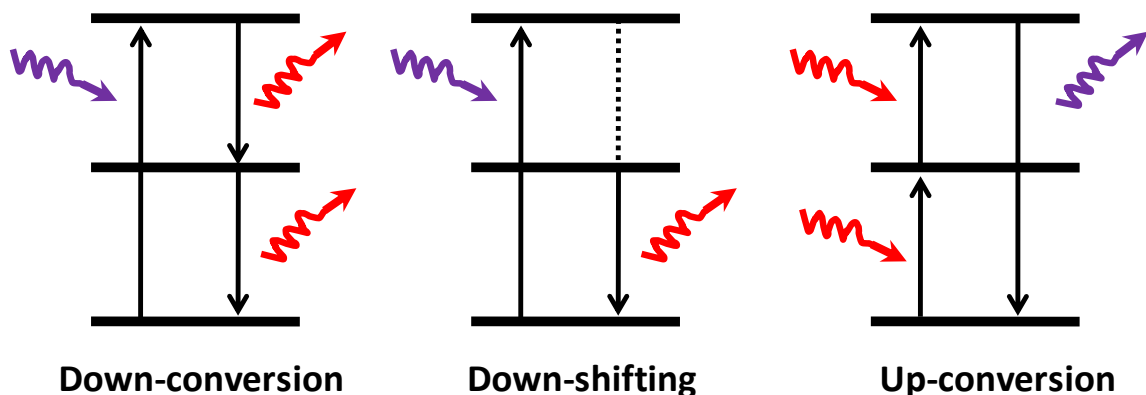


**Figure 10:** Energy diagrams showing photon absorption and subsequent down-conversion, downshifting, and up-conversion.

#### 1.4.4. Mechanism of down- and up-conversion emission

Down-conversion was theoretically suggested first by Dexter in the 1950s<sup>45</sup> and then after 20 years later it was shown experimentally using the praseodymium ( $\text{Pr}^{3+}$ ) ion-doped yttrium fluoride ( $\text{YF}_3$ ).<sup>46</sup>  $\text{Pr}^{3+}$  ion-doped yttrium fluoride was excited by 185 nm which was absorbed by the host, and its energy is transferred into the  $^1\text{S}_0$  state of the  $\text{Pr}^{3+}$  ion, from where two photons are emitted at 408 and 620 nm in a two-step process ( $^1\text{S}_0 \rightarrow ^3\text{P}_J$  at 408 nm followed by  $^3\text{P}_J \rightarrow ^3\text{F}_2$  at 620 nm).<sup>46</sup> In this way a single absorbed high energy photon results in the emission of two visible photons and the quantum efficiency was found to be higher than unity as mentioned in section 1.4.1. In nutshell, down-conversion is a linear, Stokes emission process, mechanism of which involves the absorption of high energy photon by an optically active material, resulting in conversion to low energy photon *i.e* the emitted wavelength is greater than the incident wavelength as depicted by figure 11. Based on their unique and rich energy level structure as discussed in section 1.1.2., lanthanide ions are promising candidates to realize efficient down-conversion luminescence process.

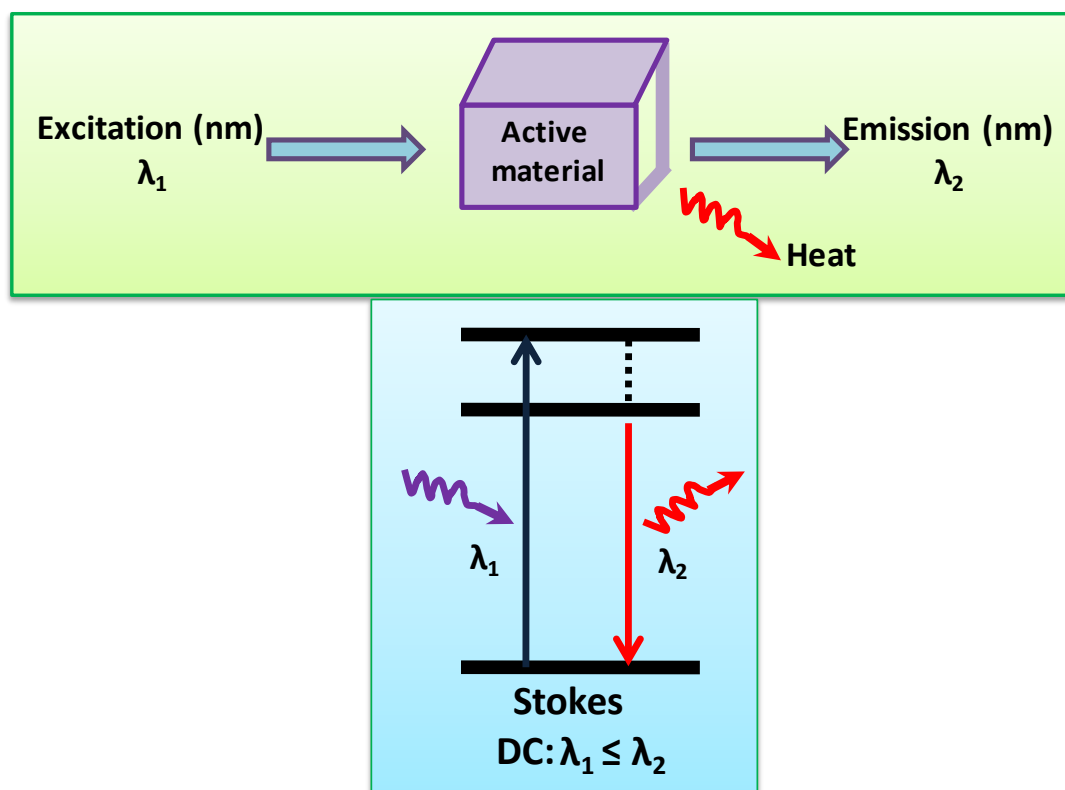


**Figure 11:** Schematic illustration of down-conversion (DC) process.

Up-conversion refers to non-linear optical, anti-Stokes emission process and is characterized by the conversion of long-wavelength radiation, for instance infrared or near infrared (NIR) radiation, to short-wavelength radiation, usually in the visible range. Notably, the general concept and a landmark experiment to witness upconverted visible emission was first recognized, formulated and reported by Francois Auzel in 1966. It was based on energy transfer between two lanthanide ions through the use of  $\text{Yb}^{3+}$  to sensitize  $\text{Er}^{3+}$  and  $\text{Tm}^{3+}$ .<sup>47</sup>

Unlike two photon absorption and second harmonic generation, photon up-conversion features sequential rather than simultaneous absorption of two or more photons *via* intermediate long-lived energy states followed by emission of light at shorter wavelength

than the excitation wavelength. There are three main processes causing up-conversion emission in rare earth-doped materials, viz. excited state absorption (ESA), energy transfer up-conversion (ETU), and photon avalanche (PA) processes. All are based on the sequential absorption of two or more photons.<sup>48</sup>

**1.) Excited state absorption (ESA):** The principle of ESA was proposed by Bloembergen in 1959.<sup>49</sup> ESA involves the successive absorption of two photons in one single ion. The first photon absorption process occurs at the energetic ground state (G) to enter in intermediate excited state and is induced by a resonant photon (ground state absorption (GSA)). It leads to the population of the metastable and long-lived E1 state. The second resonant absorption promotes the ion from E1 to the higher excited state E2, from which the emission occurs corresponding to the E2 → G transition.

**2.) Energy transfer up-conversion (ETU):** Unlike ESA process, the principle of ETU is based on energy transfer between two adjacent ions. The ETU process involves a sequential absorption of two photons that transfer energy from an excited ion (sensitizer or donor) to another neighboring ion (activator or acceptor). Each of two ions is excited via GSA to its metastable E1 state. Thereafter, the excited state energy is transferred non-radiatively (by resonant energy transfer) to the adjacent activator ion (also in the E1 state). The sensitizer/donor ion relaxes to its ground state G while the activator/acceptor ion is promoted to the excited state E2. This is followed by an emissive transition E2 → G again. ETU is by far the most efficient process, but the dopant concentration that determines the average distance between the neighboring dopant ions has a strong influence on the UC efficiency of an ETU process.

3.) **Photon avalanche (PA):** Photon avalanche, is more complex than the first two and only occurs when the pump photon intensity reaches a critical level. The phenomenon of PA was first discovered by Chivian and co-workers in  $\text{Pr}^{3+}$ -based infrared quantum counters. In the first step, weak non-resonant GSA occurs, followed by a resonant ESA at one ion which thus is promoted to energy state E2. A cross-relaxation energy transfer to an adjacent ion in its ground state results in both ions occupying E1. Further resonant ESA and cross-relaxation energy transfers exponentially increase the population of E2 and eventually it acts as reservoir for energy such that avalanche of ion population takes place at E2. Therefore up-conversion emission intensity also increases exponentially.

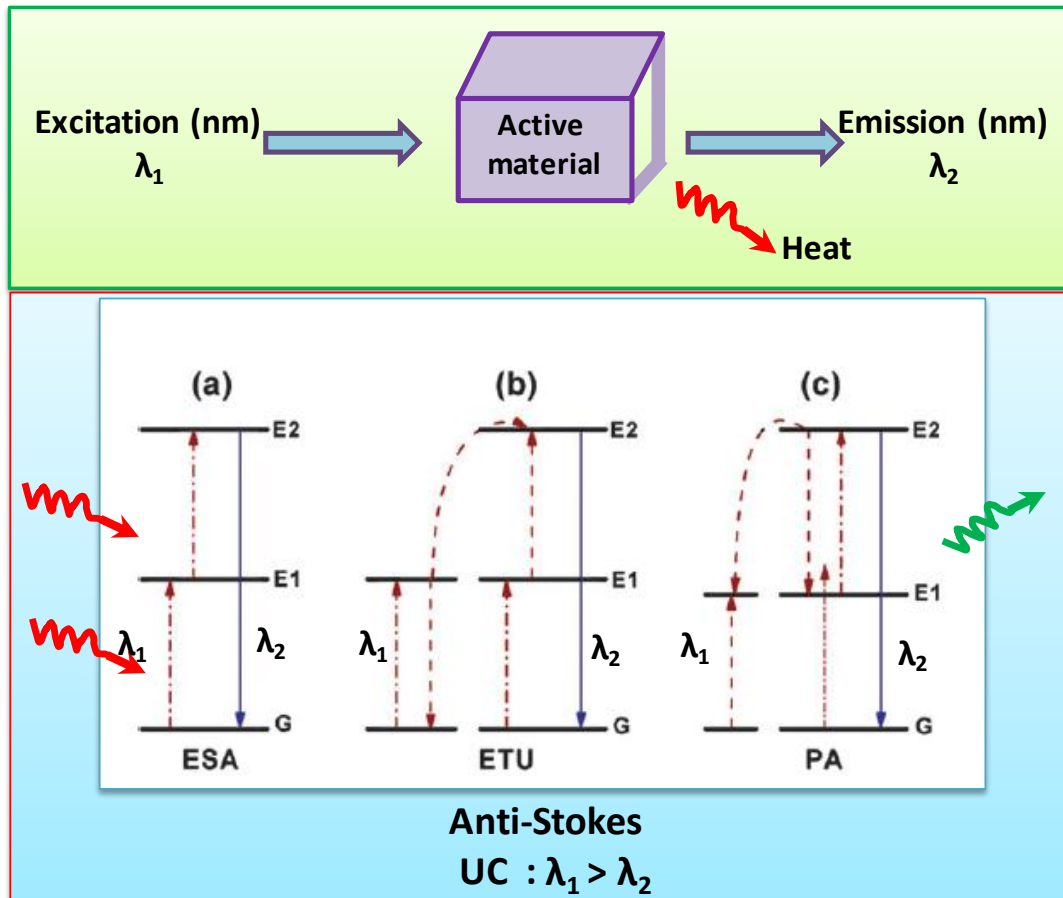


**Figure 12:** Principal UC processes for lanthanide-doped crystals: (a) excited state absorption,

(b) energy transfer up-conversion, (c) photon avalanche. The dashed/dotted, dashed, and full arrows represent photon excitation, energy transfer, and emission processes, respectively.

### 1.5. Various host matrices: “Fluoride Hosts Preferred”

Upto now, various host matrices have been used for different lanthanide ions. Few of them are listed in Figure 13, which includes oxides, hydroxides, phosphates, vanadates; orthovanadates, tungstate-molybdates, nitrides; oxynitrides, sulphides, halides, fluorides; oxyfluorides, borates, aluminates *etc.* Among these host matrices, heavy halides like chlorides, bromides and iodides generally exhibit low phonon energies of less than 300  $\text{cm}^{-1}$ . However, they are sensitive to moisture, thus of limited use. Oxides, phosphates present the desired chemical stability, but conventional oxygen based systems exhibit relatively high phonon energies generally larger than 500  $\text{cm}^{-1}$  due to the strong metal-oxygen stretching vibration of the host lattice. In comparison, fluorides usually exhibit low phonon energies ( $\sim 350 \text{ cm}^{-1}$ ) due to high ionicity of fluorine compared to other halides and oxides. Fluoride lattices permits high coordination numbers for hosted lanthanide ions. Moreover high ionicity of the rare earth-to-fluorine ( $\text{RE}^{3+} - \text{F}^-$ ) bonds leads to wide band gap and low phonon energy.<sup>50</sup> Fluorides also exhibits high chemical stability, and thus are often used as the host materials for lanthanide ion- doped phosphors.

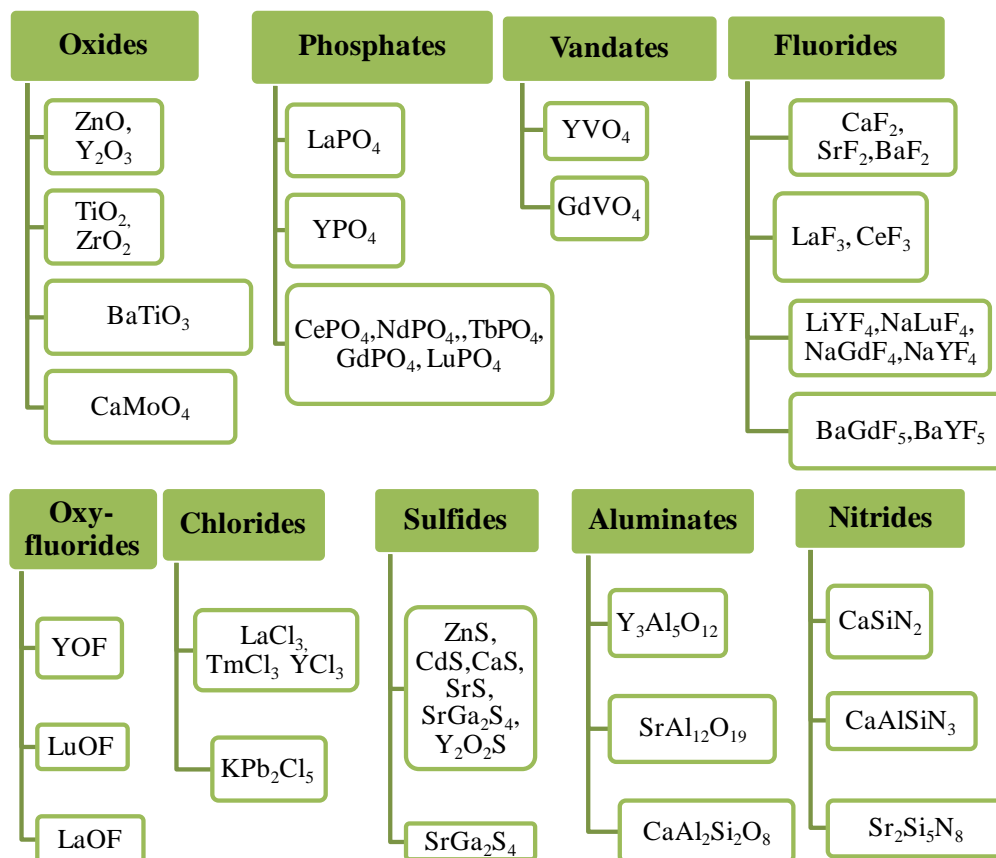


**Figure 13:** Various host matrices used for different luminescent lanthanide ion-doped phosphors.

### 1.6. Why $\beta$ -NaYF<sub>4</sub> is so special?

Among various host matrices mention above, rare earth fluorides including binary RE<sub>3</sub> and complex AREF<sub>4</sub> (RE=Rare earth, A=Alkali) have been considered as an excellent rigid host matrix for luminescence of various lanthanide ions, because of some distinct advantages of low phonon energy, high refractive index, wide band gap and high chemical stability.<sup>51</sup> Among the investigated fluorides, ternary metal fluoride NaYF<sub>4</sub>, has been demonstrated to be one of the most efficient host lattices for down-conversion (DC) and up-



conversion (UC) phosphors, thus has attracted tremendous attention in the field of material sciences.<sup>52</sup> The sodium yttrium fluoride ( $\text{NaYF}_4$ ) is deemed to be most promising due to its relatively low phonon energy as compared to popularly used host matrices for phosphors as listed in Figure 14.<sup>53–56</sup>

Host matrix	Highest phonon energy ( $\sim \text{cm}^{-1}$ )
phosphate glass	1200
silica glass	1100
Chalcogenide glass	400
fluoride glass	550
$\text{LaPO}_4$	1050
YAG	860
$\text{NaGd}(\text{WO}_4)_2$	900
$\text{YVO}_4$	600
$\text{LaF}_3$	400
$\text{NaYF}_4$	360
$\text{NaGdF}_4$	350
$\text{LiYF}_4$	570
$\text{LaCl}_3$	240

**Figure 14:** Table of selected lattice phonon energies of commonly used matrices for  $\text{Ln}^{3+}$  doping.

Moreover,  $\text{NaYF}_4$  possess wide band gap ( $\sim 8 \text{ eV}$ )<sup>57</sup> and high refractive index ( $n \sim 1.5$ )<sup>58</sup> which is beneficial to enhance the luminescence of lanthanide ions as described in section 1.3.1. It is well demonstrated that the crystals of  $\text{NaYF}_4$  exist in two polymorphic forms of phase structures namely: cubic ( $\alpha\text{-NaYF}_4$ ) and hexagonal ( $\beta\text{-NaYF}_4$ ) system, depending on the synthesis conditions and methods. The  $\alpha\text{-NaYF}_4$  is high-temperature metastable, while  $\beta\text{-NaYF}_4$  is thermodynamically stable phase.<sup>59,60</sup> The cubic phase  $\alpha\text{-NaYF}_4$

is transformed to hexagonal phase  $\beta$ -NaYF<sub>4</sub> under high temperature heat treatment and long aging time. To date, hexagonal phase  $\beta$ -NaYF<sub>4</sub> is regarded as better and efficient host lattice than the cubic  $\alpha$ -NaYF<sub>4</sub> for the luminescence of various optically active lanthanide ions.<sup>61,62</sup> The high efficiency of luminescence in the hexagonal form is due to its multisite character of the crystal lattice.<sup>63</sup> The high luminescence efficiency of hexagonal phase  $\beta$ -NaYF<sub>4</sub> is due to its crystal structure, which is explained in the next section.

### **1.7. Crystal structure of $\beta$ -NaYF<sub>4</sub> : The reason why is hexagonal phase $\beta$ -NaYF<sub>4</sub> more efficient than the cubic $\alpha$ -NaYF<sub>4</sub>**

The crystal structure of cubic phase sodium yttrium fluoride  $\alpha$ -NaYF<sub>4</sub> with space group  $Fm\bar{3}m$  is a derivative CaF<sub>2</sub> fluorite type contain one type of high-symmetry cation site with the Ca<sup>2+</sup> sites (4a) randomly occupied by Na<sup>+</sup> and RE<sup>3+</sup> ions in the cationic sublattice. The nearest-neighboring ions around Y<sup>3+</sup> on site 4a are 8 F<sup>-</sup>, and the second-nearest-neighboring ions are 6 Na<sup>+</sup> and 6 Y<sup>3+</sup>. The crystallographic symmetry for Y<sup>3+</sup> ions on site 4a is O<sub>h</sub> (Figure 15a). In contrast, the crystal structure of hexagonal phase  $\beta$ -NaYF<sub>4</sub> with space group  $P6_3/m$  consists of an ordered array of F<sup>-</sup> ions with three types of relatively low-symmetry cation sites selectively occupied by Na<sup>+</sup> and RE<sup>3+</sup> ions: a one-fold site occupied by RE<sup>3+</sup> (1a), another nine-fold coordinated site occupied randomly by  $\frac{1}{2}$  Na<sup>+</sup> and  $\frac{1}{2}$  RE<sup>3+</sup> (1f) which is coordinated by nine nearest-neighboring F<sup>-</sup> ions in the shape of a tricapped trigonal prism and 2 Na<sup>+</sup> and 6 Y<sup>3+</sup> in the second-nearest-neighboring shell, and a six-fold coordinated site occupied randomly by Na<sup>+</sup> and vacancies (2h) on third kind of site. Sites 1a and 1f both have C<sub>3h</sub> symmetry, whereas site 2h has C<sub>s</sub> symmetry.<sup>64–66,51</sup>

The optical transitions of  $\text{Ln}^{3+}$  dopants are sensitive to their local coordination, and the emission intensity of  $\text{Ln}^{3+}$ -based compounds strongly depends on the crystal structure and crystal-field (CF) surroundings around  $\text{Ln}^{3+}$ .<sup>64</sup>

The hexagonal phase  $\beta$ - $\text{NaYF}_4$  crystal structure is said to be more efficient than the cubic  $\alpha$ - $\text{NaYF}_4$  because of the following probable reasons: (1.) The selective occupation of  $\text{Na}^+$  and  $\text{RE}^{3+}$  ions at low symmetry cationic sites of  $\beta$ - $\text{NaYF}_4$  results in significant electron cloud distortion of the cations to accommodate the structural change.<sup>65</sup> (2.) Relatively low symmetry of  $\beta$ - $\text{NaYF}_4$  can easily accommodate the lanthanide ions ( $\text{Ln}^{3+}$ ) with small lattice variations which provides a flexible framework for multidopants for highly efficient luminescence.<sup>67</sup> (3.) The asymmetrical crystal field that is lower crystal symmetry of  $\beta$ - $\text{NaYF}_4$  structure around  $\text{Ln}^{3+}$  ions greatly increases the probability of electric dipole transition thus enhancing the luminescence efficiency.<sup>68</sup> (4.) The limiting feature of reduced luminescence efficiency of cubic  $\text{NaYF}_4$  is due to the random distribution of  $\text{Na}^+$  and  $\text{RE}^{3+}$  in the lattice. While, an highly ordered cation distribution in the hexagonal lattice minimizes energy loss channels by non-harmonic phonon modes due to strong coupling of distorted electron cloud at low symmetry sites with lattice.<sup>69</sup> The symmetry of spectroscopic sites for the  $\text{Ln}^{3+}$  dopants was observed to deviate from that of the crystallographic sites. Based on the microscopic model of disorder, upon  $\text{Ln}^{3+}$  ion doping into the  $\alpha$ - $\text{NaYF}_4$ , the local site symmetry of each subset of  $\text{Ln}^{3+}$  will be reduced from  $\text{O}_h$  to  $\text{C}_s$ . In  $\beta$ - $\text{NaYF}_4$  the local site symmetry of all  $\text{Ln}^{3+}$  subsets will descend from  $\text{C}_{3h}$  to  $\text{C}_s$ .<sup>64</sup> The significant change in the observed spectral patterns for  $\text{Ln}^{3+}$ -doped in  $\alpha$ - $\text{NaYF}_4$  and  $\beta$ - $\text{NaYF}_4$  crystals is exemplified in Figure 15. The sharp and distinct spectra can be clearly observed in  $\beta$ - $\text{NaYF}_4$  as compared to  $\alpha$ - $\text{NaYF}_4$ .<sup>70</sup>

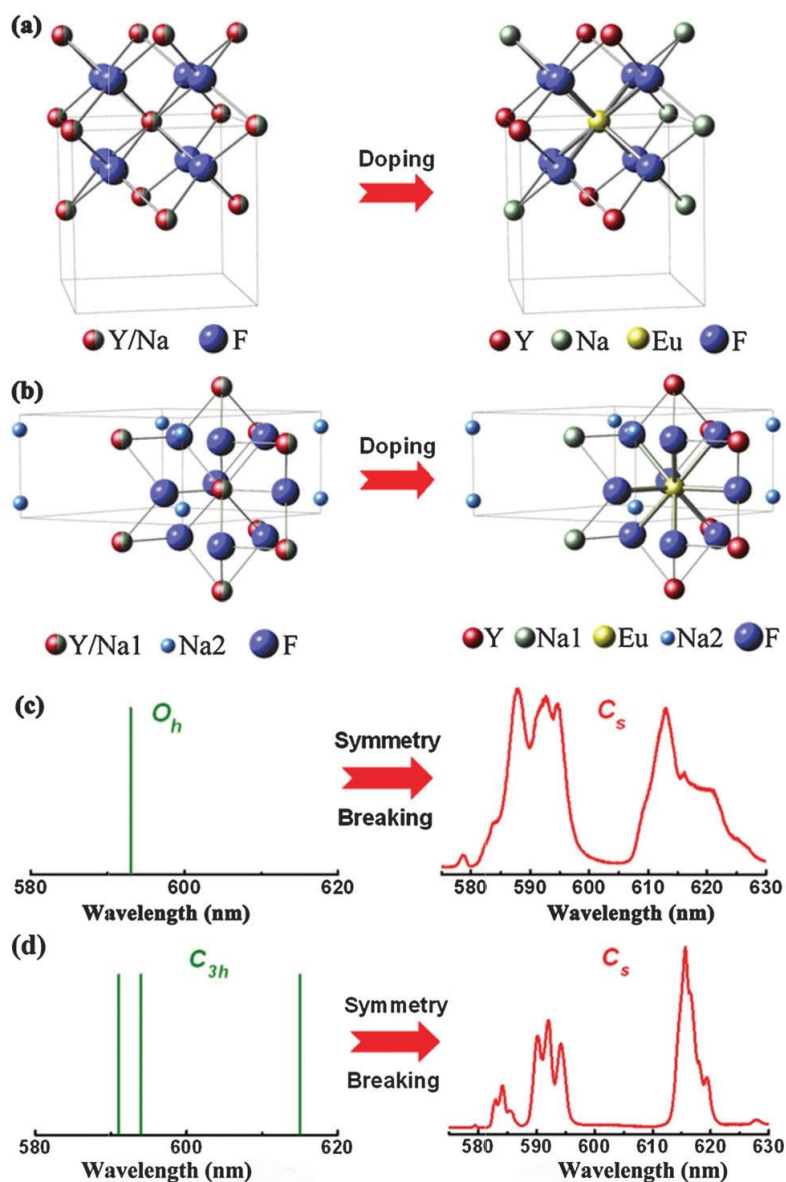


**Figure 15:** Schematic illustration showing the breakdown of the crystallographic site symmetry of  $\text{Eu}^{3+}$  in (a)  $\alpha\text{-NaYF}_4$  and (b)  $\beta\text{-NaYF}_4$  crystals. As induced by  $\text{Ln}^{3+}$ -doping for the disordered Y/Na site, the original crystallographic site symmetries of  $O_h$  in (a) and  $C_{3h}$  in (b) are distorted to  $C_s$  and  $C_s$ , respectively, as exemplified by the significant change in the

observed and theoretical predicted spectral patterns for  $\text{Eu}^{3+}$  -doped into (c)  $\alpha$ - $\text{NaYF}_4$  and (d)  $\beta$ - $\text{NaYF}_4$  crystals.

## 1.8. Properties of rare earth doped nanoparticles

### 1.8.1. Optical properties

Lanthanide ion-doped luminescent inorganic materials are tremendously undergoing widespread investigations in many fields of material and bio-sciences due to their superior physicochemical and optical properties. Moreover, these are considered to be a better alternative to conventional organic fluorophores, proteins and quantum dots which suffers from photobleaching, toxicity, broad emission profiles, interference of background noise, *etc.* In contrast, lanthanide ion-doped luminescent materials possess following optical and physicochemical features:

#### 1.8.1.1. Unique optical features

The intricate optical properties of lanthanide ions originates from unique feature of their parity forbidden electronic transitions within  $[\text{Xe}] 4f^N$  ( $N = 0-14$ ) electronic configuration.

**1.) Emissive transitions in broad spectral region:** This unique electronic structure involving radiative intra  $4f$  and  $4f-5d$  transitions, enables  $\text{Ln}^{3+}$  as excellent luminescent centres in inorganic crystals to emit photons efficiently in a broad spectral region covering from UV (e.g.,  $\text{Gd}^{3+}$  and  $\text{Tm}^{3+}$ ) to visible (e.g.,  $\text{Eu}^{3+}$ ,  $\text{Tb}^{3+}$ ,  $\text{Dy}^{3+}$  and  $\text{Sm}^{3+}$ ) and NIR (e.g.,  $\text{Nd}^{3+}$ ,  $\text{Yb}^{3+}$ ,  $\text{Ho}^{3+}$  and  $\text{Er}^{3+}$ ) as represented in Figure 16.<sup>40,71</sup>

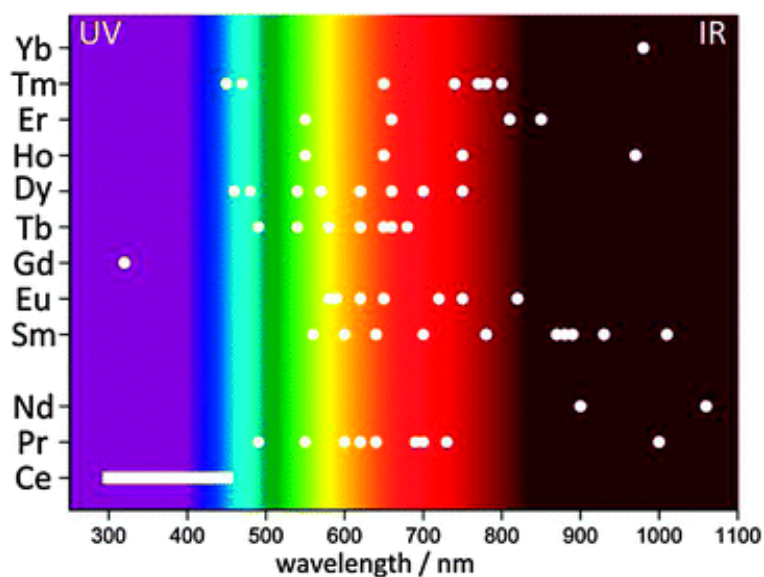


**Figure 16:** Emissive transitions of the Ln<sup>3+</sup> ions covering from near-UV to near-IR range.

2.) **Low sensitivity to surrounding environment:** As discussed in section 1.1.2, Since the  $4f$  orbitals are shielded by completely filled  $5s^25p^6$  subshells the energy levels of Ln<sup>3+</sup> are well defined and show least sensitivity to their surrounding chemical environments.

3.) **Sharp and narrow emission spectra:** Due to shielding, the intra  $4f$ - $4f$  transitions of Ln<sup>3+</sup> in lanthanide ion-doped inorganic crystals typically inherit the feature distinct set of sharp and narrow emission peaks, with a typical full width at half maximum (FWHM) smaller than 10 nm due to weak electron-phonon coupling.<sup>27</sup> The sharp emission peaks can provide distinguishable spectroscopic fingerprints for accurate interpretation of emission spectra in the event of overlapping emission spectra, which is very useful for multicolor biolabeling.

4.) **Long luminescence lifetime:** Owing to the fact that these transitions are theoretically parity forbidden, lanthanide doped-nanoparticles possess remarkably long luminescence

lifetime of the excited states in range of several micro to milli-seconds compared to the lifetime of organic fluorescent probes ( $\sim 1$  ns).<sup>27,72</sup> This feature is able to effectively suppress the short-lived background interferences such as scattered lights and autofluorescence when measuring the long-lived PL of  $\text{Ln}^{3+}$  by setting an appropriate delay time and gate time, which thus offers a signal with a remarkably high signal-to-noise ratio (Figure 17).<sup>73</sup>

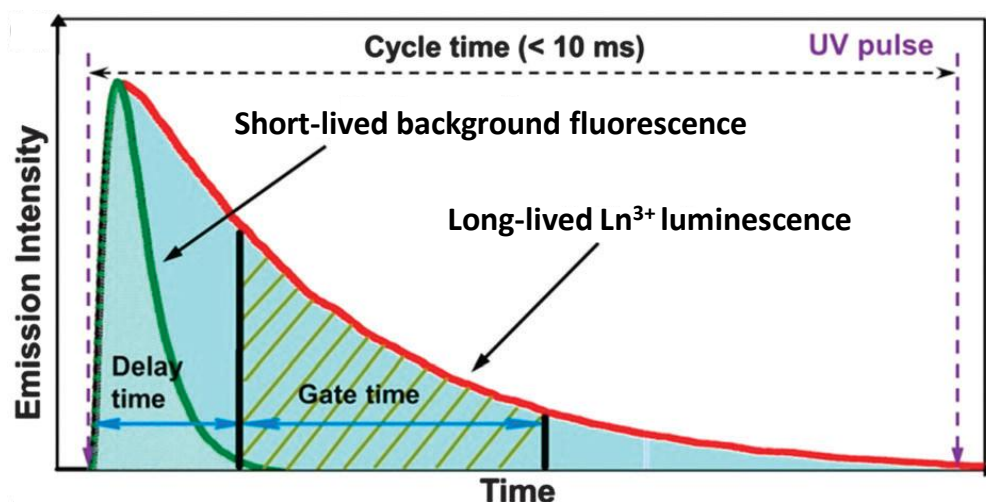


**Figure 17:** The measurement principle of the time-resolved luminescence detection technique based on long lived photoluminescence on  $\text{Ln}^{3+}$  ions.

**5.) Large Stokes and anti-Stokes shift:** Lanthanide ion-doped luminescent materials also possess large Stokes and anti-Stokes shift of greater than 200 nm, which further eliminates the background and auto-fluorescence and are highly beneficial in biosensing and imaging applications. In addition, up-conversion nanoparticles exhibiting anti-Stokes shift are excited in the near-infrared, allowing deeper tissue penetration as well as preventing photodamage.

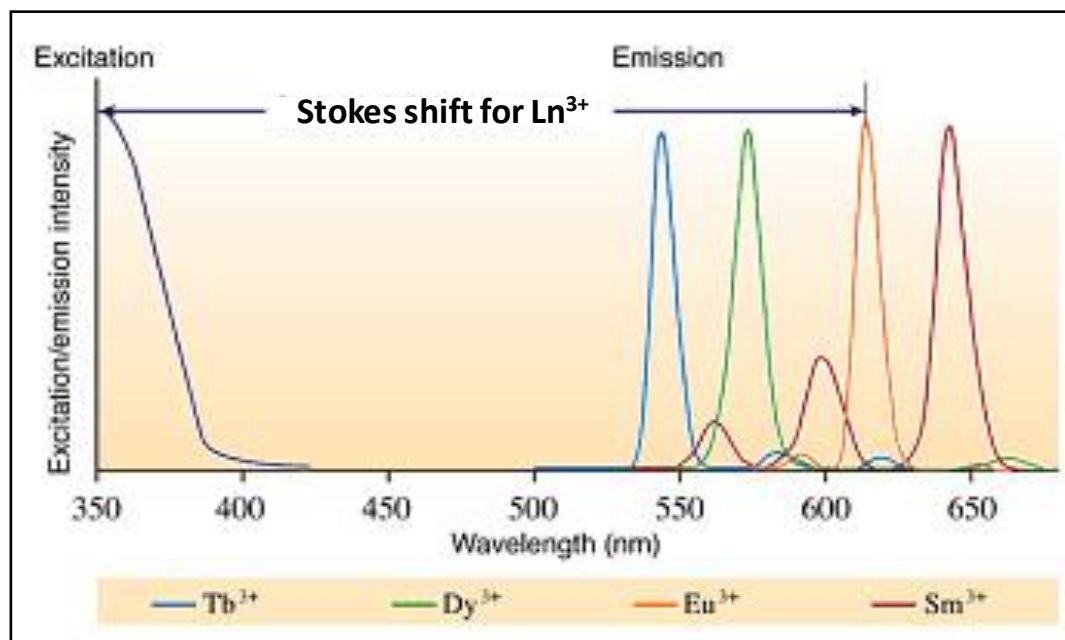


**Figure 18:** Schematic illustration showing large Stokes shift in trivalent lanthanide ions.

Apart from above mentioned characteristics, these possess low toxicity, high resistance to photobleaching and facile functionalization capability. Moreover, these also exhibits low intermittency due to discrete energy levels and due to the steady-state emissions from multiple ions in a single particle.<sup>74</sup> The above mentioned unique optical features arise from their electronic transitions within  $4f^N$  electronic structures and these optical transitions and electronic energy level diagrams of trivalent  $\text{Ln}^{3+}$  ions are understood and expressed in terms of term symbols and Dieke energy level diagram.



### 1.8.1.2. Term symbols

The occurrence of different energy levels belonging to a particular configuration is a result of several interactions within the ion. Depending on the number of electrons, the electrons are distributed over the seven  $4f$ -orbitals. In Figure 18, the interactions that split up the levels belonging to the  $[\text{Xe}] 4f^n 5d^0$  configurations are clarified, where the  $\text{Eu}^{3+}$  ion has been taken as an example for the sake of understanding.

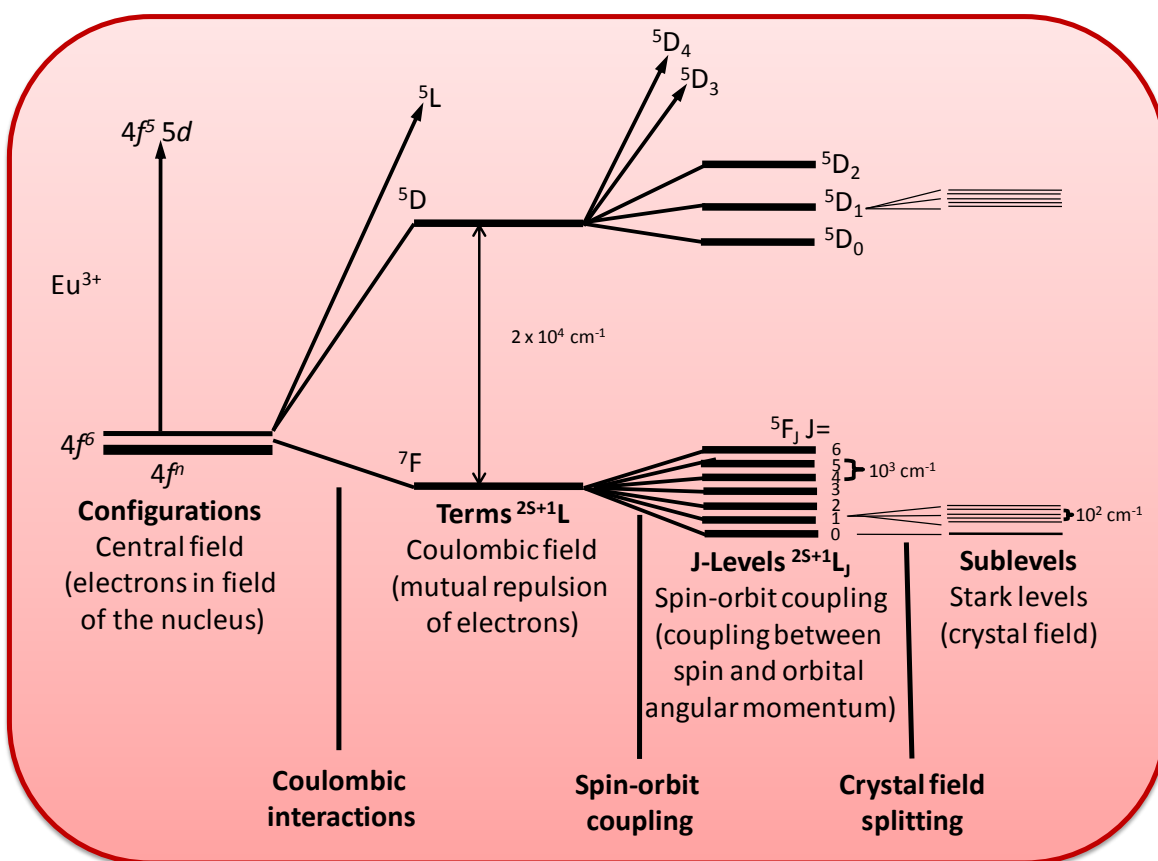


**Figure 19:** The interactions leading to the different electronic energy levels for the  $[\text{Xe}] 4f^6 5d^0$  configuration of  $\text{Eu}^{3+}$  (six electrons in the  $4f$  orbitals).

The energy levels of free  $\text{Ln}^{3+}$  ions in  $4f$  orbitals are determined by the Coulombic interaction and the spin-orbit coupling between  $f$ -electrons. The Coulombic interaction represents the mutual electron-electron repulsion within  $4f$  shell and it is largest among the  $4f$  electronic interactions. The Coulombic interaction generates the total orbital angular momentum ( $L$ ) and total spin angular momentum ( $S$ ) and yields terms with a separation in the order of  $10^4 \text{ cm}^{-1}$ . Further, the spin-orbit coupling makes the total angular momentum ( $J$ ) of the  $f$ -electrons, consequently each of these terms is split into several  $J$ -levels by spin-orbit coupling, which is relatively large ( $10^3 \text{ cm}^{-1}$ ) in lanthanide ions because of their heavy nuclei. Each set of  $L$ ,  $S$ , and  $J$  corresponds to a specific distribution of electrons within the  $4f$ -shell and defines a particular energy level.<sup>37,75,76</sup>

Thereby, the energy level of the free lanthanide ions are derived and labelled using the term symbols of  $^{2S+1}L_J$  according to their angular momentum and spin quantum numbers. Here,  $L$  refers to the total orbital angular momentum of the ion obtained by combining the orbital angular momenta of the individual electrons in the ion according to the Clebsch–Gordan series. The left superscript  $2S+1$  represents the total spin multiplicity that is the number of possible orientations of the total spin of the ion where  $S$  is the total spin of the ion. The right subscript  $J$  refers to the total angular momentum of the  $f$ -electrons and is determined using the Russell–Saunders coupling scheme.<sup>37</sup>

In the event when the lanthanide ion is present in a coordinating environment, such as a crystal or an organic ligand, the individual  $J$ -levels are split up further into stark levels by the electric field of the matrix, which is usually referred to as the crystal field. Although these may be used to gather information about the symmetry of the coordination environment, but often this splitting is ignored .

### 1.8.1.3. Dieke energy level diagram

The first overview of the  $4f^n$  energy level diagram of all trivalent lanthanides in the IR, visible and UV spectral region was given by G. H. Dieke in the 1960s.<sup>77</sup> These diagrams are useful because the energies of the  $(2S+1)L_J$  levels of lanthanide ions has least effect of crystal field/environment, thus exhibit almost negligible influence of the host lattice on the levels. Therefore, Dieke energy level diagram is universally applicable to trivalent lanthanides in any compound/chemical environment or new host. Figure 19 is representative Dieke energy level of the  $4f^n$  configurations of trivalent lanthanide ions, slightly modified to mark the anticipated emitting states in the visible, near IR and UV region with red dots. This diagram has been experimentally extended up to ca.  $70,000 \text{ cm}^{-1}$ , whereas theoretical determinations enable the description of  $4f$  configurations up to ca.  $200,000 \text{ cm}^{-1}$ .<sup>78</sup> Dieke's experimental data were largely gathered using the  $\text{LaCl}_3$  host. As this diagram developed in the 1960s, various interplay between measurements, theoretical models, and computational modeling of energy levels was studied and developed by different scientists. For an instance, W.T. Carnall and co-workers featured a important study of the spectra of trivalent lanthanide ions in  $\text{LaF}_3$  host. He performed a detailed comparison and analysis between the computational modelling using Hamiltonian parameters and the experimental data of  $\text{LaF}_3:\text{Ln}^{3+}$ .<sup>31</sup>

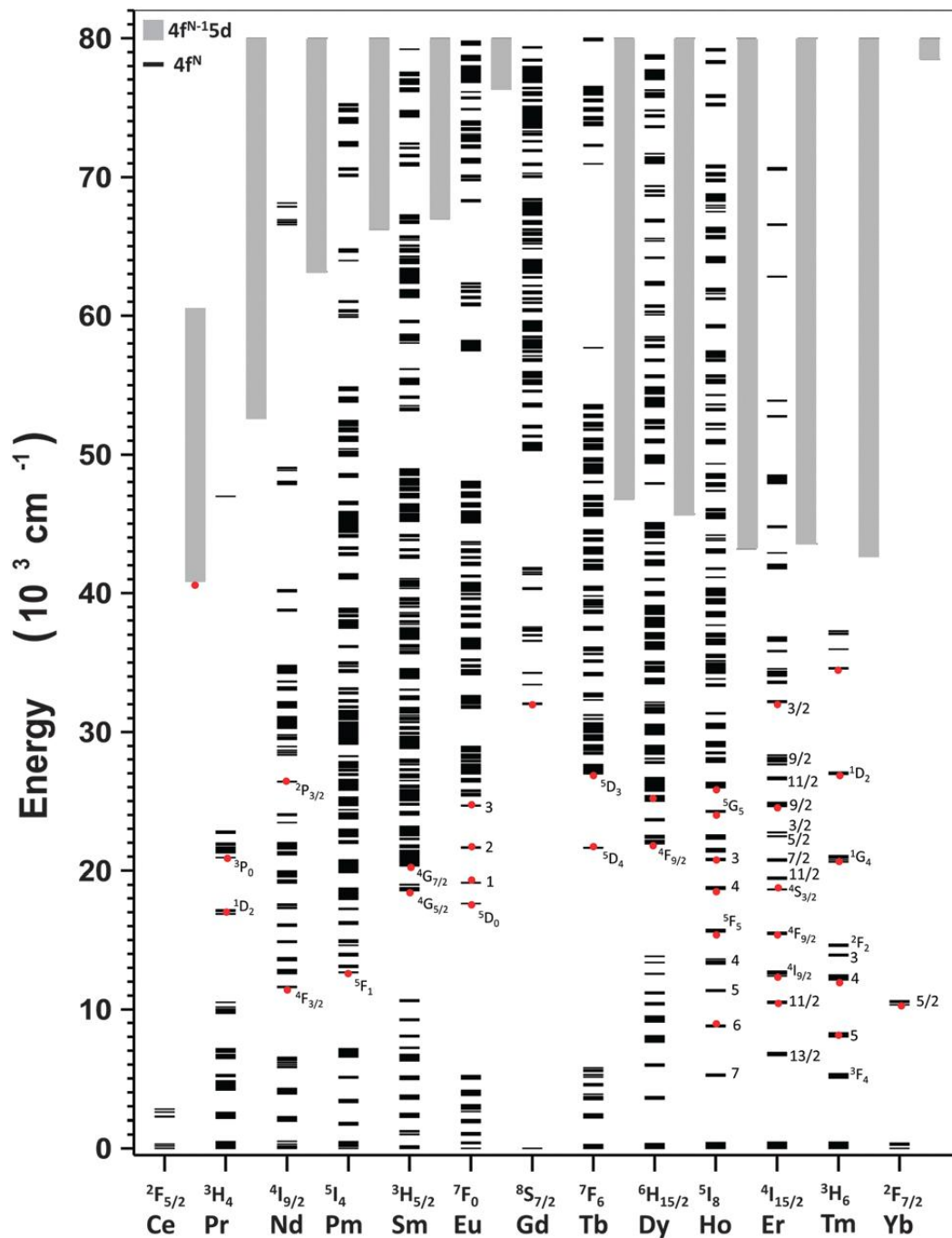


**Figure 19:** Energy levels of the  $4f^n$  configurations of trivalent lanthanides ( $\text{Ln}^{3+}$ ).

The luminescent transitions of lanthanide ions are identifiably characteristic of the specific ion and as mentioned earlier the emission can occur in the UV, visible or NIR regions. The main luminescent transitions of lanthanide ions are listed in Figure 20.<sup>4,6</sup>

Ln <sup>3+</sup>	Ground state	Emitting state	Emission region
Pr	<sup>3</sup> H <sub>4</sub>	<sup>1</sup> D <sub>2</sub> , <sup>3</sup> P <sub>0</sub> , <sup>1</sup> G <sub>4</sub>	Vis. ; Orange and NIR
Nd	<sup>4</sup> I <sub>9/2</sub>	<sup>4</sup> F <sub>3/2</sub>	NIR
Pm	<sup>5</sup> I <sub>4</sub>	<sup>5</sup> F <sub>1</sub>	NIR
Sm	<sup>6</sup> H <sub>5/2</sub>	<sup>4</sup> G <sub>5/2</sub>	Vis.; Orange
Eu	<sup>7</sup> F <sub>0</sub>	<sup>5</sup> D <sub>0</sub>	Vis.; Red
Gd	<sup>8</sup> S <sub>7/2</sub>	<sup>6</sup> P <sub>7/2</sub>	UV
Tb	<sup>7</sup> F <sub>6</sub>	<sup>5</sup> D <sub>4</sub>	Vis.; Green
Dy	<sup>6</sup> H <sub>15/2</sub>	<sup>4</sup> F <sub>9/2</sub>	Vis.; Yellow-orange
Ho	<sup>5</sup> I <sub>8</sub>	<sup>5</sup> S <sub>2</sub> , <sup>5</sup> F <sub>5</sub>	Vis. ; Green and NIR
Er	<sup>4</sup> I <sub>15/2</sub> <sup>4</sup> I <sub>3/2</sub>	<sup>4</sup> I <sub>13/2</sub>	NIR
Tm	<sup>3</sup> H <sub>6</sub>	<sup>1</sup> D <sub>2</sub> , <sup>1</sup> G <sub>4</sub> , <sup>3</sup> H <sub>4</sub>	Vis. , NIR
Yb	<sup>2</sup> F <sub>7/2</sub>	<sup>2</sup> F <sub>5/2</sub>	NIR

**Figure 20:** Main luminescent transition in trivalent lanthanide ions.

### 1.8.2. Magnetic properties

Almost all trivalent lanthanide ions, except for La<sup>3+</sup> and Lu<sup>3+</sup>, have unpaired *f*-electron(s). Among them, although dysprosium (Dy<sup>3+</sup>) and holmium (Ho<sup>3+</sup>) possess the larger magnetic moments due to spin-orbit coupling, but the asymmetry of these electronic states leads to very rapid electron spin relaxation. Gadolinium ion (Gd<sup>3+</sup>) presents relatively lower

magnetic moment than  $\text{Dy}^{3+}$  and  $\text{Ho}^{3+}$ , but it possesses the highest number (seven) of unpaired  $f$ -electrons with parallel spin. More importantly and beneficially,  $\text{Gd}^{3+}$  possess slower relaxation rate due to the symmetric S-state of  $\text{Gd}^{3+}$  and the the spin-relaxation time match the Larmor frequency of protons in suitable magnetic field, which is really beneficial for magnetic resonance imaging (MRI) applications.<sup>79</sup> Therefore,  $\text{Gd}^{3+}$  ions and based compounds are most preferred for preparing  $T_1$  contrast agents in comparison with the rest paramagnetic  $\text{Ln}^{3+}$  ions. The Gadolinium(III) Chelates ; Gd-DTPA (DTPA = diethylenetriaminepentaacetic acid) have been approved by U.S. Food and Drug Administration as a clinical  $T_1$  contrast agent. Until now, many different types of gadolinium chelates have been approved for the clinical use. Although, gadolinium chelates are widely used as contrast agents in MRI however, these have very low body circulation time, due to their low molecular weight and fast diffusion, thus show drawback in contrast agent applications. They also provide very low local contrast, because each chelate has only one  $\text{Gd}^{3+}$  ion. To overcome these drawbacks,  $\text{Gd}^{3+}$ -doped inorganic nanoparticles have been developed and this class possess distinct advantages such as (i) dramatic increase in the local  $\text{Gd}^{3+}$  ion concentration due to high number of paramagnetic atoms per unit of contrast agent, (ii) ease of functionalization without compromising  $\text{Gd}^{3+}$  binding, (iii) improvement in relaxivities and high specific signals, and (iv) control of targeting and clearance through their size.<sup>80</sup> Thus,  $\text{Gd}^{3+}$ -doped inorganic nanoparticles are receiving increasing attention as MRI contrast agents and molecular imaging probes.

### 1.9. Preparation of rare earth based nanoparticles

The controlled synthesis of high quality, in particular pure phase, monodispersed, highly crystalline, Ln<sup>3+</sup>-based nanoparticles is essential to tuning their physicochemical properties and for exploring their extended potential applications in material and medical sciences. It is important to design and fabricate the desirable controlled phase structure, narrow size distribution, morphology, surface functionalization for aqueous/solvent solubility, and even the facets of nanoparticles. To date, a few chemical synthetic methods including thermal decomposition, hydrothermal/solvothermal method, ionic-liquid method, precipitation/coprecipitation, sol-gel method, microwave and microemulsion-assisted approaches, etc., have been developed. Some of the relative advantages and disadvantages of these methods are listed as below:<sup>81-84</sup>

Synthesis method	Advantages	Disadvantages
Hydrothermal method	<ul style="list-style-type: none"> <li>•High quality crystals; high purity</li> <li>•Controllable particle size, shape and high crystallinity</li> <li>•Require relatively low reaction temperature</li> <li>•Relative low cost and high yield</li> </ul>	<ul style="list-style-type: none"> <li>•Impossibility of observing the nanocrystal growth processes</li> </ul>
Thermal decomposition	<ul style="list-style-type: none"> <li>•Highly monodisperse</li> <li>•Small size</li> <li>•High uniformity</li> </ul>	<ul style="list-style-type: none"> <li>•High temperature conditions</li> <li>•Require inert atmosphere protection</li> <li>•Highly toxic precursors</li> <li>•Require post synthetic process to introduce hydrophilicity and biocompatible coating</li> </ul>
Coprecipitation	<ul style="list-style-type: none"> <li>•Fast synthesis</li> <li>•Mild reaction condition and Simple procedure</li> <li>•Small particle size</li> <li>•Low cost</li> </ul>	<ul style="list-style-type: none"> <li>•Lack of particle size control</li> <li>•Poor crystallinity</li> <li>•Considerable aggregation</li> <li>•High temperature calcinations</li> </ul>
Sol-gel synthesis	<ul style="list-style-type: none"> <li>•Cheap precursors</li> <li>•Relatively more crystalline</li> </ul>	<ul style="list-style-type: none"> <li>•Lacks size control and monodispersity</li> <li>•High aggregation</li> <li>•High temperature calcination</li> </ul>
Microemulsion	<ul style="list-style-type: none"> <li>•Narrow size distribution</li> <li>•Homogeneity</li> </ul>	<ul style="list-style-type: none"> <li>•High degree of aggregation</li> <li>•Require annealing at high temperature</li> </ul>
Combustion	<ul style="list-style-type: none"> <li>•Scalable production method</li> </ul>	<ul style="list-style-type: none"> <li>•Lack of shape control</li> </ul>
Ionic liquid based	<ul style="list-style-type: none"> <li>•Green synthesis; non-flammable and non-volatile Capability for stabilization of metal cations; itself act as capping agent</li> </ul>	<ul style="list-style-type: none"> <li>•Lower monodispersity</li> <li>•Expensive</li> <li>•Less uniformity</li> <li>•Broader size distribution</li> </ul>

It should be noted that the above mentioned processes are not mutually exclusive, and it is often that more than one method can be combined to produce nanoparticles. Among these synthetic routes, thermal decomposition and hydrothermal/solvothermal methods are the most popular and effective to prepare high-quality target nanoparticles. In the present thesis, we have used hydrothermal method for the synthesis of  $\text{Ln}^{3+}$ -doped  $\text{NaYF}_4$  crystals. The



hydrothermal/solvothermal synthesis refers to the preparation of nanoparticles with the superheated solvents at high temperatures (often above the critical point of solvents) and the concomitant high pressure in specialized reaction vessel autoclaves to provide the sealed reaction environment. The resulting nanoparticles exhibit excellent crystallinity, which is beneficial for efficient bright luminescence.

### **1.10. Morphology tuning**

Shape control of nanocrystals is an significant objective in material/nanocrystal synthesis as different geometrical factors such as shape, dimensionality, and size of the particles can induce different optical, electronic, and catalytic properties. Surface energy of the particular facet of the crystal is the key factor in determining the morphology of the material. According to Gibbs-Wulff theorem, the shape of the crystals is determined by minimization of total surface energy for a given volume.<sup>85,86</sup> The facets with higher surface energy will disappear and facet with lowest surface energy will be expressed in the final equilibrium morphology. The morphology of a crystal can also be explained in terms of growth kinetics; wherein the fastest growing planes should disappear to leave behind the slowest growing planes as facets of the product.<sup>87</sup> The product often attains its particular equilibrium shape (Wulff polyhedron, octahedron) predicted by Wulff's construction are the result of assumption valid strictly under inert gas or vacuum at 0 K. The varied synthesis conditions such as introduction of different capping agent, pH of solution, temperature *etc* leads to deviation from Wulff's structure. This deviation is attributed to the fact that the surface energies for various faces in different synthesis conditions are being different from those in vacuum due to anisotropic interactions with capping agent, solvent and impurity.<sup>88</sup> Therefore, the introduction of appropriate reaction parameters into the reaction system can

change the free energies of the various crystallographic surfaces and thus alter their growth rates which eventually determines the morphology of the product. The precise architectural manipulation and morphology tuning of nanocrystals (NCs) with well defined morphologies and accurately tunable sizes remains a important research focus. The parameters which mainly affects the morphology of the inorganic crystals are listed below and represented in Figure 21.

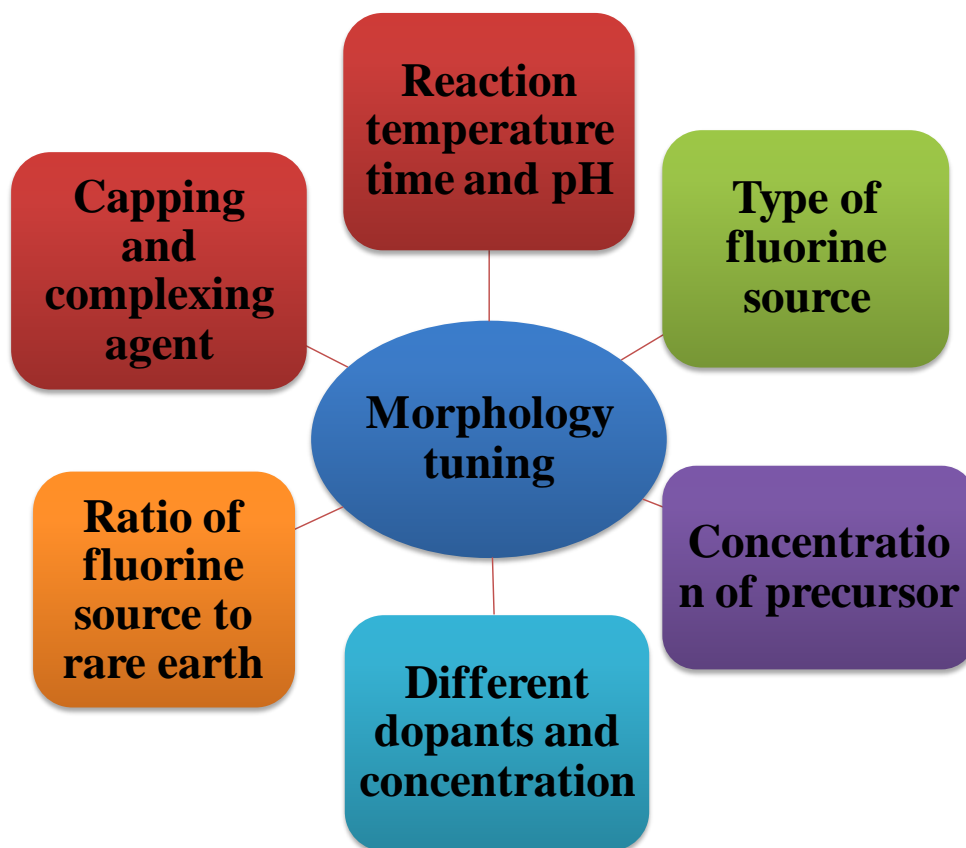


**Figure 21:** Parameters responsible for morphology tuning.

Morphology, size and crystal phase of the crystals in particular rare earth fluoride crystals can be controlled by tuning various parameters:<sup>65,68,89–93</sup>

- Effect of reaction temperature & time
- Concentration of precursor
- Fluorine Source
- Effect of different dopants and concentration
- Effect of various capping agents
- pH of the solution
- Ratio of precursor (rare earth) to fluorine (RE:F ratio)

### **1.11. Hybrids of rare earth phosphors**

Lanthanide ion-doped phosphors stands dominant among various optically active materials owing to their unique and fascinating electronic and optical features. Their properties offer admirable prospects for designing new multifunctional materials with improved desired characteristics and high added value for specific targeted applications, and thus are opening exciting new directions in material sciences and related technologies. Also, it is evident that to realize even more opportunities for lanthanide ion-doped phosphors, the fabrication or tuning of their hybrid materials is required to acquire improved or multifunctional properties. This is highly desirable in the material sciences community for widespread application from optoelectronics to biomedicine, through to more or less all facet of human life.

The strategy to prepare hybrid materials is to integrate or combine two or more different functional materials into a composite form while maintaining the beneficial aspects

of each constituent. The study of luminescent lanthanide based hybrid materials is not only of fundamental interest on their optical properties, but also for their promise of high potential for many different applications. We are briefing some of the important lanthanide ion-doped phosphors based multifunctional hybrid materials for different applications. These hybrids includes composites of  $\text{Ln}^{3+}$ -doped phosphors with metal nanoparticles (Au/Ag), semiconductors ( $\text{TiO}_2/\text{ZnO}$ ), graphene, magnetic nanoparticles ( $\text{Fe}_3\text{O}_4$ ), quantum dots *etc.*

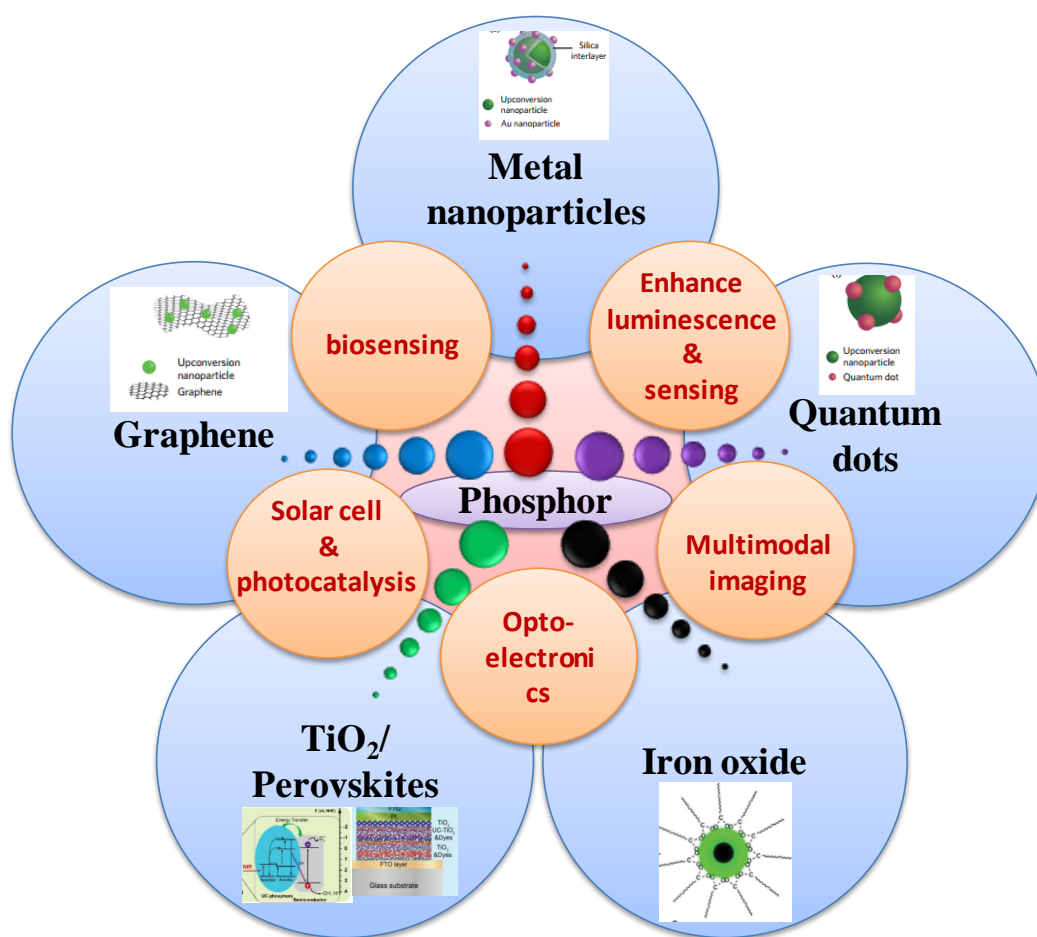


**Figure 22:** Various hybrids of lanthanide ion-doped phosphors for enhanced applications.

The integration of phosphors with other functional materials by chemical approaches, mainly includes surface modification and functionalization, core-shell processing and/or controlled assembly. Some of the  $\text{Ln}^{3+}$ -doped phosphors based hybrids are briefly introduced below:

### **1.11.1. $\text{Ln}^{3+}$ -doped phosphors-Plasmonic metal hybrid structures for luminescence enhancement and sensing applications:**

Plasmonic modulation is able to enhance the luminescence of the  $\text{Ln}^{3+}$ -doped phosphor crystals by coupling it with gold or silver nanoparticles (NPs) at critical distance via forming metal shell/film or functionalization. Some of the examples mentioned are gold nanoshell coated  $\text{NaYF}_4$ <sup>94</sup>, silver (Ag) nanoparticle (NP) embedded  $\text{La}_2\text{O}_3:\text{Er}^{3+}/\text{Yb}^{3+}$  phosphor,<sup>95</sup> metal-capped  $\text{NaGd}_{0.3}\text{Yb}_{0.7}\text{F}_4:\text{Er}$ ,<sup>96</sup>  $\text{NaYF}_4:\text{Yb}^{3+},\text{Er}^{3+}$ @Ag Core/shell Nanocomposites.<sup>97</sup> The enhancement effect by the metal NPs may be attributed to two probable factors: (1) an substantial enhancement of effective excitation flux around lanthanide emitting ions caused by local field enhancement (LFE) associated with plasmonic resonance; (2) an enhancement of emission efficiency due to the coupling of the down/up-conversion emission with the metal NP plasmonic resonance peak which will effectively increase both the non-radiative and radiative decay rate and consequent emission rate resulting in surface plasmon coupled emission (SPCE). SPCE can occur when the emission band of the phosphor overlaps with the plasmon resonance frequency of the metal nanostructures.<sup>94-96,98</sup> The guiding principle is that the luminescence efficiency of the phosphors can be enhanced by tuning the SPR peak of metal nanoparticles resonant to the excitation/absorption and emission wavelength of the phosphors and appropriate distance.

These hybrid structures may also provide a potential platform for enhanced applications in biological imaging, photothermal therapy, sensing, and detection.<sup>97,99,100</sup>

### **1.11.2. Ln<sup>3+</sup>-doped phosphors-Semiconductor hybrids for energy applications:**

The main constraint in improving the efficiency of energy conversion in solar cells and photocatalysis lies in the spectral mismatch between the energy distribution of photons in the incident solar spectrum and the bandgap of the photoactive semiconductor materials, most commonly TiO<sub>2</sub> and ZnO. Owing to wide band gap of these semiconductors, can harvest only UV region (~ 5 %) and modified or doped semiconductors can extend to harvest upto visible region (~ 40 %) of solar energy, but still the most largest near-infra red portion (~ 50 %) of clean and sustainable solar energy remains unutilized.<sup>101</sup> Thus, to harvest complete solar spectrum Ln<sup>3+</sup>-doped phosphors-semiconductor hybrids have been developed. Lanthanide-doped materials are the prime candidates to achieve efficient spectral conversion due to their rich energy level structure that allows for facile photon management.<sup>102</sup> Specially, composites of TiO<sub>2</sub> with up-conversion materials are more popular, wherein, UC phosphors absorbs NIR and convert it to UV and visible light via anti-Stokes emission which is reabsorbed by photoactive TiO<sub>2</sub> consequently harvesting complete solar spectrum and enhancing photocatalysis and solar cell efficiency. Some of the examples of such composites includes NaYF<sub>4</sub>:Yb,Tm/C-TiO<sub>2</sub>, NaYF<sub>4</sub>:Yb,Er/C-TiO<sub>2</sub>, Y<sub>2</sub>O<sub>3</sub>/YOF:Yb,Er/C-TiO<sub>2</sub>, LaF<sub>3</sub>:Yb/Er@TiO<sub>2</sub>, β-NaYF<sub>4</sub>:Yb/Er@SiO<sub>2</sub>@TiO<sub>2</sub> composites.<sup>101,102</sup>

### **1.11.3. Ln<sup>3+</sup>-doped phosphor-Magnetic material hybrids for multimodal imaging applications:**

Trivalent lanthanide ion doped nanoparticles are promising candidates as bioprobes in cell imaging due to their intriguing merits of luminescent properties as discussed in section

1.8.1.1. Although optical imaging provides excellent sensitivity for *in vitro* imaging, but still possess the shortcoming of low penetration depth and is incapable to obtain anatomical and physiological details *in vivo*. On the other hand, MRI provides an excellent spatial resolution and penetration depth for *in vivo* imaging, and provides detailed anatomical information, but suffers from limited sensitivity.<sup>103</sup> The integration of potential benefits of MRI and optical imaging can bridge gaps in sensitivity and depth of imaging between these two modalities and offers the potential to overcome the current limitations of individual imaging. This stimulated a development of hybrid magnetic fluorescent nanoprobe as new approaches in medical diagnostics and also finds way for other various potential applications in medical diagnostics, drug delivery, bioseparation and theranostics.<sup>104,105</sup> Some of the examples includes  $\text{Fe}_3\text{O}_4@\text{NaYF}_4 : \text{Yb,Er}$ ,<sup>104</sup> core-shell  $\text{Fe}_3\text{O}_4@\text{NaLuF}_4:\text{Yb,Er/Tm}$ <sup>105</sup> etc.

#### **1.11.4. Ln<sup>3+</sup>-doped phosphor-Graphene hybrids for electrochemiluminescence (ECL) based biosensing and energy applications:**

Carbon materials, such as carbon black, graphite, carbon nanotube, and graphene possess unique physical, optoelectronic and chemical properties. Specifically, graphene possesses high thermal conductivity, excellent mobility of charge carriers, large specific surface area, and good mechanical stability and thus have fascinated a huge interest for fundamental science and potential applications in various new optoelectronic devices, sensing and energy systems.<sup>106</sup> The coupling of Ln<sup>3+</sup>-doped phosphor with graphene showed excellent and amplified electrogenerated chemiluminescent (ECL) intensity by taking advantage of the wonderful electrical conduction of graphene.<sup>107,108</sup> Also the ECL based sensing application shares many superior advantages in analytical science, such as low detection limits arisen from the low background emission and simpler instrumentation.<sup>107</sup>

Graphene also exhibit the capability to be used to fabricate a sensing platform with high sensitivity and robust operation while simultaneously minimizing cost for sensing of biomolecules.<sup>109</sup> These composites can also enhance photocatalysis and solar cells efficiencies by improving the interfacial electron transport by the presence of graphene.<sup>110</sup>

The other composites of  $\text{Ln}^{3+}$ -doped phosphors with polymers, quantum dots (QDs), chalcogenides *etc* have also been studied. To name a few  $\text{Ln}^{3+}$ -doped phosphor-QDs;  $\text{NaYF}_4:\text{Yb,Tm}/\text{CdS}$ ,  $\text{NaYF}_4:\text{Yb,Tm}/\text{CdSe}$ ,<sup>111</sup>  $\text{CdSe}/\text{NaYF}_4:\text{Yb,Er}$ <sup>112</sup> have been studied for enhanced luminescence and further bioimaging applications. The polymer based  $\text{ZnS}:\text{Cu,Mn}/\text{PDMS}$  composite films have been studied for multicolor imaging.<sup>113</sup> The transition metal chalcogenide based  $\text{NaYF}_4:\text{Yb,Er}-\text{MoS}_2$  nanocomposites for the infrared optoelectronic devices.<sup>114</sup> In principle, these composite materials may possess superior mechanical, electrical or thermal properties, luminescent, magnetic, catalytic, and possess a better processability than the single system of phosphors in multifunctional application.

## 1.12. Applications

Owing to unique, beneficial and valuable optical and magnetic properties of lanthanide ion-doped down-conversion and up-conversion phosphors as discussed on 4.1.1 and 4.3, lanthanide ion-doped have emerged to the forefront as promising alternative materials in display devices, solid state lasers, light emitting devices, optical telecommunication, solar cells, catalysis, fluorescent labels for detection of biomolecules, sensing, cell-imaging, drug delivery, medical diagnostics, photodynamic therapy and security printing. The potentiality of lanthanide ion-doped phosphors for their applications has been discussed intermittently all over this chapter and prominently in section 1.2., 1.8. and 1.11. The overall picture of their applications are represented in figure below:



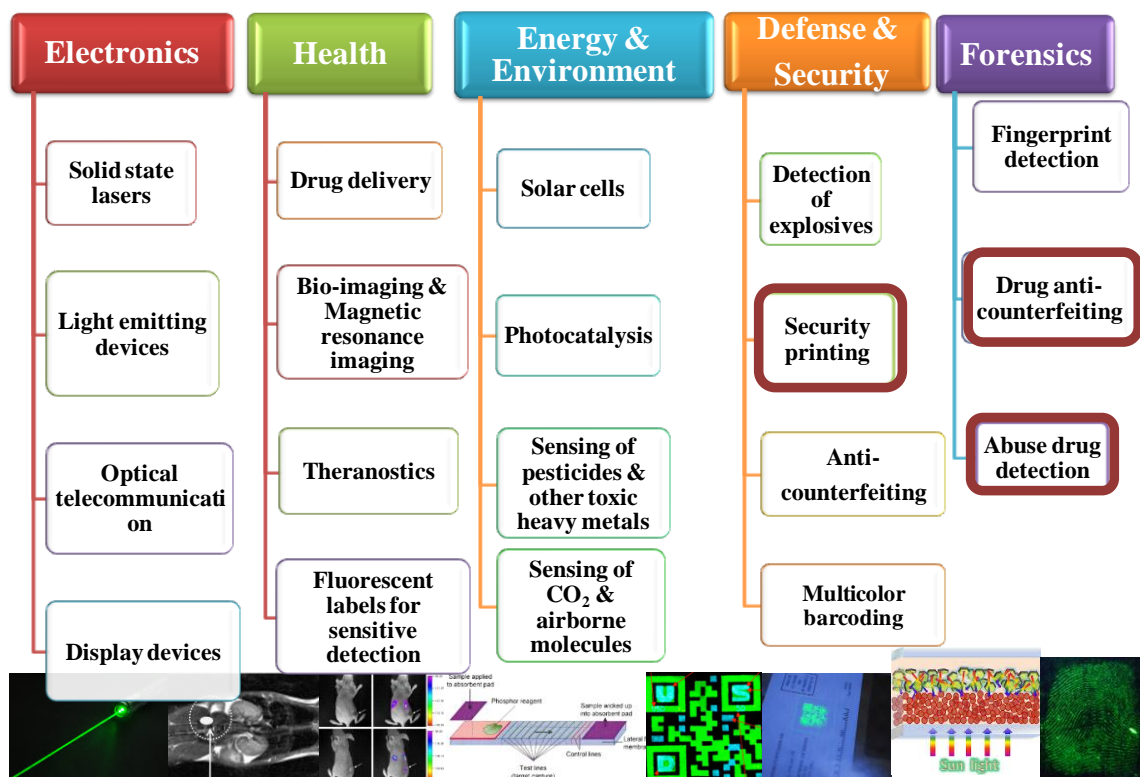


**Figure 23:** Various applications of lanthanide ion-doped rare earth phosphors. The highlighted brown outline are those ones which are upcoming and rarely explored applications.

## 2. Thesis outline

In this thesis, we aim to address and study the tunable optical properties of trivalent lanthanide ion-doped rare earth fluoride phosphors and have investigated their energy and bioapplications. Efforts are dedicated to deliberate the Ln<sup>3+</sup>-doped rare earth fluoride, specifically NaREF<sub>4</sub> system and to understand the effect of different dopants and dopant combinations, surface cappings, functionalization and their structural and optical properties and investigate various applications. We have also modified the system by conjugation of

drug molecules and other entities to make them suitable and efficient for and according to the need of targeted application. The schematic is represented below in figure 24. The present thesis mainly describes a detailed work on hexagonal phase  $\text{Ln}^{3+}$ -doped rare earth fluoride systems;  $\beta\text{-NaREF}_4\text{:Ln}^{3+}$ ;  $\beta\text{-NaYF}_4\text{:Tb}^{3+}$ ,  $\beta\text{-NaYF}_4\text{:Gd}^{3+},\text{Tb}^{3+}$  and  $\beta\text{-NaGdF}_4\text{:Yb}^{3+},\text{Er}^{3+}$ .

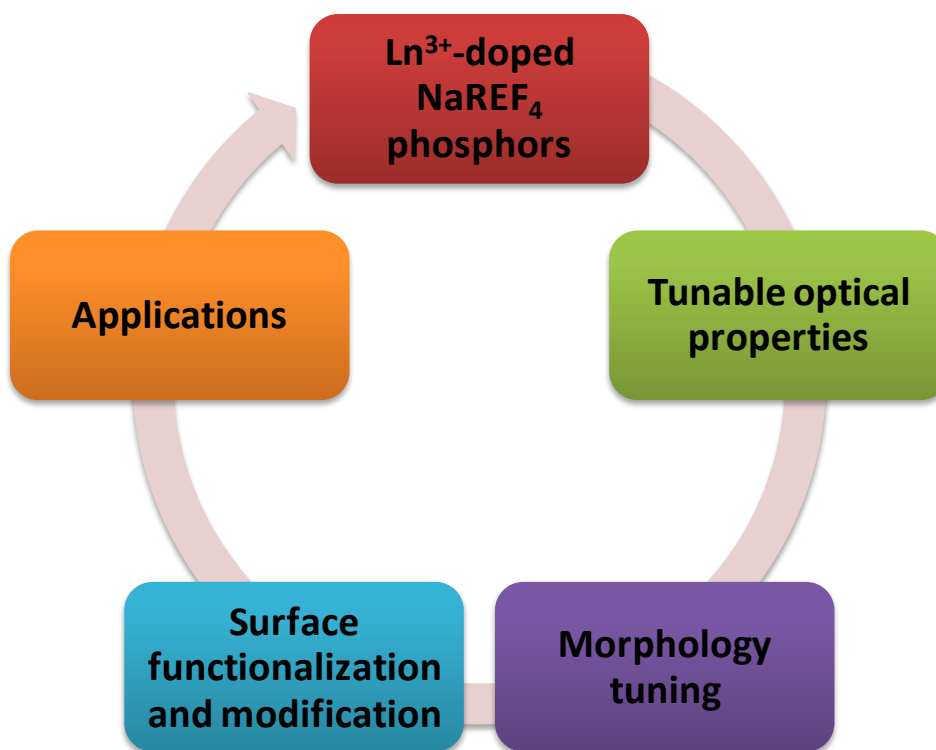


**Figure 24:** Schematic representation of showing aim of the proposed thesis work.

The second chapter describes the fundamental studies on synthesis and optical studies of highly crystalline, uniform and well defined multiform morphologies of  $\beta\text{-NaYF}_4\text{:Tb}^{3+}$  crystals. Their morphology tuning, effect of capping agents and other reaction parameters were studied in detail. Although, the as-prepared  $\beta\text{-NaYF}_4\text{:5% Tb}^{3+}$  crystals were highly luminescent, with long luminescent lifetimes, but were not suitable for bio-applications as limited by size and biocompatibility. In this viewpoint, in third chapter, we designed highly crystalline, biocompatible, PEI functionalized  $\beta\text{-NaYF}_4\text{:Gd}^{3+},\text{Tb}^{3+}$  nanorods system as

luminescent/magnetic multimodal cell imaging tool. We conjugated anticancer drug doxorubicin to  $\beta\text{-NaYF}_4\text{:Gd}^{3+},\text{Tb}^{3+}$  enabling them as a pH-triggered, site-specific drug delivery nanovehicle. We studied in detail their structural, optical, magnetic properties, cytotoxicity and cellular uptake mechanisms. It is expected that the as developed DOX-conjugated  $\beta\text{-NaYF}_4\text{:Gd}^{3+}/\text{Tb}^{3+}$  system combining efficient luminescence, paramagnetic properties, and pH-triggered drug delivery, promises to be a potential multifunctional platform for cancer theranostics, biodetection and imaging. Further, since the development of multifunctional platforms for broad range of applications has geared tremendous progress towards the design and engineering of such functional materials possessing multiple discrete functions in single composites. Keeping the similar perspective, in fourth chapter, we developed single multifunctional platform by judicious integration of up-converting luminescent and magnetic  $\beta\text{-NaGdF}_4\text{:Yb}^{3+},\text{Er}^{3+}$  and mesoporous anatase  $\text{TiO}_2$ ;  $\beta\text{-NaGdF}_4\text{:Yb}^{3+},\text{Er}^{3+}/m\text{TiO}_2$  nanocomposite system, for enhanced energy and simultaneous biomedical applications. We studied structural, optical and magnetic properties of respective pristine and  $\beta\text{-NaGdF}_4\text{:Yb}^{3+},\text{Er}^{3+}/m\text{TiO}_2$  nanocomposite in detail. We also studied their potentiality for photocatalysis, solar cell, and MRI applications and discussed their mechanism. The concluding chapter six presents the brief summary of the results achieved during the thesis work. It also describes the future scope for the present research work.

**3. References:**

- 1 J. G. Bunzli, S. Comby, A. Chauvin and C. D. B. Vandevyver, 2007, **25**, 257–274.
- 2 S. V. Eliseeva and J.-C. G. Bünzli, *New J. Chem.*, 2011, **35**, 1165-1176.
- 3 J-C. G. Bunzli, *Acc. Chem. Res.*, 2006, **39**, 53–61.
- 4 J-C. G. Bünzli and C. Piguet, *Chem. Soc. Rev.*, 2005, **34**, 1048-1077.
- 5 J. G. Bu and S. V Eliseeva, *Basics of Lanthanide Photophysics*, 2010, vol. 7.
- 6 A. J. Amoroso and S. J. A. Pope, *Chem. Soc. Rev. Chem. Soc. Rev*, 2015, **44**, 4723–4742.
- 7 P. Dorenbos, *J. Mater. Chem.*, 2012, **22**, 22344–22349.
- 8 P. A. Tanner, *Lanthanide Luminescence in Solids, In Springer Series on Fluorescence*, 2010, pp. 183–233.
- 9 S. Shinoda and H. Tsukube, *Analyst*, 2011, **136**, 431–435.
- 10 S. I. Weissman, *J. Chem. Phys.*, 1942, **10**, 214–217.
- 11 P. Escribano, B. Julián-López, J. Planelles-Aragó, E. Cordoncillo, B. Viana and C. Sanchez, *J. Mater. Chem.*, 2008, **18**, 23.
- 12 G.F. de Sa, O.L. Malta, C. de Mello Donega, Simas, A.M., L. R. Longo, P. A. Santa-Cruz and E. F. da S. Jr., *Coord. Chem. Rev.*, 2000, **196**, 165–195.
- 13 M. Li and P. R. Selvin, *J. Am. Chem. Soc.*, 1995, **117**, 8132–8138.
- 14 J. Kido and Y. Okamoto, *Chem. Rev.*, 2002, **102**, 2357–2368.
- 15 L. Pellegatti, J. Zhang, B. Drahos, S. Villette, F. Suzenet, G. Guillaumet, S. Petoud and E. Tóth, *Chem. Commun. (Camb)*, 2008, **60**, 6591–6593.
- 16 J. E. C. Da Silva, G. F. De Sá and P. A. Santa-Cruz, *J. Alloys Compd.*, 2002, **344**, 260–263.
- 17 H. A. Höpfe, *Angew. Chem. Int. Ed.*, 2009, **48**, 3572–3582.
- 18 C. Nico, R. Fernandes, M. P. F. Graça, M. Elisa, B. A. Sava, R. C. C. Monteiro, L. Rino and T. Monteiro, *J. Lumin.*, 2014, **145**, 582–587.
- 19 F. Wang, L. F. Shen, B. J. Chen, E. Y. B. Pun and H. Lin, *Opt. Mater. Express*, 2013, **3**, 1931–1943.
- 20 M. Elisa, B. A. Sava, I. C. Vasiliu, R. C. C. Monteiro, J. P. Veiga, L. Ghervase, I. Feraru and R. Iordanescu, *J. Non. Cryst. Solids*, 2013, **369**, 55–60.
- 21 D. De Graaf, S. J. Stelwagen, H. T. Hintzen and G. De With, *J. Non. Cryst. Solids*,

- 2003, **325**, 29–33.
- 22 A. Ikesue, Y. L. Aung, T. Taira, T. Kamimura, K. Yoshida and G. L. Messing, *Annu. Rev. Mater. Res.*, 2006, **36**, 397–429.
- 23 T. Nakanishi, *J. Ceram. Soc. Japan*, 2015, **123**, 862–867.
- 24 S. V Eliseeva and J.-C. G. Bünzli, *Chem. Soc. Rev.*, 2010, **39**, 189–227.
- 25 T.-W. Duan and B. Yan, *J. Mater. Chem. C*, 2014, **2**, 5098–5104.
- 26 K. Kuriki, Y. Koike and Y. Okamoto, *Chem. Rev.*, 2002, **102**, 2347–2356.
- 27 C. Bouzigues, T. Gacoin and A. Alexandrou, *ACS Nano*, 2011, **5**, 8488–8505.
- 28 Y. Sun, W. Feng, P. Yang, C. Huang and F. Li, *Chem. Soc. Rev.*, 2015, **44**, 1509–1525.
- 29 J. Shen, L.-D. Sun and C.-H. Yan, *Dalt. Trans.*, 2008, **9226**, 5687–5697.
- 30 G. Blasse and A. Bril, *Appl. Phys. Lett.*, 1967, **11**, 53–55.
- 31 W. T. Carnall, G. L. Goodman, K. Rajnak and R. S. Rana, *J. Chem. Phys.*, 1989, **90**, 3443–3457.
- 32 J. W. Stouwdam and F. C. J. M. Van Veggel, *Nano Lett.*, 2002, **2**, 733–737.
- 33 P. R. Diamente, R. D. Burke and F. C. J. M. Veggel, *Langmuir*, 2006, 2254–2260.
- 34 S. Zeng, G. Ren, C. Xu and Q. Yang, *CrystEngComm*, 2011, **13**, 1384–1390.
- 35 F. Wang and X. Liu, *Chem. Soc. Rev.*, 2009, **38**, 976–989.
- 36 M. Haase and H. Schäfer, *Angew. Chemie Int. Ed.*, 2011, **50**, 5808–5829.
- 37 A. J. Kenyon, *Progress in Quantum Electronics*, 2002, 26, 225–284.
- 38 J. M. F. van D. and M. F. H. Schuurmans, *J. Chem. Phys.*, 1983, **78**, 5317–5323.
- 39 Q. Dou and Y. Zhang, *Langmuir*, 2011, **27**, 13236–13241.
- 40 C. Liu, Y. Hou and M. Gao, *Adv. Mater.*, 2014, **26**, 6922–6932.
- 41 Y. Shang, S. Hao, C. Yang and G. Chen, *Nanomaterials*, 2015, **5**, 1782–1809.
- 42 P. Rahman and M. Green, *Nanoscale*, 2009, **1**, 214–224.
- 43 V. Badescu and A. De Vos, *J. Appl. Phys.*, 2007, **102**, 073102–7.
- 44 Y. Liu, D. Tu, H. Zhu, E. Ma and X. Chen, *Nanoscale*, 2013, **5**, 1369–84.
- 45 W. G. J. H. M. Van Sark, A. Meijerink and R. E. I. Schropp, Third generation photovoltaics, chapter 1, Solar spectrum conversion for photovoltaics using

- nanoparticles, 2012, 1–28.
- 46 W. W. Piper, J. A. DeLuca and F. S. Ham, *J. Lumin.*, 1974, **8**, 344–348.
- 47 F. Auzel, *Chem. Rev.*, 2004, **104**, 139–173.
- 48 D. E. Achatz, R. Ali and O. S. Wolfbeis, *Top curr chem*, 300, 2011, 29–50.
- 49 M. Wang, G. Abbineni, A. Clevenger, C. Mao and S. Xu, *Nanomedicine Nanotechnology, Biol. Med.*, 2011, **7**, 710–729.
- 50 M. M. Lezhnina, T. Justel, H. Katker, D. U. Wiechert and U. H. Kynast, *Adv. Funct. Mater.*, 2006, **16**, 935–942.
- 51 C. Li and J. Lin, *J. Mater. Chem.*, 2010, **20**, 6831–6847.
- 52 C. Li, Z. Quan, J. Yang, P. Yang and J. Lin, *Inorg. Chem.*, 2007, **46**, 6329–6337.
- 53 P. R. Diamente, M. Raudsepp and F. C. J. M. Van Veggel, *Adv. Funct. Mater.*, 2007, **17**, 363–368.
- 54 J. F. Suyver, J. Grimm, M. K. van Veen, D. Biner, K. W. Krämer and H. U. Güdel, *J. Lumin.*, 2006, **117**, 1–12.
- 55 J. H. Huang, X. H. Gong, Y. J. Chen, Y. F. Lin, J. S. Liao, X. Y. Chen, Z. D. Luo and Y. D. Huang, *Appl. Phys. B Lasers Opt.*, 2007, **89**, 73–80.
- 56 S. Zheng, W. Chen, D. Tan, J. Zhou, Q. Guo, W. Jiang, C. Xu, X. Liu and J. Qiu, *Nanoscale*, 2014, **6**, 5675–5679.
- 57 K. Chong, T. Hirai, T. Kawai, S. Hashimoto and N. Ohno, *J. Lumin.*, 2007, **122-123**, 149–151.
- 58 V. I. Sokolov, A. V. Zvyagin, S. M. Igumnov, S. I. Molchanova, M. M. Nazarov, a. V. Nechaev, a. G. Savelyev, a. a. Tyutyunov, E. V. Khaydukov and V. Y. Panchenko, *Opt. Spectrosc.*, 2015, **118**, 609–613.
- 59 M. Ding, W. Huang, L. Cao, C. Lu, J. Song, Y. Ni and Z. Xu, *Mater. Lett.*, 2012, **86**, 58–61.
- 60 W. Huang, M. Ding, H. Huang, C. Jiang, Y. Song, Y. Ni, C. Lu and Z. Xu, *Mater. Res. Bull.*, 2013, **48**, 300–304.
- 61 S. Heer, K. Kömpe, H.-U. Güdel and M. Haase, *Adv. Mater.*, 2004, **16**, 2102–2105.
- 62 B. Shao, Y. Feng, Y. Song, M. Jiao, W. Lü and H. You, *Inorg. Chem.*, 2016, **55**, 1912–1919.
- 63 M. D. Mathews, B. R. Ambekar, A. K. Tyagi and J. Köhler, *J. Alloys Compd.*, 2004, **377**, 162–166.
- 64 D. Tu, Y. Liu, H. Zhu, R. Li, L. Liu and X. Chen, *Angew. Chemie Int. Ed.*, 2013, **52**,

- 1128–1133.
- 65 F. Wang, Y. Han, C. S. Lim, Y. Lu, J. Wang, J. Xu, H. Chen, C. Zhang, M. Hong and X. Liu, *Nature*, 2010, **463**, 1061–1065.
- 66 R. E. Thoma, H. Insley and G. M. Hebert, *Inorg. Chem.*, 1966, **5**, 1222–1229.
- 67 B. Huang, H. Dong, K.-L. Wong, L.-D. Sun and C.-H. Yan, *J. Phys. Chem. C*, 2016, **120**, 18858–18870.
- 68 M. Ding, D. Chen, S. Yin, Z. Ji, J. Zhong, Y. Ni, C. Lu and Z. Xu, *Sci. Rep.*, 2015, **5**, 12745.
- 69 L. Wang, X. Li, Z. Li, W. Chu, R. Li, K. Lin, H. Qian, Y. Wang, C. Wu, J. Li, D. Tu, Q. Zhang, L. Song, J. Jiang, X. Chen, Y. Luo, Y. Xie and Y. Xiong, *Adv. Mater.*, 2015, **27**, 5528–5533.
- 70 W. Zheng, P. Huang, D. Tu, E. Ma, H. Zhu and X. Chen, *Chem. Soc. Rev.*, 2015, **44**, 1379–1415.
- 71 J. Heine and K. Müller-Buschbaum, *Chem. Soc. Rev.*, 2013, **42**, 9232–9242.
- 72 P. Qiu, N. Zhou, H. Chen, C. Zhang, G. Gao and D. Cui, *Nanoscale*, 2013, **5**, 11512–11525.
- 73 F. Wang, D. Banerjee, Y. Liu, X. Chen and X. Liu, *Analyst*, 2010, **135**, 1839–1854.
- 74 S. Wu, G. Han, D. J. Milliron, S. Aloni, V. Altoe, D. V Talapin, B. E. Cohen and P. J. Schuck, *PNAS.*, 2009, **106**, 10917–10921.
- 75 X. Liu, S. Han, R. Deng, X. Xie and X. Liu, *Angew. chem. Int. Ed.*, 2014, **53**, 11702–11715.
- 76 M. H. V Werts, *Science progress*, 2005, **88**, 101–131.
- 77 P. S. Peijzel, A. Meijerink, R. T. Wegh, M. F. Reid and G. W. Burdick, *J. Solid State Chem.*, 2005, **178**, 448–453.
- 78 P. C. de Sousa Filho, J. F. Lima and O. A. Serra, *J. Braz. Chem. Soc.*, 2015, **26**, 2471–2495.
- 79 P. Caravan, J. J. Ellison, T. J. McMurry and R. B. Lauffer, *Chem. Rev.*, 1999, **99**, 2293–2352.
- 80 M.-A. Fortin, R. M. Petoral Jr, F. Söderlind, A. Klasson, M. Engström, T. Veres, P.-O. Käll and K. Uvdal, *Nanotechnology*, 2007, **18**, 395501.
- 81 C. Li and J. Lin, *J. Mater. Chem.*, 2010, **20**, 6831.
- 82 J. Jin, Y.-J. Gu, C. W.-Y. Man, J. Cheng, Z. Xu, Y. Zhang, H. Wang, V. H.-Y. Lee, S. H. Cheng and W.-T. Wong, *ACS Nano*, 2011, **5**, 7838–7847.

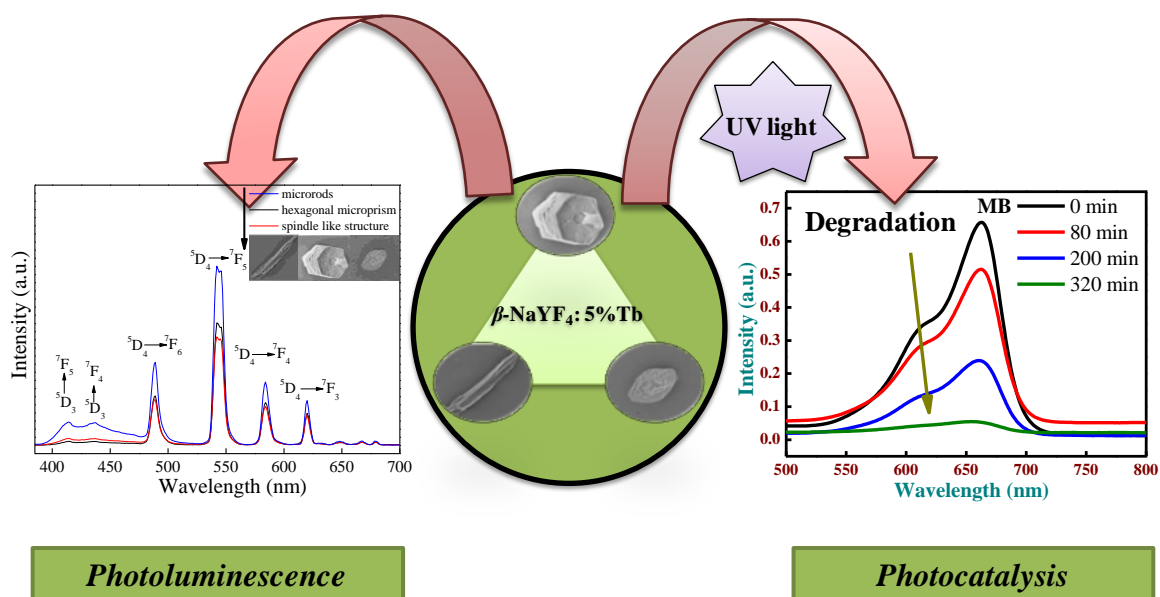
- 83 J. Chen and J. X. Zhao, *Sensors*, 2012, **12**, 2414–2435.
- 84 D. Vennerberg and Z. Lin, *Sci. Adv. Mater.*, 2011, **3**, 26–40.
- 85 P. Li, X. Zhao, C. J. Jia, H. G. Sun, Y. L. Li, L. M. Sun, X. F. Cheng, L. Liu and W. L. Fan, *Cryst. Growth Des.*, 2012, **12**, 5042–5050.
- 86 G. D. Barmparis, Z. Lodziana, N. Lopez and I. N. Remediakis, *Beilstein J. Nanotechnol.*, 2015, **6**, 361–368.
- 87 L. Xu, J. Shen, C. Lu, Y. Chen and W. Hou, *Cryst. Growth Des.*, 2009, **9**, 3129–3136.
- 88 Y. Xia, Y. Xiong, B. Lim and S. E. Skrabalak, *Angew. Chemie - Int. Ed.*, 2009, **48**, 60–103.
- 89 S. Gai, C. Li, P. Yang and J. Lin, *Chem. Rev.*, 2014, **114**, 2343–2389.
- 90 H. Lin, D. Xu, A. Li, D. Teng, S. Yang and Y. Zhang, *Sci. Rep.*, 2016, **6**, 28051.
- 91 Y. Liu, Y. Zhao, H. Luo, Z. Wu and Z. Zhang, *J. Nanoparticle Res.*, 2011, **13**, 2041–2047.
- 92 Y. Wang, S. Gai, N. Niu, F. He and P. Yang, *Phys. Chem. Chem. Phys.*, 2013, **15**, 16795–16805.
- 93 Y. Shang, S. Hao, J. Liu, M. Tan, N. Wang, C. Yang and G. Chen, *Nanomaterials*, 2015, **5**, 218–232.
- 94 A. Priyam, N. M. Idris and Y. Zhang, *J. Mater. Chem.*, 2012, **22**, 960–965.
- 95 S. P. Tiwari, K. Kumar and V. K. Rai, *Appl. Phys. B*, 2015, **121**, 221–228.
- 96 A.-H. Li, M. Lü, L. Guo and Z. Sun, *Small*, 2016, **12**, 2092–2098.
- 97 B. Dong, S. Xu, J. Sun, S. Bi, D. Li, X. Bai, Y. Wang, L. Wang and H. Song, *J. Mater. Chem.*, 2011, **21**, 6193–6200.
- 98 H. Zhang, Y. Li, I. A. Ivanov, Y. Qu, Y. Huang and X. Duan, *Angew. Chemie - Int. Ed.*, 2010, **49**, 2865–2868.
- 99 P. Kannan, F. Abdul Rahim, R. Chen, X. Teng, L. Huang, H. Sun and D. H. Kim, *ACS Appl. Mater. Interfaces*, 2013, **5**, 3508–3513.
- 100 Z. Li, L. Wang, Z. Wang, X. Liu and Y. Xiong, *J. Phys. Chem. C*, 2011, **115**, 3291–3296.
- 101 X. Wu, S. Yin, Q. Dong and T. Sato, *Appl. Catal. B Environ.*, 2014, **156-157**, 257–264.
- 102 W. Yang, X. Li, D. Chi, H. Zhang and X. Liu, *Nanotechnology*, 2014, **25**, 482001.
- 103 X. Li, D. Zhao and F. Zhang, *Theranostics*, 2013, **3**, 292–305.



- 
- 104 C. Mi, J. Zhang, H. Gao, X. Wu, M. Wang, Y. Wu, Y. Di, Z. Xu, C. Mao and S. Xu, *Nanoscale*, 2010, **2**, 1141.
- 105 X. Zhu, J. Zhou, M. Chen, M. Shi, W. Feng and F. Li, *Biomaterials*, 2012, **33**, 4618–4627.
- 106 L. Han, P. Wang and S. Dong, *Nanoscale*, 2012, **4**, 5814.
- 107 M. Yin, L. Wu, Z. Li, J. Ren and X. Qu, *Nanoscale*, 2012, **4**, 400–4.
- 108 L. Wu, J. Wang, M. Yin, J. Ren, D. Miyoshi, N. Sugimoto and X. Qu, *Small*, 2014, **10**, 330–336.
- 109 L. Yan, Y.-N. Chang, W. Yin, X. Liu, D. Xiao, G. Xing, L. Zhao, Z. Gu and Y. Zhao, *Phys. Chem. Chem. Phys.*, 2014, **16**, 1576–1582.
- 110 Y. Li, G. Wang, K. Pan, B. Jiang, C. Tian, W. Zhou and H. Fu, *J. Mater. Chem.*, 2012, **22**, 20381.
- 111 J. Chang, Y. Liu, J. Li, S. Wu, W. Niu and S. Zhang, *J. Mater. Chem. C*, 2013, **1**, 1168–1173.
- 112 C. Yan, A. Dadvand, F. Rosei and D. F. Perepichka, *J. Am. Chem. Soc.*, 2010, **132**, 8868–8869.
- 113 S. M. Jeong, S. Song, S.-K. Lee and N. Y. Ha, *Adv. Mater.*, 2013, **25**, 6194–6200.
- 114 W. Niu, H. Chen, R. Chen, J. Huang, H. Sun and A. I. Y. Tok, *Chem. Commun.*, 2015, **51**, 9030–9033.

## Chapter 2

### Optical and photocatalytic properties of uniform, monodispersed, and highly crystalline up/down-converting, lanthanide ion-doped $\beta$ -NaYF<sub>4</sub> phosphor crystals with controlled multiform morphologies



*Photoluminescence*

*Photocatalysis*

## Outline

---

This chapter presents the fabrication of lanthanide ion-doped, single-crystalline hexagonal phase NaYF<sub>4</sub> microcrystals with multiform morphologies, such as microrods, hexagonal microprisms, and spindle-like structures via cationic/anionic binary capping agents: CTAB and tri-sodium citrate-assisted hydrothermal route. The influence of synthesis conditions on the crystalline morphology was studied and the possible growth mechanisms are presented systematically. The down-conversion and up-conversion photoluminescence (PL) properties of  $\beta$ -NaYF<sub>4</sub>: Ln<sup>3+</sup> (Ln=Tb, Yb/Er, and Yb/Tm) were investigated. The morphology dependent static and dynamic PL studies of  $\beta$ -NaYF<sub>4</sub>:5 % Tb<sup>3+</sup> were performed that showed strong dependence of luminescent properties on the crystalline morphology. Furthermore, photocatalytic studies of  $\beta$ -NaYF<sub>4</sub>:5 % Tb<sup>3+</sup> phosphors were investigated under UV as well as solar light irradiation, and that showed enhanced selectivity towards methylene blue. Moreover, the morphological effect on the photocatalytic activity of  $\beta$ -NaYF<sub>4</sub>:5 % Tb<sup>3+</sup> crystals have also been studied. The high luminescence efficiency and strong photocatalytic activity of  $\beta$ -NaYF<sub>4</sub>:5 % Tb<sup>3+</sup>, make them a potential phosphor material and promises to provide a gateway into other applications as in biology and material sciences.

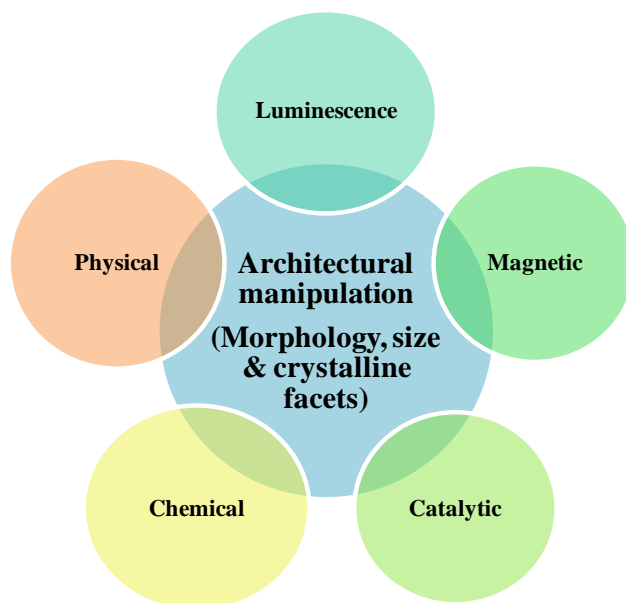
## 2.1. Introduction

Due to their unique, tailored, optical properties, lanthanide ion-doped luminescent materials have attracted tremendous attention as phosphors, and thus possess potential wide-ranging applications in diverse fields; as in display devices, solid state lasers, light emitting devices, optical telecommunication, solar cells, fluorescent labels for detection of biomolecules, cell-imaging, catalysis, and medical diagnostics.<sup>1-5</sup> As discussed in chapter 1, the unique photophysical properties of trivalent lanthanide-ions arise from electronic transitions within the parity forbidden  $4f$  shell, which are shielded by filled  $5s$  and  $5p$  orbitals.<sup>6,7</sup> This unique electronic configuration renders fascinating properties to these materials, such as narrow and sharp emission spectra, long luminescent lifetime, photostability, large Stokes and anti-Stokes shift, non-blinking feature, and low autofluorescence. These characteristics of  $\text{Ln}^{3+}$ -doped materials give them an edge over conventional organic fluorescent dyes or quantum-dots for various biological and non-biological applications.<sup>8-11</sup>

To effectively utilize the novel luminescence of  $\text{Ln}^{3+}$  ions, it is necessary to choose an appropriate host-lattice combination with low phonon-energy to minimize non-radiative losses.<sup>12,13</sup> Among various classes of rare-earth compounds, such as oxides, fluorides, phosphates, vanadates etc., fluorides possess lowest phonon-energy (ca.  $350\text{ cm}^{-1}$ ) of crystal lattice and wide bandgap.<sup>14</sup> Among the investigated rare earth fluorides,  $\text{NaYF}_4$  possesses low phonon-energy ( $\sim 360\text{ cm}^{-1}$ ) and wide bandgap ( $\sim 8\text{ eV}$ ).<sup>15</sup> Consequently,  $\text{NaYF}_4$  is considered to be an excellent and most efficient host matrix for down-conversion (DC) and up-conversion (UC) processes. The crystal structure of  $\text{NaYF}_4$  exists in two polymorphic forms: cubic ( $\alpha$ -) and hexagonal ( $\beta$ -) phases depending upon the crystal growth environment.

The cubic phase is a metastable phase and hexagonal phase ( $\beta$ -NaYF<sub>4</sub>) is thermodynamically stable phase.<sup>16</sup> The hexagonal  $\beta$ -phase NaYF<sub>4</sub> is considered a better host than  $\alpha$ -NaYF<sub>4</sub> for enhanced luminescence efficiency of various optically-active lanthanide-ions.<sup>17,18</sup> The overall luminescence emission of the  $\beta$ -NaYF<sub>4</sub> is ~ 4.4 times greater than those for  $\alpha$ -NaYF<sub>4</sub>.<sup>19</sup> Thus, it is desirable and important to synthesize hexagonal  $\beta$ -NaYF<sub>4</sub> phase to achieve a brighter phosphor.

In modern chemistry and materials science, the precise architectural manipulation of anisotropic crystals with well-defined morphologies and accurately tunable sizes remain a research focus and a challenging issue due to the fact that the physical, chemical, luminescent, magnetic, and catalytic properties of the materials are closely interrelate with geometrical factors such as shape, size, and crystalline facets as represented below in scheme 1.<sup>20,21,22</sup> Moreover, various properties of the materials often significantly vary for different crystalline facets, as demonstrated by our group previously.<sup>23</sup>



**Scheme 1:** Interrelation of various properties of materials with their geometrical factors.

In the growth process of crystals, a series of external factors, such as reaction temperature, time, pH of precursor-solution, and organic additives drastically influence the shape-evolution of the crystals. A variety of organic additives and shape directing agents such as sodium citrate<sup>24,25</sup>, ethylenediaminetetraacetic acid (EDTA)<sup>26,27</sup>, cetyltrimethylammonium bromide (CTAB)<sup>28</sup>, oleic-acid<sup>29,18</sup>, and sodium dodecylbenzenesulfonate (SDBS)<sup>30</sup> etc. are used to control and tune the crystallinity, and morphology of the anisotropic crystals. The capping agents get selectively adsorbed on certain crystalline facets, inducing anisotropic growth<sup>31</sup> and the difference in the relative growth-rates of various crystal facets results in a diverse outlook of the crystallites.

The mixed cationic/anionic surfactants represent an interesting binary capping agent-directed synthesis system by controlling the nucleation and growth via synergistic interactions of binary surfactant molecules with metals ions, as well as specific crystalline planes.<sup>32</sup> Earlier studies have shown the successful use of such system in the shape control of semiconductors and metal nanocrystals.<sup>33,34</sup> Highly uniform star-shaped and octahedral PbS nanocrystals<sup>33</sup> and single-crystalline gold nanobelts and nanocombs<sup>34</sup> were formed in the presence of the cationic surfactant CTAB and the anionic surfactant sodium dodecyl sulphate (SDS). Rare-earth ion-doped hexagonal-phase NaYF<sub>4</sub> nanowires were hydrothermally synthesized at the cooperative effect of sodium citrate with anionic surfactant sodium bis (2-ethylhexyl) sulfosuccinate (AOT).<sup>35</sup> Nevertheless, the effect of presence of both cationic CTAB and anionic trisodium citrate (TSC) surfactants together, and their optical studies is rarely explored. Moreover, these materials are expected to show photocatalytic properties, but only few reports of lanthanide ion-doped materials are known till date. Recently, the

photocatalytic activity of lanthanide-ion activated SrWO<sub>4</sub> phosphors<sup>36</sup> and CaMoO<sub>4</sub><sup>37</sup> nanocrystals have been studied.

In this thesis, we studied the effect of binary capping agents on the formation of highly uniform, monodispersed, and single crystalline  $\beta$ -NaYF<sub>4</sub>:5 % Tb<sup>3+</sup> crystals with diverse architectures. We explored the influence of reaction temperature and pH of precursor solution on the morphology of the crystals and their growth mechanism. Additionally, morphology dependent luminescence properties of  $\beta$ -NaYF<sub>4</sub>: 5 % Tb<sup>3+</sup> were also studied. To the best of our knowledge, for the first time we investigated the photocatalytic properties of as-prepared  $\beta$ -NaYF<sub>4</sub>:5 % Tb<sup>3+</sup> crystals under UV and solar irradiation.

## **2.2. Materials and method**

### **2.2.1. Materials**

All the chemicals were of analytical grade and used as-received without any further purification. Yttrium (III) nitrate hexahydrate (Y(NO<sub>3</sub>)<sub>3</sub>.6H<sub>2</sub>O) (purity  $\geq$  99.89%), and terbium(III) nitrate hexahydrate (Tb(NO<sub>3</sub>)<sub>3</sub>.6H<sub>2</sub>O) (purity  $\geq$  99.89%), were purchased from Sigma Aldrich Inc. Sodium fluoride (NaF) and trisodium citrate dihydrate (Na<sub>3</sub>C<sub>6</sub>H<sub>5</sub>)<sub>7</sub>.2H<sub>2</sub>O were received from Thomas Baker chemicals Pvt. Ltd. N-cetyl-N,N,N,trimethyl ammonium bromide (C<sub>19</sub>H<sub>42</sub>BrN) was purchased from Loba Chemie Pvt. Ltd. Deionized water was used throughout the experiments.

### **2.2.2. Synthesis**

All of the doping ratios of Ln<sup>3+</sup> are molar in our experiments. In a typical procedure for the preparation of  $\beta$ -NaYF<sub>4</sub>:5% Tb<sup>3+</sup> crystals, Y(NO<sub>3</sub>)<sub>3</sub> and Tb(NO<sub>3</sub>)<sub>3</sub> (0.2 M) were added into 30 mL of aqueous solution containing 2 mmol of trisodium citrate (0.5882 g) to form the metal-citrate complex. After vigorous stirring for 30 min, 0.1 M of CTAB and 2 M of NaF

were introduced into the above solution, respectively. After another agitation for several minutes, the solution was transferred into a stainless steel autoclave with Teflon liner of 80 mL capacity, sealed and heated at 220 °C for 24 h. After that, the autoclave was cooled to room temperature, and the resulting product was separated centrifugally and was washed with distilled water and absolute ethanol. Then, the product was dried under vacuum at 60 °C for 8 h. NaYF<sub>4</sub>:18 % Yb<sup>3+</sup>, 2 % Er<sup>3+</sup> and NaYF<sub>4</sub>:18 % Yb<sup>3+</sup>, 2 % Tm<sup>3+</sup> samples were prepared in a manner similar to that for NaYF<sub>4</sub>:5 % Tb<sup>3+</sup> sample. Additionally, different hydrothermal treatment temperatures (150 °C, 190 °C and 220 °C, 24 h) and pH values (3, 7 and 11, 220 °C, 24 h) were selected to investigate the effect of these factors on the morphology, structural and optical properties of the samples. The pH of the mixture was regulated at certain specific values by adding dilute ammonia solution or HCl. Furthermore, control experiments were done in the absence of CTAB or trisodium citrate (either in the presence of CTAB only or trisodium citrate only) respectively to investigate the evolutionary process of morphology and structure.

### **2.2.3. Characterization techniques**

The phase purity and crystallinity of the as-prepared samples were characterized by powder X-ray diffraction (PXRD) using a PANalytical X'PERT PRO instrument and the iron-filtered Cu-K $\alpha$  radiation ( $\lambda = 1.54 \text{ \AA}$ ) in the  $2\theta$  range of 10-80° with a step size of 0.02°. To analyze the shape and size of the samples, field emission scanning electron microscopy (FESEM: Hitachi S-4200) was done. Energy-dispersive X-ray analysis (EDXA) of the samples was performed during field emission scanning electron microscopy measurements to obtain the elemental composition of the samples. The specific structure details and morphology were obtained by using FEI Tecnai F30 high resolution transmission electron



microscope (HRTEM) equipped with a super-twin lens (s-twin) operated at 300 keV accelerating voltage with Schottky field emitter source with maximum beam current (> 100 nA) and small energy spread (0.8 eV or less). The point-to-point resolution of the microscope is 0.20 nm and line resolution of 0.102 nm with spherical aberration of 1.2 mm and chromatic aberration of 1.4 mm with 70  $\mu$ m objective aperture size. The powder samples obtained were dispersed in ethanol and then drop-casted on carbon-coated copper TEM grids with 200 mesh and loaded to a single tilt sample holder.

The optical properties of the as-synthesized samples were investigated by a Jasco UV-vis-NIR (Model V570) dual beam spectrometer operated at a resolution of 2 nm. PL spectra were acquired using a Fluorolog Horiba Jobin Yvon fluorescence spectrophotometer, equipped with a 400 W Xe lamp as an excitation source and a Hamamatsu R928 photomultiplier tube (PMT) as a detector. Lifetime measurements were carried by using an Edinburgh Instruments FLSP 920 system, having a 60 W microsecond flash lamp as the excitation source. Around 30 mg sample was mixed with one ml methanol, made into a slurry and spread over a quartz plate and dried under ambient conditions and introduced into the sample chamber of the instrument prior to luminescence measurements. The UC emission spectra were obtained using an ACTON SP2300 spectrometer attached to a PMT under 980 nm CW diode laser excitations. The photocatalytic activity of  $\beta$ -NaYF<sub>4</sub>:5 % Tb<sup>3+</sup> was studied by degradation of dyes in aqueous medium under UV light using a 400 W mercury lamp ( $\lambda$ =200 to 400 nm). All the measurements were performed at room temperature.

## 2.3. Results and Discussion

### 2.3.1. Structural and morphological investigations:

The composition, crystallinity and phase purity of the phosphors were first examined by XRD. Figure 1 shows, typical XRD patterns of the as-synthesized NaYF<sub>4</sub>: Ln<sup>3+</sup> (Ln= Tb, Yb/Er and Yb/Tm).

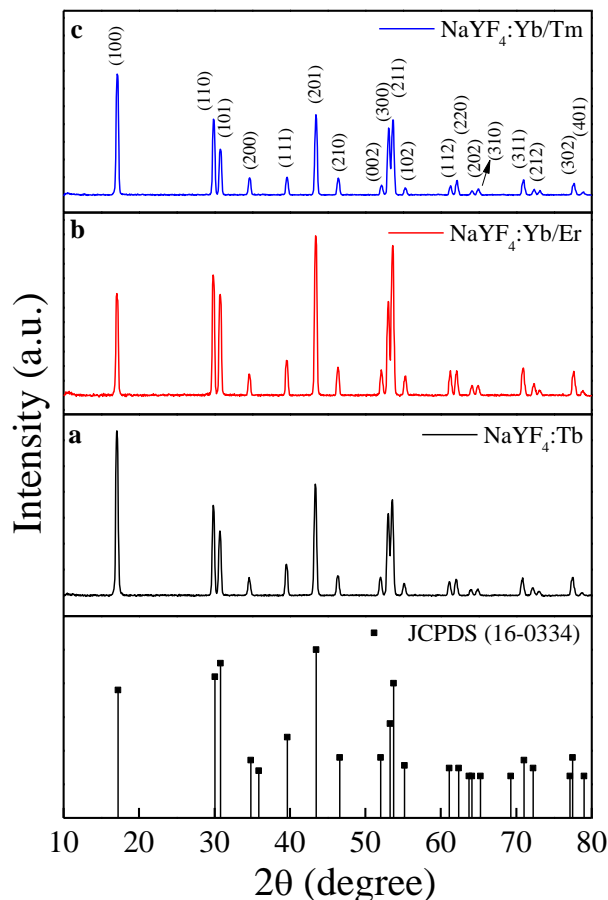


**Figure 1:** The XRD patterns for the as-prepared (a) NaYF<sub>4</sub>:5 % Tb<sup>3+</sup>, (b) NaYF<sub>4</sub>: 18 % Yb<sup>3+</sup>/2 % Er<sup>3+</sup>, (c) NaYF<sub>4</sub>: 18 % Tb<sup>3+</sup>/2 % Tm<sup>3+</sup>.

All of the three samples exhibit sharp diffraction peaks that can be indexed to pure hexagonal-phase  $\beta$ -NaYF<sub>4</sub> (space group:  $P6_3/m$ ). The full-width at half maxima (FWHM)

values of all the reflections are relatively small, suggesting larger crystallite size of the as-prepared samples. The calculated lattice parameters are  $a = 5.9 \text{ \AA}$ ,  $c = 3.5 \text{ \AA}$ , which are in good agreement with the reported data (JCPDS no. 16-0334). No secondary phase is observed in the XRD patterns, revealing that  $\text{Tb}^{3+}$ ,  $\text{Yb}^{3+}/\text{Er}^{3+}$  and  $\text{Yb}^{3+}/\text{Tm}^{3+}$  have been effectively doped into the  $\beta$ -NaYF<sub>4</sub> host lattice. The high crystallinity, as evident by the XRD patterns, is advantageous to the phosphors, as it translates in to less trap centers for photon emission and consequently stronger luminescence.

In general, doping of different lanthanide-ions does not affect the structures and the morphologies of  $\beta$ -NaYF<sub>4</sub>. Thus, here we studied the effect of external factors on the morphologies of  $\beta$ -NaYF<sub>4</sub>:5 %  $\text{Tb}^{3+}$  crystals.

### **2.3.1.1. Effect of reaction temperature:**

Temperature plays a critical role in determining the crystalline phase and its morphology. Keeping all the other reaction parameters unperturbed, we investigated the role of the crystal-growth temperatures (150 °C, 190 °C and 220 °C, 24 h, pH=7) on the crystallinity of the  $\beta$ -NaYF<sub>4</sub>:5 % Tb particles (Figure 2) which coincides well with the JCPDS No. 16-0334. The noticeable feature was a large difference in the relative intensities of (100), (101), and (201) peaks, indicating the temperature driven preferential orientational growth.

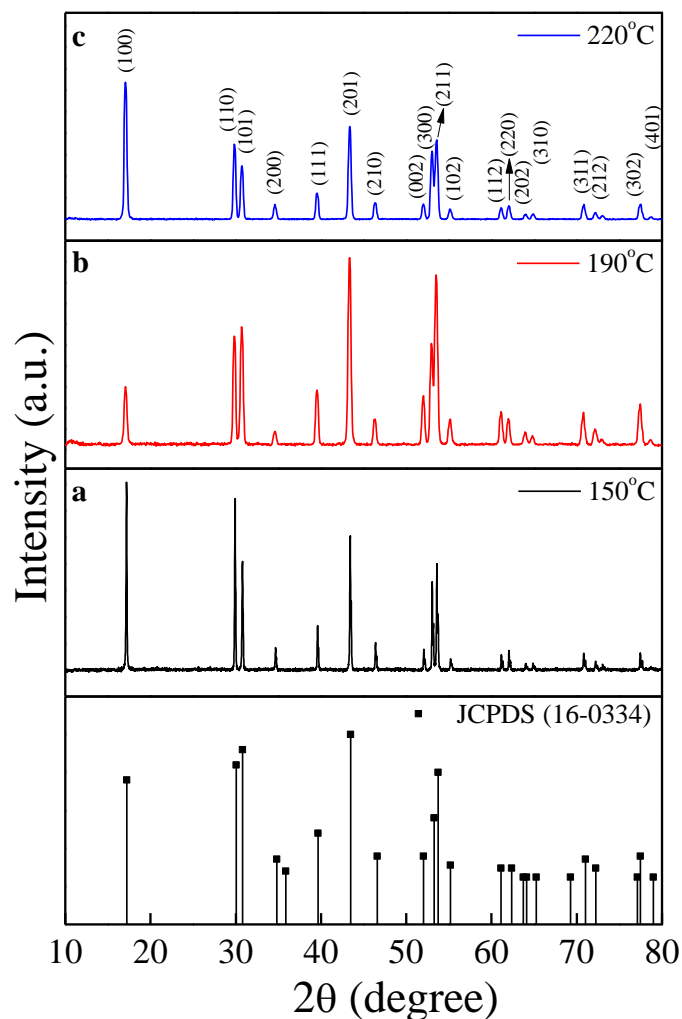


**Figure 2:** The XRD patterns of  $\beta$ -NaYF<sub>4</sub>: 5% Tb<sup>3+</sup> prepared at different temperatures (a) 150 °C, (b) 190 °C, (c) 220 °C and the standard data of hexagonal  $\beta$ -NaYF<sub>4</sub> (JCPDS- 16-0334) as a reference.

The TEM and FESEM images, in Figure 3 (a) shows that, the  $\beta$ -NaYF<sub>4</sub>:5 % Tb<sup>3+</sup> crystals prepared at 150 °C are grown in nearly hexagonal shape and the size is quite polydispersed with average diameter  $\sim 2.7 \mu\text{m}$  and length  $\sim 3.1 \mu\text{m}$ . In comparison, the crystals grown at 190 °C (Figures 3 (b) & (g)) consist of hexagonal microprisms with perfect

uniformity, monodispersity, and well-defined crystallographic facets. In TEM image (Figure 3 (b)), regular hexagonal and rectangular particles are observed, which correspond to hexagonal microprisms that are perpendicular and parallel to the copper grids, respectively. The mean diameter and length of particles is estimated to be  $\sim 2.5 \mu\text{m}$  and  $\sim 1.7 \mu\text{m}$  respectively. At temperature  $220 \text{ }^\circ\text{C}$  (Figures 3 (c), 3 (h)), hexagonal microprisms with average diameter  $\sim 2.1 \mu\text{m}$  and length  $\sim 2.5 \mu\text{m}$  were observed, most of them were oriented parallel to the substrate. Moreover, both the tops and bottoms of these microprisms exhibit apparent deep concave centres while the side planes are relatively smoother (Figures 3 (c), 3 (h)). This is because, the growth process occurs at the circumferential edge of each cylindrical  $\beta$ -NaYF<sub>4</sub> seed.<sup>38</sup> This also demonstrated that, in this current system, the higher temperature (*i.e.* from  $190$  to  $220 \text{ }^\circ\text{C}$ ) facilitate the longitudinal growth along the  $\langle 001 \rangle$  direction and elevation in degree of concave structures at the top/bottom surfaces. As we mentioned earlier that, a comparison between the XRD patterns of the  $\beta$ -NaYF<sub>4</sub>:5 % Tb<sup>3+</sup> crystals grown at different temperature showed the variation in the relative peak intensities which provides further information on the crystal growth (Figure 2). However, the variation in intensity of XRD peaks can be affected by texturing effect. It should be noted that, the particles prepared at  $150 \text{ }^\circ\text{C}$  are not discussed, because of their non-uniformity and polydispersibility, and thus the FESEM image is also not presented. Based on the above analysis, we reasonably believe that the hydrothermal reaction temperature has significant impact on obtaining the  $\beta$ -NaYF<sub>4</sub> microcrystals with uniform morphology and size.

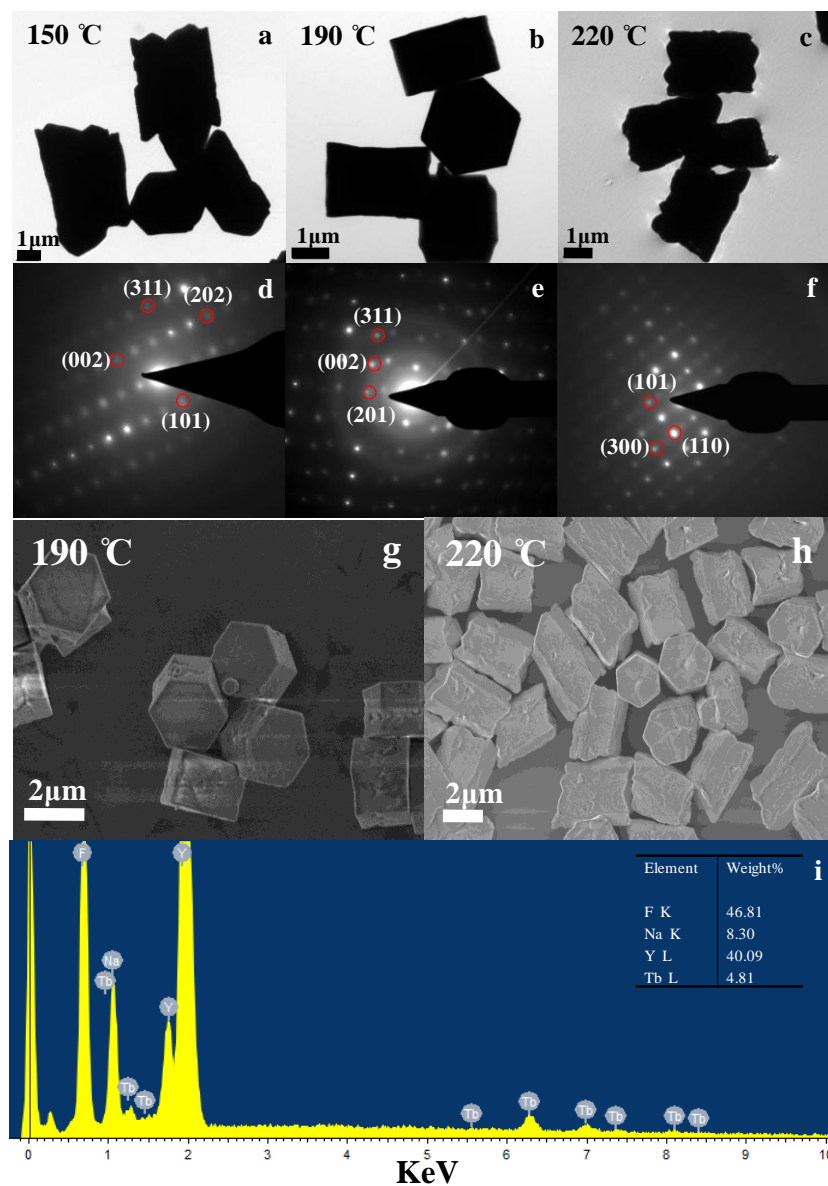
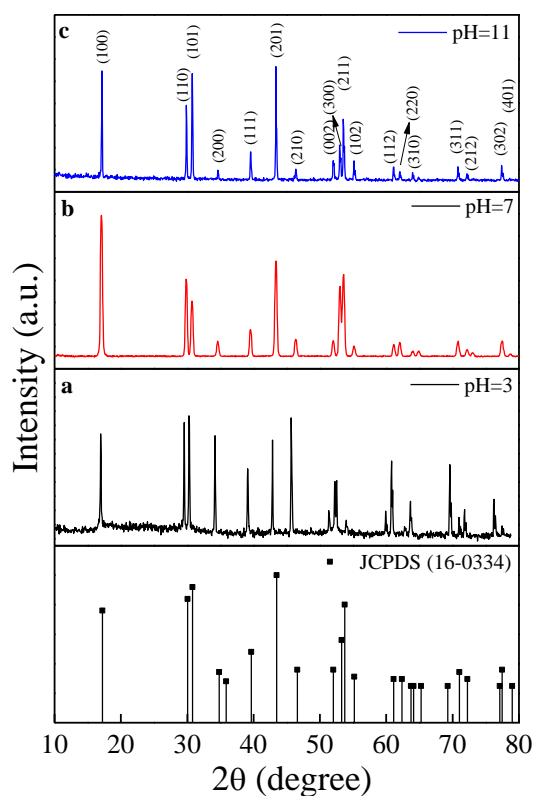


**Figure 3:** TEM images in the top row shows the influence of the synthesis temperature on the shape of  $\beta$ -NaYF<sub>4</sub>: 5 % Tb<sup>3+</sup> crystals ((a) 150 °C, (b) 190 °C, (c) 220 °C). The middle row shows corresponding SAED patterns in the same order. The FESEM images in the bottom row shows, the change in morphology of  $\beta$ -NaYF<sub>4</sub>: 5 % Tb<sup>3+</sup> crystals prepared at (g) 190 °C and (h) 220 °C. (i) Energy-dispersive X-ray analysis (EDXA) patterns of  $\beta$ -NaYF<sub>4</sub>: 5 % Tb<sup>3+</sup> crystals.

Further, the chemical composition of the  $\beta$ -NaYF<sub>4</sub>: 5 % Tb<sup>3+</sup> crystals were characterized by EDXA analysis. As can be seen by Figure 3 (i), all the elements including Na, Y, F and Tb can be detected in the spectrum.

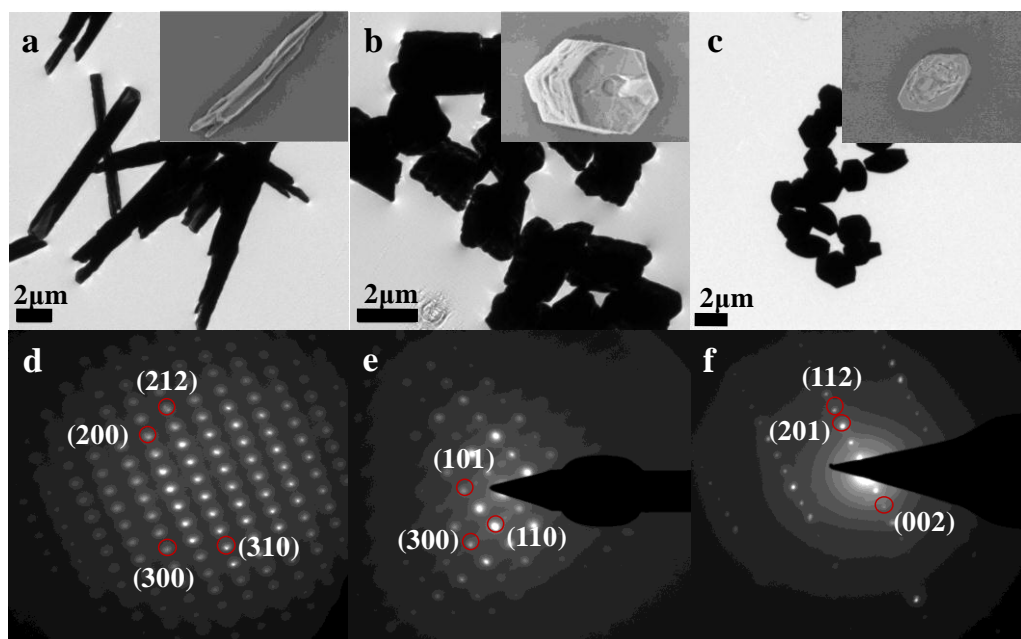
### 2.3.1.2. Effect of pH

Figure 4 compares, the typical XRD patterns of the  $\beta$ -NaYF<sub>4</sub>: 5 % Tb<sup>3+</sup> synthesized at different pH values- 3, 7, and 11 (temperature 220 °C) which could be indexed to pure hexagonal phase  $\beta$ -NaYF<sub>4</sub>, but the relative intensities of (100), (110), (101), (200), and (210) peaks are different from each other signifying the possibility of different preferential orientation growth under altered pH conditions.



**Figure 4:** The XRD pattern of  $\beta$ -NaYF<sub>4</sub>: 5 % Tb<sup>3+</sup> at different pH values of solution (a) pH=3, (b) pH=7, (c) pH=11 and the standard data of hexagonal  $\beta$ -NaYF<sub>4</sub> (JCPDS-16-0334) as reference.

In Figure 5, the TEM images show the morphologies of the  $\beta$ -NaYF<sub>4</sub>: 5 % Tb<sup>3+</sup> crystallites, (grown at ~220 °C) as a function of pH values. It has been observed that at neutral pH, hexagonal microprisms were formed with average diameter ~ 2.1  $\mu$ m and length ~ 2.5  $\mu$ m. While, the crystallites obtained at pH=3 are composed of microrods with chipped ends, having average length ~ 8.7  $\mu$ m in and diameter ~ 1.1  $\mu$ m. At pH=11, spindle-like structures were formed with the average length ~ 3.1  $\mu$ m and diameter ~ 2.1  $\mu$ m. The corresponding SAED patterns (bottom row, Figure 5) reveal that, the crystals are highly single-crystalline in nature.



**Figure 5:** TEM images show the influence of pH on the shape of  $\beta$ -NaYF<sub>4</sub>: 5 % Tb<sup>3+</sup> crystals. (a) Prismatic microrods with chipped ends obtained at pH=3. (b) Hexagonal microprisms at pH=7. (c) Spindle-like crystals at pH=11. The images in insets show the zoom view of the corresponding FESEM images for the sake of comparison. (d, e, f) showing corresponding SAED patterns.



The detailed observations at various pH, was then shown by FESEM images in Figure 6. A very little change in the morphology is observed at pH=9 and 10. On the other hand, the morphology remains almost unchanged at pH=5, while microrods start to form at pH=4. Our study on the effect of pH on morphology of NaYF<sub>4</sub> crystals suggests that, the morphology remain unaffected in pH range 5 to 10, while morphology changes below pH=5 and above pH=10. The plausible reason for the modulation in morphology at varied pH is discussed in the next section.

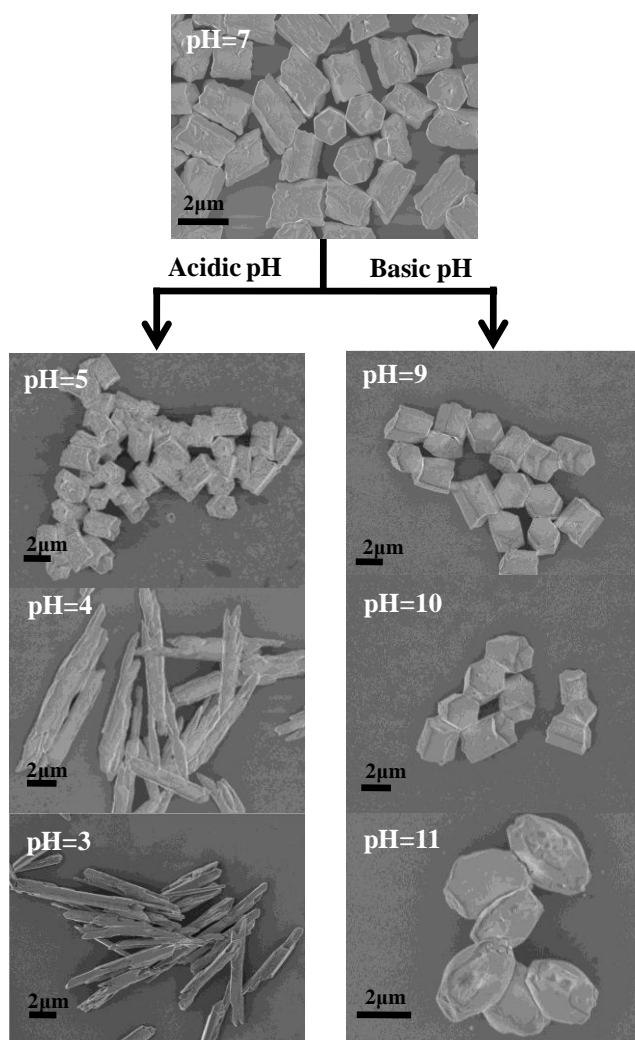


**Figure 6:** FESEM images showing influence of pH on the shapes of  $\beta$ -NaYF<sub>4</sub>: 5 % Tb<sup>3+</sup> microcrystals.

### 2.3.2. Formation mechanism of multiform structures

Here, we explain the growth mechanism of formation of hexagonal microprisms based on the cooperative effect of trisodium citrate (TSC) and CTAB. It is well known that the surfaces of a hexagonal prisms are typically  $\{0001\}$  for top/bottom planes and a family of six energetically equivalent  $\{10\bar{1}0\}$  prismatic side planes [ $(10\bar{1}0)$ ,  $(\bar{1}010)$ ,  $(0\bar{1}10)$ ,  $(01\bar{1}0)$ ,  $(1\bar{1}00)$ , and  $(\bar{1}100)$ ] as shown in Figure 7(a).<sup>39</sup> It is widely accepted that, for hexagonal prismatic NaYF<sub>4</sub> structures, the citrate ions adsorb at the  $\{0001\}$  facets and thus inhibits the growth at top/bottom planes.<sup>24,25</sup> On the other hand, the detailed observation on the crystal structure of  $\beta$ -NaYF<sub>4</sub><sup>40</sup> (Figure 7(b)) revealed that, the density of Y<sup>3+</sup> on  $\{10\bar{1}0\}$  plane is greater, which results in preferential absorption ability of Br<sup>-</sup> ions of CTAB at the  $\{10\bar{1}0\}$  side planes, similar to the case of gold nanorod formation using CTAB as surfactant.<sup>41,42</sup>

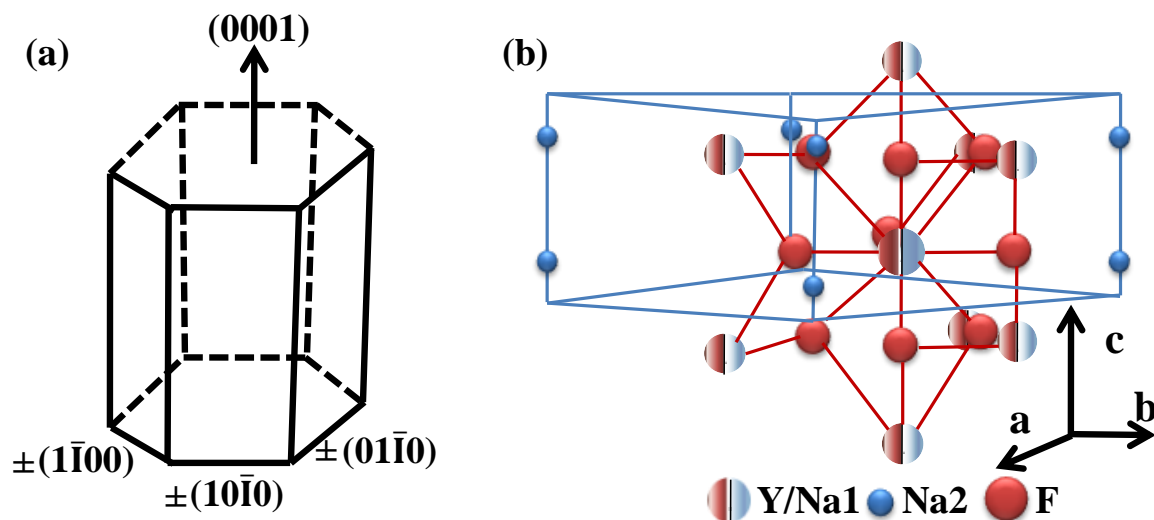


**Figure 7:** (a) The anisotropy of the  $\beta$ -NaYF<sub>4</sub> crystal, and (b) schematic presentation of hexagonal phase  $\beta$ -NaYF<sub>4</sub> crystal structure.

Based on FESEM observations and above studies, the formation mechanism of  $\beta$ -NaYF<sub>4</sub> hexagonal prisms is deduced as follows: In a typical hydrothermal process, trisodium citrate plays dual role of chelating as well as structure-directing agent. First, at the neutral pH, H<sub>3-n</sub>Cit<sup>n-</sup> ions exist as Cit<sup>3-</sup> and so the chelation between Y<sup>3+</sup> cations and Cit<sup>3-</sup> strengthens and thus forms steady Y<sup>3+</sup>-citrate complexes. This can be confirmed by the formation of white precipitates after the mixing of aqueous solution containing Y<sup>3+</sup> and trisodium citrate at neutral pH. The strong Y<sup>3+</sup>-citrate complexes effectively render the slow nucleation and subsequent growth of crystal. Under the hydrothermal conditions, the Y<sup>3+</sup>-citrate complex would be weakened and Y<sup>3+</sup> ions would be released gradually. On the other hand, the released Y<sup>3+</sup> combines with Na<sup>+</sup> and F<sup>-</sup> to generate NaYF<sub>4</sub> nuclei. During subsequent growth stage, the presence of trisodium citrate inhibits the growth of {0001} facets at top/bottom planes with a relative enhancement of the growth sideways to some degree, whereas, the presence of CTAB tends to just mildly inhibit the {10 $\bar{1}$ 0} side facets. This favors the formation of hexagonal microprisms with well-defined, smooth and sharp edges of prismatic side planes. Conversely, samples prepared by using only CTAB are rod-shaped and when only trisodium citrate is used, the product obtained are still hexagonal prisms; but the edges of prismatic side planes are comparatively not much smoother and sharper as obtained by using CTAB and TSC simultaneously, as shown by arrows in Figure 8 (A) and (B).

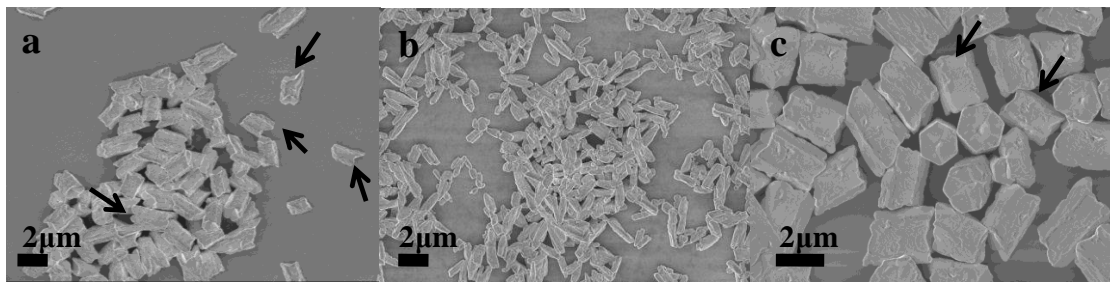


**Figure 8.A:** FESEM imaged of  $\beta$ -NaYF<sub>4</sub>:5 % Tb<sup>3+</sup> crystals prepared using only (a) trisodium citrate, (b) only CTAB and (c) trisodium citrate together with CTAB.

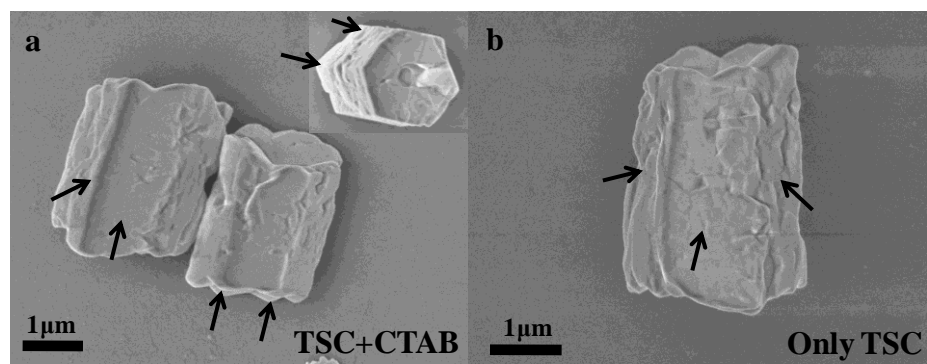


**Figure 8.B:** Magnified FESEM images of  $\beta$ -NaYF<sub>4</sub>:5 % Tb<sup>3+</sup> crystals prepared using (a) trisodium citrate and CTAB both and (b) only trisodium citrate. Arrows indicating well define, smooth and sharp edges of prismatic side planes formed in presence of both trisodium citrate and CTAB in converse to relatively less smooth and sharp prismatic side plane, when prepared using only trisodium citrate.

Further, the formation of microrods and spindle-like structures at varied pH are presented in Figure 9 (a-c) and is explained as follows: if the pH value of the solution is changed, the existing form of Cit<sup>3-</sup> changes to HCit<sup>2-</sup>, H<sub>2</sub>Cit<sup>-</sup>, or H<sub>3</sub>Cit, and the chelation between H<sub>3-n</sub> Cit<sup>n-</sup> and the Y<sup>3+</sup> ions are affected. Moreover, at different pH values, the ability

of Cit<sup>3-</sup> to adsorb on certain crystal facets is different from each other, leading to the differential growth rate of crystal facets, which results in the formation of anisotropic geometries.<sup>20</sup>

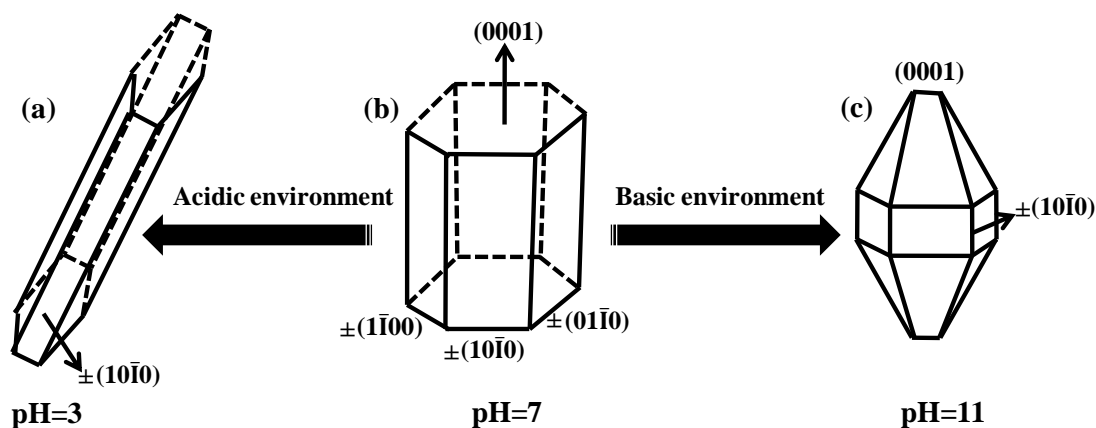


**Figure 9:** Schematic diagram showing the effect of pH (a-c) on the morphology of  $\beta$ -NaYF<sub>4</sub>.

In acidic pH, Cit<sup>3-</sup> anions are not able to bind selectively and effectively on {0001} facets, rather possibly bind to  $\{10\bar{1}0\}$  facets of growing  $\beta$ -NaYF<sub>4</sub> crystallites, and therefore, allow the particles to grow along [0001] direction leading to the formation of 1-D prismatic microrods. It is worth mentioning here that, CTAB is known to play a role to form gold nanorods by binding at {100} and {110} planes in acidic pH.<sup>43</sup> While in alkaline environment, the existent form of Cit<sup>3-</sup> is not affected, rather Cit<sup>3-</sup> ions adsorb strongly on to the {0001} surfaces and promote the growth more prominently along the side directions forming spindle-like structures. However, the effect of CTAB on crystal morphology at basic pH is not very clear to us.

### 2.3.3. Optical studies

#### 2.3.3.1. UV-visible studies

The UV-vis absorption spectra of  $\beta$ -NaYF<sub>4</sub>:5 % Tb<sup>3+</sup> (Figure 10 (a)) shows a strong absorbance peak at  $\sim$  253 nm, indicating large bandgap of  $\beta$ -NaYF<sub>4</sub>: 5 % Tb<sup>3+</sup> followed by a broad absorbance above  $\sim$  400 nm onwards.

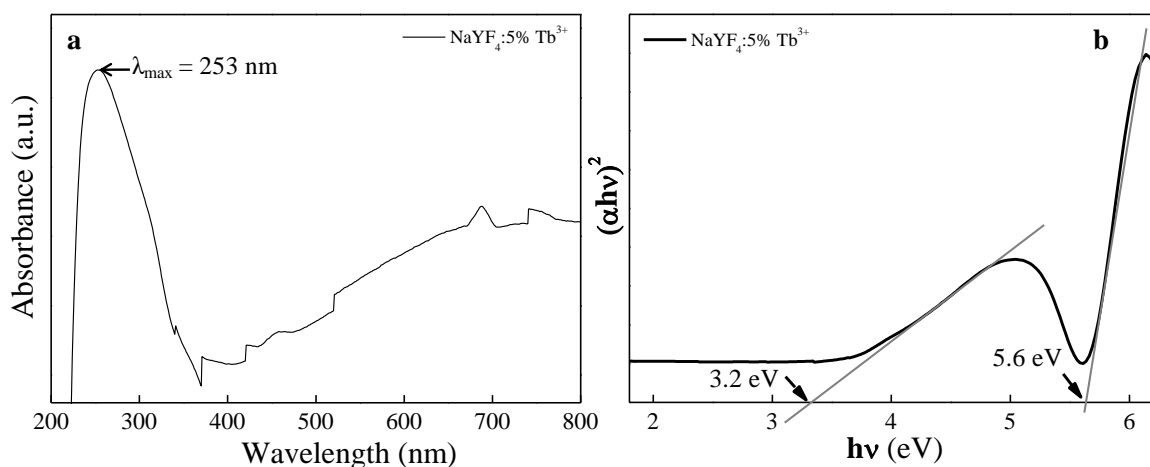


**Figure 10:** (a) UV-visible absorption spectra and (b) tauc plot for the estimation of optical band gap energy of  $\beta$ -NaYF<sub>4</sub>: 5 % Tb<sup>3+</sup>.

The optical bandgap was determined by Tauc plot as shown in Figure 10 (b). The bandgap for the as-prepared  $\beta$ -NaYF<sub>4</sub>: 5 % Tb<sup>3+</sup> was calculated to be  $\sim$  5.6 eV. Surprisingly, a new and strong energy level was observed, with an absorption edge at  $\sim$  3.2 eV, which might be due to the Tb<sup>3+</sup> doping in the host lattice and a strong function of doping concentration.<sup>44</sup>

### 2.3.3.2. Static and dynamic photoluminescence studies

#### 2.3.3.2.1. $\beta$ -NaYF<sub>4</sub>:Tb<sup>3+</sup>

Owing to the non-existence of *d*-electrons in Y<sup>3+</sup> ([Kr] 4d<sup>0</sup>) in un-doped NaYF<sub>4</sub>, the probability of emission is negligible in the host matrix. Figure 11 compares, the excitation (a) and emission (b) photoluminescence spectra of microrods, hexagonal microprisms and spindle-shaped Tb<sup>3+</sup> ion-doped NaYF<sub>4</sub> crystals. It can be evidently seen that, in all the three samples the peak-positions in excitation and emission spectra remain similar, and the bands differ only in their relative intensities. The excitation spectrum monitored at  $\lambda_{\text{ex}}=544$  nm, consist of the characteristic *f-f* transition lines within the Tb<sup>3+</sup> 4f<sup>8</sup> configuration. The excitation lines can be assigned to the transition from <sup>7</sup>F<sub>6</sub> ground state to the different excited states of Tb<sup>3+</sup>, so as at, ~ 288 nm (<sup>5</sup>I<sub>6</sub>), ~ 306 nm (<sup>5</sup>H<sub>6</sub>), ~ 321 nm (<sup>5</sup>D<sub>0</sub>), ~ 344 nm (<sup>2</sup>G<sub>3</sub>), ~ 356 nm (<sup>5</sup>D<sub>2</sub>), ~ 372 nm (<sup>5</sup>G<sub>6</sub>), and ~ 383 nm (<sup>5</sup>D<sub>3</sub>), respectively. The obtained emission spectra monitored at  $\lambda_{\text{ex}} = \sim 375$  nm, yielded weak blue and intense green emissions in the regions of 400-450 nm and 480-680 nm respectively, which are due to the <sup>5</sup>D<sub>3</sub>→<sup>7</sup>F<sub>*J*</sub> (*J* = 3, 4, 5, 6) and <sup>5</sup>D<sub>4</sub>→<sup>7</sup>F<sub>*J*</sub> (*J* = 3, 4, 5, 6) transitions of Tb<sup>3+</sup> ions, respectively. Specifically, the emission bands at ~ 414 and ~ 436 nm are attributed to the emission transitions of <sup>5</sup>D<sub>3</sub>→<sup>7</sup>F<sub>5</sub> and <sup>5</sup>D<sub>3</sub>→<sup>7</sup>F<sub>4</sub> respectively. Four prominent emission peaks centered at ~ 488, ~ 544, ~ 584, and ~ 619 nm, originates from the transitions of <sup>5</sup>D<sub>4</sub>→<sup>7</sup>F<sub>6</sub>, <sup>5</sup>D<sub>4</sub>→<sup>7</sup>F<sub>5</sub>, <sup>5</sup>D<sub>4</sub>→<sup>7</sup>F<sub>4</sub>, and <sup>5</sup>D<sub>4</sub>→<sup>7</sup>F<sub>3</sub> respectively.<sup>45</sup> Among these transitions, the green emission <sup>5</sup>D<sub>4</sub>→<sup>7</sup>F<sub>5</sub> at ~ 544 nm is the most intense emission, which corresponds to a magnetic dipole transition.

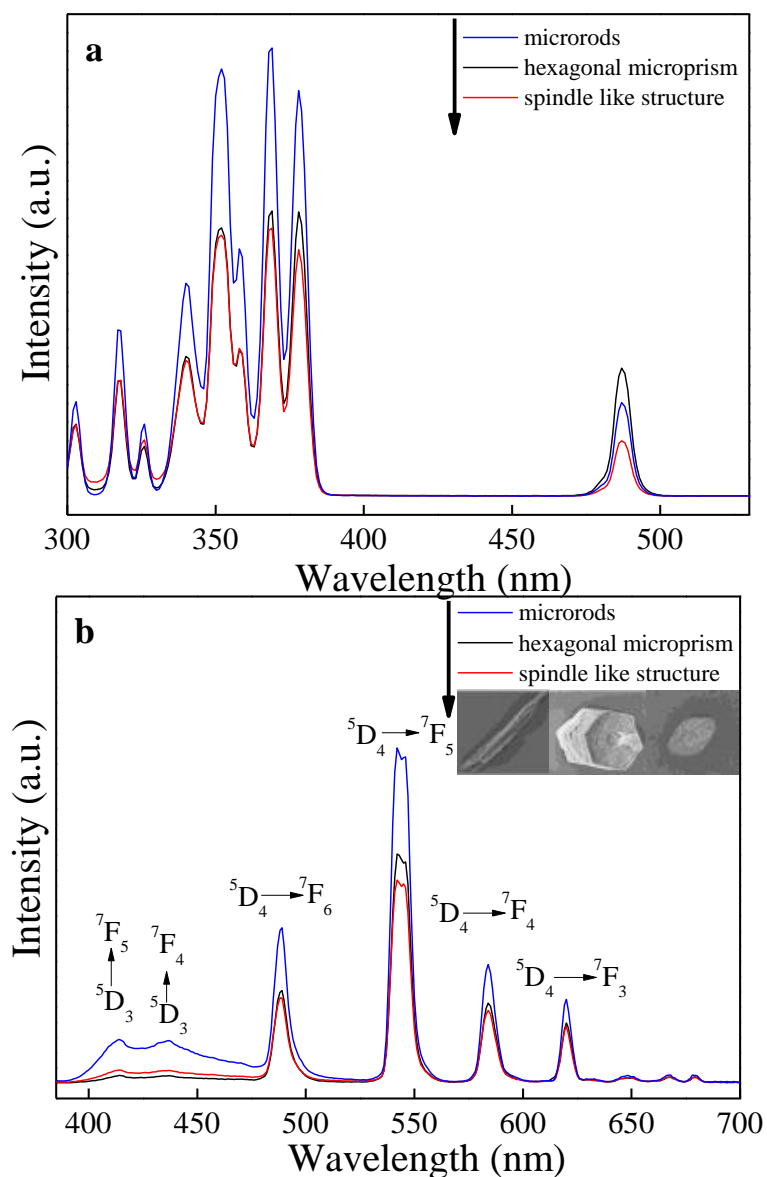


**Figure 11:** A comparison of static photoluminescence (a) excitation spectra at  $\lambda_{em} = 544$  nm, and (b) emission spectra at  $\lambda_{ex} = 375$  nm of  $\beta$ -NaYF<sub>4</sub>: 5 % Tb<sup>3+</sup> crystals with different shapes.

The optical properties of inorganic materials are strongly dependent on their size, morphology, doping, crystallinity and other parameters, that affect its band structure. We observed that under similar measurement conditions, the microrods possess highest emission intensity, while spindle-like structures have lowest emission intensity. The relative intensity



of hexagonal microprisms lies in between microrods and spindle-like structures. The difference in relative intensities might occur due to the difference in the effects of crystal field perturbation on individual  $f-f$  transition, as a consequence of the different morphologies and size of the samples.<sup>46</sup> The other reason might be, the difference in surface area of different facets, as in an anisotropic material, the interaction with light and photon emission also get influence by the material crystallinity and exposed facets. Large surface area also introduces larger number of defects into the phosphor crystal. Defects may quench the luminescence intensity of phosphors by non-radiative recombination in electrons and holes. Thus, the phosphor with reduced surface area would show improved PL intensity.<sup>47</sup> Herein, we believe that, the microrods possessed smallest and spindle-like structures possessed largest surface area based on results obtained by PL decay studies. Moreover, the SAED pattern of microrods in Figure 5 (d), showed highest crystallinity, thus lesser defects and highest luminescence intensity.

The PL decay curves for the luminescence of  $\text{Tb}^{3+}$  in  $\beta\text{-NaYF}_4:5\% \text{Tb}^{3+}$  are shown in Figure 12. These curves can be well fitted by a single exponential function as  $I(t) = I_0 \exp(-t/\tau)$  where,  $I_0$  is the initial emission intensity at  $t=0$ ,  $\tau$  is the  $1/e$  lifetime of the emission centre. The lifetimes for  $^5\text{D}_4$  were detected at 544 nm for  $^5\text{D}_4 \rightarrow ^7\text{F}_5$  transition of  $\text{Tb}^{3+}$  by excitation at 375 nm and were determined to be 4.39 ms, 4.10 ms and 4.09 ms for microrods, hexagonal microprisms and spindle-like structures respectively (Figure 12). The lifetime values and fitted parameters for different samples are listed in Table 1. The variation in luminescence lifetimes is consistent with that of emission spectra. Spindle-like structures showed lowest luminescence lifetime. This infers that, they possess largest surface area, because heavy non-radiative transitions at larger surfaces lead to shortest luminescence lifetime.<sup>48</sup> Consequently,

on the basis of lifetime dependence on surface area, we confirm that spindle-like structures possess largest surface area; tend to shortest luminescence lifetime and lowest luminescence intensity and the vice-versa for microrods.

**Table 1:** Luminescence lifetime values of  $\beta$ -NaYF<sub>4</sub>: 5 % Tb<sup>3+</sup> with different shapes.

Sample	$\tau$ (ms)	$\chi^2$
Microrod	4.39	1.78
Hexagonal microprism	4.10	1.72
Spindle-like structure	4.09	1.67

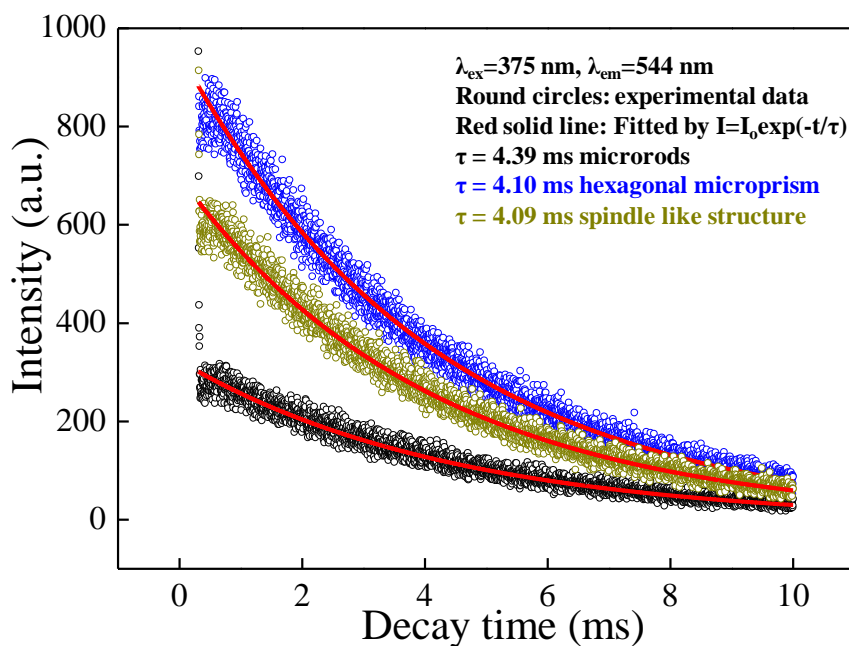


**Figure 12:** The luminescence decay curves for the  ${}^5D^4 \rightarrow {}^7F^5$  emission of Tb<sup>3+</sup> ( $\lambda_{\text{ex}}=375$  nm,  $\lambda_{\text{em}}=544$  nm) in  $\beta$ -NaYF<sub>4</sub>:5 % Tb<sup>3+</sup> with different morphologies: microrods, hexagonal microprisms, spindle-like structures. The fitted lifetime values are indicated inside the figures.

The varying luminescence intensities for different morphologies of  $\beta$ -NaYF<sub>4</sub>:5 % Tb<sup>3+</sup> are also represented by CIE chromaticity diagram as shown in Figure 14. The CIE coordinate values for the emission spectrum of  $\beta$ -NaYF<sub>4</sub>:5 % Tb<sup>3+</sup> are determined as x=0.2690, y=0.4692 (microrods), x=0.3256, y=0.5277 (hexagonal microprisms) and x=0.3091, y=0.4838 (spindle-like structures), located in the green region.

### 2.3.3.2.2. $\beta$ -NaYF<sub>4</sub>:Yb<sup>3+</sup>/Er<sup>3+</sup>:

Figure 13 (a) shows, the up-conversion luminescence spectra of Yb<sup>3+</sup>, Er<sup>3+</sup>- co-doped  $\beta$ -NaYF<sub>4</sub> hexagonal microprisms, under 980 nm NIR laser excitation. The spectra display four distinct Er<sup>3+</sup> emission bands. The emission peak at ~408 nm is assigned to transition from <sup>2</sup>H<sub>9/2</sub>→<sup>4</sup>I<sub>15/2</sub>. The emission peaks at ~521 and ~540 nm in the green region are assigned to transitions from <sup>2</sup>H<sub>11/2</sub> and <sup>4</sup>S<sub>3/2</sub> to <sup>4</sup>I<sub>15/2</sub>. The red emission peak at ~655 nm results from <sup>4</sup>F<sub>9/2</sub> to <sup>4</sup>I<sub>15/2</sub> transition. The CIE coordinate values for the emission spectrum of  $\beta$ -NaYF<sub>4</sub>:Yb<sup>3+</sup>/Er<sup>3+</sup> are determined as x=0.2805, y=0.6836, located in green region as shown in Figure 14.

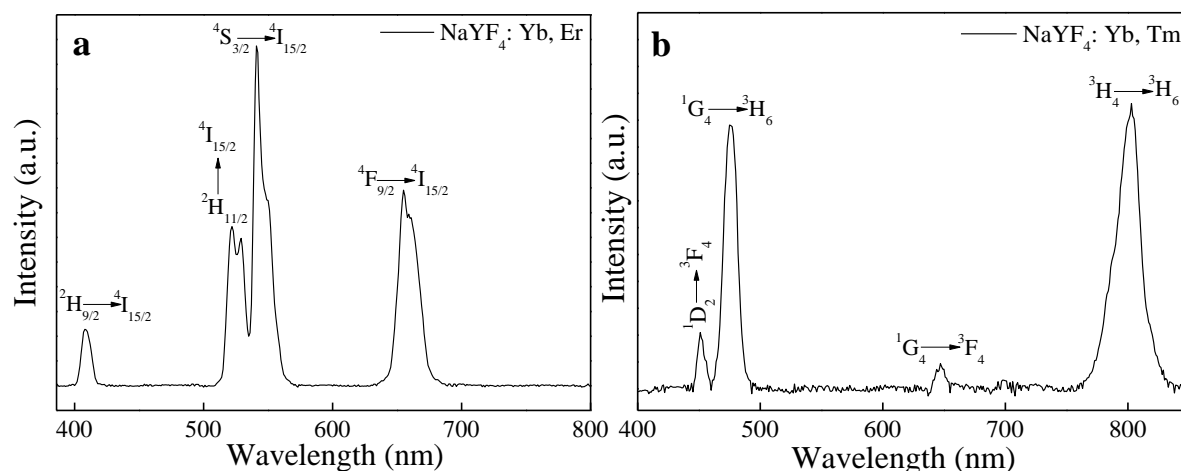


**Figure 13:** Up-conversion emission spectra of (a) NaYF<sub>4</sub>:Yb<sup>3+</sup>/Er<sup>3+</sup> and (b) NaYF<sub>4</sub>:Yb<sup>3+</sup>/Tm<sup>3+</sup> hexagonal microprisms under 980 nm laser excitation.

### 2.3.3.2.3. $\beta$ -NaYF<sub>4</sub>:Yb<sup>3+</sup>/Tm<sup>3+</sup>:

Figure 13 (b) shows the up-conversion luminescence spectra of Yb<sup>3+</sup>, Tm<sup>3+</sup>- co-doped  $\beta$ -NaYF<sub>4</sub> hexagonal microprisms under 980 nm NIR laser excitation. The spectra show four distinct emission lines of Tm<sup>3+</sup>. The emission peaks at ~450 and ~646 nm are assigned to transitions from <sup>1</sup>D<sub>2</sub> and <sup>1</sup>G<sub>4</sub> to <sup>3</sup>F<sub>4</sub>. The emission peaks at ~475 and ~804 nm are results from <sup>1</sup>G<sub>4</sub> and <sup>3</sup>H<sub>4</sub> to <sup>3</sup>H<sub>6</sub> transition. The CIE coordinate values for the emission spectrum of  $\beta$ -NaYF<sub>4</sub>:Yb<sup>3+</sup>/Tm<sup>3+</sup> are determined as x=0.1286, y=0.0840, located in blue region as shown in Figure 14.

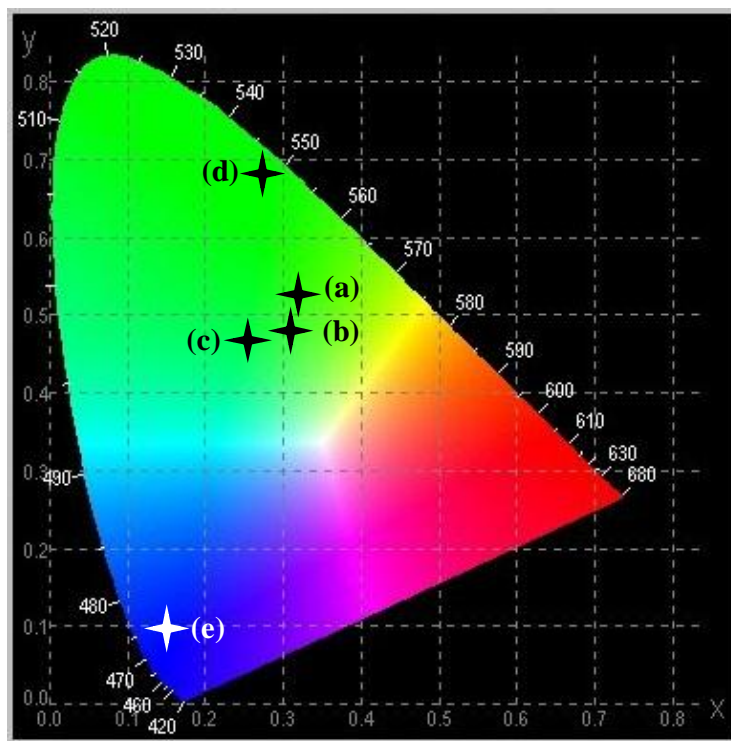


**Figure 14:** CIE chromaticity diagram showing the emission colors for (a)  $\beta$ -NaYF<sub>4</sub>:5 % Tb<sup>3+</sup> at pH=7, (b)  $\beta$ -NaYF<sub>4</sub>:5 % Tb<sup>3+</sup> at pH=11, (c)  $\beta$ -NaYF<sub>4</sub>:5 % Tb<sup>3+</sup> at pH=3, (d)  $\beta$ -NaYF<sub>4</sub>:Yb<sup>3+</sup>/Er<sup>3+</sup>, (e)  $\beta$ -NaYF<sub>4</sub>:Yb<sup>3+</sup>, Tm<sup>3+</sup>.

### 2.3.4. Photocatalytic Studies

#### 2.3.4.1. Photoselectivity of $\beta$ -NaYF<sub>4</sub>:5 % Tb<sup>3+</sup> phosphors

Photocatalytic measurements were performed by exposing  $\beta$ -NaYF<sub>4</sub>: 5 % Tb<sup>3+</sup> phosphors to the irradiation of a 400 W mercury lamp ( $\lambda=200$  to 400 nm). Because of the presence of broad absorption above  $\sim 400$  nm onwards (Figure 10 (a)) and the additional inter-band energy level in  $\beta$ -NaYF<sub>4</sub>: 5 % Tb<sup>3+</sup> as shown in Figure 10 (b) (discussed earlier in section 2.3.3.1.), it was tested for the photocatalytic properties under UV irradiation.

The presence of inter-band energy level, accelerates the interfacial electron transfer process, and thus facilitates photocatalysis reaction in visible and ultraviolet light irradiation as demonstrated by Xie *et.al.*, in Ce<sub>x</sub>Ti<sub>(1-x)</sub>O<sub>2</sub>.<sup>49</sup> To study the photoselectivity of  $\beta$ -NaYF<sub>4</sub>: 5 % Tb<sup>3+</sup> phosphors, we studied the degradation behavior of four different dyes namely, methyl orange (MO), methylene blue (MB), rhodamine B (RhB) and malachite green (MG).

The sample suspensions were kept in dark overnight to reach the equilibrium. The UV-visible absorbance spectra for degradation of different dyes using  $\beta$ -NaYF<sub>4</sub>: 5 % Tb<sup>3+</sup> are compared in Figure 15.

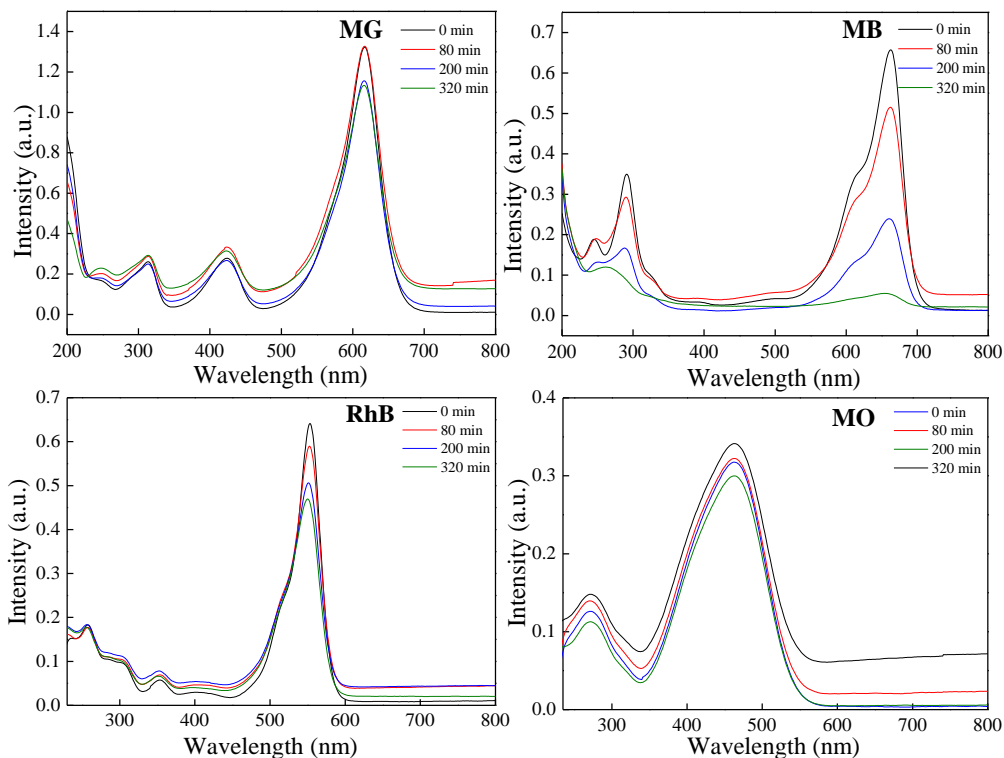


**Figure 15:** Photocatalytic selectivity of  $\beta$ -NaYF<sub>4</sub>: 5 % Tb<sup>3+</sup> for different dyes: MG, MB, RhB, and MO, under irradiation of 400 W mercury lamp for 320 min.

The degradation of dyes was observed through reduction in absorbance peak intensity with an increase in the irradiation time. The kinetics of the reaction was plotted as  $(C/C_0)$  against time ( $t$ ), where  $C_0$  is the initial concentration and  $C$  is the final concentration of different dyes (Figure 16 and 17). The characteristic absorbance peaks of MB, RhB, MO, and MG were found at  $\lambda = \sim 662$  nm,  $\sim 555$  nm,  $\sim 463$  nm, and  $\sim 617$  nm, respectively, which were used as references for photocatalytic degradation for respective dyes.

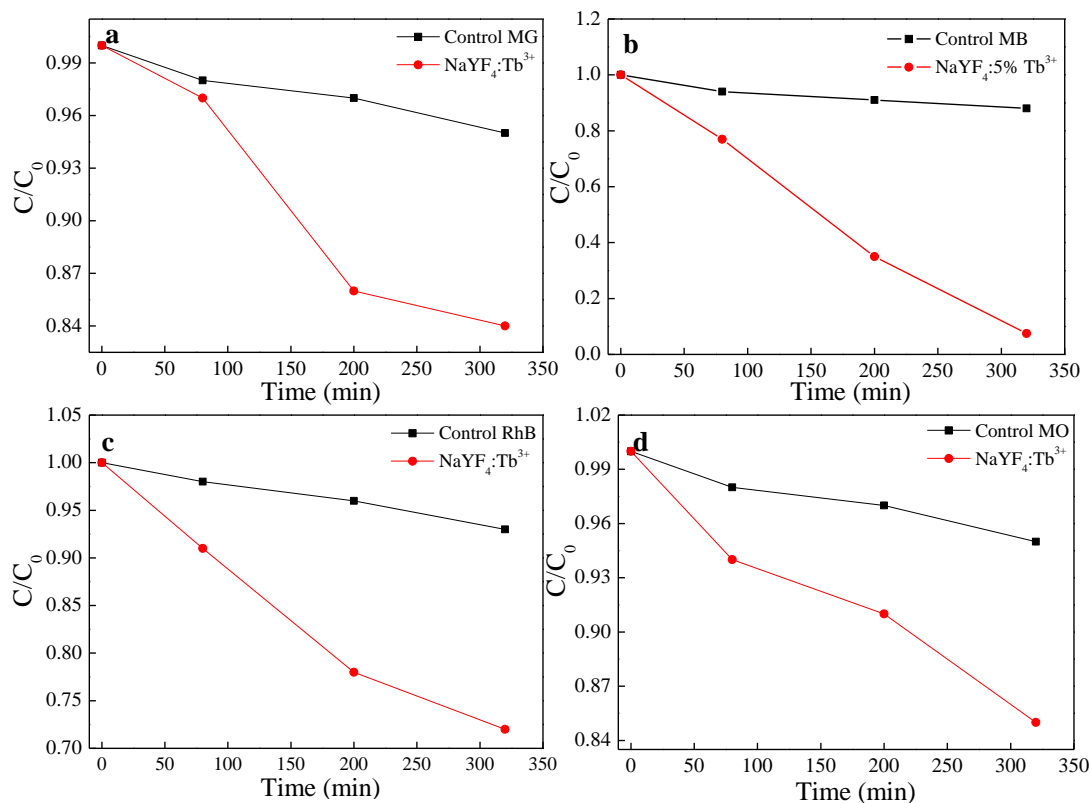


**Figure 16:** Plots of dye concentrations ( $C/C_0$ ) vs. time showing photodegradation of different dyes: (a) MG, (b) MB, (c) RhB, and (d) MO, under irradiation of 400 W mercury lamp for 320 min.

Following the exposure, the degradation of all dyes was negligible in the absence of  $\beta$ -NaYF<sub>4</sub>: 5 % Tb<sup>3+</sup> phosphors which are shown by the control dye analysis (Figure 16). The  $\beta$ -NaYF<sub>4</sub>: 5 % Tb<sup>3+</sup> phosphors degraded ~ 11 %, ~ 14 %, ~ 28 % and ~ 92 % of MO, MG, RhB and MB respectively within 320 min of UV irradiation (Figure 17). It is clear that, RhB degraded to some extent and MB decomposed dramatically during the irradiation period. However, the absorption lines of other two dyes MO and MG are hardly affected (Figure 17). One probable reason for selectivity for RhB is that, the emission of  $\beta$ -NaYF<sub>4</sub>: 5 % Tb<sup>3+</sup> locates in green region (540-570 nm) which overlaps with the absorption of rhodamine B. We

believe that, the highest selectivity for MB is might be due to its molecular structure. According to previous studies,  $-\text{CH}_3$  elimination and C-N cleaving can certainly occur in MB molecules via formation of  $\text{OH}^\cdot$  radical.<sup>50</sup>

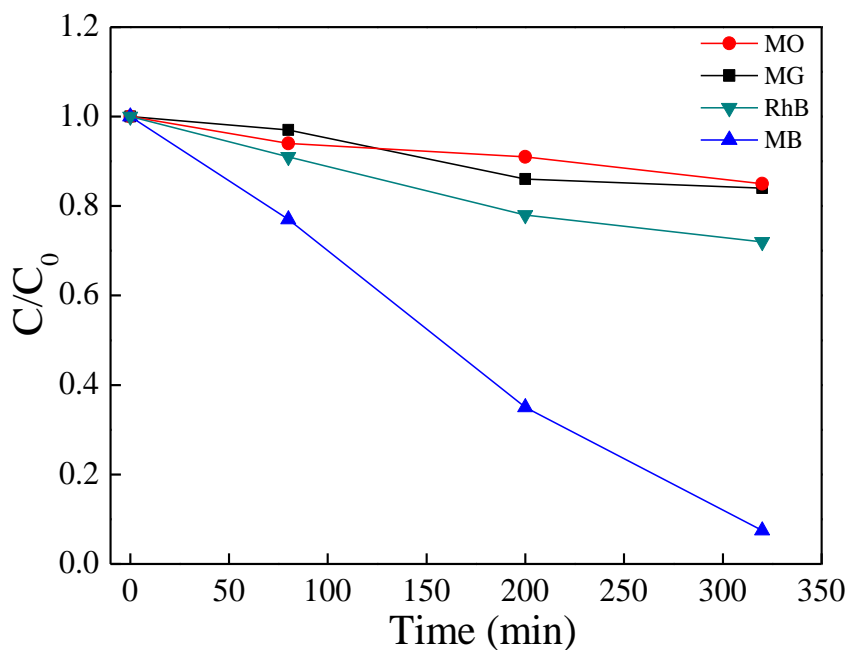


**Figure17:** Plots of dye concentrations ( $C/C_0$ ) vs. time showing comparison of photodegradation of different dyes: MO, MG, RhB and MB with hexagonal prisms.

In addition, we also investigated the photocatalytic activity of MB under sunlight irradiation, which showed  $\sim 80\%$  degradation efficiency (Figure 18).



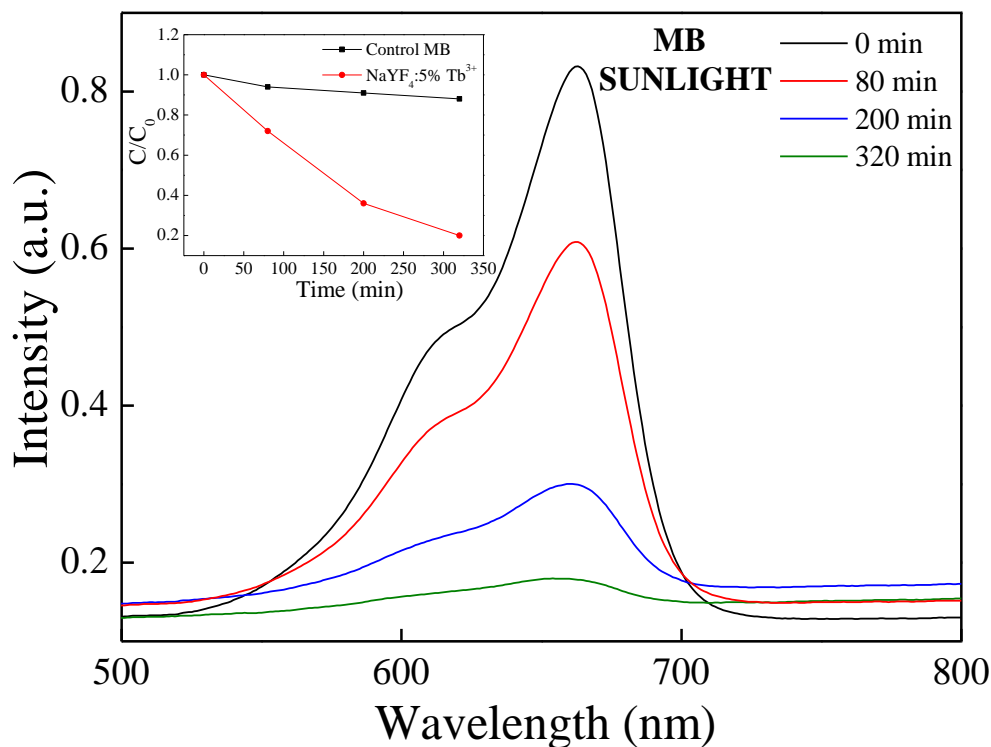


**Figure 18:** Photocatalytic degradation of MB in presence of  $\beta$ -NaYF<sub>4</sub>: 5 % Tb<sup>3+</sup> under solar light irradiation. Inset showing corresponding plot of  $(C/C_0)$  vs. time.

#### 2.3.4.2. Mechanism of MB degradation

The plausible mechanism involved in degradation of MB is as follows: Upon irradiation, the photon absorption leads to formation of a hole ( $h^+$ ) in the valance band and electron ( $e^-$ ) in conduction band.<sup>51</sup> The hole oxidizes water molecules to produce hydroxyl radicals ( $OH^\cdot$ ), whereas the electron in the conduction band reduces the oxygen adsorbed on the particles to  $\cdot O^{2-}$ . The active oxygen and radical species such as  $\cdot OH$  and  $\cdot O^{2-}$  degrade the MB dye molecules by directly cleaving the aromatic ring at azo bond and forming various

by-products such as carbon dioxide, water, nitrate, sulphate and ammonia<sup>52</sup> as represented as scheme in Figure 19.

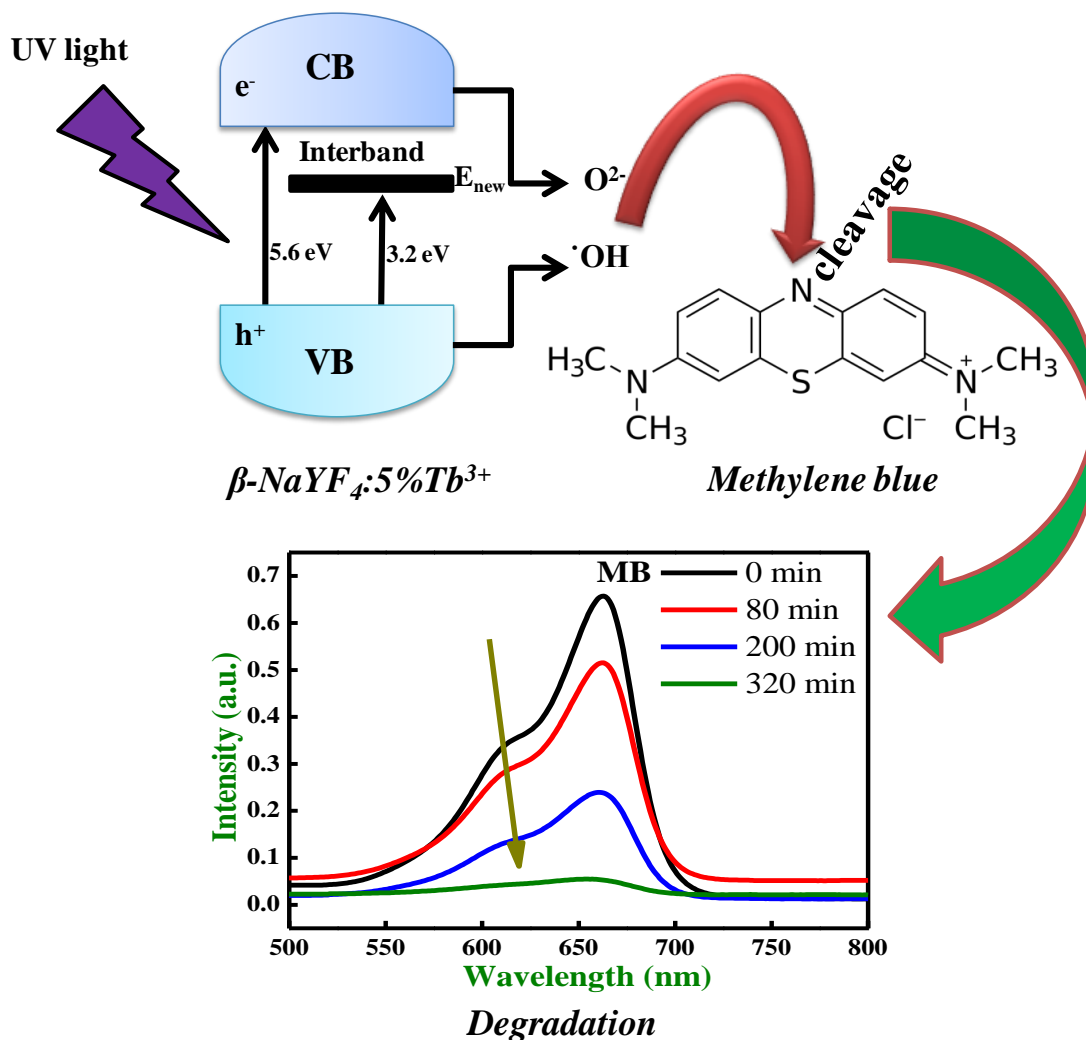


**Figure 19:** Schematic representation for the photocatalysis mechanism of methylene blue in presence of  $\beta$ -NaYF<sub>4</sub>: 5 % Tb<sup>3+</sup> crystals.

### 2.3.4.3. Morphology dependence on photocatalytic properties of $\beta$ -NaYF<sub>4</sub>:5 % Tb<sup>3+</sup> crystals

Extensive studies on photocatalysts have demonstrated that, the size and shape of particles profoundly affect their activity as the photocatalytic reactions are typically surface-based processes.<sup>53</sup> These facts entuse us to check-out, the morphology dependent photocatalysis studies of our samples. The photo-selectivity studies were performed with hexagonal prism-shaped crystals, and then the degradation of MB was compared with the as-prepared microrods and spindle-like structures to study the morphological dependence on photocatalytic activity. The photocatalytic results as shown in Figure 20 indicate that, ~ 92 % of MB molecules degraded by hexagonal prism shaped crystals, while ~ 82 % and ~ 71 % MB dye degraded by spindle-like structures and microrods respectively in 320 min.

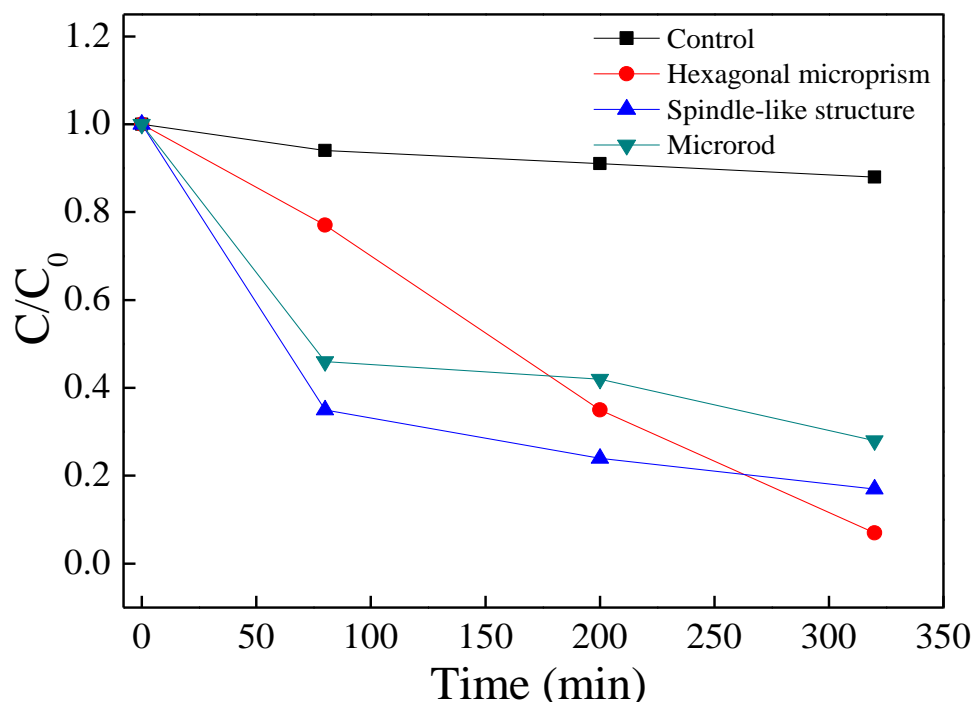


**Figure 20:** Photodegradation of MB using  $\beta$ -NaYF<sub>4</sub>: 5 % Tb<sup>3+</sup> with different shapes, under irradiation of 400 W mercury lamp.

Additionally, it is observed that although hexagonal prisms showed highest degradation after complete reaction, but in the initial and intermediate period, *i.e.* after 80 min and 200 min, spindle shaped particles showed highest degradation (~ 64 % and ~ 75 %) as compare to hexagonal prisms (~ 21 % and ~ 64 %) and microrods (~ 53 % and ~ 57 %). The initial higher degradation by spindle shaped particles may be attributed to their larger surface area. From luminescence studies, we assume that spindle like structures have larger and microrods have smaller surface area. Moreover, FESEM images show the greater roughness of spindle like structures. Photocatalysis results are well consistent with PL and FESEM observations. The larger surface area and roughness of spindle like structures provide more catalytic active sites, thus showed greater degradation initially. This is because, it has been well documented that, larger surface area consist of low-coordinated atoms located in the defects such as edges, kinks, and vacancies which offers more active sites.<sup>54</sup> Microrods with lowest surface area showed lowest degradation performance. But at this stage, it cannot be fully understood that, why  $\beta$ -NaYF<sub>4</sub>: 5 % Tb<sup>3+</sup> hexagonal prisms showed highest degradation efficiency (~ 92 %) after complete reaction of 320 min. We believe that, this might be due to well-defined highly crystalline facets of hexagonal prism shaped crystals (Figure 5 and 6). It has been demonstrated that, the surface atoms of different facets have unique coordination environment and different surface energies yielding, different and distinct catalytic properties.<sup>54</sup>

Our group have also previously demonstrated the enhanced photocatalytic activity of {001} faceted BiOCl crystals.<sup>55</sup> Therefore, the facets of hexagonal prisms with high surface energies might have exposed, that could have increased the number of catalytic active sites, which in turn, might have rendered enhanced photocatalytic degradation of MB. More interestingly, it has also been observed that, in case of degradation by microrods and spindle-like structures, the absorption peak diminished as well as gets broadened and showed hypsochromic effect with increasing time (Figure 21).

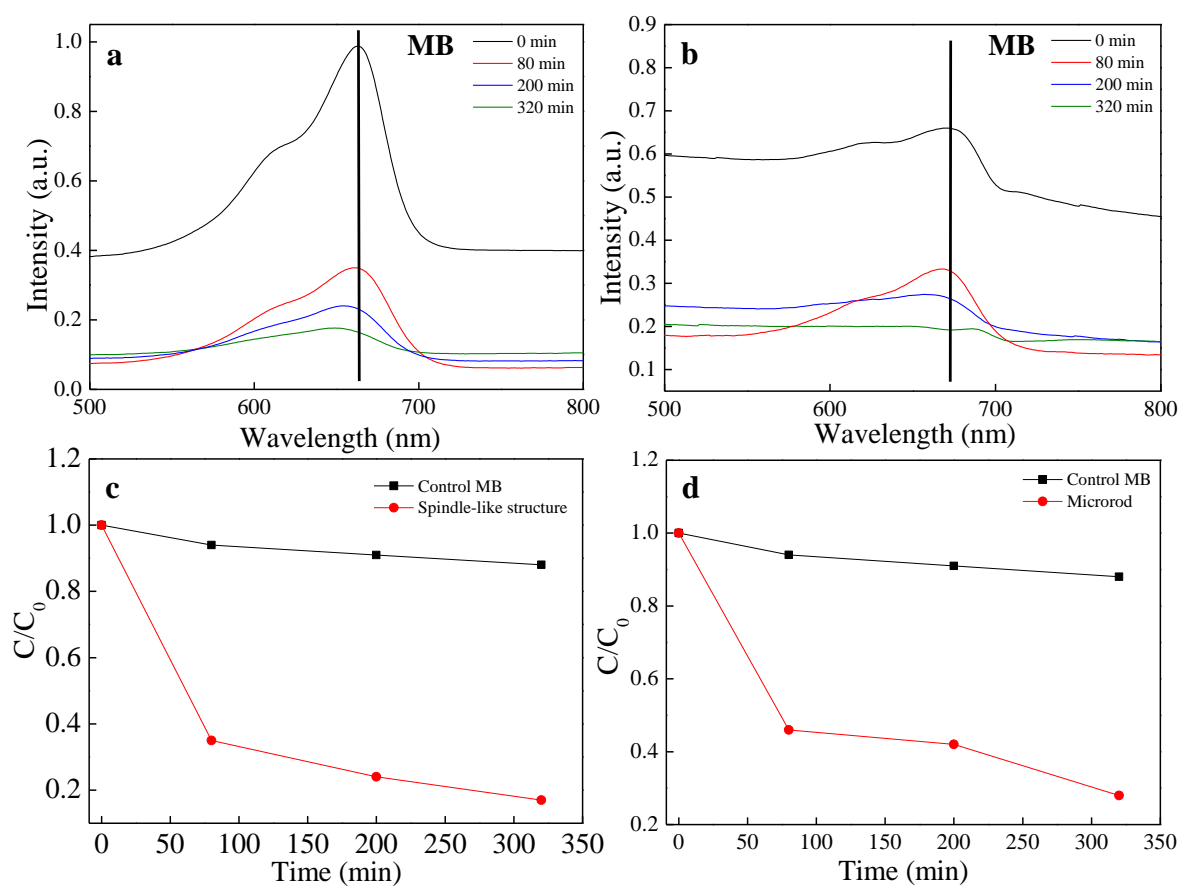


**Figure 21:** Photocatalytic degradation of MB in presence of  $\beta$ -NaYF<sub>4</sub>: 5% Tb<sup>3+</sup> with (a) spindle-like structure, and (b) microrods under irradiation of 400 W mercury lamp for 320

min. Plots of dye concentrations ( $C/C_0$ ) vs. time for (c) spindle-like structure and (d) microrods.

The absorption peak of MB shifted by  $\sim 12$  nm (*i.e.* from 662 nm to 550 nm) towards lower wavelength with increasing time. This blue shift may be attributed to oxidized MB by formation of demethylated dye, resulting from N-demethylation of dimethylamino group in MB that occurs concomitantly with oxidative degradation.<sup>56</sup>

## 2.4. Conclusion

In summary, hexagonal phase of NaYF<sub>4</sub>: Ln<sup>3+</sup> (Ln=Tb, Yb/Er and Yb/Tm) microcrystals with multiform morphologies were successfully synthesized via cationic/anionic binary capping agent system: CTAB and trisodium citrate-assisted hydrothermal route. Under UV excitation, the as-prepared  $\beta$ -NaYF<sub>4</sub>: 5 % Tb<sup>3+</sup> crystals emit strong green emission and possess long luminescence lifetime in milliseconds. In contrast, under 980 nm NIR excitation, the Yb/Er- and Yb/Tm-co-doped NaYF<sub>4</sub> samples exhibit strong green and blue up-conversion luminescence, respectively. The experimental results indicate that, the luminescence properties of the  $\beta$ -NaYF<sub>4</sub>: 5 % Tb<sup>3+</sup> phosphors are strongly dependent on their crystalline size and shape. The photocatalytic studies showed that,  $\beta$ -NaYF<sub>4</sub>: 5 % Tb<sup>3+</sup> phosphors are highly selective for MB. In addition, we have also discussed the correlation between the morphologies and photocatalytic activities. Apart from their photocatalytic properties, the unique luminescence properties and controlled morphologies of these phosphors may endow potential applications in field of color displays, light-emitting diodes (LEDs) and solid state lasers.

## 2.5. References

1. Y. Liu, D. Tu, H. Zhuab and X. Chen, *Chem. Soc. Rev.*, 2013, **42**, 6924-6958.
2. J. W. Stouwdam and F. C. J. M. van Veggel, *Nano Lett.*, 2002, **2**, 733-737.
3. G. Wang, Q. Peng, and Y. Li, *Accounts of chemical research.*, 2011, **44**, 322-332.
4. C. Li and J. Lin, *J. Mater. Chem.*, 2010, **20**, 6831-6847.
5. J. C. G. Bunzli and C. Piguet, *Chem. Soc. Rev.*, 2005, **34**, 1048-1077.
6. V. Sudarsan, F. C. J. M. van Veggel, R. A. Herring and M. Raudsepp, *J. Mater. Chem.*, 2005, **15**, 1332-1342.
7. C. Sun, C. Carpenter, G. Pratz, L. Xing, *Nanoscale Res Lett* , 2011, **6**, 24.
8. Y. Wang, Y. Liu, Q. Xiao, H. Zhu, R. Lia and X. Chen, *Nanoscale*, 2011, **3**, 3164-3169.
9. Y. Liu, D. Tu, H. Zhu, E. Maa and X. Chen, *Nanoscale*, 2013, **5**, 1369-1384.
10. C. Bouzigues, T. Gacoin, and A. Alexandrou, *ACS Nano*, 2011, **5**, 8488-8505.
11. H. A. Hoppe, *Angew. Chem. Int. Ed.*, 2009, **48**, 3572-3582.
12. L. Wang, P. Li, and Y. Li, *Adv. Mater.*, 2007, **19**, 3304-3307.
13. F. Wang and X. Liu, *Chem. Soc. Rev.*, 2009, **38**, 976-989.
14. M. Haase and H. Schafer, *Angew. Chem. Int. Ed.*, 2011, **50**, 5808-5829.
15. M. Banski , M. Afzaal, A. Podhorodecki , J. Misiewicz , A. L. Abdelhady , P. O'Brien, *J Nanopart Res.*, 2012, **14**, 1228.
16. M. Ding, W. Huang, L.Cao, C. Lu , J. Song, Y.Ni, Z.Xu, *Materials Letters.*, 2012, **86**, 58-61.
17. L. Wang and Y. Li, *Chem. Mater.*, 2007, **19**, 727-734.
18. S. Zeng, G. Ren, C. Xu and Q. Yang, *CrystEngComm.*, 2011, **13**, 1384-1390.

19. K. W. Kramer, D. Biner, G. Frei, H. U. Gudel, M. P. Hehlen, and S. R. Luthi, *Chem. Mater.*, 2004, **16**, 1244-1251.
20. C. Li, J. Yang, Z. Quan, P. Yang, D. Kong, and J. Lin, *Chem. Mater.*, 2007, **19**, 4933-4942.
21. T. Jiang, W. Song, S. Liu, W. Qin, *Journal of Fluorine Chemistry.*, 2012, **140**, 70-75.
22. R. Das and P. Poddar, *J. Phys. Chem. C.*, 2014, **118**, 13268-13275.
23. S. Sadhu, A. Jaiswal, S. Adyanthaya and P. Poddar, *RSC Adv.*, 2013, **3**, 1933-1940.
24. C. Li, Z. Quan, J. Yang, P. Yang, and J. Lin, *Inorganic Chemistry.*, 2007, **46**, 6329-6337.
25. S. Huang, J. Xu, Z. Zhang, X. Zhang, L. Wang, S. Gai, F. He, N. Niu, M. Zhang and P. Yang, *J. Mater. Chem.*, 2012, **22**, 16136-16144.
26. M. Zhang, H. Fan, B. Xi, X. Wang, C. Dong, and Y. Qian, *J. Phys. Chem. C.*, 2007, **111**, 6652-6657.
27. H. Qiu, G. Chen, L. Sun, S. Hao, G. Han and C. Yang, *J. Mater. Chem.*, 2011, **21**, 17202-17208.
28. J. H. Zeng, J. Su, Z.H. Li, R. X. Yan, and Y. D. Li, *Adv.Mater.*, 2005, **17**, 2119-2123.
29. F. Zhang, Y. Wan, T. Yu, F. Zhang, Y. Shi, S. Xie, Y. Li, L. Xu, B. Tu, and D. Zhao, *Angew. Chem. Int. Ed.*, 2007, **46**, 7976-7979.
30. D. Ma, D. Yang, J. Jiang, P. Cai and S. Huang, *CrystEngComm.*, 2010, **12**, 1650-1658.
31. S. G-Grana, F. Hubert, F. Testard, A. G-Martínez, I. Grillo, L. M. L-Marzan, and O. Spalla, *Langmuir.*, 2012, **28**, 1453-1459.



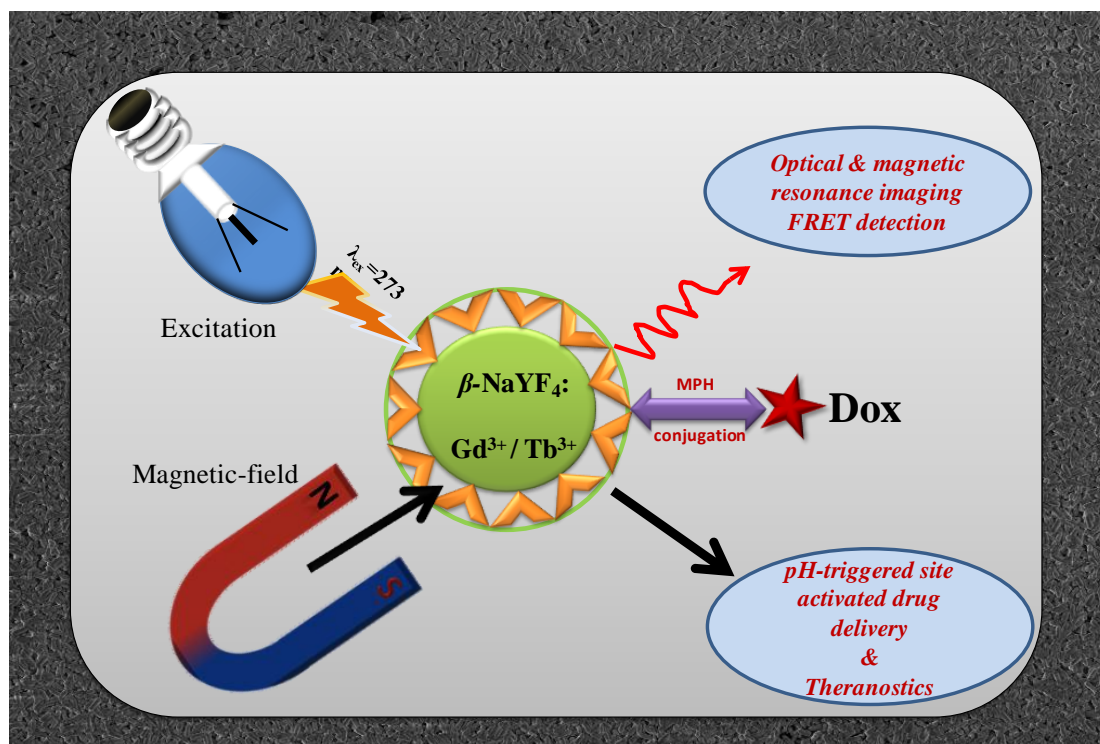
32. J. Xiao and L. Qi, *Nanoscale.*, 2011, **3**, 1383-1396.
33. N. Zhao and L. Qi, *Adv. Mater.*, 2006, **18**, 359-362.
34. N. Zhao, Y. Wei, N. Sun, Q. Chen, J. Bai, L. Zhou, Y. Qin, M. Li, and L. Qi, *Langmuir.*, 2008, **24**, 991-998.
35. D-K. Ma, S-M. Huang, Y-Y. Yu, Y-F. Xu, and Y-Q. Dong, *J. Phys. Chem. C.*, 2009, **113**, 8136-8142.
36. Y. Zheng, J. Lina and Q. Wang, *Photochem. Photobiol. Sci.*, 2012, **11**, 1567-1574.
37. C. Hazra, T. Samanta, A. V. Asaithambi and V. Mahalingam, *Dalton Trans.*, 2014, **43**, 6623-6630.
38. C. Li, C. Zhang, Z. Hou, L. Wang, Z. Quan, H. Lian, and J. Lin, *J. Phys. Chem. C.*, 2009, **113**, 2332-2339.
39. M. Ding, C. Lu, L. Cao, Y. Ni and Z. Xu, *CrystEngComm.*, 2013, **15**, 8366-8373.
40. D. Tu, Y. Liu, H. Zhu, R. Li, L. Liu, and X. Chen, *Angew. Chem. Int. Ed.*, 2013, **52**, 1128 -1133.
41. C. J. Johnson, E. Dujardin, S. A. Davis, C. J. Murphy and S. Mann, *J. Mater. Chem.*, 2002, **12**, 1765-1770.
42. H. Li, C. Kan, Z. Yi, X. Ding, Y. Cao, and J. Zhu, *Journal of Nanomaterials.*, 2010, **2010**, 1-8.
43. M. Grzelczak, J. P-Juste, P. Mulvaney and L. M. L-Marzan, *Chem. Soc. Rev.*, 2008, **37**, 1783-1791.
44. M. Han, K. Jiang, J. Zhang, W. Yu, Y. Li, Z. Hu and J. Chu, *J. Mater. Chem.*, 2012, **22**, 18463-18470.
45. Simanta Kundu, Arik Kar, Amitava Patra, *Journal of Luminescence*, 2012, **132**,

1400–1406

46. L. Xu, J. Shen, C. Lu, Y. Chen, and W. Hou, *Crystal Growth & Design.*, 2009, **9**, 3129- 3136.
47. Z. Xu, X. Kang, C. Li, Z. Hou, C. Zhang, D. Yang, G. Li, and J. Lin, *Inorg. Chem.*, 2010, **49**, 6706-6715.
48. J. Wu, S. Shi, X. Wang, J. Li, R. Zong and W.Chen, *J. Mater. Chem. C.*, 2014, **2**, 2786-2792
49. Y. Xie and C. Yuan, *Applied Catalysis B: Environmental.*, 2003, **46** .251-259.
50. K. Zhang and W. Oh, *Journal of the Korean Ceramic Society.*, 2009, **46**, 561-567.
51. Z. Liu, D. D. Sun, P. Guo, and J. O. Leckie, *Chem. Eur. J.*, 2007, **13**, 1851-1855.
52. A. S. Bhadwal, R. M. Tripathi, R. Kumar Gupta, N. Kumar, R. P. Singh and A. Shrivastav, *RSC Adv.*, 2014, **4**, 9484-9490.
53. P. Dong, Y. Wang, Huihui Li, Hao Li, X. Ma and L. Han, *J. Mater. Chem. A.*, 2013, **1**, 4651-4656.
54. Y. Li and W. Shen, *Chem. Soc. Rev.*, 2014, **43**, 1543-1574.
55. A. Biswas, R. Das, C. Dey, R. Banerjee, and P. Poddar, *Cryst. Growth Des.*, 2014, **14**, 236–239.
56. T. Zhang, T. Oyama, A. Aoshima, H. Hidaka, J. Zhao, N. Serpone, *J. photoch A.*, 2001, **140**, 163-172.

### Chapter 3

**Doxorubicin-conjugated  $\beta$ -NaYF<sub>4</sub>: Gd<sup>3+</sup>/Tb<sup>3+</sup> multifunctional phosphor:  
A multimodal, luminescent-magnetic probe for simultaneous optical,  
magnetoresonance imaging and an excellent pH-triggered anti-cancer  
drug delivery nanovehicle**



## Outline

Here, we fabricated a multifunctional nanoprobe based on highly monodispersed, optically and magnetically active, biocompatible, PEI-functionalized, highly crystalline  $\beta$ -NaYF<sub>4</sub>: Gd<sup>3+</sup>/Tb<sup>3+</sup> nanorods as an excellent multimodal optical/magnetic imaging tool and a pH-triggered intracellular drug delivery nanovehicle. The static and dynamic photoluminescence spectroscopy studies were performed. The static magnetic susceptibility measurements, nuclear magnetic resonance (NMR) measurements and magnetoresonance imaging of  $\beta$ -NaYF<sub>4</sub>: Gd<sup>3+</sup>/Tb<sup>3+</sup> were also deliberated. In addition, doxorubicin (DOX) was conjugated to the amine-functionalized  $\beta$ -NaYF<sub>4</sub>: Gd<sup>3+</sup>/Tb<sup>3+</sup> nanorods via a pH-sensitive hydrazone bond linkage enabling them as a pH-triggered, site-specific drug delivery nanovehicle for the DOX release inside the tumor cells. A comparison of *in vitro* DOX release studies at a normal physiological (pH 7.4) and acidic environment (pH 5.0) showed an enhanced DOX dissociation at pH 5.0. These multifunctional structures were also applied as an optical probe to confirm the conjugation of DOX and to monitor the DOX release. The cytotoxicity and cellular uptake studies were demonstrated using MTT assay, confocal laser scanning microscopy and flow cytometry. A comparative cellular uptake of free DOX and DOX-conjugated  $\beta$ -NaYF<sub>4</sub>: Gd<sup>3+</sup>/Tb<sup>3+</sup> nanorods were studied in tumor microenvironment condition (pH 6.5) by confocal imaging, which showed the increased uptake of DOX-conjugated  $\beta$ -NaYF<sub>4</sub>: Gd<sup>3+</sup>/Tb<sup>3+</sup> nanorods. Thus, DOX-conjugated  $\beta$ -NaYF<sub>4</sub>: Gd<sup>3+</sup>/Tb<sup>3+</sup> nanorods combining pH-triggered drug delivery, efficient luminescence and paramagnetic properties promise a potential multifunctional platform for cancer therapy, biodetection probe, optical and magnetoresonance imaging.

### 3.1. Introduction

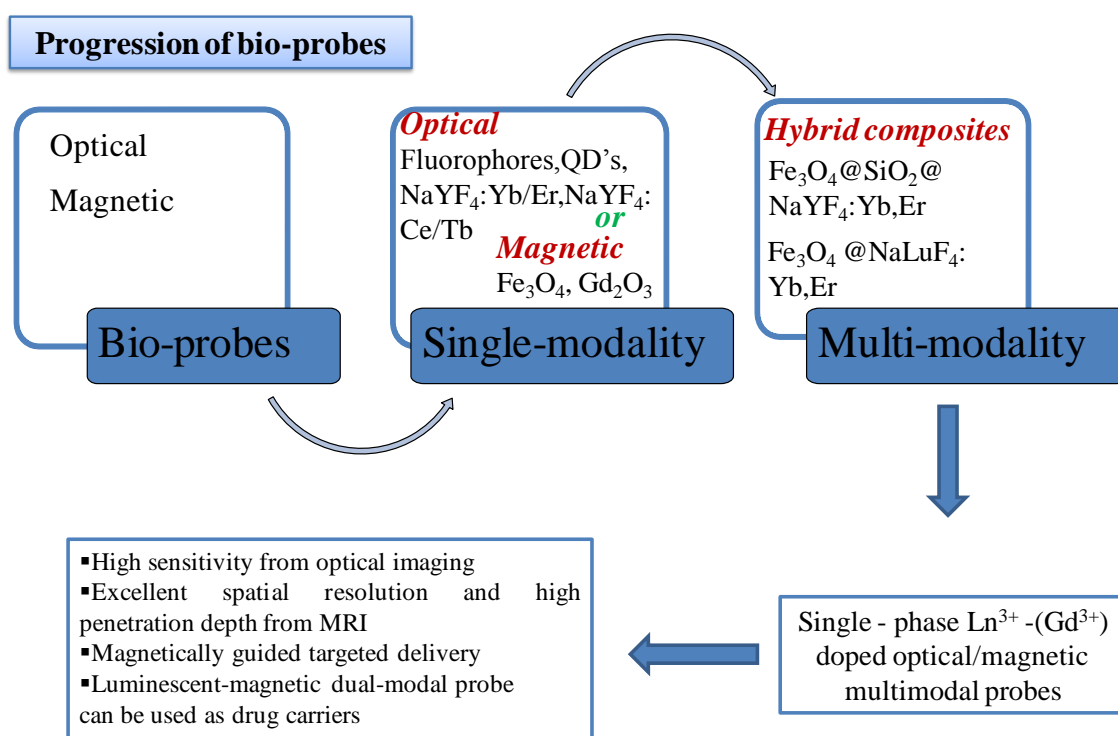
The widespread varieties of fluorescent probes have been used in bioimaging, biomedicine, diagnostics, theranostics, and multiplex sensing.<sup>1-6</sup> The trivalent lanthanide (Ln<sup>3+</sup>)-ion-doped phosphors have emerged at the forefront as multifunctional nano probes, for a variety of biological applications. This is due to their unique optical features, arising from parity forbidden *f-f* transition, which are shielded by filled 5*s* and 5*p* orbitals. As demonstrated in earlier chapters compared to the conventional organic dyes, fluorophores and semiconductor quantum-dots (QDs), the lanthanide ion-doped phosphors exhibit intriguing merits involving low-bandwidth, intense, tunable emission with long luminescent lifetime, large Stokes and anti-Stokes shift (down-/up-conversion), high photo-stability, low auto-fluorescence, photo-blinking and low toxicity.<sup>7, 8</sup> In addition, some lanthanide ions, specifically Gd<sup>3+</sup> ions are highly paramagnetic due to the presence of seven unpaired electrons with large magnetic moments ( $\sim 7.94 \mu_B$ ). Moreover, Gd<sup>3+</sup> ions also possess longer electronic relaxation time, making them an excellent candidate as contrast agents for magnetoresonance imaging (MRI).<sup>9, 10</sup> These superior features relative to organic fluorescent dyes and QDs make the Ln<sup>3+</sup>-doped phosphors, a better alternative for various biological applications. Apart from biological applications, lanthanide ion-doped phosphors have already been proven to be highly technically important candidates in wide-ranging applications such as light emitting devices, optical telecommunication, solar cells, and catalysis.<sup>11, 12</sup>

As known, higher level of crystallinity of an inorganic phosphor play an important role in achieving a brighter phosphor. As mentioned in chapter 1, inorganic fluorides, in particular NaYF<sub>4</sub>, possess wide bandgap and low phonon energy which is favorable for lower nonradiative losses and enhanced emission. In contrast the oxides phosphors usually show higher non-radiative losses.<sup>13</sup> The YVO<sub>4</sub> lattice has phonon energy of 880

cm<sup>-1</sup>. In addition, for tetragonal NaGd(WO<sub>4</sub>)<sub>2</sub>, tetragonal GdVO<sub>4</sub>, and cubic Y<sub>2</sub>O<sub>3</sub>, the phonon thresholds of the host lattices are ~ 1000, ~ 880 and ~ 600 cm<sup>-1</sup> respectively.<sup>14-16</sup> Thus, NaYF<sub>4</sub> based phosphors are considered as an excellent host matrix for down- and up-conversion luminescence processes.<sup>17</sup> Among two polymorphic forms- cubic ( $\alpha$ -) and hexagonal ( $\beta$ -) phases of NaYF<sub>4</sub>, the hexagonal-phase of  $\beta$ -NaYF<sub>4</sub> is thermodynamically stable<sup>18</sup> which is desirable to achieve enhanced luminescence efficiency for various Ln<sup>3+</sup>-doped phosphors. In previous chapter we reported the high luminescence efficiency and efficient photocatalytic activity of  $\beta$ -NaYF<sub>4</sub>:5 % Tb<sup>3+</sup> phosphors.<sup>19</sup> In spite of high luminescence efficiency, these crystals were larger in size and lacked biocompatibility which limited their biological application. Thus, in this work we attempted to design a phosphor system that would be suitable for biomedical applications.

The development of multifunctional, hybrid nanoparticles, which integrate different functional properties into one entity, are promising as new research frontiers of multimodal bio-probes. The progression of bio-probes in biomedical diagnostics and theranostics is represented in scheme 1. Earlier only single modality probes were in studies; either optical probe or magnetic probes. The multifunctional nanoparticles with combined optical and magnetic properties can be immensely useful in multimodality imaging, where optical imaging provides the highest sensitivity for an *in vitro* cell imaging and MRI provide high penetration depth, excellent spatial resolution and anatomical information for *in vivo* imaging.<sup>20</sup> Usually, most of the conventional optically and magnetically active materials are composites that are produced by coupling traditional optically-active materials such as QDs and organic dyes with magnetic ones such as iron oxides etc. Recently, hybrids such as, dye-doped silica nanoparticles mixed with magnetite nanocrystals<sup>21</sup>, Fe<sub>3</sub>O<sub>4</sub>@NaLuF<sub>4</sub>:Yb/Er<sup>22</sup> and Fe<sub>3</sub>O<sub>4</sub>@LaF<sub>3</sub>:Yb/Er<sup>23</sup> have been successfully synthesized for imaging. However, such hybrids suffer the disadvantage of

photo-bleaching and toxicity of dyes, non-persistence of particle size and complex synthesis processes with multiple steps. To overcome these drawbacks, single-phase, dual-function, superparamagnetic, Gd<sup>3+</sup> containing inorganic nanocrystals have been developed as a new class of multimodal probes. Thus, inorganic crystals doped with optically active Ln<sup>3+</sup> ions along with magnetic Gd<sup>3+</sup> ions, not only bring together the advantage of multimodal imaging/bi-detection, but also effectively reduces the toxicity of free Gd<sup>3+</sup> in rigid crystal environment.



**Scheme 1:** Schematic representation of evolution of bio-probes in biomedical diagnostics and theranostics.

The optical-magnetic nanoprobe is also expected to be used as drug-carriers for drug delivery and therapeutics. Doxorubicin (DOX) is the most established and commonly used chemotherapeutic anti-cancer drug. However, when the DOX is administered directly, it lacks targeting ability at tumor sites and shows minimal drug internalization.<sup>24</sup> According to the Warburg effect; increased anaerobic glycolysis results

in lactic acid accumulation in cancer cells, which leads to lower extracellular pH (6.5 to 6.8) of many tumors.<sup>25</sup> Thus, the cellular uptake of weakly basic drug doxorubicin tend to reduce at low pH, which is in accordance with the pH partition theory.<sup>26</sup> The acidic extracellular microenvironment of tumors is therefore predicted to confer a degree of physiological resistance to weakly basic drugs (e.g. doxorubicin) as well as it produces serious undesirable side effects such as cardiotoxicity etc.<sup>24, 25</sup> An imperative approach to overcome the toxicity and low cellular uptake concern of free doxorubicin drug is to develop the drug carrier system for tumor targeted drug delivery that can specifically respond to cancer cells with low pH values while staying inactive under normal physiological conditions.

The prime advantages of using nano-sized particles in various bio-applications are due to their distinct optical, electronic, thermal and magnetic properties along with small size, and greater available surfaces for further modification.<sup>27</sup> In particular, for a drug delivery system the nano-sized particles are beneficial as they possess longer circulation half-lives and enhanced permeability and retention effect (EPR) resulting in better drug accumulation at tumor site and consequent reduced side effects.<sup>28</sup> Herein, we designed and developed multifunctional nanorods, which can function as a dual-mode optical and magnetic bioprobe, integrated with the pH-triggered drug delivery capability. In particular, the nanorods are beneficial for intracellular drug delivery because the rod-shaped structures possess larger surface area and high surface energy. This leads to high drug conjugation efficiency and maximal drug loading capacity thereby making them as an efficient carrier for the drug delivery.<sup>29</sup> Thus, the amine functionalized  $\beta$ -NaYF<sub>4</sub>:Gd<sup>3+</sup>/Tb<sup>3+</sup> nanorods were synthesized and utilized as luminescent/magnetic bioprobes, where the Tb<sup>3+</sup> ions act as luminescent centers and Gd<sup>3+</sup> ions render the paramagnetic property to the system. The DOX was then chemically conjugated with



amine functionalized  $\beta$ -NaYF<sub>4</sub>:Gd<sup>3+</sup>/Tb<sup>3+</sup> nanorods via a pH-sensitive hydrazone bond linkage ( $\beta$ -NaYF<sub>4</sub>:Gd<sup>3+</sup>/Tb<sup>3+</sup>@ PEI-3-maleimidopropionic acid hydrazide (MPH)-DOX) for the pH-triggered drug delivery system. The photoluminescence and the magnetic properties were investigated. The drug release property, cytotoxicity and cellular uptake behavior were also studied in detail.

## 3.2. Materials and method

### 3.2.1. Materials

All the chemicals were of analytical grade and were used as-received without any further purification. Yttrium (III) nitrate hexahydrate (Y(NO<sub>3</sub>)<sub>3</sub>.6H<sub>2</sub>O) (purity  $\geq$  99.89%), gadolinium (III) nitrate hexahydrate (Gd(NO<sub>3</sub>)<sub>3</sub>.6H<sub>2</sub>O), terbium (III) nitrate hexahydrate (Tb(NO<sub>3</sub>)<sub>3</sub>.6H<sub>2</sub>O) (purity  $\geq$  99.89%), polyethyleneimine branched polymer (PEI, average MW  $\sim$ 25,000), 1-ethyl-3-(3-dimethylaminopropyl) carbodiimide hydrochloride (EDC), 3-mercaptopropionic acid (MPA) and N-hydroxysuccinimide (NHS) were purchased from Sigma Aldrich Inc. Ammonium fluoride (NH<sub>4</sub>F) and sodium chloride (NaCl) were received from Thomas Baker chemicals Pvt. Ltd. Doxorubicin was provided by Emcure Pharmaceuticals Ltd., Pune, India. The reagent 3-maleimidopropionic acid hydrazide (MPH) was obtained from Thermo Fisher Scientific India Pvt. Ltd. Deionized water was used throughout the experiments.

### 3.2.2. Synthesis

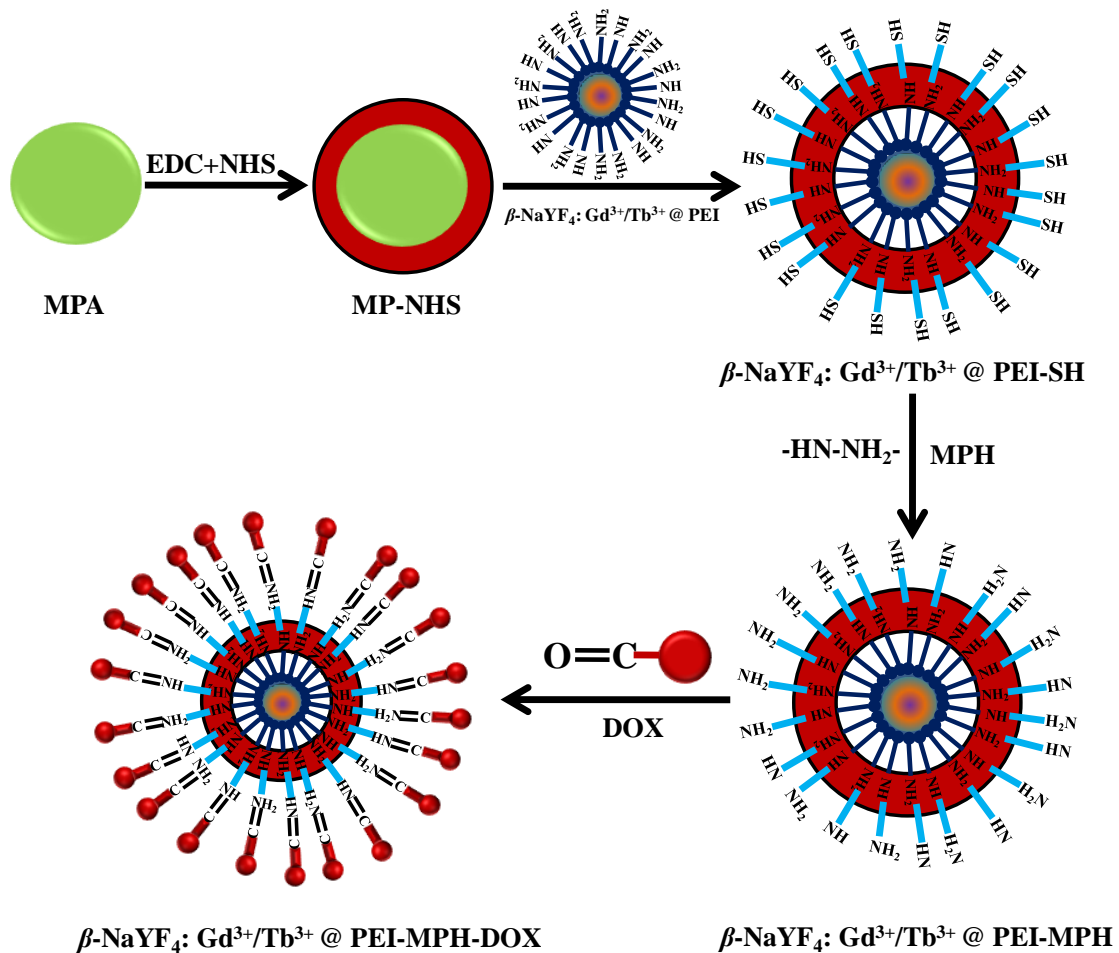
#### 3.2.2.1. One-pot synthesis of amine functionalized $\beta$ -NaYF<sub>4</sub>: 15%Gd/ 5% Tb

In a typical procedure, Y(NO<sub>3</sub>)<sub>3</sub>.6H<sub>2</sub>O, Gd(NO<sub>3</sub>)<sub>3</sub>.6H<sub>2</sub>O, and Tb(NO<sub>3</sub>)<sub>3</sub>.6H<sub>2</sub>O (0.2 M) were added to 10 mL NaCl solution (0.2 M). Under vigorous stirring, 20 mL of ethanol and 10 mL of PEI solution (5 wt %) were added to the above solution. After stirring of 30 min, NH<sub>4</sub>F (0.5 M) was introduced into the above solution. After another agitation for several minutes, the solution was transferred into a stainless steel autoclave

with Teflon liner of 80 mL capacity, sealed and heated at 200 °C for 24 h. After that, the autoclave was cooled to room temperature, and the resulting product was separated centrifugally and was washed with distilled water and absolute ethanol. Then, the product was dried under vacuum at 60 °C for 8 h.

### 3.2.2.2. Synthesis of doxorubicin conjugated $\beta$ -NaYF<sub>4</sub>: 15%Gd<sup>3+</sup>/ 5%Tb<sup>3+</sup>

The doxorubicin was conjugated with  $\beta$ -NaYF<sub>4</sub>: Gd<sup>3+</sup>/Tb<sup>3+</sup> via the pH-sensitive hydrazone bond to render the pH-triggered drug delivery following a modified method reported elsewhere.<sup>30</sup> NHS (27.6 mg), EDC (46.0 mg), and MPA (5.2  $\mu$ L) were dissolved in 3 mL methanol. The mixture was stirred at room temperature for 5 h to form 3-mercaptopropanyl-N-hydroxysuccinimide ester (MP-NHS). PEI-functionalized  $\beta$ -NaYF<sub>4</sub>: Gd<sup>3+</sup>/Tb<sup>3+</sup> (200.0 mg) was dispersed in 3 mL methanol, and the MP-NHS was added. The mixture was stirred for 12 h under nitrogen atmosphere, to form the thiolated PEI ( $\beta$ -NaYF<sub>4</sub>: Gd<sup>3+</sup>/Tb<sup>3+</sup> @ PEI-SH). MPH (13.2 mg) was then added to the thiolated PEI *i.e.*  $\beta$ -NaYF<sub>4</sub>: Gd<sup>3+</sup>/Tb<sup>3+</sup> @ PEI-SH to form PEI-MPH through the covalence of thiol and maleoyl. After 5 h of stirring, the methanol was evaporated and the solid ( $\beta$ -NaYF<sub>4</sub>: Gd<sup>3+</sup>/Tb<sup>3+</sup> @ PEI-MPH) was hydrated and dialyzed against deionized water for 12 h. The freeze-dried  $\beta$ -NaYF<sub>4</sub>: Gd<sup>3+</sup>/Tb<sup>3+</sup> @ PEI-MPH (50 mg) and DOX in excess were combined in methanol and allowed to react for 24 h while being protected from light to form the  $\beta$ -NaYF<sub>4</sub>: Gd<sup>3+</sup>/Tb<sup>3+</sup> @ PEI-MPH-DOX conjugate ( $\beta$ -NaYF<sub>4</sub>: Gd<sup>3+</sup>/Tb<sup>3+</sup> - MPH - DOX). The reaction mixture was evaporated to dryness under reduced pressure, and the solid was dissolved in 5 mL water. This solution was dialyzed (MWCO 8000-1400) against deionized water at 4 °C and freeze-dried. The synthesis route is illustrated in Scheme 2.



**Scheme 2:** Schematic illustration of the synthesis route for the conjugation of doxorubicin with  $\beta$ -NaYF<sub>4</sub>: Gd<sup>3+</sup>/Tb<sup>3+</sup> nanorods via pH-sensitive hydrazone bond through MPH for pH-triggered drug delivery system.

### 3.2.3. Stability test of $\beta$ -NaYF<sub>4</sub>: Gd<sup>3+</sup>/Tb<sup>3+</sup> nanorods and DOX-conjugated $\beta$ -NaYF<sub>4</sub>:Gd<sup>3+</sup>/Tb<sup>3+</sup>

To demonstrate the stability of the  $\beta$ -NaYF<sub>4</sub>: Gd<sup>3+</sup>/Tb<sup>3+</sup> nanorods and DOX-conjugated  $\beta$ -NaYF<sub>4</sub>:Gd<sup>3+</sup>/Tb<sup>3+</sup>, the samples were incubated in Fetal Bovine Serum (FBS) at 37 °C for 3 days. The emission intensity of nanorods in serum was measured at  $\lambda_{\text{ex}} =$

375 nm and the doxorubicin release was measured by excitation at 480 nm, emission maximum at 590 nm using fluorescence spectrophotometer at predetermined time intervals.

#### 3.2.4. DOX loading and *in vitro* release of DOX from conjugates

The amount of DOX loaded on to the nanorods was calculated and determined by the characteristic DOX optical absorbance at 490 nm. 1 mg  $\beta$ -NaYF<sub>4</sub>:Gd<sup>3+</sup>/Tb<sup>3+</sup> @PEI-MPH-DOX conjugate was dissolved in 1 mL water for the UV-vis measurement. The free DOX solutions of various concentrations were prepared, and the absorptions of the solutions were measured by UV-vis spectrophotometer to generate the calibration curve. The loading level was determined from the obtained calibration curve.

The DOX release studies were carried out in phosphate-buffered saline (PBS buffer) with different pH values (pH 7.4 and 5.0) at 37 °C. The  $\beta$ -NaYF<sub>4</sub>:Gd<sup>3+</sup>/Tb<sup>3+</sup> @PEI-MPH-DOX conjugate was dispersed in 1mL of PBS and placed in a dialysis bag with a molecular weight cut-off of 3.5 kDa. The dialysis bags were then immersed in 10 mL of the release medium and kept in a shaker maintained at 100 rpm and 37 °C. One mL of the medium was sampled at selected time intervals, and replaced with fresh buffer solution. The amounts of released DOX were measured by UV-vis spectrophotometer.

To validate the loading of DOX on nanorods by chemical conjugation and pH-triggered release of DOX by cleavage of hydrazone bond, a control experiment was performed. The physical mixture of equal amount of  $\beta$ -NaYF<sub>4</sub>: Gd<sup>3+</sup>/ Tb<sup>3+</sup> and DOX was dissolved in methanol and allowed to react for 24 h, in dark condition and further processed in the same way as for  $\beta$ -NaYF<sub>4</sub>: Gd<sup>3+</sup>/ Tb<sup>3+</sup>-MPH-DOX synthesis. The loading of DOX was determined by the characteristic DOX optical absorbance at 490 nm. For DOX release studies, the physical mixture of equal amount of  $\beta$ -NaYF<sub>4</sub>: Gd<sup>3+</sup>/ Tb<sup>3+</sup> and DOX was dissolved in methanol and allowed to react for 24 h, in dark condition. The

reaction mixture was evaporated to dryness under reduced pressure. The solid was dispersed in PBS buffer with different pH values (pH 7.4 and 5.0) at 37 °C. The DOX release studies were then carried out in the similar way as for  $\beta$ -NaYF<sub>4</sub>:Gd<sup>3+</sup>/Tb<sup>3+</sup> @PEI-MPH-DOX conjugate.

### **3.2.5. *In vitro* cytotoxicity of DOX-conjugated $\beta$ -NaYF<sub>4</sub>: Gd<sup>3+</sup>/Tb<sup>3+</sup> nanoparticles**

#### **3.2.5.1. Cell culture**

The breast cancer cell line MCF-7 and NIH3T3 were cultured in Dulbeccòs modified Eagles medium (DMEM) supplemented with 10 % heat inactivated fetal bovine serum, penicillin (100 U/mL) and streptomycin (100 µg/mL) (Invitrogen Corporation, CA, USA) and incubated at 37 °C in 5 % CO<sub>2</sub> incubator (Thermo Scientific, NC).

#### **3.2.5.2. Proliferation assay**

The *in vitro* cell viability was assessed using 3-(4, 5-dimethylthiazol-2-yl)-2,5-diphenyltetrazolium bromide (MTT) proliferation assay in NIH3T3 and MCF-7 cells. The MCF-7 and NIH3T3 cells in monolayer culture were cultivated in DMEM media supplemented with 10 % heat inactivated fetal bovine serum, penicillin (100 U/mL) and streptomycin (100 µg/mL) (Invitrogen Corporation, CA, USA). Cells were trypsinized and plated at a density of ~ 20, 000 cells / well in 96-well plate. After ~ 24 h, cells were treated with varying concentration of free DOX,  $\beta$ -NaYF<sub>4</sub>:Gd<sup>3+</sup>/Tb<sup>3+</sup> nanorods and DOX-conjugated  $\beta$ -NaYF<sub>4</sub>:Gd<sup>3+</sup>/Tb<sup>3+</sup>, and then cells were incubated in 5% CO<sub>2</sub> at 37 °C for 24 h. After the treatment, medium was removed and 10 µL of MTT (methylthiazole tetrazolium, 10 mg/mL) was added in each well and further incubated for 4 h at 37°C. Formazan crystals thus formed were solubilized in 100 µL iso-propanol and the absorbance of the MTT was measured at 570 nm with microplate reader (Theromo Multiskan go).

### 3.2.6. Cellular uptake of DOX-conjugated $\beta$ -NaYF<sub>4</sub>: Gd<sup>3+</sup>/Tb<sup>3+</sup> nanorods

Cellular uptake was examined using confocal laser scanning microscope (CLSM) and flow cytometry. MCF-7 breast cancer cells were seeded into chambered slide and allowed to grow for 24 h in DMEM medium containing 10 % FCS. On reaching 70 % cell confluence, the medium was replaced with 1 mL of fresh culture medium having pH 7.2 and pH 6.5 for cellular uptake study. The cells were treated with DOX-conjugated  $\beta$ -NaYF<sub>4</sub>: Gd<sup>3+</sup>/Tb<sup>3+</sup> ( $\beta$ -NaYF<sub>4</sub>: Gd<sup>3+</sup>/Tb<sup>3+</sup> - MPH - DOX) nanorods (20  $\mu$ g/mL) and incubated at 37 °C for 30 min, 2 h and 8 h, respectively. The cells were washed three times with PBS and fixed with 2 % paraformaldehyde at 37 °C for 10 min, and then rinsed with PBS three times again. After washing the cells thoroughly, the cells were overlaid with mounting medium containing DAPI (Sigma). The cover slips were placed on the slide and fluorescence images were recorded by using the fluorescence of DOX and  $\beta$ -NaYF<sub>4</sub>: Gd<sup>3+</sup>/Tb<sup>3+</sup>, excited at 488 nm and 405 nm and emission was collected at 591 (red fluorescence) and 530 nm (green fluorescence) respectively. Similarly, the cells were treated with  $\beta$ -NaYF<sub>4</sub>: Gd<sup>3+</sup>/Tb<sup>3+</sup> nanorods (20  $\mu$ g/mL) and incubated at 37 °C, for 30 min and followed the same procedure as for DOX-conjugated  $\beta$ -NaYF<sub>4</sub>: Gd<sup>3+</sup>/Tb<sup>3+</sup> for collecting green fluorescence from nanorods. The fluorescence emission (between 530 and 630 nm) was visualized by the confocal laser scanning microscope (Leica Microsystems and Carl Zeiss, Germany). The cellular uptake of free DOX and DOX-conjugated  $\beta$ -NaYF<sub>4</sub>: Gd<sup>3+</sup>/Tb<sup>3+</sup> nanorods were also compared by confocal microscopy. Free DOX and  $\beta$ -NaYF<sub>4</sub>: Gd<sup>3+</sup>/Tb<sup>3+</sup>-MPH-DOX nanorods were incubated with MCF-7 breast cancer cells at 37 °C for 30 min, 2 h and 8 h, respectively at pH 6.5 and followed the same above mention procedure. The fluorescence images were recorded by using the fluorescence of DOX excited at 488 nm and emission was collected at 591 (red

fluorescence). For the flow cytometry studies, breast cancer MCF-7 cells were seeded in 6 well cell culture plates. The cells were then treated with the free DOX and DOX-conjugated  $\beta$ -NaYF<sub>4</sub>: Gd<sup>3+</sup>/Tb<sup>3+</sup> nanorods for 4 h. To make single cell suspension, cells were trypsinized with 0.05 % trypsin-EDTA (Life Technologies) and washed with PBS. The cells were then resuspended in PBS buffer to a final concentration of  $1 \times 10^6$  per mL for the flow cytometric analysis using a FACS Calibur flow cytometer (Becton Dickinson). The results were analyzed with Cell Quest software. The excitation wavelength and emission wavelength were 488 nm and 575 nm, respectively.

### **3.2.7. *In vivo* toxicity of DOX-conjugated $\beta$ -NaYF<sub>4</sub>: Gd<sup>3+</sup>/Tb<sup>3+</sup>**

The tumors were introduced in severe combined immunodeficiency (SCID) mice model by injecting MDA-MB 231 cell lines in the breast pad of SCID mice. After grown for 1 week, the tumors sizes reached the size about 10–12 mm. Then, the tumor bearing mice was treated with the injections of (i)  $\beta$ -NaYF<sub>4</sub>: Gd<sup>3+</sup>/Tb<sup>3+</sup> and (ii) DOX-conjugated  $\beta$ -NaYF<sub>4</sub>: Gd<sup>3+</sup>/Tb<sup>3+</sup> with a dose of 2 mg/Kg of body weight. The tumor sizes were monitored after 4 week of treatment.

### **3.2.8. Spin relaxation measurement of $\beta$ -NaYF<sub>4</sub>: Gd<sup>3+</sup>/Tb<sup>3+</sup> nanorods and DOX-conjugated $\beta$ -NaYF<sub>4</sub>: Gd<sup>3+</sup>/Tb<sup>3+</sup> as Magnetic Resonance Imaging Contrast Agents**

For the solvent longitudinal relaxation times ( $T_1$ ) measurements, the samples were dispersed in D<sub>2</sub>O and the relaxivity values ( $r_1$ ) were measured by a standard inversion-recovery pulse sequence on a Bruker Advance NMR spectrometer at 20 °C and 9.4 T (400 MHz). The ability of proton relaxation enhancement of  $\beta$ -NaYF<sub>4</sub>: Gd<sup>3+</sup>/Tb<sup>3+</sup> is expressed by the term ionic relaxivity  $r_1$ , which is determined by the slope of following equation<sup>31</sup> in the units of  $\text{mM}^{-1} \text{S}^{-1}$ :

$$(1/T_1)_{\text{obs}} = (1/T_1)_d + r_1[M]$$

Where,  $(1/T_1)_{\text{obs}}$  and  $(1/T_1)_d$  are the observed values in the presence and absence of the paramagnetic species ( $\beta$ -NaYF<sub>4</sub>: Gd<sup>3+</sup>/Tb<sup>3+</sup>) and [M] is the concentration of the  $\beta$ -NaYF<sub>4</sub>: Gd<sup>3+</sup>/Tb<sup>3+</sup> nanorods.

To investigate the contrast enhancement effect, the T<sub>1</sub>-weighted magnetic resonance images were acquired at RT using a 3 T Philips MR scanner using Standard Spin-Echo (SE) sequence. Various concentrations of samples (0, 0.05, 0.25, 0.5, 0.8 mM) in water were placed in a series of 2 mL tubes for T<sub>1</sub>-weighted MRI images. The following parameters were adopted: repetition time (TR) = 500 ms, echo time (TE) = 9.4 ms, matrix size = 128 pixels × 128 pixels, field of view (FOV) = 90, number of signal averages = 2, and slice thickness = 3 mm.

### 3.2.9. Characterization techniques

The phase purity and crystallinity of the as-prepared samples were characterized by X-ray diffraction (XRD) using a PANalytical X'PERT PRO instrument and the iron-filtered Cu- K<sub>α</sub> radiation ( $\lambda = 1.5406 \text{ \AA}$ ) in the  $2\theta$  range of 10-80° with a step size of 0.02°. To analyze the shape and size of the samples, field emission scanning electron microscopy (FESEM: Hitachi S-4200) was used. Energy-dispersive X-ray analysis (EDXA) of the samples was performed during FESEM measurements to obtain the elemental composition of the samples. The specific structure details, morphology, and size were obtained by using FEI Tecnai F30 high resolution transmission electron microscope (HRTEM) equipped with a super-twin lens (s-twin) operated at 300 keV accelerating voltage with Schottky field emitter source with maximum beam current (> 100 nA) and small energy spread (0.8 eV or less). The point-to-point resolution of the microscope is 0.20 nm and line resolution of 0.102 nm with a spherical aberration of 1.2 mm and chromatic aberration of 1.4 mm with 70  $\mu\text{m}$  objective aperture size. The powder



samples obtained were dispersed in ethanol and then drop-casted on carbon-coated copper TEM grids with 200 mesh and loaded to a single tilt sample holder.

The optical properties of the as-synthesized samples were investigated by a Jasco UV-vis-NIR (Model V570) dual beam spectrometer operated at a resolution of 2 nm. PL spectra were acquired using a Cary eclipse fluorescence spectrophotometer, equipped with a 400 W Xe lamp as an excitation source and a Hamamatsu R928 photomultiplier tube (PMT) as a detector. Lifetime measurements were carried by using an Edinburgh Instruments FLSP 920 system, having a 60 W microsecond flash lamp as the excitation source. Around 30 mg sample was mixed with one ml methanol, made into a slurry and spread over a quartz plate and dried under ambient conditions and introduced into the sample chamber of the instrument prior to luminescence measurements. Fourier transform infrared spectrum (FTIR) was recorded by FTIR – 8300 Fourier transform infrared spectrophotometer (SHIMADZU) and Bruker FT-IR (ATR mode) spectrophotometer. Confocal laser scanning microscopy (CLSM) images were observed by Leica Microsystems and Carl Zeiss, Germany confocal microscope. The flow cytometry studies were performed by Calibur flow cytometer (Becton Dickinson) with an excitation wavelength of 480 nm. Magnetic property measurements of samples were performed using VSM (Vibrating Sample Magnetometer) attachment of Physical Property Measurement System (PPMS) from Quantum Design Inc., San Diego, CA, equipped with a 9 T superconducting magnet. For dc magnetic measurements, the samples were precisely weighed and packed inside a plastic sample holder which fit into a brass sample holder with negligible contribution in the overall magnetic signal. The M–H loops were collected at a rate of 75 Oe/s in a field sweep from –40 to 40 kOe at the vibrating frequency of 40 Hz.

### 3.3. Result and discussion

#### 3.3.1. Structural and morphological characterization of $\beta$ -NaYF<sub>4</sub>: Gd<sup>3+</sup>/Tb<sup>3+</sup> and DOX-conjugated $\beta$ -NaYF<sub>4</sub>: Gd<sup>3+</sup>/Tb<sup>3+</sup>

Previous studies suggested that the cytotoxicity and cellular uptake efficiency of NPs can be largely affected by charge on the particles due to electrostatic interactions between nanoparticles and cell membrane.<sup>32</sup> Therefore, the surface coating on nanoparticles would play an important role in their cell internalization. Earlier studies also demonstrated that the positively charged, PEI-coated NPs significantly enhances cellular uptake in several human cell lines including cervical carcinoma (HeLa), glioblastoma (U87MG), and breast carcinoma (MCF-7) cells.<sup>32</sup> Therefore, PEI was chosen to render the  $\beta$ -NaYF<sub>4</sub>: Gd<sup>3+</sup>/Tb<sup>3+</sup> nanorods water solubility and amine functionalization.

X-ray diffraction analysis was used to characterize the phase purity, crystallinity and composition of  $\beta$ -NaYF<sub>4</sub>: Gd<sup>3+</sup>/Tb<sup>3+</sup> nanorods. The X-ray diffraction pattern, as shown in Figure 1, exhibits sharp diffraction peaks that can be indexed to pure hexagonal-phase  $\beta$ -NaYF<sub>4</sub> (space group:  $P6_3/m$ ).

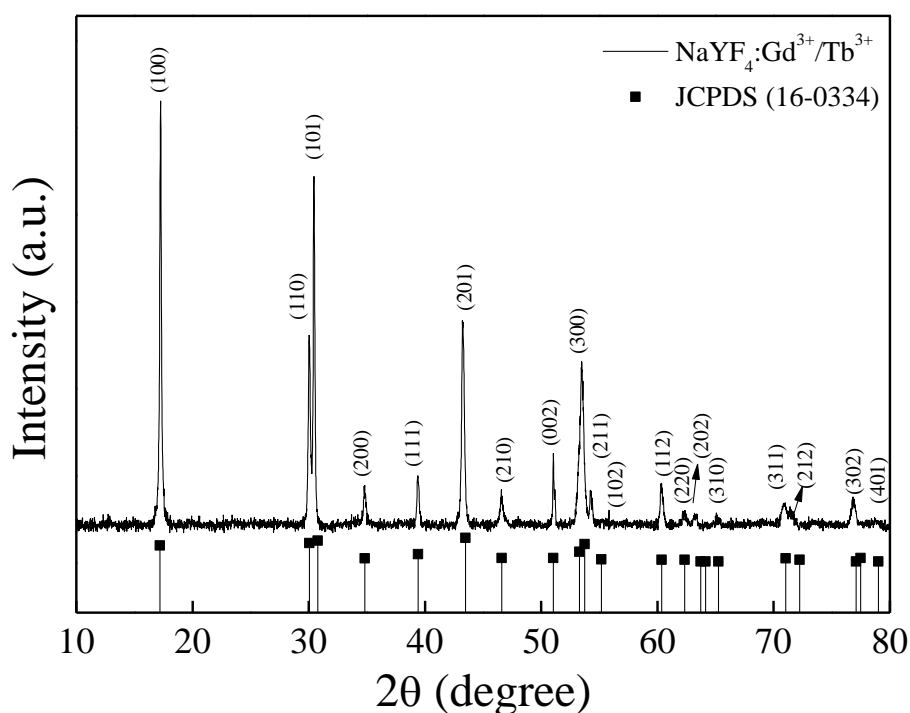


**Figure 1:** The comparison of XRD patterns of as-prepared  $\beta$ -NaYF<sub>4</sub>: Gd<sup>3+</sup>/Tb<sup>3+</sup> nanorods and the reference data of hexagonal  $\beta$ -NaYF<sub>4</sub> (JCPDS- 16-0334) plotted as a reference. The overall peak profile demonstrates an excellent crystallinity of the nanorods.

The absence of any other phase in XRD pattern indicates the high purity of as-prepared samples. The calculated lattice parameters are  $a = 5.9 \text{ \AA}$ ,  $c = 3.5 \text{ \AA}$ , which coincide well with the reported data (JCPDS no. 16-0334). Moreover, the sharpness of peaks in XRD pattern also indicates the high crystallinity of nanorods, which is beneficial to higher luminescence yield of phosphors, as the high crystallinity leads to less trap sites and subsequently gives strong emission.

The size, shape and structure of the as-prepared nanorods were characterized by TEM and FESEM (Figures 2 and 3). TEM and FESEM images, as shown in Figures 2 (a) and 3 (a), show that the PEI capped  $\beta$ -NaYF<sub>4</sub>: Gd<sup>3+</sup>/Tb<sup>3+</sup> crystals possess rod-shape with an average diameter  $\sim 60 \text{ nm}$  and length of  $\sim 230 \text{ nm}$ . It can be clearly seen that, the  $\beta$ -NaYF<sub>4</sub>: Gd<sup>3+</sup>/Tb<sup>3+</sup> nanorods are highly uniform and monodispersed in nature. Even after conjugation of DOX on the surface, the nanoparticles showed good uniformity and

monodispersity without any sign of aggregation (Figure 2 (b) and 3 (b)). The corresponding selected area electron diffraction patterns (SAED) and high resolution TEM images shown in Figure 2 (c, e) and (d, f) demonstrate that the as-synthesized  $\beta$ -NaYF<sub>4</sub>: Gd<sup>3+</sup>/Tb<sup>3+</sup> nanorods and DOX-conjugated  $\beta$ -NaYF<sub>4</sub>: Gd<sup>3+</sup>/Tb<sup>3+</sup> nanorods are highly crystalline in nature. Meanwhile, the lattice fringes with interplanar spacing of 0.3 nm and 0.2 nm were ascribed to (101) and (201) planes of  $\beta$ -NaYF<sub>4</sub>: Gd<sup>3+</sup>/Tb<sup>3+</sup> nanorods and DOX-conjugated  $\beta$ -NaYF<sub>4</sub>: Gd<sup>3+</sup>/Tb<sup>3+</sup> nanorods, respectively.

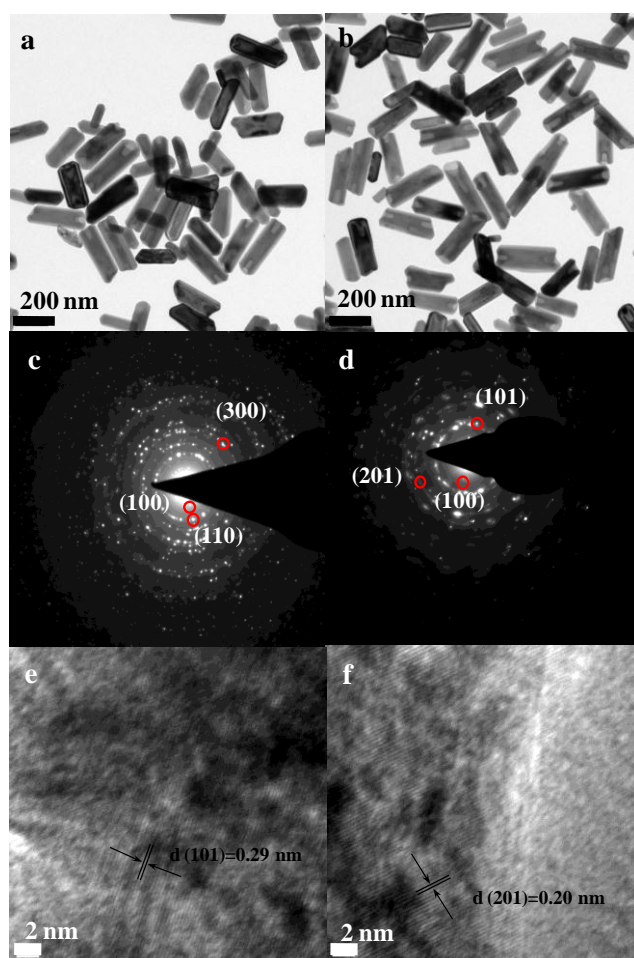


**Figure 2:** TEM images of (a) PEI-capped  $\beta$ -NaYF<sub>4</sub>:Gd<sup>3+</sup>/Tb<sup>3+</sup> nanorods and (b) DOX – conjugated PEI capped  $\beta$ -NaYF<sub>4</sub>:Gd<sup>3+</sup>/Tb<sup>3+</sup> nanorods. (c, d) and (e, f) are corresponding SAED patterns and HRTEM images. The nanorods are highly crystalline and well-separated even after drug conjugation.

Further, the elemental composition of the  $\beta$ -NaYF<sub>4</sub>: Gd<sup>3+</sup>/Tb<sup>3+</sup> nanorods were determined by Energy Dispersive X-ray Analysis (EDX). As can be seen by Figure 3 (c), all the elements including Na, Y, F, Gd and Tb can be detected in the spectrum.

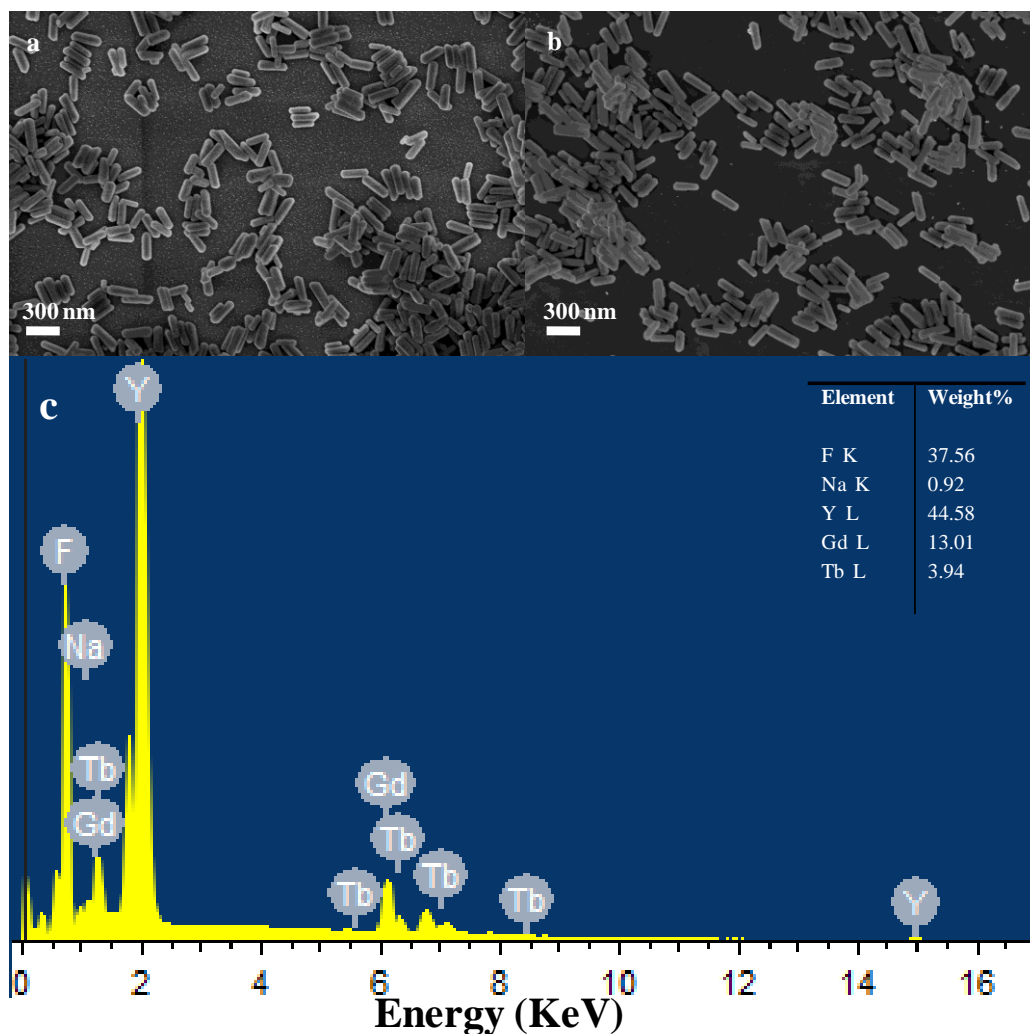


**Figure 3:** SEM images of (a) PEI capped  $\beta$ -NaYF<sub>4</sub>:Gd<sup>3+</sup>/Tb<sup>3+</sup> nanorods and (b) DOX – conjugated  $\beta$ -NaYF<sub>4</sub>:Gd<sup>3+</sup>/Tb<sup>3+</sup> nanorods. The rods remain nicely separated and monodispersed. (c) Energy-dispersive X-ray analysis (EDX) patterns of  $\beta$ -NaYF<sub>4</sub>:Gd<sup>3+</sup>/Tb<sup>3+</sup> nanorods showing elemental composition.

### 3.3.2. Surface properties

The zeta potential and FTIR spectroscopy were employed to study the surface modification of  $\beta$ -NaYF<sub>4</sub>: Gd<sup>3+</sup>/Tb<sup>3+</sup> nanorods by PEI and further conjugation of DOX on the  $\beta$ -NaYF<sub>4</sub>: Gd<sup>3+</sup>/Tb<sup>3+</sup> nanorods. The  $\zeta$ -potential of  $\beta$ -NaYF<sub>4</sub>: Gd<sup>3+</sup>/Tb<sup>3+</sup> aqueous solution (pH=7) was measured to be + 57 mV, indicating the successful capping of PEI on the surface of  $\beta$ -NaYF<sub>4</sub>: Gd<sup>3+</sup>/Tb<sup>3+</sup> nanorods. Owing to amino group capping on the surface, the nanorods were steadily dispersed in water to form a stable and optically transparent dispersion. The amino groups on the surface of nanorods were further verified by FTIR spectroscopy (Figure 4).

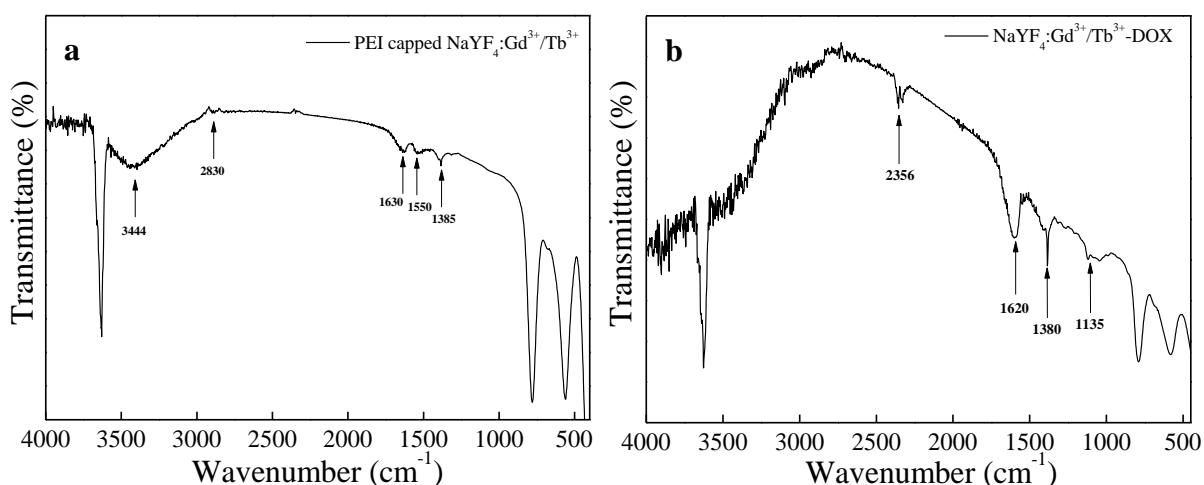


**Figure 4:** The FT-IR spectra of (a) PEI-capped  $\beta$ -NaYF<sub>4</sub>:Gd<sup>3+</sup>/Tb<sup>3+</sup> nanorods and (b) DOX -conjugated  $\beta$ -NaYF<sub>4</sub>:Gd<sup>3+</sup>/Tb<sup>3+</sup> nanorods indicating the capping of PEI at the surface of  $\beta$ -NaYF<sub>4</sub>:Gd<sup>3+</sup>/Tb<sup>3+</sup> nanorods and further the conjugation of DOX with the amine functionalized  $\beta$ -NaYF<sub>4</sub>:Gd<sup>3+</sup>/Tb<sup>3+</sup> nanorods.

The  $\beta$ -NaYF<sub>4</sub>: Gd<sup>3+</sup>/Tb<sup>3+</sup> nanorods exhibited a sharp absorption band at 3626 cm<sup>-1</sup> due to O-H stretching vibration. Meanwhile, absorption bands at 1385 cm<sup>-1</sup> and 2830 cm<sup>-1</sup> are attributed to the stretching vibrations of the C-N band symmetric stretching vibrations of C-H bond respectively. The IR-band centered at 1630 cm<sup>-1</sup> was observed, which can be attributed

to the N-H bending mode of amino group (-NH<sub>2</sub>), and also a broad band at 3443 cm<sup>-1</sup> is related to the N-H stretching vibration of amino group, thereby revealing the capping of PEI on the surface of nanorods.<sup>31, 33</sup> Further, when DOX was conjugated to the PEI coated nanorods via MPH, a feature peak at 1620 cm<sup>-1</sup> appeared (Figure 4b) which can be assigned to -C=N- bond, resulting from reaction between hydrazide group of nanorods and carbonyl group at the 13-keto position of DOX. Moreover, the characteristic bands at 1135 cm<sup>-1</sup> and 1380 cm<sup>-1</sup> correspond to the absorption of DOX.<sup>34</sup> These results demonstrate that, the DOX molecules have been chemically conjugated to  $\beta$ -NaYF<sub>4</sub>: Gd<sup>3+</sup>/Tb<sup>3+</sup> nanorods via hydrazone bond.

### 3.3.3. Optical properties

#### 3.3.3.1. UV-visible absorbance studies

The conjugation of doxorubicin with  $\beta$ -NaYF<sub>4</sub>: Gd<sup>3+</sup>/Tb<sup>3+</sup> nanorods was further determined by the characteristic DOX absorption band at ~ 490 nm as shown by a comparison of UV-vis absorbance spectra of free DOX,  $\beta$ -NaYF<sub>4</sub>: Gd<sup>3+</sup>/Tb<sup>3+</sup>-DOX conjugate and bare  $\beta$ -NaYF<sub>4</sub>: Gd<sup>3+</sup>/Tb<sup>3+</sup> (Figure 5).

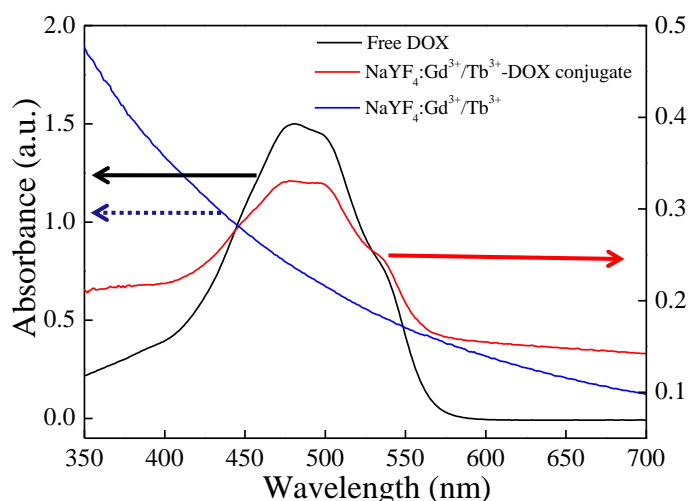


**Figure 5:** Comparison of UV-vis absorbance of free DOX, bare  $\beta$ -NaYF<sub>4</sub>: Gd<sup>3+</sup> / Tb<sup>3+</sup> nanorods and  $\beta$ -NaYF<sub>4</sub>:Gd<sup>3+</sup>/Tb<sup>3+</sup>- DOX conjugate nanorods indicating conjugation of DOX with  $\beta$ -NaYF<sub>4</sub>:Gd<sup>3+</sup>/Tb<sup>3+</sup> nanorods.

### 3.3.3.2. Static photoluminescence studies

A comparison of the photoluminescence (PL) spectra of Tb<sup>3+</sup> in  $\beta$ -NaYF<sub>4</sub>: 5 % Tb<sup>3+</sup> and  $\beta$ -NaYF<sub>4</sub>: 15 % Gd<sup>3+</sup>/ 5 % Tb<sup>3+</sup> nanorods, when Tb<sup>3+</sup> is excited directly (375 nm) and indirectly (273 nm) respectively, is shown in Figure 6 (a). It is evident that, in both the samples, the peak-positions in emission spectra remain similar, and the bands differ only in their relative intensities. The obtained emission spectra monitored at  $\lambda_{\text{ex}} = 273$  nm, yielded intense green emissions in the regions of 480-680 nm, which are due to the  $^5\text{D}_4 \rightarrow ^7\text{F}_J$  ( $J = 3, 4, 5, 6$ ) transitions of Tb<sup>3+</sup> ions, respectively. Specifically, four prominent emission peaks centered at  $\sim 488$ ,  $\sim 544$ ,  $\sim 584$ , and  $\sim 619$  nm, originates from the transitions of  $^5\text{D}_4 \rightarrow ^7\text{F}_6$ ,  $^5\text{D}_4 \rightarrow ^7\text{F}_5$ ,  $^5\text{D}_4 \rightarrow ^7\text{F}_4$ , and  $^5\text{D}_4 \rightarrow ^7\text{F}_3$  respectively.<sup>35</sup> Among these transitions, the green emission  $^5\text{D}_4 \rightarrow ^7\text{F}_5$  at  $\sim 544$  nm is the most intense emission, which corresponds to a magnetic dipole transition.

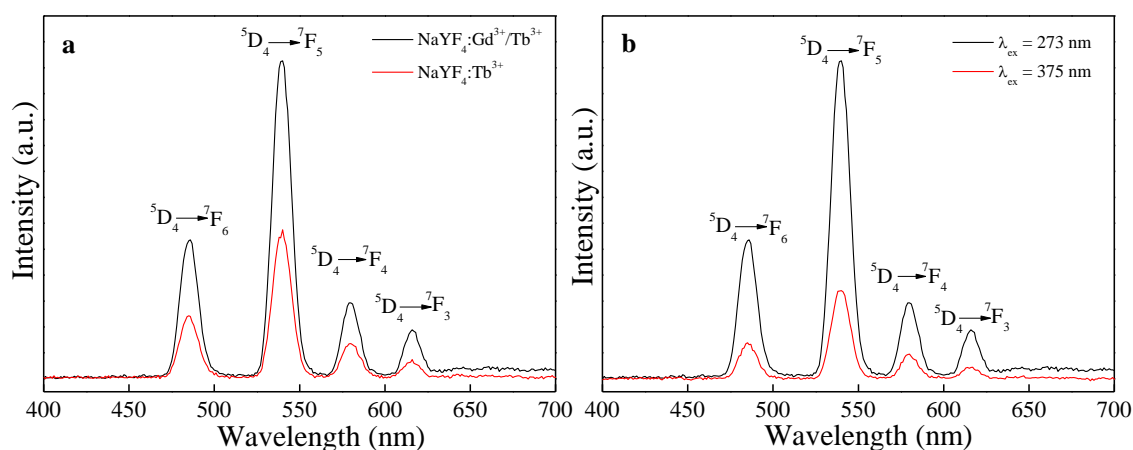
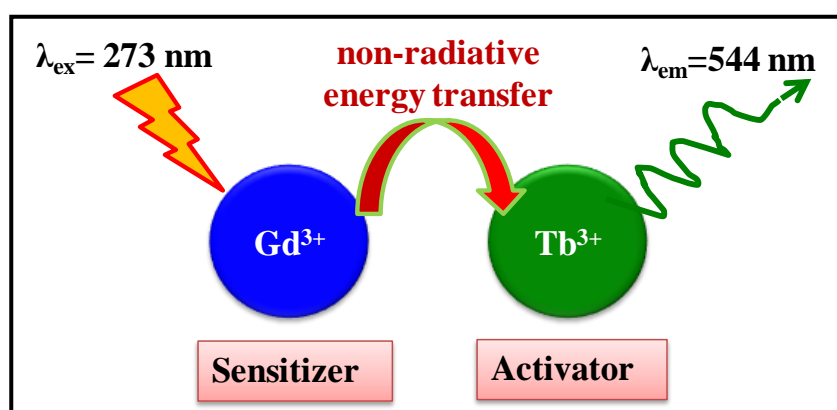


**Figure 6:** The comparison of static photoluminescence spectra showing the effect of sensitizer Gd<sup>3+</sup> on the emission intensity. (a) Emission spectra of  $\beta$ -NaYF<sub>4</sub>:5 % Tb<sup>3+</sup> nanorods (red curve) at  $\lambda_{\text{ex}} = 375$  nm and emission spectra of  $\beta$ -NaYF<sub>4</sub>:Gd<sup>3+</sup>/Tb<sup>3+</sup> nanorods (black curve) at  $\lambda_{\text{ex}} = 273$  nm. (b) Comparative emission spectra of  $\beta$ -



NaYF<sub>4</sub>:Gd<sup>3+</sup>/Tb<sup>3+</sup> nanorods at  $\lambda_{\text{ex}} = 273$  nm and at  $\lambda_{\text{ex}} = 375$  nm respectively. Here the background of curves is normalized to compare the intensities with each other.

An important advantage of doping Gd<sup>3+</sup> into the matrix is that, Gd<sup>3+</sup> ions not only render paramagnetic property to the material but also act as sensitizer which enhances photoluminescence intensity via energy transfer from sensitizer Gd<sup>3+</sup> to activator Tb<sup>3+</sup> ion as depicted in scheme 3.



**Scheme 3:** Schematic representation showing enhanced emission of Tb<sup>3+</sup> ion due to presence of Gd<sup>3+</sup> ion *via* non-radiative energy transfer.

It is well documented that, Gd<sup>3+</sup> serves as an ideal UV sensitizer or intermediate to activate specific luminescence of Ln<sup>3+</sup> ions such as Tb<sup>3+</sup>, inducing green emissions in the visible region.<sup>36</sup> It is also evident from PL spectra in Figure 6 (b), emission intensity of  $\beta$ -NaYF<sub>4</sub>: 15 % Gd<sup>3+</sup>/ 5 % Tb<sup>3+</sup> nanorods is greatly enhanced upon excitation at  $\lambda_{\text{ex}} = 273$  nm as compared with  $\lambda_{\text{ex}} = 375$  nm, which is the most effective direct excitation wavelength for Tb<sup>3+</sup> ions.<sup>19</sup> We have also shown a comparative emission spectra of  $\beta$ -NaYF<sub>4</sub>: 15 % Gd<sup>3+</sup>/ 5 % Tb<sup>3+</sup> and  $\beta$ -NaYF<sub>4</sub>: 5 % Tb<sup>3+</sup> (Figure 6 (a)), it can be clearly seen that  $\beta$ -NaYF<sub>4</sub>: 15 % Gd<sup>3+</sup>/ 5 % Tb<sup>3+</sup> possess higher luminescence emission intensity, which is due to sensitization by Gd<sup>3+</sup> ions. Previously, our group have studied the optical properties of Gd<sup>3+</sup> ions and demonstrated that Gd<sup>3+</sup> ions exhibit strong absorption band at

273 nm due to  $^8S_{7/2} \rightarrow ^6I_{11/2}$  transition in Gd<sup>3+</sup> ions.<sup>37</sup> Thus, Gd<sup>3+</sup> containing nanoparticles exhibit a very intense Ln<sup>3+</sup> excitation band at 273 nm due to the  $^8S_{7/2} \rightarrow ^6I_J$  transition in Gd<sup>3+</sup> ions followed by a non-radiative energy transfer to Ln<sup>3+</sup> ions.<sup>38</sup> In the present  $\beta$ -NaYF<sub>4</sub>: 15 % Gd<sup>3+</sup>/ 5 % Tb<sup>3+</sup> system, upon excitation at  $\lambda_{\text{ex}} = 273$  nm Gd<sup>3+</sup> ions absorb energy and subsequently efficiently transfer energy to neighbouring Tb<sup>3+</sup> ions giving rise to high luminescence emission intensity.

### 3.3.3.3. Time-resolved photoluminescence studies

The PL decay curves for the luminescence of Tb<sup>3+</sup> in  $\beta$ -NaYF<sub>4</sub>: 15 % Gd<sup>3+</sup>/ 5 % Tb<sup>3+</sup> nanorods are shown in Figure 7. This curve can be well fitted by a single exponential function as  $I(t) = I_0 \exp(-t/\tau)$  where,  $I_0$  is the initial emission intensity at  $t=0$ ,  $\tau$  is the 1/e lifetime of the emission centre. The lifetime for  $^5D_4$  were detected at 544 nm for  $^5D_4 \rightarrow ^7F_5$  transition of Tb<sup>3+</sup> by excitation at 273 nm and was determined to be 3.49 ms.

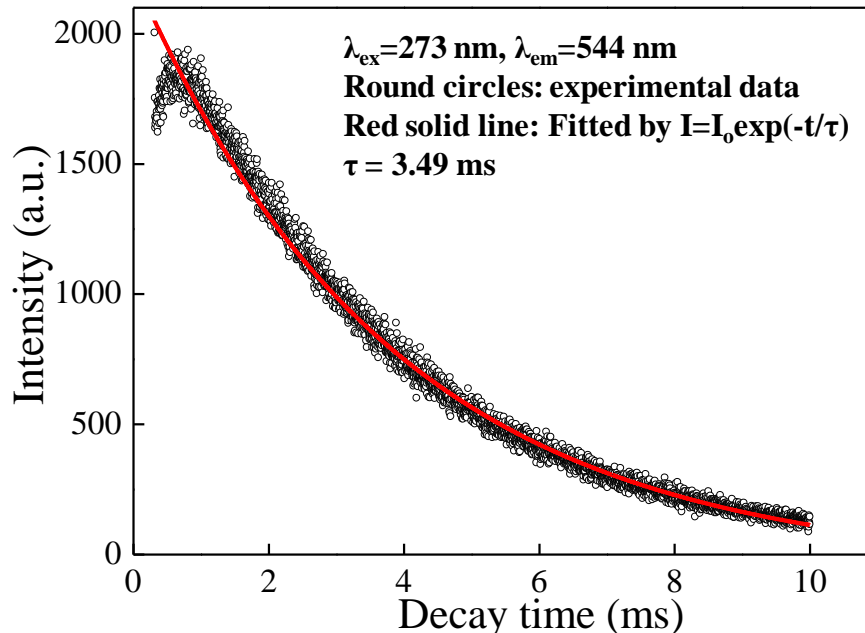


**Figure 7:** The luminescence decay curves for the  $^5D_4 \rightarrow ^7F_5$  emission of Tb<sup>3+</sup> ( $\lambda_{\text{ex}}=273$  nm,  $\lambda_{\text{em}}=544$  nm) in  $\beta$ -NaYF<sub>4</sub>:Gd<sup>3+</sup>/Tb<sup>3+</sup> nanorods.

The long luminescence lifetime is favorable for most of the biological applications, as the short lived fluorescence such as background fluorescence and autofluorescence can be easily suppressed which thus offers remarkably high signal-to-noise ratio.<sup>7</sup>

### **3.3.4. *In vitro* cytotoxicity**

#### **3.3.4.1. *In vitro* cytotoxicity in NIH3T3 fibroblast cell lines**

To evaluate the biocompatibility of the amine functionalized  $\beta$ -NaYF<sub>4</sub>: 15 % Gd<sup>3+</sup>/ 5 % Tb<sup>3+</sup> nanorods, the standard MTT assay was performed on the NIH3T3 cells. The Figure 8 (a) shows the viability of NIH3T3 cells incubated with amine functionalized  $\beta$ -NaYF<sub>4</sub>: 15 % Gd<sup>3+</sup>/ 5 % Tb<sup>3+</sup> nanorods at different concentrations for 24 h. It can be seen that, the  $\beta$ -NaYF<sub>4</sub>: 15 % Gd<sup>3+</sup>/ 5 % Tb<sup>3+</sup> nanorods did not show any evident cytotoxicity to the NIH3T3 cells. The cell viabilities of almost 100 % were observed for a wide range of concentrations from 3.12  $\mu$ g/mL to 200  $\mu$ g/mL after incubation for 24 h. The cytotoxicity effect of free DOX and DOX-conjugated- $\beta$ -NaYF<sub>4</sub>: Gd<sup>3+</sup>/ Tb<sup>3+</sup> nanorods were checked in the NIH3T3 cells (Figure 8 (b)) and the results showed the potential decrease in the cytotoxicity of DOX-conjugated- $\beta$ -NaYF<sub>4</sub>: Gd<sup>3+</sup>/ Tb<sup>3+</sup>, indicating that toxic effects of DOX is reduced when conjugated with the  $\beta$ -NaYF<sub>4</sub>: Gd<sup>3+</sup>/ Tb<sup>3+</sup> nanorods.

These results coincide with the well established fact that the free DOX, when administered directly, confers adverse effects on the normal cells. The reason behind the reduced toxicity of the DOX-conjugated- $\beta$ -NaYF<sub>4</sub>: Gd<sup>3+</sup>/ Tb<sup>3+</sup> nanorods in comparison to free DOX might be the protection of carbonyl group of DOX by  $\beta$ -NaYF<sub>4</sub>: Gd<sup>3+</sup>/ Tb<sup>3+</sup>. It is believed that, doxorubicin cardiotoxicity is caused by doxorubicinol, which is the primary circulating metabolite of doxorubicin formed by the carbonyl reductase at the 13-keto position<sup>39</sup>, thus the lack of a C-13 carbonyl moiety in DOX-conjugated- $\beta$ -NaYF<sub>4</sub>: Gd<sup>3+</sup>/ Tb<sup>3+</sup> prevents the formation of doxorubicinol, which itself promises reduced

cardiotoxicity and adverse side effects as compared to free DOX delivery. The MTT results signify that, the amine functionalized  $\beta$ -NaYF<sub>4</sub>: 15 % Gd<sup>3+</sup>/ 5 % Tb<sup>3+</sup> nanorods possess good biocompatibility as drug carriers and are also promising as fluorescent probes in bioimaging and other biological applications.

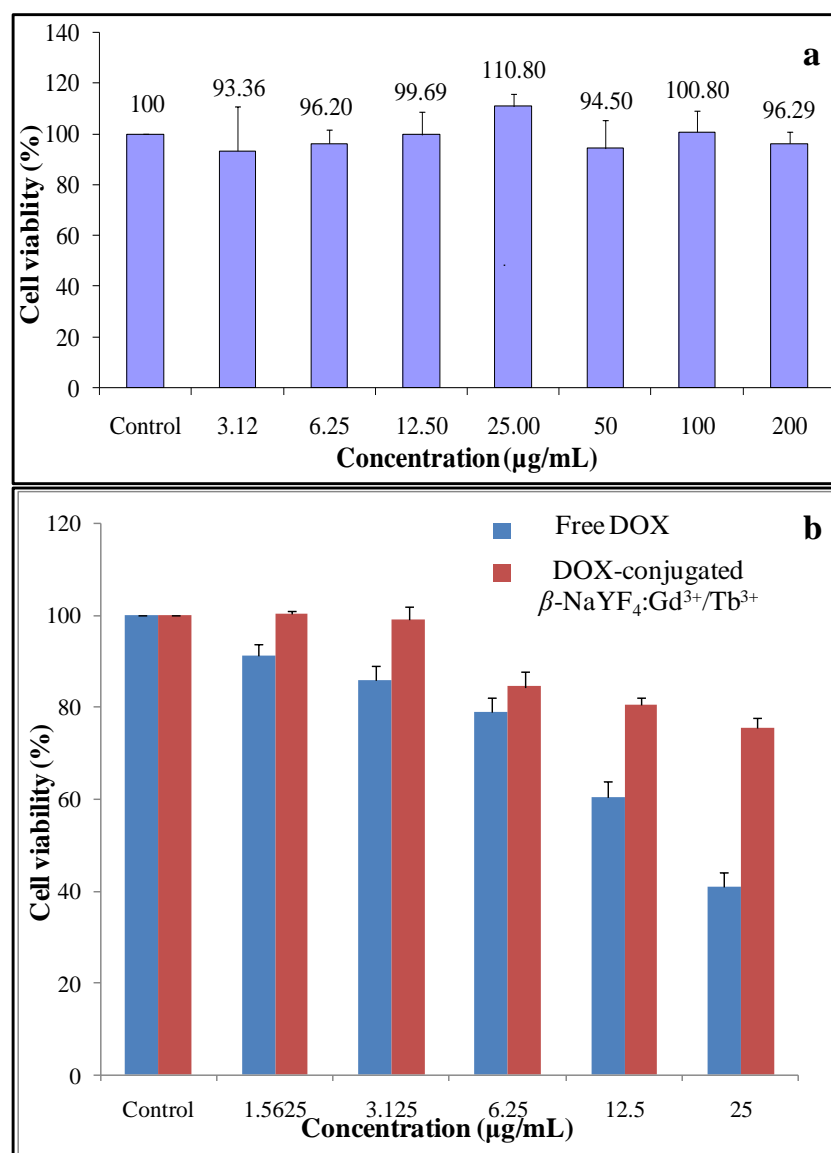


**Figure 8:** MTT assay showing the cytotoxicity of (a) the PEI-coated  $\beta$ -NaYF<sub>4</sub>: Gd<sup>3+</sup>/Tb<sup>3+</sup> nanorods, and (b) Free DOX and DOX-conjugated  $\beta$ -NaYF<sub>4</sub>: Gd<sup>3+</sup>/Tb<sup>3+</sup> in NIH3T3 cells by incubating them with NIH3T3 cells at 37 °C for 24 h.

### 3.3.4.2. *In vitro* cytotoxicity in MCF-7 cancer cell lines

To demonstrate the cytotoxic effect of  $\beta$ -NaYF<sub>4</sub>: Gd<sup>3+</sup>/Tb<sup>3+</sup> - MPH - DOX nanorods *in vitro* against the cancer cells, the MTT assay of nanorods was performed against the MCF-7 cancer cells at pH 7.4.

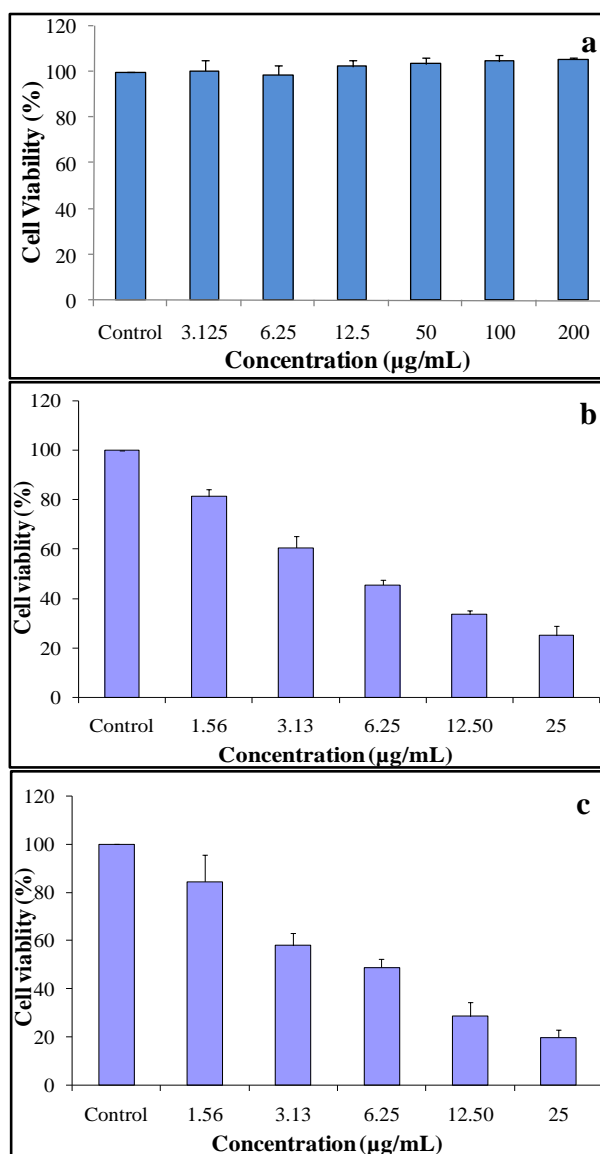


**Figure 9:** *In vitro* MCF-7 cancer cell viabilities after incubation of 24 h with (a)  $\beta$ -NaYF<sub>4</sub>: Gd<sup>3+</sup>/Tb<sup>3+</sup> nanorods, (b) free DOX and (c) DOX-conjugated  $\beta$ -NaYF<sub>4</sub>: Gd<sup>3+</sup>/Tb<sup>3+</sup> nanorods at different concentrations. DOX conjugated  $\beta$ -NaYF<sub>4</sub>: Gd<sup>3+</sup>/Tb<sup>3+</sup> nanorods exhibit an increasing inhibition against MCF-7 cancer cells with increasing

concentration, while  $\beta$ -NaYF<sub>4</sub>: Gd<sup>3+</sup>/ Tb<sup>3+</sup> nanorods do not possess toxicity to cancer cells.

The Figure 9 shows the cell viabilities against  $\beta$ -NaYF<sub>4</sub>: Gd<sup>3+</sup>/ Tb<sup>3+</sup> nanorods, DOX conjugated  $\beta$ -NaYF<sub>4</sub>: Gd<sup>3+</sup>/ Tb<sup>3+</sup> nanorods and free DOX. Free DOX was taken as positive control to compare the cytotoxicity of  $\beta$ -NaYF<sub>4</sub>: Gd<sup>3+</sup>/ Tb<sup>3+</sup> nanorods and DOX conjugate. The concentration of free DOX was set as the same as the DOX conjugated  $\beta$ -NaYF<sub>4</sub>: Gd<sup>3+</sup>/ Tb<sup>3+</sup>.

The samples were incubated with MCF-7 cancer cells for 24 h at 37 °C at different concentrations. The pure  $\beta$ -NaYF<sub>4</sub>: Gd<sup>3+</sup>/ Tb<sup>3+</sup> nanorods without the DOX conjugation exhibited no cytotoxicity to the cancer cells even after 24 h of treatment at concentrations as high as 200  $\mu$ g/mL. In contrast, both free DOX and DOX conjugated  $\beta$ -NaYF<sub>4</sub>: Gd<sup>3+</sup>/ Tb<sup>3+</sup> nanorods exhibited an increasing inhibitory effect against the MCF-7 cancer cell proliferation with increasing concentration. The probable reason behind this may be attributed to the fact that the free DOX are small molecules, thus diffuse and spread faster into the cells, while DOX loaded nanocarriers have to be endocytosed to enter the cells. Thus, when the concentration is higher, more DOX conjugated nanoparticles would be endocytosed to enter the cancer cells and release DOX inside to induce the cell death.<sup>40, 41</sup>

### **3.3.5. Stability assay**

The stability of  $\beta$ -NaYF<sub>4</sub>: Gd<sup>3+</sup>/ Tb<sup>3+</sup> nanorods and DOX-conjugated  $\beta$ -NaYF<sub>4</sub>: Gd<sup>3+</sup>/ Tb<sup>3+</sup> nanorods was studied in fetal bovine serum (FBS) up to 3 days at 37 °C to mimic the physiological conditions. As shown in Figure 10 (a), the emission intensity of the  $\beta$ -NaYF<sub>4</sub>: Gd<sup>3+</sup>/ Tb<sup>3+</sup> nanorods were hardly changed even over 60 h, indicating the significant stability of nanorods in the serum. The emission intensity is diminished by

only 5 % which is not a significant drop. This small drop might be due to interaction of organic molecules present in the serum with the surface of nanorods.

In the same way, the DOX-conjugated  $\beta$ -NaYF<sub>4</sub>: Gd<sup>3+</sup>/ Tb<sup>3+</sup> nanorods were also stable in the FBS (Figure 10 (b)). After 60 h of incubation in FBS, the maximal release of doxorubicin was amounted to be only 7.6 %, indicating that doxorubicin is significantly stably bound to the nanorods under the physiological conditions.

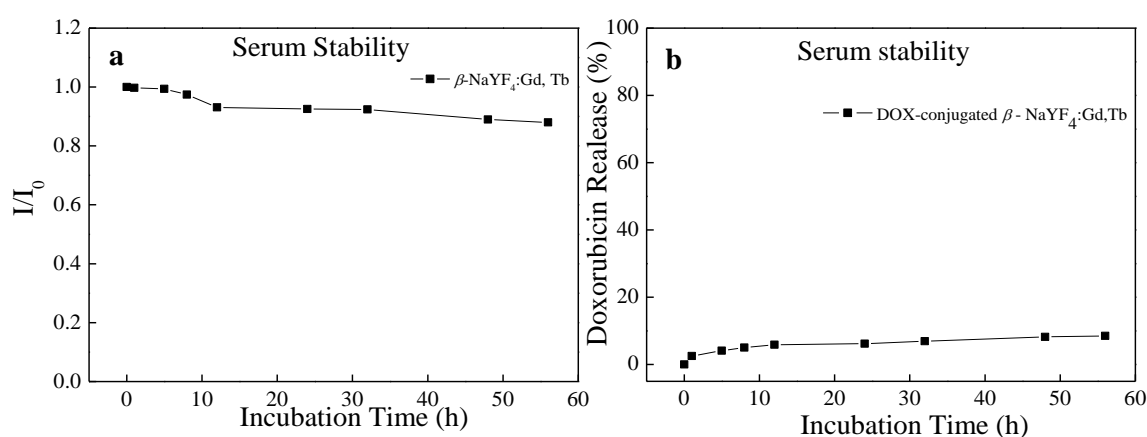


**Figure 10:** Stability of (a)  $\beta$ -NaYF<sub>4</sub>: Gd<sup>3+</sup>/ Tb<sup>3+</sup> and (b) DOX-conjugated  $\beta$ -NaYF<sub>4</sub>: Gd<sup>3+</sup>/ Tb<sup>3+</sup> in FBS for 3 days at 37 °C.

### 3.3.6. Controlled DOX release studies of DOX-conjugated $\beta$ -NaYF<sub>4</sub>:Gd<sup>3+</sup>/ Tb<sup>3+</sup> nanorods

We further studied the drug loading and release abilities of the DOX-conjugated  $\beta$ -NaYF<sub>4</sub>: 15 % Gd<sup>3+</sup>/ 5 % Tb<sup>3+</sup> nanorods through the pH-dependent cleavage of the hydrazone bond. The loading level of DOX in the nanorods is calculated to be 0.22 mg DOX/  $\beta$ -NaYF<sub>4</sub>: 15 % Gd<sup>3+</sup>/ 5 % Tb<sup>3+</sup> mg, which is determined by the characteristic DOX optical absorbance at 490 nm. The Figure 11 illustrates the DOX release profiles of  $\beta$ -NaYF<sub>4</sub>:Gd<sup>3+</sup>/Tb<sup>3+</sup> -MPH-DOX conjugated nanorods in the PBS buffer solutions of

different pH values (pH 7.4 and 5.0) at 37 °C. It can be clearly seen that, the DOX release rate at acidic pH i.e. at pH 5.0 is much faster than that at pH 7.4.

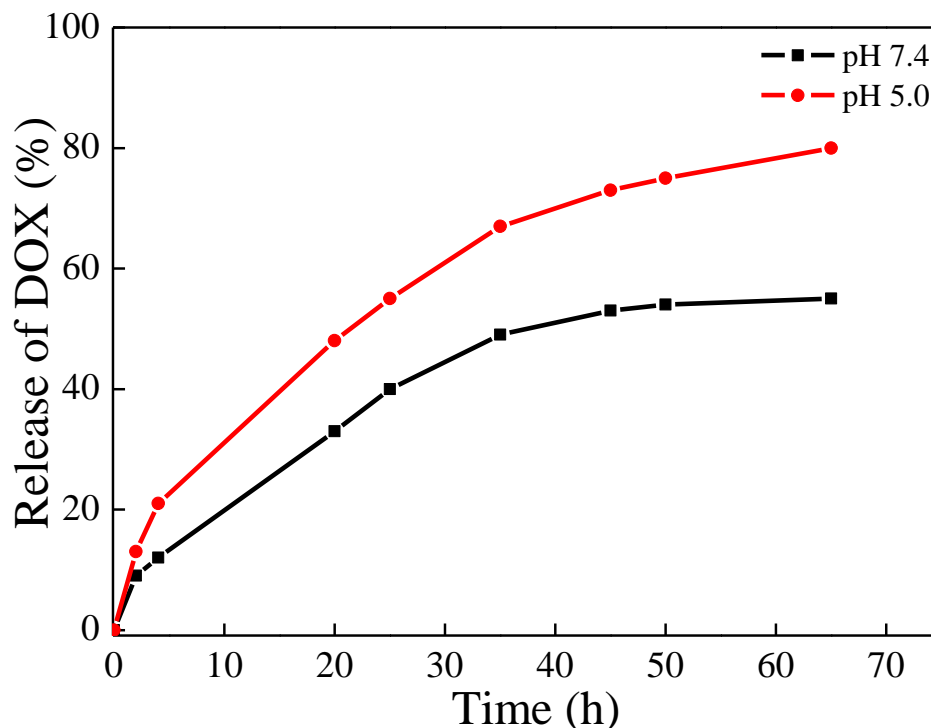


**Figure 11:** DOX release from DOX-conjugated  $\beta$ -NaYF<sub>4</sub>: Gd<sup>3+</sup>/Tb<sup>3+</sup> nanorods over the period of time in PBS buffer at pH 7.4 and pH 5.0. The DOX release rate at acidic pH i.e. at pH 5.0 is much faster than that at pH 7.4 due to cleavage of pH-sensitive hydrazone bond linkage at pH 5.0.

Since the microenvironment of cancer cells is acidic (6.5 - 6.8), the pH-triggered drug delivery system can be considered as an smart drug carrier system in cancer therapy. The pH-triggered DOX release behavior in our system is acquired by conjugating DOX to PEI coated  $\beta$ -NaYF<sub>4</sub>:Gd<sup>3+</sup>/Tb<sup>3+</sup> nanorods via pH sensitive hydrazone bond linkage ( $\beta$ -NaYF<sub>4</sub>:Gd<sup>3+</sup>/Tb<sup>3+</sup> -MPH-DOX), which is quite stable at normal physiological conditions i.e. at neutral pH (pH 7.4), but cleaves quickly in the acidic environment (pH 4.5-5.0). As observed from the Figure 10, DOX release rate markedly increased under the acidic conditions. More than ~ 52 % DOX released within 24 h and ~ 80 % of DOX released at



the later stage *i.e.* at 65 h at acidic pH (pH 5); however at neutral pH (pH 7.4) nearly less than ~ 38 % DOX released within 24 h and, only ~ 54 % of DOX released in 65 h. To validate that the DOX was loaded on the nanorods by conjugation with hydrazone bond, but not simply by the physical absorption and the DOX release is taking place by cleavage of hydrazone bond in the acidic pH, we performed a control experiment where we combined DOX and  $\beta$ -NaYF<sub>4</sub>: Gd<sup>3+</sup>/ Tb<sup>3+</sup> in methanol and allowed to react for 24 h, in dark condition and further processed in the same way as for  $\beta$ -NaYF<sub>4</sub>: Gd<sup>3+</sup>/ Tb<sup>3+</sup>-MPH-DOX synthesis. The loading of the DOX on nanorods was checked by UV-vis spectrometer, but the characteristic signature absorbance band of the DOX (at 490 nm) was not observed. This indicates that the physical absorption of the DOX on the nanorod surfaces is negligible to render absorbance in the UV-vis spectrum. The release behaviour of DOX-nanorods incubated mixed solution was also studied. The Figure 12 demonstrates the release profile of DOX-nanorod mixture in PBS buffer solutions of different pH values (pH 7.4 and 5.0) at 37 °C.

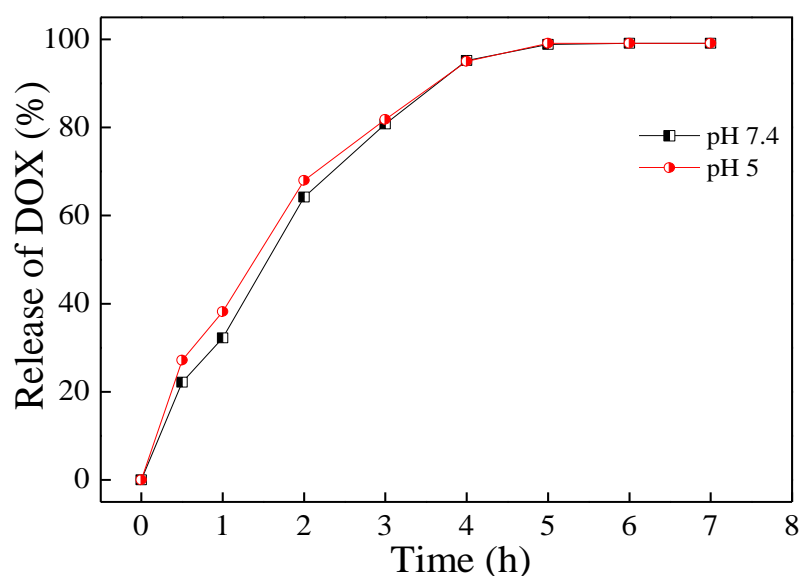


**Figure 12:** Release behavior of doxorubicin in the physically mixed solution of doxorubicin and  $\beta$ -NaYF<sub>4</sub>: Gd<sup>3+</sup>/ Tb<sup>3+</sup> nanorods at different time interval in PBS buffer at pH 7.4 and pH 5.

It can be clearly seen that, the unbound or non-specifically bound DOX (physically absorbed DOX if present), is rapidly diffused or released within 4 h, indicating uncontrolled release behavior of DOX. The release rate at different pH is also hardly affected. On the other hand,  $\beta$ -NaYF<sub>4</sub>: Gd<sup>3+</sup>/Tb<sup>3+</sup>-MPH-DOX showed controlled release kinetics (Figure 11) and minimal activity loss, which is important for targeted anticancer therapy. Further, we also confirmed the cleavage of hydrazone bond in DOX-conjugated  $\beta$ -NaYF<sub>4</sub>: Gd<sup>3+</sup>/Tb<sup>3+</sup> by FTIR (ATR mode). The time dependent FTIR study of DOX-conjugated  $\beta$ -NaYF<sub>4</sub>: Gd<sup>3+</sup>/Tb<sup>3+</sup> in PBS buffer of pH 5 at 37 °C as a function of time was performed. As can be seen from Figure 13, the feature band of hydrazone bond (–C=N–) at  $\sim 1620$  cm<sup>-1</sup> and band of DOX at  $\sim 1380$  cm<sup>-1</sup> found to be gradually depleted with time. A broad and weak band appeared at  $\sim 1585$  cm<sup>-1</sup> in the late stage ( $\sim 52$  h) is might be due to presence of hydrazide group remained on the surface of nanorods after release of DOX.<sup>34</sup>

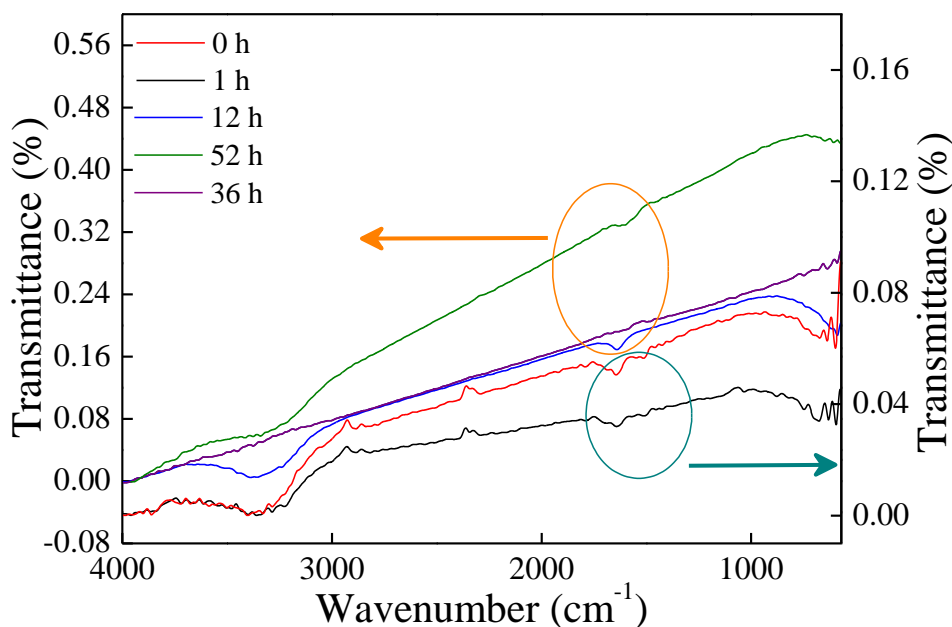
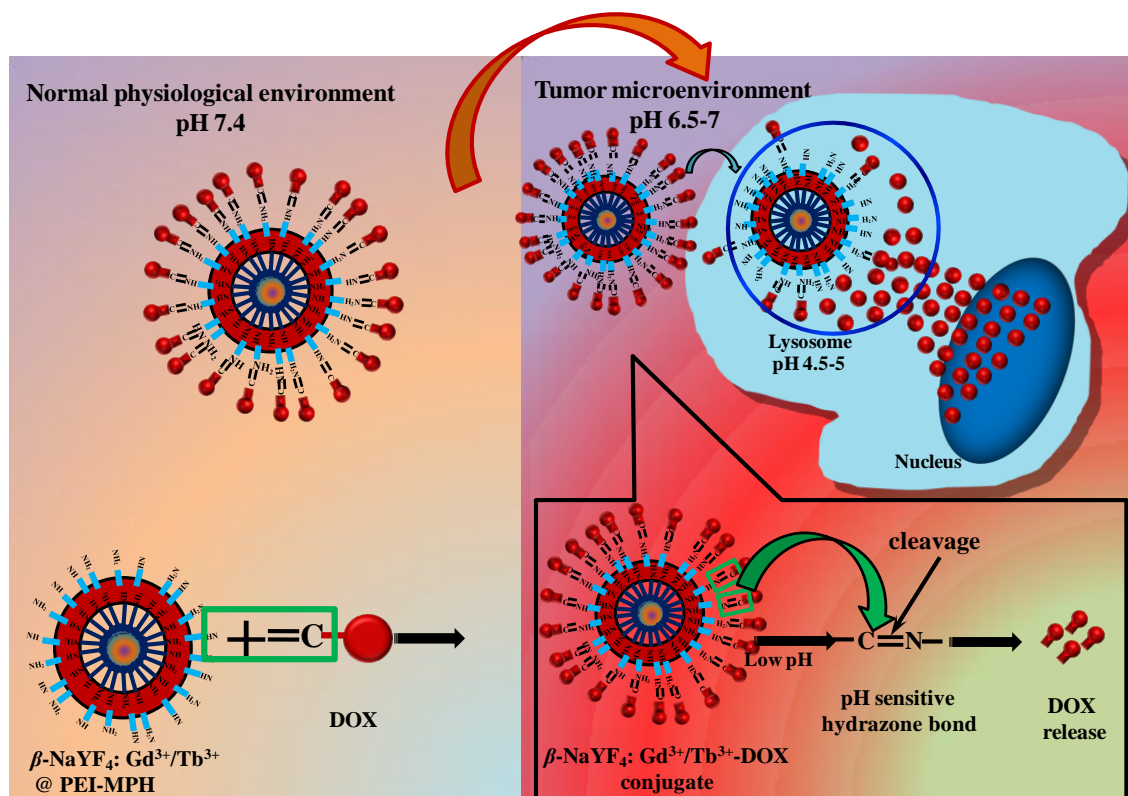


**Figure 13:** FT-IR spectra of DOX-conjugated  $\beta$ -NaYF<sub>4</sub>: Gd<sup>3+</sup>/Tb<sup>3+</sup> at different time intervals during dialysis in PBS at pH 5, showing cleavage of hydrazone bond.

These results implicate that the loss of drug from  $\beta$ -NaYF<sub>4</sub>: Gd<sup>3+</sup>/ Tb<sup>3+</sup> - MPH - DOX could be reduced during blood circulation at normal physiological environment (pH 7.4), while the drug release can be accelerated into the acidic environment and prominently release at lysosomes and consequently inside the cancer cells. Thereby, the DOX conjugated to  $\beta$ -NaYF<sub>4</sub>: Gd<sup>3+</sup>/ Tb<sup>3+</sup> via pH-sensitive hydrazone bond may be effectively delivered and targeted to the tumor tissues and cancer cells by site-specific activation. It is well accepted that, as compared with the normal tissues, the tumors have acidic microenvironment, as tumor tend to accumulate high level of lactic acid due to anaerobic glycolysis.<sup>25</sup> Meanwhile, the cellular uptake and internalization of weakly basic drug doxorubicin is reduced at low pH due to pH gradient. Moreover, doxorubicin exhibit poor distribution, development of drug resistance and harmful side effects such as systemic toxicity, cardiotoxicity, suppression of immune system etc.<sup>24, 26</sup> Our present system  $\beta$ -NaYF<sub>4</sub>: Gd<sup>3+</sup>/ Tb<sup>3+</sup> - MPH - DOX, where doxorubicin is conjugated to  $\beta$ -NaYF<sub>4</sub>: Gd<sup>3+</sup>/ Tb<sup>3+</sup> via pH-sensitive hydrazone bond through MPH renders pH triggered targeted site activation DOX delivery by cleavage of hydrazone bond at pH 5.0 inside the tumor cells (scheme 4) and also significantly prevents the serious adverse effects and toxicity of DOX.



**Scheme 4:** A schematic representation of pH-triggered drug delivery system of DOX-conjugated  $\beta$ -NaYF<sub>4</sub>:Gd<sup>3+</sup>/Tb<sup>3+</sup> nanorods showing the release of DOX inside the tumor cells via cleavage of pH sensitive hydrazone bond linkage at lysosomes (pH 4.5-5) and consequent internalization into the cells.

### 3.3.7. Fluorescence resonance energy transfer (FRET) between $\beta$ -NaYF<sub>4</sub>: Gd<sup>3+</sup>/ Tb<sup>3+</sup> nanoparticles and DOX

The DOX conjugated  $\beta$ -NaYF<sub>4</sub>: Gd<sup>3+</sup>/ Tb<sup>3+</sup> nanorods can also be applied as an optical probe to confirm the conjugation of DOX to  $\beta$ -NaYF<sub>4</sub>: Gd<sup>3+</sup>/ Tb<sup>3+</sup> and to monitor the release of DOX via fluorescence resonance energy transfer, also termed as Förster resonance energy transfer (FRET) between  $\beta$ -NaYF<sub>4</sub>: Gd<sup>3+</sup>/ Tb<sup>3+</sup> and DOX. The luminescence of  $\beta$ -NaYF<sub>4</sub>: Gd<sup>3+</sup>/ Tb<sup>3+</sup> are quenched by DOX through energy transfer

between FRET pair. As shown in Figures 14 (a, b), the broad absorbance of DOX occurs between 450 nm to 550 nm, which overlaps the green emission of  $\beta$ -NaYF<sub>4</sub>: Gd<sup>3+</sup>/Tb<sup>3+</sup> at 488 nm and 540 nm. This spectral overlap enables the quenching of luminescence intensity of  $\beta$ -NaYF<sub>4</sub>: Gd<sup>3+</sup>/Tb<sup>3+</sup> after the reaction with DOX (Figure 14 (c)). We can also monitor the release of DOX by FRET mechanism. It is well demonstrated that, the FRET process results from dipole-dipole interactions and thus FRET is extremely sensitive to distance between donor and acceptor, consequently FRET can effectively occur only when the donor and acceptor are in close proximity.<sup>42, 43</sup> At pH 5.0, DOX has been released from  $\beta$ -NaYF<sub>4</sub>: Gd<sup>3+</sup>/Tb<sup>3+</sup> nanorods by cleavage of hydrazone bond and thus diffused away from the nanorods, which cease the FRET process. Therefore, we can register the increase in luminescence intensity of  $\beta$ -NaYF<sub>4</sub>: Gd<sup>3+</sup>/Tb<sup>3+</sup> with the gradual release of DOX (scheme 5). This is established by studying the photoluminescence spectra of DOX-conjugated  $\beta$ -NaYF<sub>4</sub>: Gd<sup>3+</sup>/Tb<sup>3+</sup> in PBS buffer of pH 5 at 37 °C as a function of time.

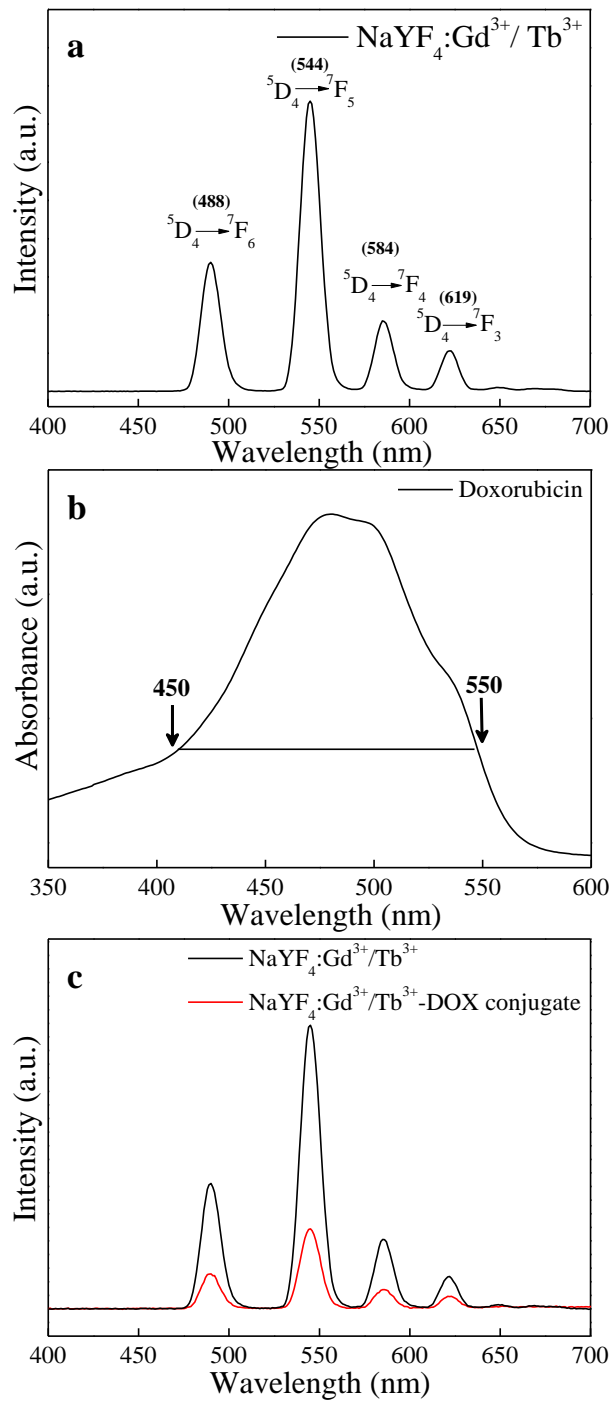


**Figure 14:** (a) The photoluminescence emission spectra of  $\beta$ -NaYF<sub>4</sub>:Gd<sup>3+</sup>/Tb<sup>3+</sup> at  $\lambda_{\text{ex}} = 273$  nm, and (b) the UV-vis absorption spectra of DOX showing a spectral overlap. (c) A comparison of the photoluminescence emission spectra of bare  $\beta$ -NaYF<sub>4</sub>:Gd<sup>3+</sup>/Tb<sup>3+</sup> nanorods, and  $\beta$ -NaYF<sub>4</sub>:Gd<sup>3+</sup>/Tb<sup>3+</sup>-DOX conjugates taken in same concentrations. It is

seen that due to FRET mechanism the emission intensity of phosphor nanorods comes down after conjugation with DOX.

As shown in Figure 15 (a), the luminescence of  $\beta$ -NaYF<sub>4</sub>: Gd<sup>3+</sup>/Tb<sup>3+</sup> has gradually recovered along with the release of DOX. Moreover, the fluorescence of DOX conjugated  $\beta$ -NaYF<sub>4</sub>: Gd<sup>3+</sup>/Tb<sup>3+</sup> have also been considerably quenched as compare to free DOX, when excited at 490 nm (Figure 15 (b)).

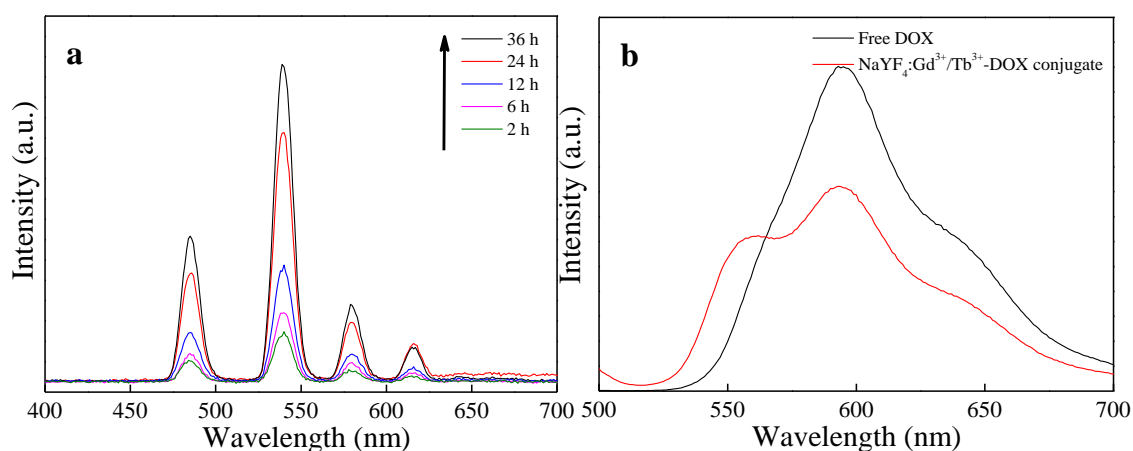
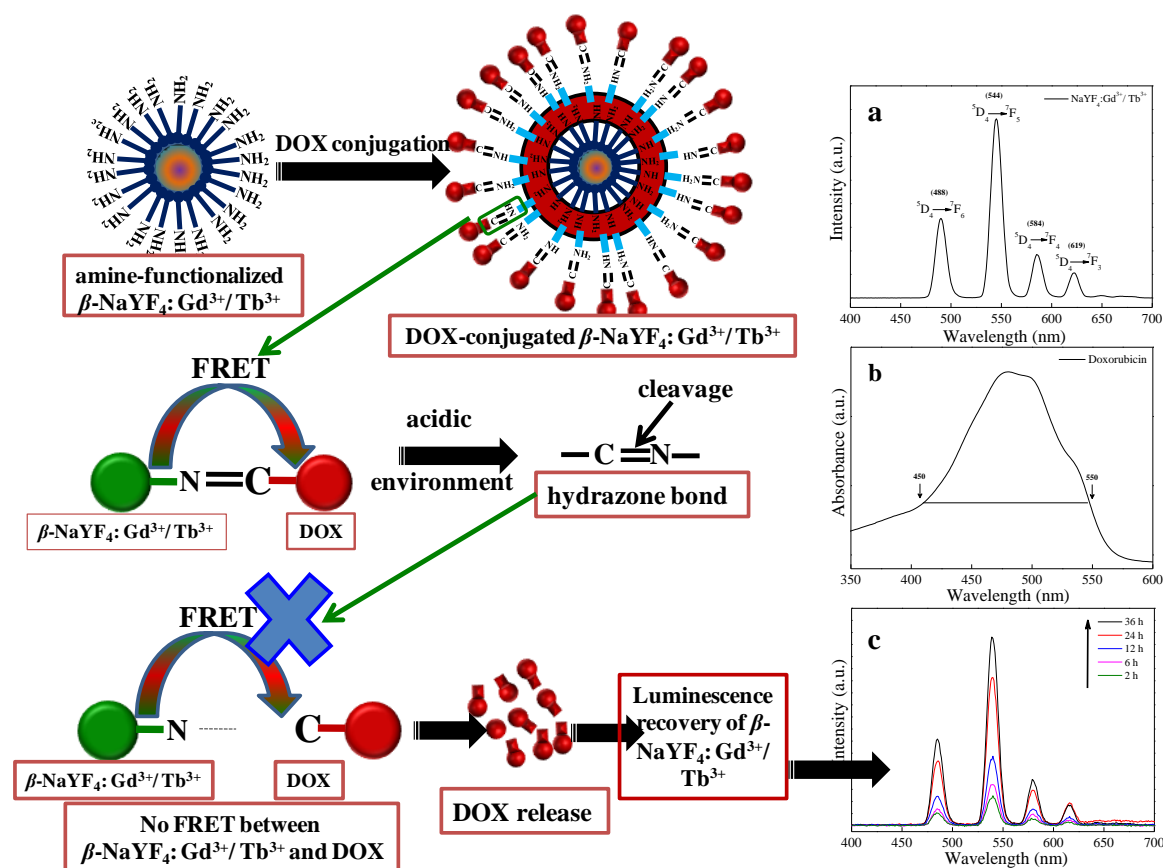


**Figure 15:** (a) The photoluminescence emission intensity of DOX conjugated -  $\beta$ -NaYF<sub>4</sub>:Gd<sup>3+</sup>/Tb<sup>3+</sup> nanorods as a function of DOX-release time at pH 5 and 37 °C in PBS buffer showing recovery of photoluminescence along with the release of DOX with increasing time by disabling FRET and (b) Photoluminescence spectra of free DOX and  $\beta$ -NaYF<sub>4</sub>:Gd<sup>3+</sup>/Tb<sup>3+</sup>- DOX conjugate solutions.

In previous studies, it has been reported that, the fluorescence of DOX has been quenched due to hydrophobic interaction between the hydrocarbon chains of oxidized oleic acid on the nanoparticle surface and the anthraquinone ring of doxorubicin molecule.<sup>44</sup> In another report, the quenching effect in DOX-NP conjugate was observed due to the intermolecular interactions between DOX molecules after its dense packing on the surface of nanoparticles.<sup>45</sup>

In present work, interaction between hydrazide group on nanorod's surface and 13- C carbonyl group of might have resulted in quenching of DOX fluorescence. Further, a detailed mechanism is required to be studied in future. The FRET based detection probe for monitoring the DOX conjugation and release in the present system is represented by the following scheme 5:



**Scheme 5:** Schematic representation of DOX conjugated- $\beta$ -NaYF<sub>4</sub>:Gd<sup>3+</sup>/Tb<sup>3+</sup> nanorod system as FRET based detection probe.



### 3.3.8. Cellular uptake studies

#### 3.3.8.1. Cellular uptake studies by CLSM

The cell uptake process has been measured using confocal laser scanning microscopy (CLSM) after incubating  $\beta$ -NaYF<sub>4</sub>: Gd<sup>3+</sup>/Tb<sup>3+</sup>-MPH-DOX nanorods with MCF-7 breast cancer cells in different time period. The green emission is from  $\beta$ -NaYF<sub>4</sub>: Gd<sup>3+</sup>/Tb<sup>3+</sup> nanorods and red fluorescence is from DOX. In the initial 30 min time period (Figures 16 A), very few nanorods could be taken up by the MCF-7 cells. It can be clearly seen that the accumulation of the red emitting particles (red fluorescence from DOX) are apparently increased after incubation of 2 h. After prolong incubation period of 8 h, increased fluorescence from DOX have been appeared inside the cells. Similarly, green emission was increased with prolonging time.

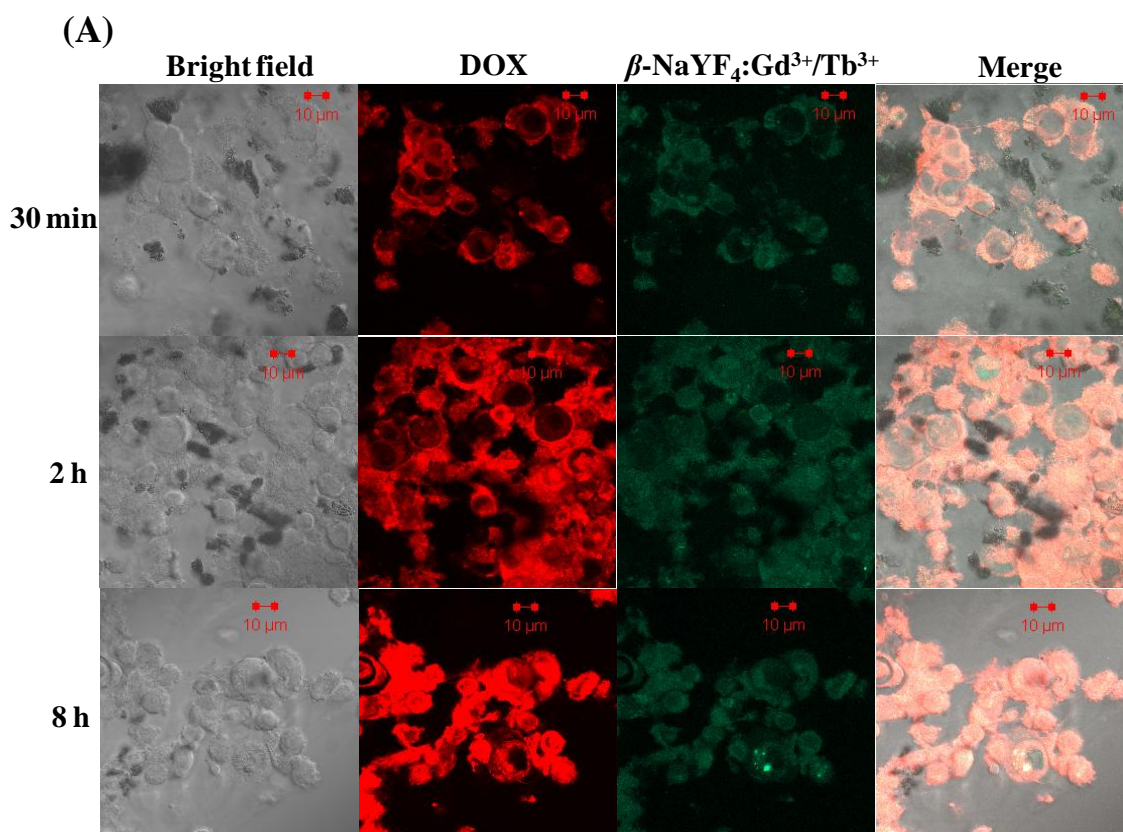


**Figure 16 (A):** Confocal laser scanning microscopy (CLSM) images of MCF-7 cancer cells incubated with DOX-conjugated  $\beta$ -NaYF<sub>4</sub>:Gd<sup>3+</sup>/Tb<sup>3+</sup> nanorods for 30 min, 2 h, and 8

h, at 37 °C. Emissions from  $\beta$ -NaYF<sub>4</sub>:Gd<sup>3+</sup>/Tb<sup>3+</sup> (green colored) and DOX fluorescence (red colored) were recorded in the wavelength ranges of 500-550 nm and 500-600 nm.

The scale bar is 10  $\mu$ m.

(B)

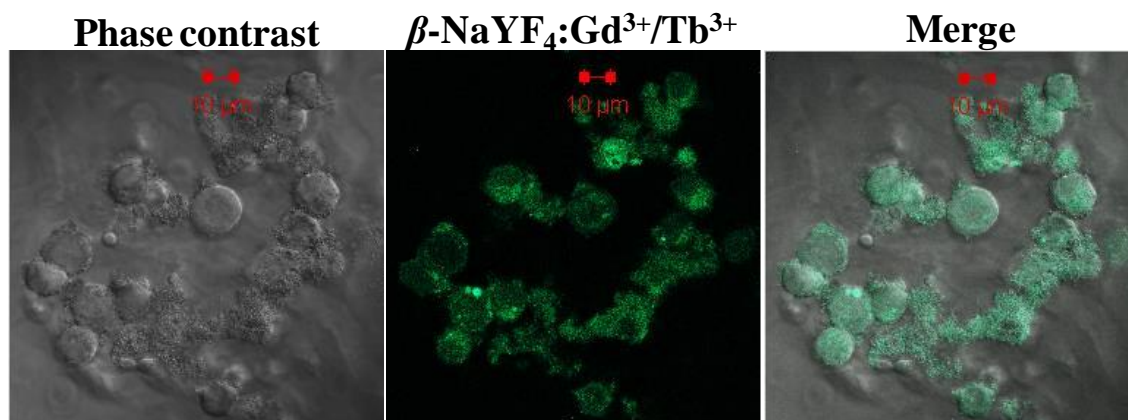


**Figure 16 (B):** Confocal laser scanning microscopy (CLSM) images of MCF-7 cancer cells incubated with  $\beta$ -NaYF<sub>4</sub>: Gd<sup>3+</sup>/ Tb<sup>3+</sup> nanorods. The scale bar is 10  $\mu$ m.

Confocal laser scanning microscopy (CLSM) images of MCF-7 cancer cells incubated with  $\beta$ -NaYF<sub>4</sub>: Gd<sup>3+</sup>/ Tb<sup>3+</sup> nanorods are also shown in Figure 16 (B). The green emission signals observed from  $\beta$ -NaYF<sub>4</sub>: Gd<sup>3+</sup>/ Tb<sup>3+</sup> (Figure 16 (A) and 16 (B)), demonstrates that these could also be used as an optical probe for imaging. These results indicated the efficient internalization of  $\beta$ -NaYF<sub>4</sub>: Gd<sup>3+</sup>/ Tb<sup>3+</sup>-MPH-DOX nanorods by the MCF-7 breast cancer cells. The red fluorescence from the released DOX was observed in both cytoplasm and the cell nucleus (Figure 17). CSLM images clearly shown time course increase in the fluorescence intensity of doxorubicin-conjugated  $\beta$ -NaYF<sub>4</sub>: Gd<sup>3+</sup>/ Tb<sup>3+</sup> which correlates to release of DOX inside the cell. Here, we predict that more doxorubicin release is due to the internalization of  $\beta$ -NaYF<sub>4</sub>: Gd<sup>3+</sup>/ Tb<sup>3+</sup>-MPH-DOX nanoparticles in different acidic compartments of cells such as endosomes and lysosomes where there is low pH ranging from (pH 4 - 6). The acidic environment cleaves the pH-sensitive hydrazone bond to enable the release of doxorubicin.

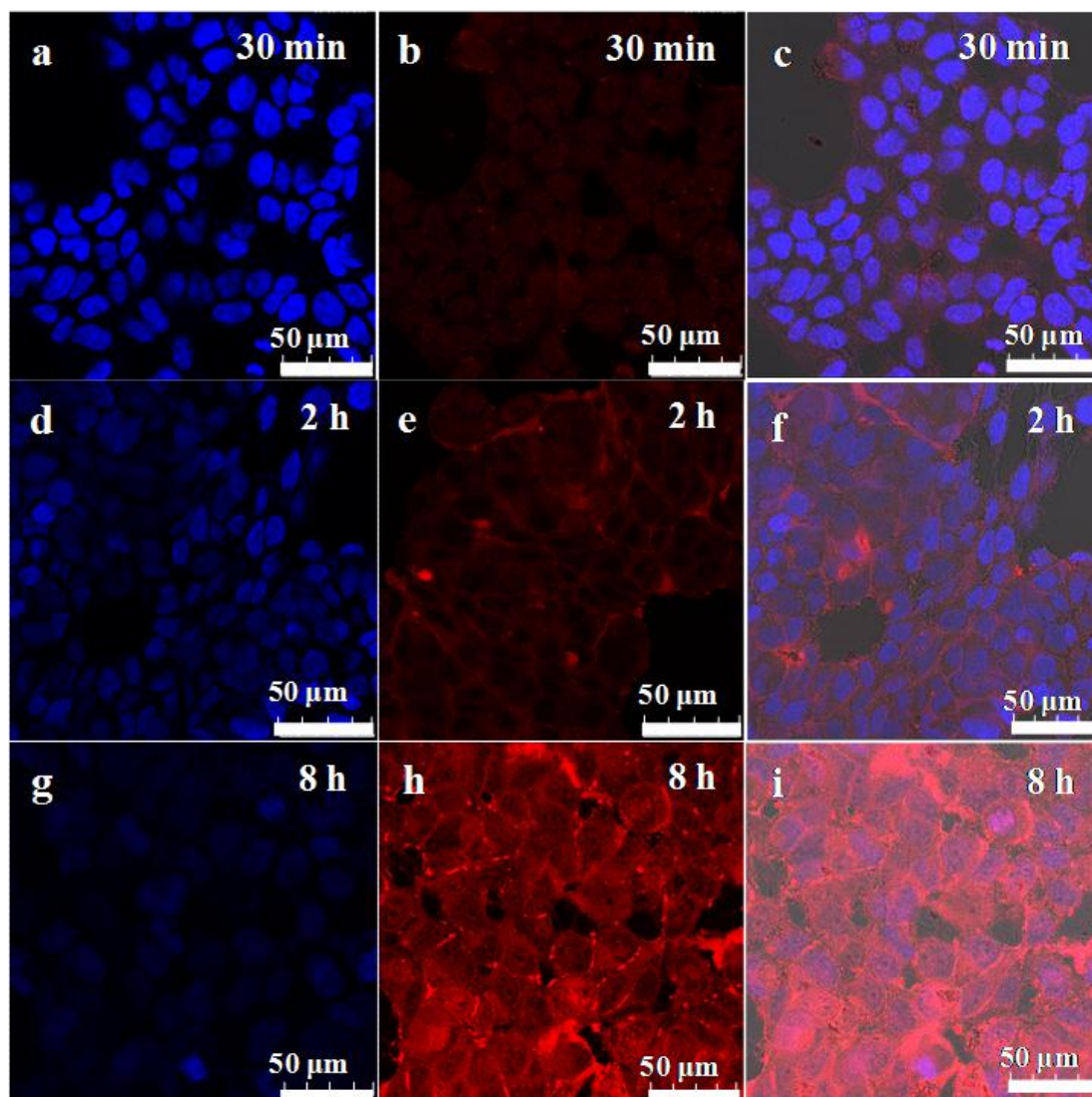


**Figure 17:** Confocal laser scanning microscopy (CLSM) images of MCF-7 cancer cells incubated with DOX-conjugated  $\beta$ -NaYF<sub>4</sub>:Gd<sup>3+</sup>/Tb<sup>3+</sup> nanorods for 30 min (a-c), 2 h (d-f), and 8 h (g-i) at 37 °C. The columns can be classified as (left) the nuclei of cells (being dyed in blue by DAPI for visualization), (middle) DOX-conjugated  $\beta$ -NaYF<sub>4</sub>:Gd<sup>3+</sup>/Tb<sup>3+</sup> nanorods and (right) a merge of the two channels of both. The red emission (591nm) is from DOX molecules.

Further to establish the benefit of DOX-conjugated  $\beta$ -NaYF<sub>4</sub>: Gd<sup>3+</sup>/Tb<sup>3+</sup> nanorods in targeting cancer cells, pH dependent uptake of free DOX and DOX-conjugated  $\beta$ -NaYF<sub>4</sub>: Gd<sup>3+</sup>/Tb<sup>3+</sup> nanorods in MCF-7 breast cancer cell was further studied. We compared the cellular uptake of free DOX and DOX-conjugated  $\beta$ -NaYF<sub>4</sub>: Gd<sup>3+</sup>/Tb<sup>3+</sup> nanorods by confocal microscopy. Free DOX and  $\beta$ -NaYF<sub>4</sub>: Gd<sup>3+</sup>/Tb<sup>3+</sup>-MPH-DOX nanorods were incubated with MCF-7 breast cancer cells for different time period at pH 6.5, which mimic the tumor microenvironment where the pH is between 6.5 - 6.8. As can be clearly seen from Figure 18, the red fluorescence from DOX, i.e. the accumulation of DOX is increased when incubated with DOX-conjugated  $\beta$ -NaYF<sub>4</sub>: Gd<sup>3+</sup>/Tb<sup>3+</sup> nanorods as compared to free DOX at pH 6.5.

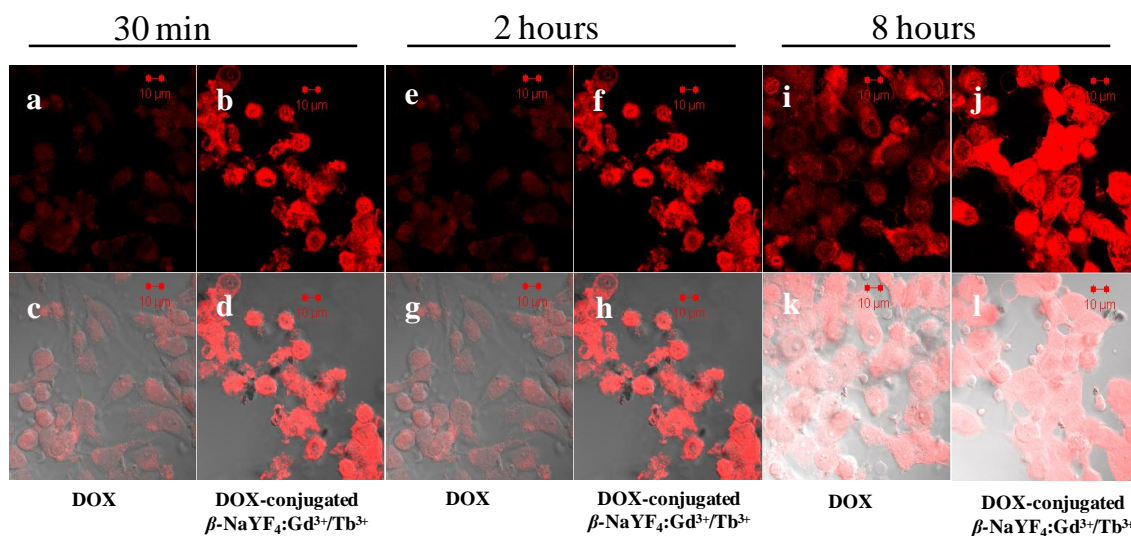


**Figure 18:** Cellular uptake of free doxorubicin in MCF-7 cancer cells at 30 min (a, c), 2 h (e, g), 8 h (i, k), and DOX-conjugated  $\beta$ -NaYF<sub>4</sub>:Gd<sup>3+</sup>/Tb<sup>3+</sup> at 30 min (b, d), 2 h (f, h), 8 h (j, l), at pH 6.5, 37 °C. The lower row is corresponding merge images.

The objective behind designing DOX-conjugated  $\beta$ -NaYF<sub>4</sub>: Gd<sup>3+</sup>/Tb<sup>3+</sup> ( $\beta$ -NaYF<sub>4</sub>: Gd<sup>3+</sup>/Tb<sup>3+</sup>-MPH-DOX) based drug delivery system is the sustained release of weakly basic DOX in an ideal acidic tumor microenvironment, as the native DOX cannot be

effectively taken up at acidic condition. It can be clearly seen that (Figure 18) DOX-conjugated  $\beta$ -NaYF<sub>4</sub>: Gd<sup>3+</sup>/Tb<sup>3+</sup> could be able to work more effectively than free DOX at low pH. This indicates that in the present system,  $\beta$ -NaYF<sub>4</sub>: Gd<sup>3+</sup>/Tb<sup>3+</sup> nanorods when conjugated to DOX via hydrazone bond increase the cellular uptake and delivery of DOX in the tumor cells.

### 3.3.8.2. Cellular uptake studies by flow cytometry

Flow cytometry analysis of free DOX and DOX-conjugated  $\beta$ -NaYF<sub>4</sub>: Gd<sup>3+</sup>/Tb<sup>3+</sup> nanorods was further performed to confirm the uptake of DOX-conjugated  $\beta$ -NaYF<sub>4</sub>: Gd<sup>3+</sup>/Tb<sup>3+</sup> nanorods by the MCF-7 cells by means of measuring the fluorescence intensities of DOX in the cells. The  $\beta$ -NaYF<sub>4</sub>: Gd<sup>3+</sup>/Tb<sup>3+</sup>-MPH-DOX nanorods were used to deliver DOX to the cells. Thus, the cell uptake degree of the  $\beta$ -NaYF<sub>4</sub>: Gd<sup>3+</sup>/Tb<sup>3+</sup>-MPH-DOX conjugate can be quantified using flow cytometry by determining the red fluorescence emitted from the released DOX.

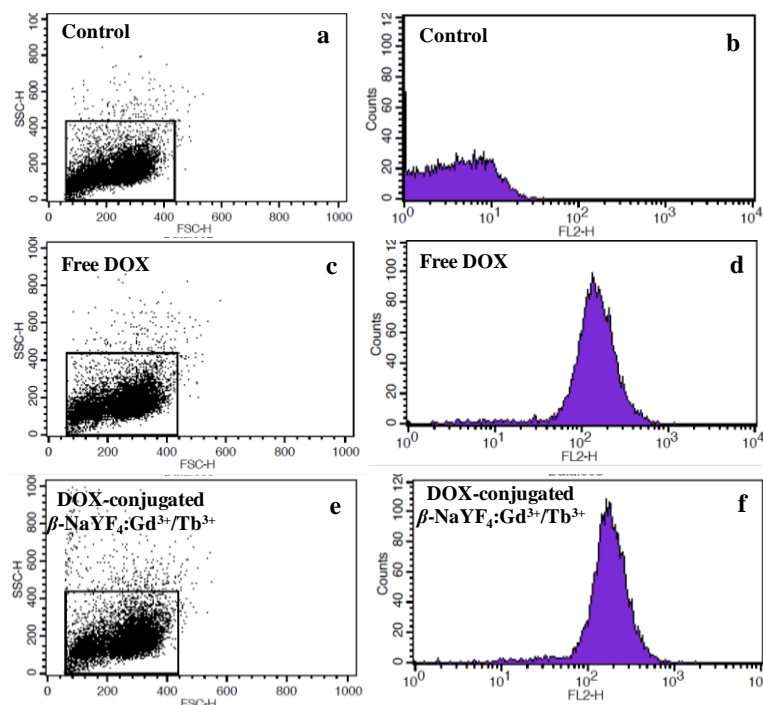


**Figure 19:** Flow cytometry analysis of MCF-7 breast cancer cells. (a, b) the control cells, (c, d) incubated with free DOX and, (e, f) incubated with DOX-conjugated  $\beta$ -

NaYF<sub>4</sub>:Gd<sup>3+</sup>/Tb<sup>3+</sup> nanorods for 4 h demonstrating the uptake of DOX conjugated  $\beta$ -NaYF<sub>4</sub>: Gd<sup>3+</sup>/Tb<sup>3+</sup> by the MCF-7 cells.

For flow cytometry analysis, the cells were seeded and incubated with free DOX and  $\beta$ -NaYF<sub>4</sub>: Gd<sup>3+</sup>/Tb<sup>3+</sup>-MPH-DOX nanorods for 4 h. Single cell suspension were prepared and the fluorescence intensity of the control cells and the sample cells were measured. It can be clearly noted that, the amount of red fluorescence in sample cells (Figures 19 c, d and e, f) is much higher than the control cells (Figure 19 a, b).

The flow cytometry results further confirmed that the  $\beta$ -NaYF<sub>4</sub>: Gd<sup>3+</sup>/Tb<sup>3+</sup>-MPH-DOX nanorods were taken up by MCF-7 breast cancer cells. Therefore, the DOX conjugated  $\beta$ -NaYF<sub>4</sub>: Gd<sup>3+</sup>/Tb<sup>3+</sup> nanorods enter and get internalized by the cancer cells and assemble into the cytoplasm. Meanwhile, the DOX is released from  $\beta$ -NaYF<sub>4</sub>: Gd<sup>3+</sup>/Tb<sup>3+</sup> nanorods by the cleavage of hydrazone bond into the nucleus and, consequently kill the cancer cells by causing DNA damage by intercalation, inhibition of nucleic acid and protein synthesis and disruption of DNA repair enzymes.<sup>46,47</sup>

### 3.3.9. *In vivo* studies

The therapeutic efficacy of DOX-conjugated  $\beta$ -NaYF<sub>4</sub>: Gd<sup>3+</sup>/Tb<sup>3+</sup> nanorods were validated in SCID mice bearing a MDA-MB 231 tumor model. As a proof of principle experiments, the breast tumor-bearing mice were treated with  $\beta$ -NaYF<sub>4</sub>: Gd<sup>3+</sup>/Tb<sup>3+</sup> and DOX-conjugated  $\beta$ -NaYF<sub>4</sub>: Gd<sup>3+</sup>/Tb<sup>3+</sup> and *in vivo* tumor regression studies were performed. The  $\beta$ -NaYF<sub>4</sub>: Gd<sup>3+</sup>/Tb<sup>3+</sup> were taken as control vehicle. The doses were 2 mg/Kg of body weight and monitored for 4 weeks. As can be clearly observed in figure 20, tumor-bearing mice when treated with DOX-conjugated  $\beta$ -NaYF<sub>4</sub>: Gd<sup>3+</sup>/Tb<sup>3+</sup>, the tumor was significantly inhibited (size ~ 5 mm) as compared to control vehicle (size ~ 12 mm), because of pH triggered targeted drug delivery system.

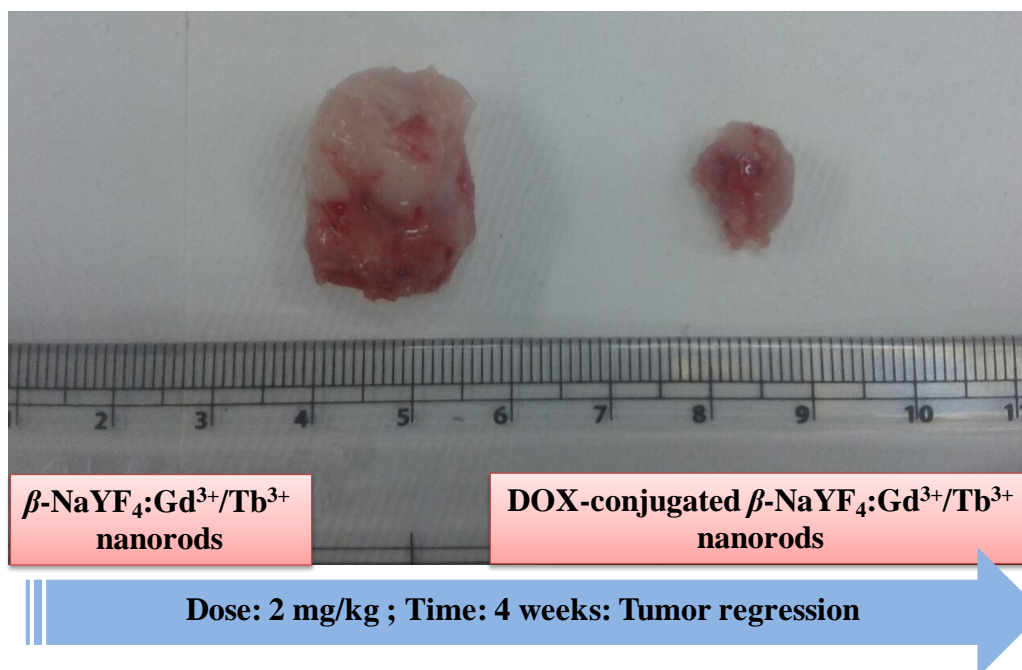


**Figure 20:** Representative photographs of tumors collected from the mice at the end of treatment (4 weeks) after treatment with  $\beta$ -NaYF<sub>4</sub>: Gd<sup>3+</sup>/ Tb<sup>3+</sup> control vehicle and DOX-conjugated  $\beta$ -NaYF<sub>4</sub>: Gd<sup>3+</sup>/ Tb<sup>3+</sup>.

These results prove that  $\beta$ -NaYF<sub>4</sub>: Gd<sup>3+</sup>/ Tb<sup>3+</sup> phosphors are the proper candidates for multimodal imaging tool along with drug carrier nanovehicle system.

### 3.3.10. Magnetic measurements

#### 3.3.10.1. Magnetic mass susceptibility

In addition to the excellent luminescence property, the amine functionalized  $\beta$ -NaYF<sub>4</sub>: 15 % Gd<sup>3+</sup>/ 5 % Tb<sup>3+</sup> nanorods as well as DOX-conjugated  $\beta$ -NaYF<sub>4</sub>: 15 % Gd<sup>3+</sup>/ 5 % Tb<sup>3+</sup> nanorods exhibited paramagnetism (Figure 21), which makes these nanorods suitable as dual modality optical-magnetic multifunctional nanophosphors. The Figures 21 (a) and (b), shows the room temperature (RT) magnetization (M) as a function of the

applied magnetic field ( $H$ ) for amine functionalized  $\beta$ -NaYF<sub>4</sub>: 15 % Gd<sup>3+</sup>/ 5 % Tb<sup>3+</sup> nanorods and DOX-conjugated  $\beta$ -NaYF<sub>4</sub>: 15 % Gd<sup>3+</sup>/ 5 % Tb<sup>3+</sup> nanorods respectively. These nanorods exhibit typical paramagnetic behavior at 300 K and applied field in range from - 40 to + 40 kOe. The paramagnetic properties of the Gd<sup>3+</sup> ions arise from seven unpaired inner 4f electrons, which are closely bound to the nucleus and effectively shielded from crystal field by the outer 5s<sup>2</sup> 5p<sup>6</sup> shell electrons. Thus, it prohibits sufficient overlap of the orbital's associated with the partially filled 4f electrons shells of the Gd<sup>3+</sup> ions necessary for ferromagnetism. It turns out that the magnetic moments associated with the Gd<sup>3+</sup> ions are all localized and non-interacting giving rise to paramagnetism.<sup>48</sup>

The room temperature magnetic mass susceptibility of amine functionalized  $\beta$ -NaYF<sub>4</sub>: 15 % Gd<sup>3+</sup>/ 5 % Tb<sup>3+</sup> nanorods and DOX-conjugated  $\beta$ -NaYF<sub>4</sub>: 15 % Gd<sup>3+</sup>/ 5 % Tb<sup>3+</sup> nanorods are 3.83 X 10<sup>-5</sup> emu g<sup>-1</sup> Oe<sup>-1</sup> and 2.49 X 10<sup>-5</sup> emu g<sup>-1</sup> Oe<sup>-1</sup>, respectively. Furthermore, the magnetization of  $\beta$ -NaYF<sub>4</sub>: 15 % Gd<sup>3+</sup>/ 5 % Tb<sup>3+</sup> nanorods and DOX-conjugated  $\beta$ -NaYF<sub>4</sub>: 15 % Gd<sup>3+</sup>/ 5 % Tb<sup>3+</sup> nanorods is ~ 0.76 emu g<sup>-1</sup> and ~ 0.49 emu g<sup>-1</sup>, respectively at 20 k Oe. These values are close to the reported values of nanoparticles used very frequently for bioseparation and also successfully used as T<sub>1</sub>-MRI contrast agent.<sup>33, 49</sup>



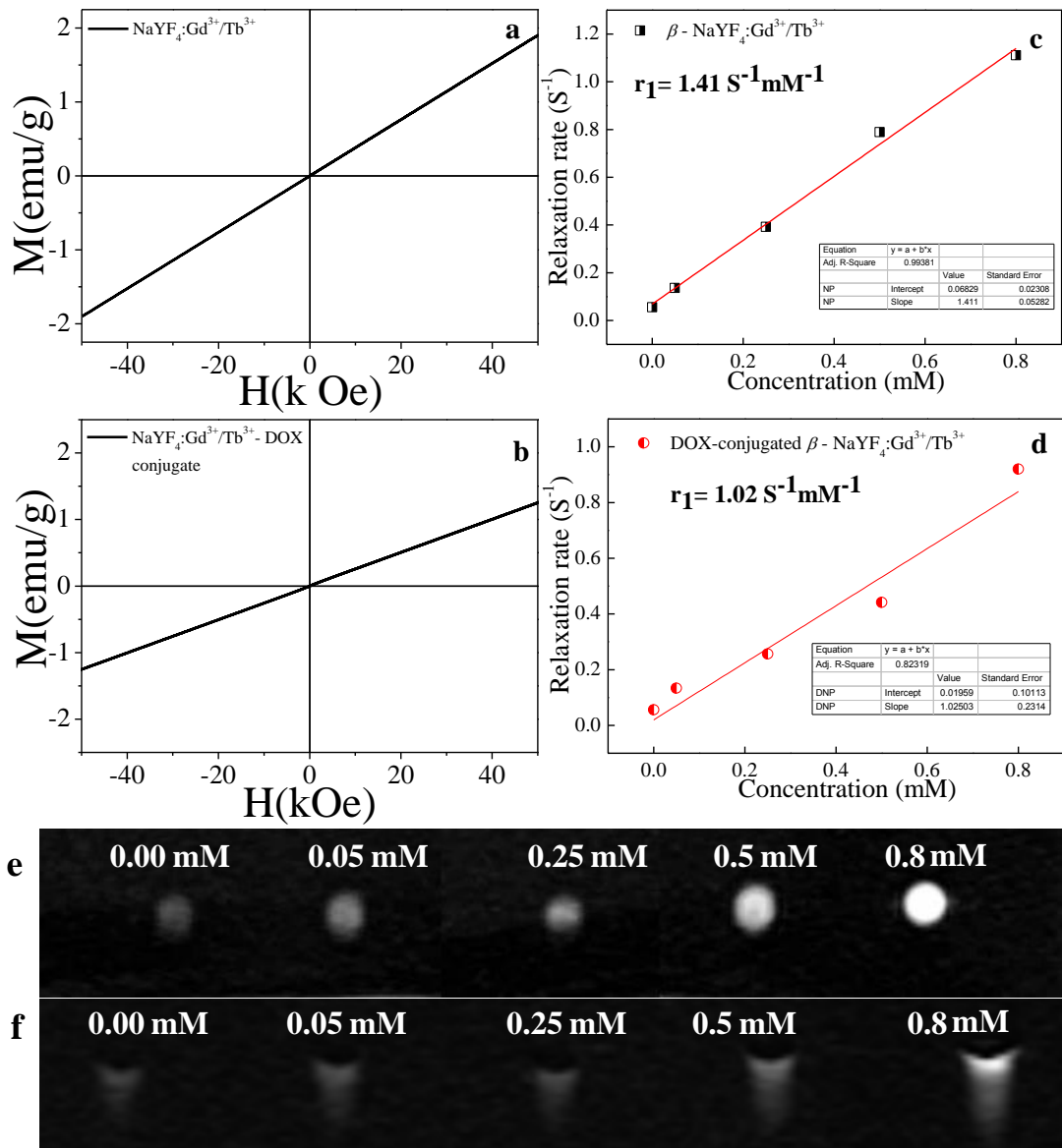


**Figure 21:** Magnetization as a function of applied field for (a)  $\beta$ -NaYF<sub>4</sub>:Gd<sup>3+</sup>/Tb<sup>3+</sup> nanorods and (b)  $\beta$ -NaYF<sub>4</sub>:Gd<sup>3+</sup>/Tb<sup>3+</sup>-DOX conjugate at room temperature showing paramagnetic behavior. The plot of  $^1\text{H}$  spin-lattice relaxation rate ( $1/T_1$ ) as a function of molar concentration (mM) of (c)  $\beta$ -NaYF<sub>4</sub>:Gd<sup>3+</sup>/Tb<sup>3+</sup> nanorods and (d)  $\beta$ -NaYF<sub>4</sub>:Gd<sup>3+</sup>/Tb<sup>3+</sup>-DOX conjugate at RT and 9.4 T.  $T_1$  weighted MRI images of (e)  $\beta$ -NaYF<sub>4</sub>:Gd<sup>3+</sup>/Tb<sup>3+</sup> nanorods and (f)  $\beta$ -NaYF<sub>4</sub>:Gd<sup>3+</sup>/Tb<sup>3+</sup>-DOX conjugate at various molar concentrations in water. Deionised water (0.00 mM) was taken as reference.

### 3.3.10.2. Longitudinal relaxivity and magnetic resonance imaging

To further demonstrate the potential application of  $\beta$ -NaYF<sub>4</sub>: Gd<sup>3+</sup>/Tb<sup>3+</sup> nanorods as a MRI contrast agent, a series of  $\beta$ -NaYF<sub>4</sub>: Gd<sup>3+</sup>/Tb<sup>3+</sup> nanorods and DOX-conjugated  $\beta$ -NaYF<sub>4</sub>: Gd<sup>3+</sup>/Tb<sup>3+</sup> nanorods with different molar concentrations were used for the ionic longitudinal relaxivity ( $r_1$ ) study using the NMR spectrometer. From the slope of plot of  $1/T_1$  versus Gd<sup>3+</sup> concentration (Figure 21 (c, d)), the relaxation rate  $1/T_1$  ( $r_1$ ) value for the  $\beta$ -NaYF<sub>4</sub>: Gd<sup>3+</sup>/Tb<sup>3+</sup> nanorods and the DOX-conjugated  $\beta$ -NaYF<sub>4</sub>: Gd<sup>3+</sup>/Tb<sup>3+</sup> were determined to be  $1.41 \text{ s}^{-1} \text{ mM}^{-1}$  and  $1.02 \text{ s}^{-1} \text{ mM}^{-1}$  respectively. Figure 21 (e) and (f) shows typical  $T_1$ -weighted MRI images of  $\beta$ -NaYF<sub>4</sub>: Gd<sup>3+</sup>/Tb<sup>3+</sup> nanorods and DOX-conjugated  $\beta$ -NaYF<sub>4</sub>: Gd<sup>3+</sup>/Tb<sup>3+</sup>. The  $T_1$ -weighted imaging for the samples was performed for 4 different concentrations varying from 0.05 to 0.8 mM (water for the reference signal) on a 3 T MR scanner. With the increasing concentration, the  $T_1$ -weighted MRI signal intensity was clearly enhanced, thus showed positive enhancement effect, demonstrating that the  $\beta$ -NaYF<sub>4</sub>: Gd<sup>3+</sup>/Tb<sup>3+</sup> nanorods might be an effective  $T_1$ -MRI contrast agent.

Therefore, the as-prepared amine functionalized  $\beta$ -NaYF<sub>4</sub>: 15 % Gd<sup>3+</sup>/ 5 % Tb<sup>3+</sup> are multifunctional nanorods with high luminescence properties and intrinsic paramagnetism, thus, these may find useful applications in bio-imaging, bio-separation and magnetic resonance imaging.

### 3.4. Conclusion

In summary, we have developed multi-modal probe based on PEI capped  $\beta$ -NaYF<sub>4</sub>: Gd<sup>3+</sup>/Tb<sup>3+</sup>, which possess excellent photoluminescence as well as paramagnetic properties, making them suitable for optical bioimaging and MRI applications. A widely used anti-cancer drug, doxorubicin, was conjugated to PEI capped  $\beta$ -NaYF<sub>4</sub>: Gd<sup>3+</sup>/Tb<sup>3+</sup> via pH-sensitive hydrazone bond linkage. This system displays the pH-triggered drug delivery system, where the doxorubicin is released by cleavage of hydrazone bond in the

acidic microenvironment of tumor, which reduces the side-effects of chemotherapeutics. The pH dependent *in vitro* DOX release studies shown that, the DOX release at acidic pH are significantly faster than at pH 7.4. Furthermore, the luminescence quenching of  $\beta$ -NaYF<sub>4</sub>: Gd<sup>3+</sup>/Tb<sup>3+</sup> by DOX due to FRET mechanism can be applied as optical probe to confirm the DOX conjugation and monitor the DOX release. Cell toxicity assays revealed that the PEI capped  $\beta$ -NaYF<sub>4</sub>: Gd<sup>3+</sup>/Tb<sup>3+</sup> possess very low toxicity. Meanwhile, the *in vitro* cytotoxicity of DOX- conjugated  $\beta$ -NaYF<sub>4</sub>: Gd<sup>3+</sup>/Tb<sup>3+</sup> on MCF-7 cancer cells exhibited comparable cellular toxicity with respect to free DOX. The cellular uptake of DOX-conjugated  $\beta$ -NaYF<sub>4</sub>: Gd<sup>3+</sup>/Tb<sup>3+</sup> by MCF-7 cells are established by confocal laser scanning microscopy study. The cellular uptake of DOX-conjugated  $\beta$ -NaYF<sub>4</sub>: Gd<sup>3+</sup>/Tb<sup>3+</sup> by MCF-7 cells were enhanced compared to free DOX at pH 6.5, which mimic tumor microenvironment. Along with high luminescence efficiency, the magnetic mass susceptibility of  $\beta$ -NaYF<sub>4</sub>: Gd<sup>3+</sup>/Tb<sup>3+</sup> and longitudinal relaxivity ( $r_1$ ) were close to those of materials reported for MRI and bio-separation. It is expected that DOX-conjugated  $\beta$ -NaYF<sub>4</sub>: Gd<sup>3+</sup>/Tb<sup>3+</sup> combining pH-triggered drug delivery, efficient luminescence and paramagnetic properties promises as potential multifunctional platform for cancer theranostics, biodetection probe and imaging.

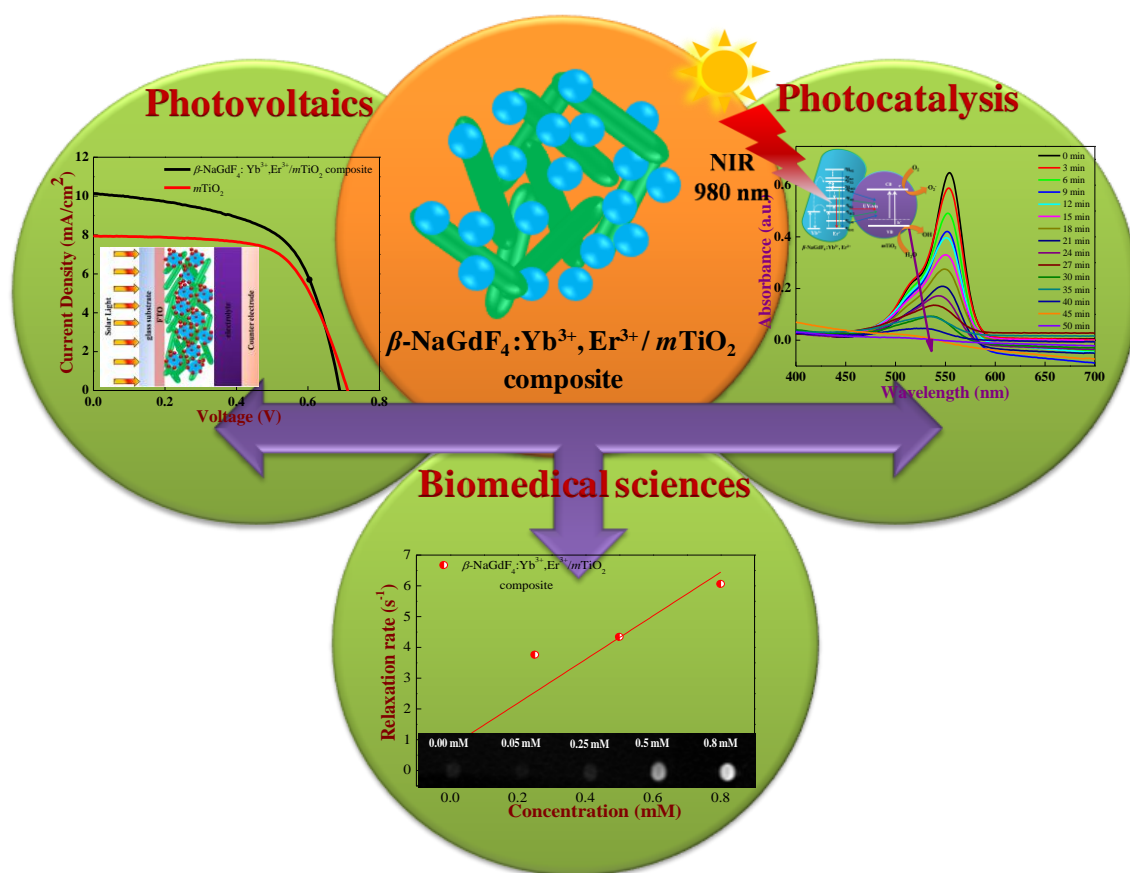
### 3.5. References

1. J. H. Lee, Y.M. Huh, Y. W. Jun, J. W. Seo, J.T. Jang, H. T. Song, S. Kim, E. J. Cho, H. G. Yoon, J. S. Suh and J. Cheon, *Nature Medicine* ., 2006, **13**, 95-99.
2. S. K. Bhunia, A. Saha, A. R. Maity, S. C. Ray and N. R. Jana, *Scientific Reports.*, 2013, **3**, 1-7.
3. Q. Zhao, C. Huanga and F. Li, *Chem. Soc. Rev.*, 2011, **40**, 2508-2524.
4. D. GeiBler, L. J. Charbonniere, R. F. Ziessel, N. G. Butlin, H.G. Lohmannsroben, and N. Hildebrandt, *Angew. Chem. Int. Ed.*, 2010, **49**, 1396-1401.
5. L. Shao, Y. Gao and F. Yan, *Sensors.*, 2011, **11**, 11736-11751.
6. A. Thibon and V. C. Pierre, *Anal Bioanal Chem.*, 2009, **394**,107–120.
7. Y. Liu, D. Tu, H. Zhuab and X. Chen, *Chem. Soc. Rev.*, 2013, **42**, 6924-6958.
8. Y. Liu, D. Tu, H. Zhu, E. Ma and X. Chen, *Nanoscale*, 2013, **5**, 1369-1384.
9. H. B. Na, I. C. Song, and T. Hyeon, *Adv. Mater.*, 2009, **21**, 2133-2148.
10. K. N. Raymond and V. C. Pierre, *Bioconjugate Chem.*, 2005, **16**, 3-8.
11. J. W. Stouwdam and F. C. J. M. van Veggel, *Nano Lett.*, 2002, **2**, 733-737.
12. G. Wang, Q. Peng and Y. Li, *ACCOUNTS OF CHEMICAL RESEARCH.*, 2011, **44** 322-332.
13. F. Wang and X. Liu, *Chem. Soc. Rev.*, 2009, **38**, 976-989.
14. J. H. Huang, X.H. Gong, Y. J. Chen, Y.F. Lin, J.S. Liao, X.Y. Chen, Z.D. Luo, and Y. D. Huang, *Applied Physics B* , 2007, **89**, 73-80.
15. A. A. Kaminskii, O. Lux, H. Rhee, H.J. Eichler, K. Ueda, H. Yoneda, A. Zhao, B. Shirakawa, J. Chen, J. Dong, and J. Zhang, *Laser Phys. Lett* ., 2012, **9**, 879-887.
16. J. A. Capobianco, F. Vetrone, and J. C. Boyer, *J. Phys. Chem. B.*, 2002, **106**, 1181-1187.

17. C. Li, C. Zhang, Z. Hou, L. Wang, Z. Quan, H. Lian, and J. Lin, *J. Phys. Chem. C.*, 2009, **113**, 2332-2339.
18. C. Li, Z. Quan, J. Yang, P. Yang, and J. Lin, *Inorganic Chemistry.*, 2007, **46**, 6329-6337.
19. P. Padhye and P. Poddar, *J. Mater. Chem. A.*, 2014, **2**, 19189-19200.
20. R. Kumar, M. Nyk, T. Y. Ohulchansky, C.A. Flask, and P. N. Prasad, *Adv. Funct. Mater.*, 2009, **19**, 853-859.
21. J. E. Lee, N. Lee, H. Kim, J. Kim, S. H. Choi, J. H. Kim, T. Kim, I. C. Song, S.Pyo Park, W. K. Moon, and T. Hyeon, *J. AM. CHEM. SOC.*, 2010, **132**, 552-557.
22. X. Zhu, J. Zhou, M. Chen, M. Shi, W. Feng, F. Li, *Biomaterials.*, 2012, **33**, 4618-4627.
23. L. Zhang, Y.S. Wang, Y. Yang, F. Zhang, W. F. Dong, S. Y. Zhou, W. H. Pei, H. D. Chen and H. B. Sun, *Chem. Commun.*, 2012, 48, 11238-11240.
24. A. Madhusudhan , G. B. Reddy , M. Venkatesham, G.Veerabhadram, D. A. Kumar, S.Natarajan, M. Y. Yang, A.Hu, and S. S. Singh, *Int. J. Mol. Sci.*, 2014, **15**, 8216-8234.
25. K. Newell, A. Franchi, J. Pouyssegur, and I. Tannock, *Proc. Natl. Acad. Sci. USA.*, 1993, **90**, 1127-11231.
26. P. Swietach, A. Hulikova, S.Patiar, R. D. Vaughan-Jones, A. L. Harris, *PLoS ONE*; 2012, **7**, 1-9.
27. P.R. Sajanalal, T. S. Sreeprasad, A. K. Samal, and T. Pradeep, *Nano Reviews.*, 2011, **2**, 5883.
28. C. M. J Hu, S. Aryal, and L. Zhang , *Therapeutic Delivery.*, 2010, **1**, 323-334.
29. R. Venkatesan, A. Pichaimani, K. Hari, P.K. Balasubramanian, J. Kulandaivel, and K. Premkumar, *J. Mater. Chem. B.*, 2013, **1**, 1010-1018.

30. D. W. Dong, S.W. Tong, X. R. Qi, *J Biomed Mater Res Part A.*, 2013, **101**, 1336-1344.
31. Q. Ju, D. Tu, Y. Liu, R. Li, H. Zhu, J. Chen, Z. Chen, M. Huang, and X. Chen, *J. Am. Chem. Soc.*, 2012, **134**, 1323-1330.
32. J. Jin, Y. J. Gu, C. W. Yin Man, J. Cheng, Z. Xu, Y. Zhang, H. Wang, V. H.Y. Lee, S. H. Cheng, and W. T. Wong, *ACS Nano.*, 2011, **5**, 7838-7847.
33. S. Zeng, M. K. Tsang, C. F. Chan, K. L. Wong, B. Fei and J. Hao, *Nanoscale.*, 2012, **4**, 5118-5424.
34. F. H. Chen, L. M. Zhang, Q. T. Chen, Y. Zhang and Z. J. Zhang, *Chem. Commun.*, 2010, **46**, 8633-8635.
35. Z. Hao, J.Zhang, X. Zhang, S. Lu, and X. Wang, *Journal of The Electrochemical Society.*, 2009, **156**, 193-196.
36. Y. Liu , D. Tu , H. Zhu , R. Li , W. Luo , and X. Chen, *Adv. Mater.*, 2010, **22**, 3266-71.
37. A. Jaiswal, R. Das, S. Adyanthaya, P. Poddar, *J Nanopart Res.*, 2011, **13**,1019-10127.
38. M. Banski, A. Podhorodecki, J. Misiewicz, M. Afzaal, A. L. Abdelhady and P. O'Brien, *J. Mater. Chem. C.*, 2013, **1**, 801-807.
39. M. Shi, K. Ho, A. Keating, and M. S. Shoichet, *Adv. Funct. Mater.*, 2009, **19**, 1-8.
40. D. Yang, X. Yang, P. Ma, Y. Dai, Z. Hou, Z. Cheng, C. Li, J. Lin, *Biomaterials.*, 2012, **34**, 1601-1612.
41. X. Li, Z. Hou, P. Ma, X. Zang, C. Li, Z. Cheng, J. Lian, J. Lin, *RSC Adv.*, 2013, **3**, 8517–8526.
42. A. R. Clapp, I. L. Medintz, J. M. Mauro, B. R. Fisher, M. G. Bawendi, and H. Mattoussi, *J. AM. CHEM. SOC.*, 2004, **126**, 301-310.

43. A. A. Deniz, M. Dahan, J. R. Grunwell, T. Ha, A. E. Faulhaber, D. S. Chemla, S. Weiss and P. G. Schultz, *Proc. Natl. Acad. Sci. USA.*, 1999, **96**, 3670-3675.
44. Y. Dai, D. Yang, P. Ma, X. Kang, X. Zhang, C. Li, Z. Hou, Z. Cheng, J. Lin, *Biomaterials.*, 2012, **33**, 8704-8713.
45. C. Wang, L. Cheng, and Z. Liu, *Biomaterials.*, 2011, **32**, 1110-1120.
46. C. F. Thorn, C. Oshiro, S. Marshe, T. H. Boussard, H. McLeod, T. E. Klein, and R. B. Altman, *Pharmacogenet Genomics.*, 2011, **21**, 440-446.
47. A. Hekmat, A. A. Saboury, and A. Divsalar, *J. Biomed. Nanotechnol.*, 2012, **8**, 968-982.
48. H. T. Wong, H. L. W. Chan, and J. H. Hao, *APPLIED PHYSICS LETTERS.*, 2009, **95**, 0225121-3.
49. H. T. Wong, M. K. Tsang, C. F. Chan, K. L. Wong, B. Feic and J. Hao, *Nanoscale.*, 2013, **5**, 3465-3473.

Chapter4**A broad spectrum photon responsive, paramagnetic  $\beta$ -NaGdF<sub>4</sub>: Yb<sup>3+</sup>, Er<sup>3+</sup> - mesoporous anatase titania nanocomposite**



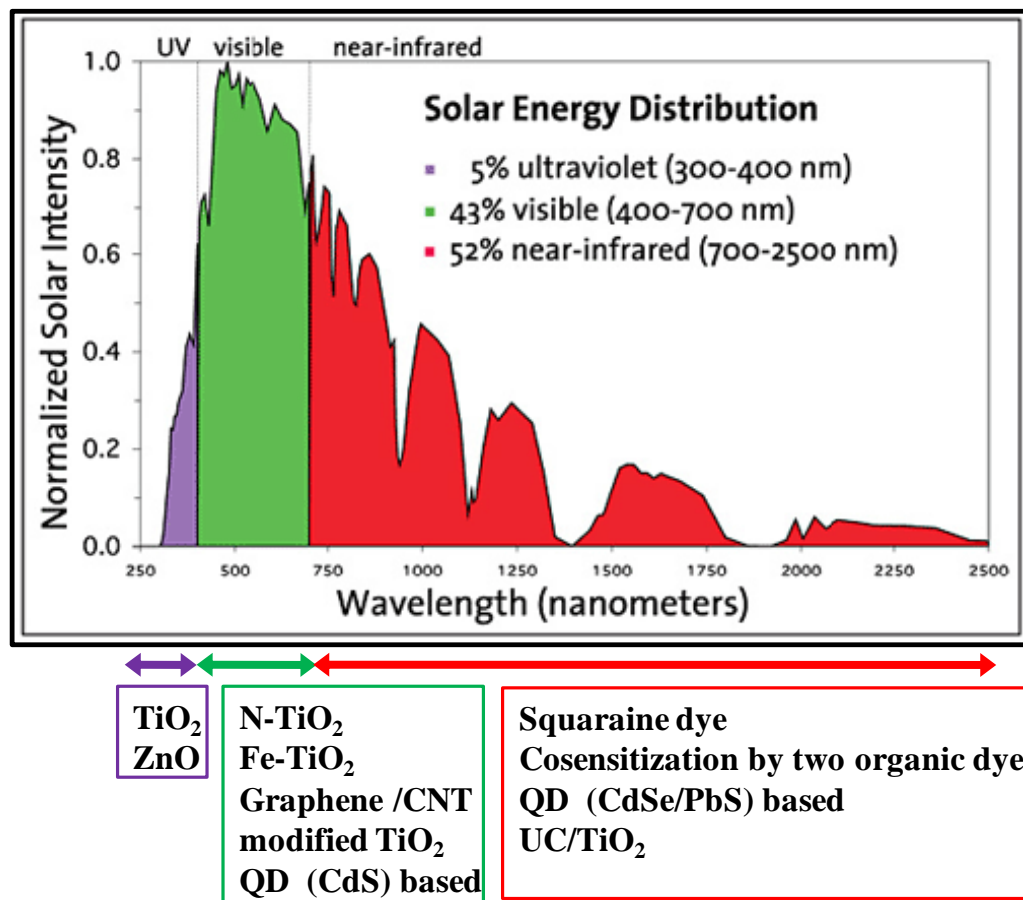
## Outline

In this research work, we developed a single multifunctional platform based on broad-spectrum photoactive  $\beta$ -NaGdF<sub>4</sub>: 18 % Yb<sup>3+</sup>, 2 % Er<sup>3+</sup> and mesoporous anatase TiO<sub>2</sub> for enhanced energy and simultaneous biomedical applications. Currently, the photoactive materials for solar energy harvesting applications have limitations in their efficiency due to their narrow photon absorption spectrum. The up-conversion phosphor  $\beta$ -NaGdF<sub>4</sub>: Yb<sup>3+</sup>, Er<sup>3+</sup> nanorods collect and harvest the NIR photons (~ 980 nm) of sunlight and transform into visible light via anti-Stokes emission ( $\lambda_{em}$  ~ 521 and ~ 540 nm), and the photoactive mesoporous anatase TiO<sub>2</sub> (*m*TiO<sub>2</sub>) utilizes UV and weak visible photons, thus the composite forms a broad spectrum photon-capture system and improved power conversion efficiency for enhanced applications in photocatalysis, and dye sensitized solar cells (DSSCs). The photocatalytic activity and solar cell efficiency of the nanocomposite showed an improvement over *m*TiO<sub>2</sub>. The nuclear magnetic resonance (NMR) measurements and magnetic resonance imaging of  $\beta$ -NaGdF<sub>4</sub>: Yb<sup>3+</sup>, Er<sup>3+</sup>/*m*TiO<sub>2</sub> nanocomposite revealed them to be suitable for simultaneous magnetoresonance imaging. The as-designed multifunctional  $\beta$ -NaGdF<sub>4</sub>:Yb<sup>3+</sup>, Er<sup>3+</sup>/*m*TiO<sub>2</sub> nanocomposite possessed simultaneous multiple discrete functionalities with excellent luminescence properties, intrinsic paramagnetism, biocompatibility, improved photocatalytic activity, and solar cell efficiency. This work provides a promising system to utilize NIR light, which will contribute to the efficient photon harvesting and biological applications.

## 4.1. Introduction

For the applications such as water splitting, solar cells, and the dye-degradation based on photocatalysis process, it is challenging to design the materials for the broadband photon absorption for the increased efficiency. Usually, the photon absorbing species such as dye-molecules, semiconductors (e.g. titania, perovskite materials, quantum dots etc.) work in a specific spectral range. The increase in the industrial waste water effluence into the rivers, containing highly toxic organic compounds generates by the untreated dyes from textile, leather, paint industries cause severe environmental issues worldwide.<sup>1</sup> The photocatalysis is an effective and environment-friendly technique for the degradation of these toxic pollutants.<sup>2</sup> On the other hand, a considerable attention is also emerging towards enhancing the solar energy harvesting for the photovoltaic technologies such as the dye-sensitized solar cell (DSSC).<sup>3</sup> In both of these important applications (and several others light based applications such as water splitting etc.) the TiO<sub>2</sub> is undoubtedly the most widely utilized semiconductor due to favorable electronic properties, availability and stability etc.<sup>4-6</sup> Among the four polymorphs of TiO<sub>2</sub> (rutile, anatase, brookite and TiO<sub>2</sub> (B)), anatase TiO<sub>2</sub> shows the highest photocatalytic activity.<sup>7</sup> However, unfortunately the wide bandgap of TiO<sub>2</sub> (~ 3.2 eV) has limited its widespread applications.<sup>8,9</sup> The UV light occupies only ~ 5 % of solar-spectrum, whereas the percentages of visible light and near-infrared (NIR) light are about ~ 45 % and ~ 50 %, respectively which allows only ~ 5 % of the solar energy impinging on the Earth's surface to be utilized which limits the efficiency of pure TiO<sub>2</sub>.<sup>10</sup> The schematic diagram representing solar energy distributions and various photoactive materials working in that particular region is represented in scheme 1. Methods such as doping with metallic/non-metallic elements, surface modification, coupling with other semiconductors, dye-sensitizing,

inclusion of graphitic carbon etc., have been used which essentially modify the electronic structure of TiO<sub>2</sub> thus extend and enhance the light absorption of TiO<sub>2</sub> in visible and NIR regions.<sup>11-15</sup> Although, the TiO<sub>2</sub> absorption in visible and NIR range is adjusted by employing above-mentioned strategies, but the overall catalytic activity was found to decrease due to an increased recombination of photogenerated electrons and holes.<sup>9</sup>



**Scheme 1:** Schematic representation of solar energy distribution in the solar spectrum and some of the photoactive materials efficient in respective regions.

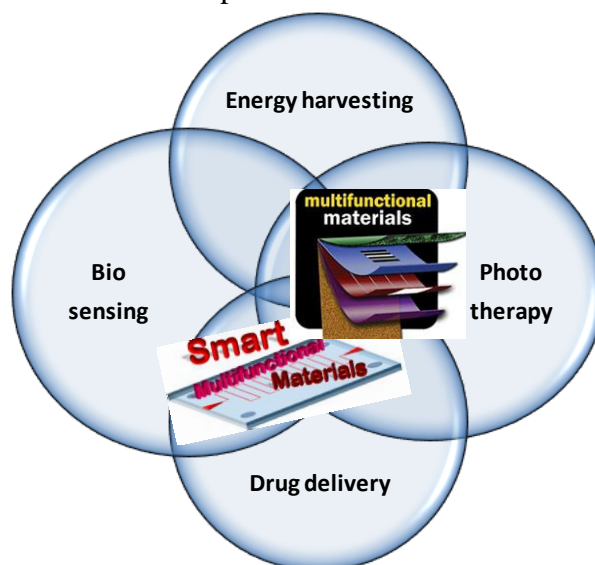
In addition to the conventional materials such as titania, the focus is shifted to other optically active materials to develop the composite with higher efficiency. Many new catalysts are also developed in an attempt to enhance the photocatalytic activity.<sup>16,17</sup> Some of

them include NaYF<sub>4</sub>: 5 % Tb microprisms, microrods and spindle-like structures<sup>18</sup>, {001}-faceted BiOCl single crystals<sup>19</sup>, and DyCrO<sub>3</sub> nanoplatelets<sup>20</sup>. On the other hand, to achieve the NIR photon harvesting of the solar spectrum in DSSCs, novel dyes (e.g., thienothiophene and thiophene based dyes, changing of thiocyanate or bipyridyl ligands in Ru dyes, substituting osmium for ruthenium, using squaraine dye and indoline based organic dyes), quantum dots (QDs) (e.g., CdSe, PbS, InP), and co-sensitizers have been reported.<sup>21-23</sup> However, the organic dyes decompose relatively easily and QDs are quite sensitive to water and ions. Our group reported the template-free fabrication of highly oriented, single crystalline 1D-rutile TiO<sub>2</sub>-multiwalled carbon nanotube (MWCNT) composite film directly grown on a fluorine doped conducting oxide (FTO) substrate, which improved the transport of the electrons and resulted into the enhancement in the DSSC efficiency due to reduced grain boundary and exciton recombination.<sup>24</sup>

Here, we investigate an alternative and effective way to harvest the larger part of the solar spectrum in photocatalysis and the photocurrent density in DSSCs by utilizing the upconverting phosphors in combination with the conventional materials such as titania and dye-molecules. These materials can transform the longer wavelength NIR photons to shorter wavelength UV and visible photons.<sup>25</sup> Recently these optically active hybrid materials have found increasing interest also in the biomedical applications. Thus, this composite material can be used in drug delivery and cancer theranostics applications owing to high penetration depth of the NIR radiation. Here, titania gives an edge in drug delivery and cancer therapy by reactive oxygen species (ROS) production due to its high activity, stability, non-toxicity, however, low tissue penetration and UV photodamage limits its use. To overcome these issues, the composites of TiO<sub>2</sub> with upconverting phosphor, N-TiO<sub>2</sub> /NaYF<sub>4</sub>:Yb, Tm have

been developed for NIR-triggered drug release and targeted cancer cell ablation.<sup>26</sup> Since, under NIR light excitation, UCNPs are capable of emitting high-energy UV/visible light, UCNPs can activate surrounding photosensitizer (PS) molecules to produce singlet oxygen to kill cancer cells. Owing to the high tissue penetration depth of NIR light, NIR-excited UCNPs can be used to activate PS molecules in much deeper tissues compared to traditional PDT induced by visible or ultraviolet (UV) light.<sup>27, 28</sup> Thus, in our proposed composite system, anatase  $m\text{TiO}_2$  act as a photosensitizer molecule which can trigger the production of ROS by formation of electron-hole pair, upon activation by safe and deeper NIR excitation for PDT, as a future application.

The development of multifunctional platforms for broad range of applications have geared tremendous progress towards the design and engineering of various functional materials with multiple discrete functions judiciously integrated in to form nanostructured composites.<sup>29, 30</sup> The below scheme represents the same.



**Scheme 2:** Schematic diagram showing design of single multifunctional platform with multiple discrete functionalities for various applications.

Here, it worth mentioning that the lanthanide-ion (Ln<sup>3+</sup>) doped up-/down-converting nanomaterials have received considerable attention due to their unique tunable electronic and magnetic properties that enable wide applications in optoelectronics, solid state lasers, security printing, biomedical diagnostics, sensors, catalysis and biological imaging.<sup>31-34</sup> However, their applications in the energy conversion is not frequently reported. The unique electronic/optical properties of the rare earth phosphors arise from the parity forbidden  $f$ - $f$  transitions shielded by filled  $5s$  and  $5p$  orbitals and the phonon energy of the host lattice. Lanthanide-ion doped luminescent materials exhibit sharp emission, long luminescence-lifetime (in ms), large and tunable Stokes and anti-Stokes shift, low autofluorescence and background noise, non-blinking feature and low toxicity.<sup>35,36</sup> In particular, the up-conversion is a unique photoluminescence process that involves the conversion of lower energy (e.g. near-infra red (NIR)) photons into higher energy (e.g. visible or ultraviolet (UV)) photons.<sup>37</sup> The lattice structure (and its effect on the phonon energy, electronic levels) and morphology of the host matrix is quite important for the efficient electronic transition between rare earth energy levels. An appropriate host-lattice combination with low phonon-energy is desirable to minimize the non-radiative losses.<sup>38</sup> Among various classes of rare-earth compounds (e.g. oxides, fluorides, phosphates, vanadates etc.), the rare earth fluorides, as host matrices, possess lowest phonon-energy (ca.  $350\text{ cm}^{-1}$ ) of crystal lattice and wide band gap.<sup>37, 39</sup> Among the rare earth fluorides investigated so far, NaYF<sub>4</sub> possesses lower phonon energy ( $\sim 360\text{ cm}^{-1}$ ), wider band-gap ( $\sim 8\text{ eV}$ ) and high refractive index.<sup>40, 41</sup> Thermodynamically stable hexagonal phase  $\beta$ -NaGdF<sub>4</sub> is another efficient host matrix for the down-conversion (DC) and up-conversion (UC) luminescence processes due to half filled  $4f$  orbital resulting in minimal non-radiative electronic transition.<sup>42, 43</sup> Moreover, the Gd<sup>3+</sup> substitution renders paramagnetic

properties, thus the Ln<sup>3+</sup> doped  $\beta$ -NaGdF<sub>4</sub> phosphors result in multifunctional luminescent-magnetic probes.<sup>42, 43</sup>

In this research work, we designed and fabricated a novel, multifunctional NIR active  $\beta$ -NaGdF<sub>4</sub>: 18 % Yb<sup>3+</sup>, 2 % Er<sup>3+</sup> mesoporous TiO<sub>2</sub> (*m*TiO<sub>2</sub>) nanocomposite. We explored its applications in photocatalysis, photovoltaics and biomedical sciences. This composite is designed to significantly improve the photon absorption in broader area of the solar spectrum. The up-conversion phosphor  $\beta$ -NaGdF<sub>4</sub>: 18 % Yb<sup>3+</sup>, 2 % Er<sup>3+</sup> harvest NIR photons and induce anti-Stokes visible emission and the *m*TiO<sub>2</sub> absorbs in the UV and weak visible spectrum, thereby improving broad photon capture and photon conversion efficiency (PCE). Moreover, the mesoporous TiO<sub>2</sub> is expected to increase the photocatalytic activity by increasing the active sites and enhancing the dye-adsorption in the DSSCs. Moreover, the mesoporous TiO<sub>2</sub> can also enhance the drug loading for PDT and enhanced chemotherapy as combined therapy for the treatment of cancer. Simultaneously, the  $\beta$ -NaGdF<sub>4</sub>:Yb, Er UCNPs can endow luminescence-magnetic resonance imaging guided cancer therapy. In this study, the  $\beta$ -NaGdF<sub>4</sub>: Yb<sup>3+</sup>, Er<sup>3+</sup>/*m*TiO<sub>2</sub> nanocomposite was characterized for various physical properties and its photoluminescence and magnetic properties were also investigated. The photocatalytic and photovoltaic properties of the  $\beta$ -NaGdF<sub>4</sub>: Yb<sup>3+</sup>, Er<sup>3+</sup>/*m*TiO<sub>2</sub> nanocomposite were also studied. To the best of our knowledge, for the first time we have proposed and designed a multifunctional  $\beta$ -NaGdF<sub>4</sub>: Yb<sup>3+</sup>, Er<sup>3+</sup>/*m*TiO<sub>2</sub> nanocomposite as a single platform with simultaneous multiple discrete functionalities.

## 4.2. Materials and method

### 4.2.1. Materials

All the chemicals were of analytical grade and were used as-received without any further purification. Gadolinium (III) nitrate hexahydrate ( $\text{Gd}(\text{NO}_3)_3 \cdot 6\text{H}_2\text{O}$ ), ytterbium (III) nitrate hexahydrate ( $\text{Yb}(\text{NO}_3)_3 \cdot 6\text{H}_2\text{O}$ ), and erbium (III) nitrate hexahydrate ( $\text{Er}(\text{NO}_3)_3 \cdot 6\text{H}_2\text{O}$ ) (purity  $\geq 99.89\%$ ), polyethyleneimine branched polymer (PEI, average MW  $\sim 25,000$ ), and titanium butoxide were purchased from Sigma Aldrich Inc. Ammonium fluoride ( $\text{NH}_4\text{F}$ ) and sodium chloride ( $\text{NaCl}$ ) were received from Thomas Baker Chemicals Pvt. Ltd. Absolute ethanol (purity  $\geq 99.9\%$ ) was obtained from Cympran Gludt BV, Belgium. Deionized water was used throughout the experiment.

### 4.2.2. Synthesis

#### 4.2.2.1. One-pot synthesis of $\beta$ -NaGdF<sub>4</sub>: 18 % Yb<sup>3+</sup>, 2 % Er<sup>3+</sup>

In a typical procedure,  $\text{Gd}(\text{NO}_3)_3 \cdot 6\text{H}_2\text{O}$ ,  $\text{Yb}(\text{NO}_3)_3 \cdot 6\text{H}_2\text{O}$  and  $\text{Er}(\text{NO}_3)_3 \cdot 6\text{H}_2\text{O}$  (0.2 M) were added to 10 mL  $\text{NaCl}$  solution (0.2 M). Under vigorous stirring, 20 mL of ethanol and 10 mL of PEI solution (5 wt %) were added to the above solution. After stirring of 30 min,  $\text{NH}_4\text{F}$  (0.5 M) was introduced into the above solution. After another agitation for several minutes, the solution was transferred into a stainless steel autoclave with Teflon liner of 80 mL capacity, sealed and heated at 200 °C for 24 h. After that, the autoclave was cooled to the room temperature, and the resulting product was separated centrifugally and was washed with distilled water and absolute ethanol. Then, the product was dried under vacuum at 60 °C for 8 h.



#### 4.2.2.2. Synthesis of $\beta$ -NaGdF<sub>4</sub>: 18 % Yb<sup>3+</sup>, 2 % Er<sup>3+</sup>/*m*TiO<sub>2</sub> composite

For a typical synthesis of (1:1)  $\beta$ -NaGdF<sub>4</sub>: 18 % Yb<sup>3+</sup>, 2 % Er<sup>3+</sup> / TiO<sub>2</sub> nanocomposite, 0.45 g of NaGdF<sub>4</sub>: 18 % Yb<sup>3+</sup>, 2 % Er<sup>3+</sup> nanoparticles were dispersed in 15 mL ethanol with continuous stirring for 30 min. After that, 0.45 mL titanium tetra-n-butoxide was introduced dropwise to the suspension followed by another 30 min of magnetic stirring. Subsequently, ethanol/water (7.5 mL: 0.375 mL) solution was added dropwise to the suspension and which was stirred for 60 min. The resulting suspension was then transferred into a 25 mL capacity Teflon-lined stainless steel autoclave, sealed and heated at 190 °C for 24 h. After that, the autoclave was cooled down to the room temperature, and the resulting product was separated centrifugally and was washed with distilled water and absolute ethanol. Then, the product was calcined at 250 °C for 1 h in ambient condition.

#### 4.2.2.3. Synthesis of *m*TiO<sub>2</sub>

For a comparison, the mesoporous TiO<sub>2</sub> was prepared by a similar process without the addition of  $\beta$ -NaGdF<sub>4</sub>: 18 % Yb<sup>3+</sup>, 2 % Er<sup>3+</sup> nanoparticles.

#### 4.2.3. Fabrication of DSSC

To fabricate a solar cell, at first, the screen-printing-paste of *m*TiO<sub>2</sub> and composite was prepared from their respective powders by following the method originally reported by the Gratzel's group.<sup>44</sup> The as-synthesized *m*TiO<sub>2</sub> and composite paste was deposited on the FTO substrate and annealed in air at 400 °C for 30 min. The substrate was cooled-down to 80 °C and immersed in a 0.5 mM ethanolic solution of N-719 dye for 24 h in order to enable sufficient adsorption of dye which acts as the sensitizer in the presence of light. After complete dye adsorption, the substrate was washed very carefully with ethanol and dried for 1 h. After that, a platinum coated FTO substrate (which will be used as the counter electrode),

was placed above the dye adsorbed FTO substrate, and an electrolyte containing 0.6 M 1-hexyl-2, 3- dimethylimidazolium iodide, 0.1 M LiI, 0.05 M I<sub>2</sub>, and 0.5 M 4- tert-butylpyridine in methoxyacetonitrile was injected into the space between the anode and the cathode to complete the assembly of the DSSC.

#### 4.2.4. Spin relaxation measurement of $\beta$ -NaGdF<sub>4</sub>: Yb<sup>3+</sup>, Er<sup>3+</sup> nanorods and $\beta$ -NaGdF<sub>4</sub>: Yb<sup>3+</sup>, Er<sup>3+</sup>/mTiO<sub>2</sub> composite as magnetic resonance imaging (MRI) contrast agents

For the solvent longitudinal relaxation times ( $T_1$ ) measurements, the samples were dispersed in D<sub>2</sub>O and the relaxivity values ( $r_1$ ) were measured by a standard inversion-recovery pulse sequence on a Bruker Advance NMR spectrometer at 20 °C and 9.4 T (400 MHz). The ability of proton relaxation enhancement of  $\beta$ -NaGdF<sub>4</sub>: Yb<sup>3+</sup>, Er<sup>3+</sup> is expressed by the term ionic relaxivity  $r_1$ , which is determined by the slope of following equation<sup>45</sup> in the units of mM<sup>-1</sup> S<sup>-1</sup>:

$$(1/T_1)_{\text{obs}} = (1/T_1)_d + r_1[M]$$

where,  $(1/T_1)_{\text{obs}}$  and  $(1/T_1)_d$  are the observed values in the presence and absence of the paramagnetic species ( $\beta$ -NaGdF<sub>4</sub>: Yb<sup>3+</sup>, Er<sup>3+</sup>) and  $[M]$  is the concentration of the  $\beta$ -NaGdF<sub>4</sub>: Yb<sup>3+</sup>, Er<sup>3+</sup> nanorods.

To investigate the contrast enhancement effect, the  $T_1$ -weighted magnetic resonance images were acquired at RT using a 3 T Philips MR scanner using Standard Spin-Echo (SE) sequence. Various concentrations of samples (0, 0.05, 0.25, 0.5, 0.8 mM) in water were placed in a series of 2 mL tubes for  $T_1$ -weighted MRI images. The following parameters were adopted: repetition time (TR) = 500 ms, echo time (TE) = 9.4 ms, matrix size = 128 pixels  $\times$  128 pixels, field of view (FOV) = 90, number of signal averages = 2, and slice thickness = 3 mm.

#### **4.2.5. Characterization techniques**

The phase purity and crystallinity of the as-prepared samples were characterized by X-ray diffraction (XRD) using a PANalytical X'PERT PRO instrument and the iron-filtered Cu- $K_{\alpha}$  radiation ( $\lambda = 1.5406 \text{ \AA}$ ) in the  $2\theta$  range of  $10\text{-}80^{\circ}$  with a step size of  $0.02^{\circ}$ . To further confirm the crystalline phase and formation of composite material, Raman spectroscopy measurements were recorded at room temperature on an HR 800 Raman spectrophotometer (Jobin Yvon, Horiba, France) equipped with achromatic Czerny-Turner type monochromator (800 mm focal-length) with silver treated mirrors. Monochromatic radiation emitted by a He-Ne laser (633 nm) and 325 nm laser, operating at 20 mW was used. A detector with accuracy in the range between 450 and 850 nm of  $\pm 1 \text{ cm}^{-1}$ , equipped with thermoelectrically cooled (with Peltier junctions), multi-channel, spectroscopic grade charge coupled detector ( $1024 \times 256$  pixels of  $26 \text{ }\mu\text{m}$ ) with dark current lower than  $0.002 \text{ electrons pixel}^{-1} \text{ s}^{-1}$  was used. To analyze the morphology of the samples, field emission scanning electron microscopy (FESEM: Hitachi S-4200) was done. Energy-dispersive X-ray analysis (EDXA) of the samples was performed during field emission scanning electron microscopy measurements to obtain the elemental composition of the samples. The specific structure details, morphology, and size were obtained by using FEI Tecnai F30 high resolution transmission electron microscope (HRTEM) equipped with a super-twin lens (s-twin) operated at 300 keV accelerating voltage with Schottky field emitter source with maximum beam current ( $> 100 \text{ nA}$ ) and small energy spread (0.8 eV or less). The point-to-point resolution of the microscope is 0.20 nm and line resolution of 0.102 nm with a spherical aberration of 1.2 mm and chromatic aberration of 1.4 mm with  $70 \text{ }\mu\text{m}$  objective aperture size. The powder samples

obtained were dispersed in ethanol and then drop-casted on carbon-coated copper TEM grids with 200 mesh and loaded to a single tilt sample holder.

The optical properties of the as-synthesized samples were investigated by a Jasco UV-vis-NIR (Model V570) dual beam spectrometer operated at a resolution of 2 nm. The up-conversion emission spectra were obtained using an ACTON SP2300 spectrometer attached to a PMT under 980 nm CW diode laser excitations. Lifetime measurements were carried by using an Edinburgh Instruments FLSP 920 system, having a 60 W microsecond flash lamp as the excitation source under 980 nm pulse laser excitation. Brunauer–Emmett–Teller (BET) surface area and porosity analysis were measured by using Quantachrome surface area analyzer under N<sub>2</sub> atmosphere. Fourier transform infrared spectrum (FTIR) was recorded by FTIR – 8300 Fourier transform infrared spectrophotometer (SHIMADZU). Magnetic property measurements of samples were performed using VSM (Vibrating Sample Magnetometer) attachment physical property measurement system (PPMS) from Quantum Design Inc., San Diego, CA, equipped with a 9 T superconducting magnet. For dc magnetic measurements, the samples were precisely weighed and packed inside a plastic sample holder which fit into a brass sample holder with negligible contribution in the overall magnetic signal. The M–H loops were collected at a rate of 75 Oe/s in a field sweep from –40 to 40 kOe at the vibrating frequency of 40 Hz. Current–voltage characteristics were calculated by irradiating the cell with 100 mW/cm<sup>2</sup> (450 W xenon lamp, Oriel instrument); 1 sun AM 1.5 G filter was used to simulate the solar spectrum. The active area of the cell was 0.5 cm<sup>2</sup>. The photocurrent was measured by using a Series 2400 Source Measure Unit from Keithley Instruments, Inc., Cleveland, Ohio.

### 4.3. Result and discussion

#### 4.3.1. Phase and morphology characterization

The composition, crystallinity and phase purity of the as-prepared samples were first examined by XRD. The Figure 1 compares, typical XRD patterns of the as-synthesized (1) NaGdF<sub>4</sub>: 18 % Yb<sup>3+</sup>, 2 % Er<sup>3+</sup>, (2) TiO<sub>2</sub>, and (3) NaGdF<sub>4</sub>: 18 % Yb<sup>3+</sup>, 2 % Er<sup>3+</sup>/ TiO<sub>2</sub> nanocomposite. The sharp diffraction peaks of the NaGdF<sub>4</sub>: 18 % Yb<sup>3+</sup>, 2 % Er<sup>3+</sup> (Figure 1 (a)) can be indexed to the pure hexagonal phase  $\beta$ -NaGdF<sub>4</sub> (space group:  $P6_3/m$ ). The calculated lattice parameters are  $a = 6.0 \text{ \AA}$ ,  $c = 3.6 \text{ \AA}$ , which is in good agreement with the reported data (JCPDS no. 27-0699). The absence of any secondary phase in the XRD patterns indicates the high purity of as-prepared samples. This also reveals that, the Yb<sup>3+</sup> and Er<sup>3+</sup> ions have been effectively doped into the  $\beta$ -NaGdF<sub>4</sub> host lattice. The diffraction peaks of the TiO<sub>2</sub> (Figure 1 (b)) can be indexed to pure anatase phase (space group:  $I4_1$ ). The calculated lattice parameters are  $a = 3.7 \text{ \AA}$ ,  $c = 9.5 \text{ \AA}$ , which are consistent with reported data (JCPDS no. 89-4921). As shown in the XRD pattern of  $\beta$ -NaGdF<sub>4</sub>: 18 % Yb<sup>3+</sup>, 2 % Er<sup>3+</sup>/ TiO<sub>2</sub> nanocomposite (Figure 1 (c)), the characteristic diffraction peaks of anatase phase TiO<sub>2</sub> are observed, and also the  $\beta$ -NaGdF<sub>4</sub>: 18 % Yb<sup>3+</sup>, 2 % Er<sup>3+</sup> still maintains the pure hexagonal phase structure.

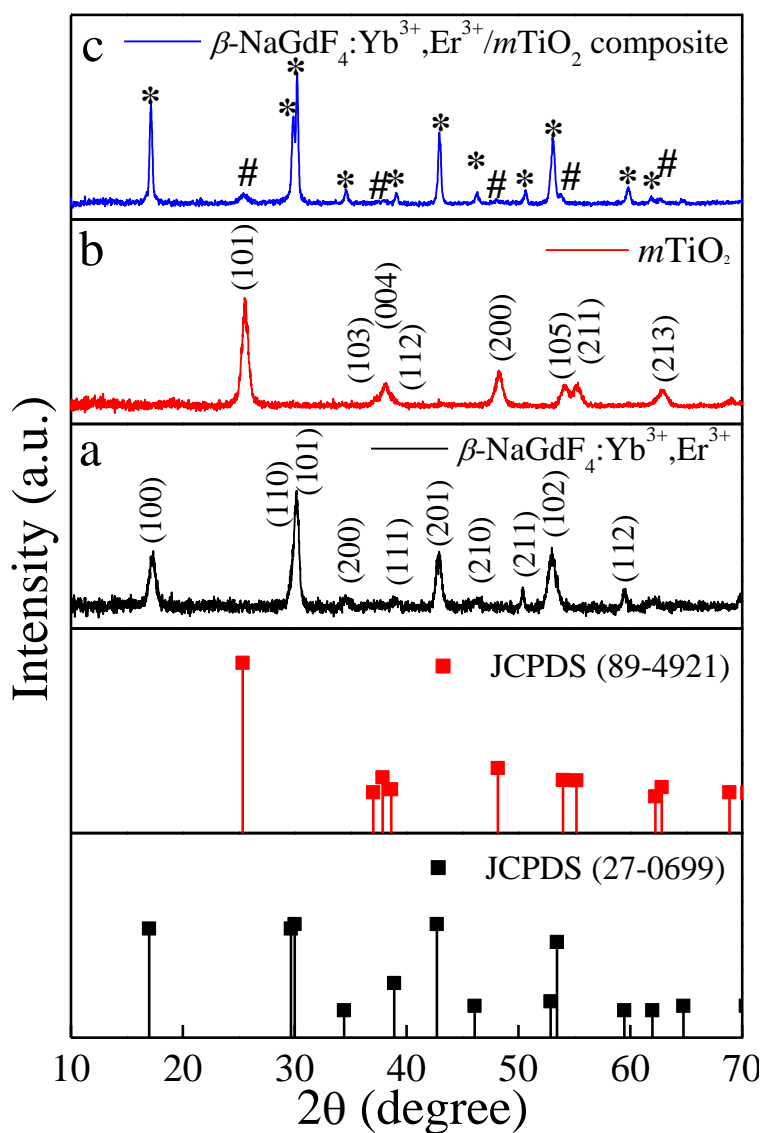


**Figure 1:** The XRD patterns of (a) Pure  $\beta$ -NaGdF<sub>4</sub>:Yb<sup>3+</sup>,Er<sup>3+</sup> (b) Pure  $m$ TiO<sub>2</sub>, and (c)  $\beta$ -NaGdF<sub>4</sub>:Yb<sup>3+</sup>,Er<sup>3+</sup>/ $m$ TiO<sub>2</sub> nanocomposite and the standard data of hexagonal  $\beta$ -NaGdF<sub>4</sub> (JCPDS- 27-0699) and anatase TiO<sub>2</sub> (JCPDS- 89-4921) as a reference. The nanocomposite exhibits diffraction peaks of both  $\beta$ -NaGdF<sub>4</sub>:Yb<sup>3+</sup>, Er<sup>3+</sup> (\*) and  $m$ TiO<sub>2</sub> (#).

The size, shape and structure of the as-prepared samples were characterized by FESEM and TEM (Figures 2 and 3). As shown in Figures 2 (a) and 3 (a),  $\beta$ -NaGdF<sub>4</sub>: 18 % Yb<sup>3+</sup>, 2 % Er<sup>3+</sup> crystals possess highly monodispersed rod-shape structure with an average

diameter  $\sim$  100 nm and length of  $\sim$  300 nm. The TiO<sub>2</sub> particles have quasi-spherical structure with average size of  $\sim$  40 nm (Figures 2 (b) and 3 (b)). The images of  $\beta$ -NaGdF<sub>4</sub>: 18 % Yb<sup>3+</sup>, 2 % Er<sup>3+</sup>/ mTiO<sub>2</sub> nanocomposite (Figures 2 (c) and 3 (c)) possesses TiO<sub>2</sub> nanoparticles dispersed around the  $\beta$ -NaGdF<sub>4</sub>: 18 % Yb<sup>3+</sup>, 2 % Er<sup>3+</sup> nanorods.

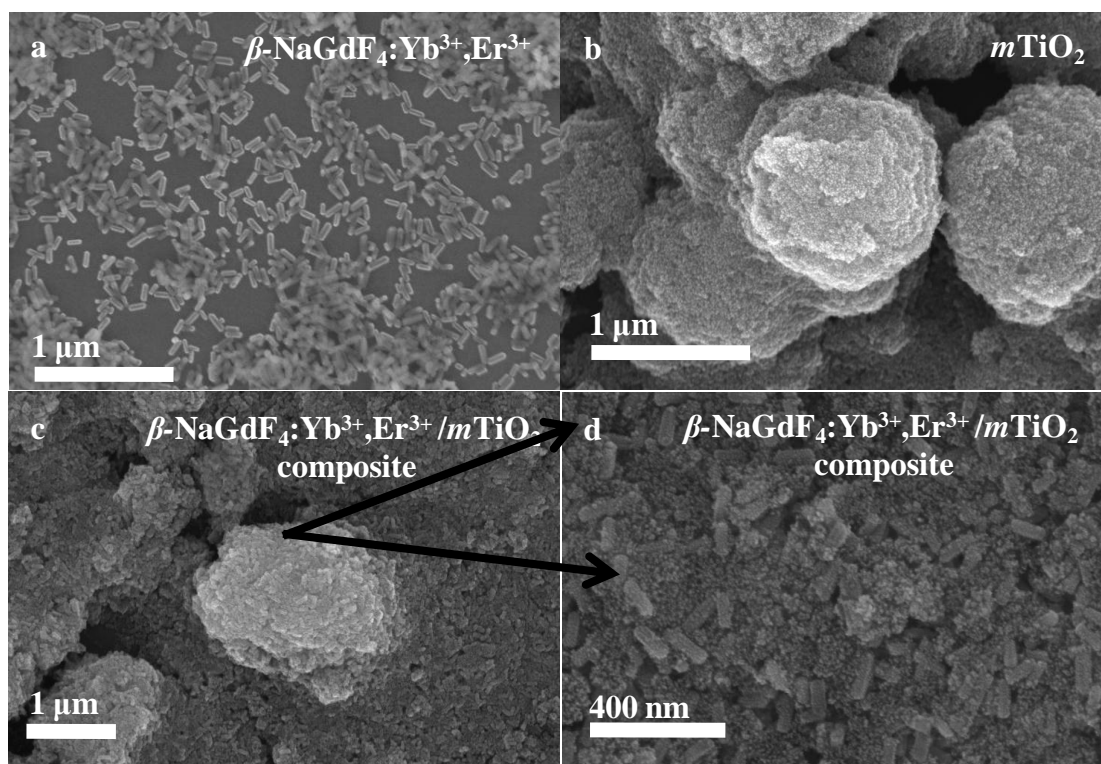


**Figure 2:** The FESEM images of (a)  $\beta$ -NaGdF<sub>4</sub>:Yb<sup>3+</sup>,Er<sup>3+</sup> (b) mTiO<sub>2</sub>, (c)  $\beta$ -NaGdF<sub>4</sub>:Yb<sup>3+</sup>,Er<sup>3+</sup> /mTiO<sub>2</sub> nanocomposite, and (d) Zoom view of the image (c) shown by arrows.

The high resolution TEM (HRTEM) images of  $\beta$ -NaGdF<sub>4</sub>: 18 % Yb<sup>3+</sup>, 2 % Er<sup>3+</sup> (Figure 3 (d)), TiO<sub>2</sub> (Figure 3 (e)) and  $\beta$ -NaGdF<sub>4</sub>: 18 % Yb<sup>3+</sup>, 2 % Er<sup>3+</sup>/ TiO<sub>2</sub> nanocomposite (Figure 3 (f)) reveal highly crystalline nature of the as-prepared products which is consequent with the XRD patterns. The lattice fringes with interplanar spacing of 0.18 nm and 0.21 nm were ascribed to (200) and (201) planes of anatase TiO<sub>2</sub> nanoparticles and hexagonal phase  $\beta$ -

NaGdF<sub>4</sub>: 18 % Yb<sup>3+</sup>, 2 % Er<sup>3+</sup> nanorods, respectively. The HRTEM image of  $\beta$ -NaGdF<sub>4</sub>: 18 % Yb<sup>3+</sup>, 2 % Er<sup>3+</sup>/ *m*TiO<sub>2</sub> nanocomposite shows lattice fringes from both *m*TiO<sub>2</sub> nanoparticles ( $d(004) = 0.23$  nm) and  $\beta$ -NaGdF<sub>4</sub>: 18 % Yb<sup>3+</sup>, 2 % Er<sup>3+</sup> nanorods ( $d(101) = 0.29$  nm).

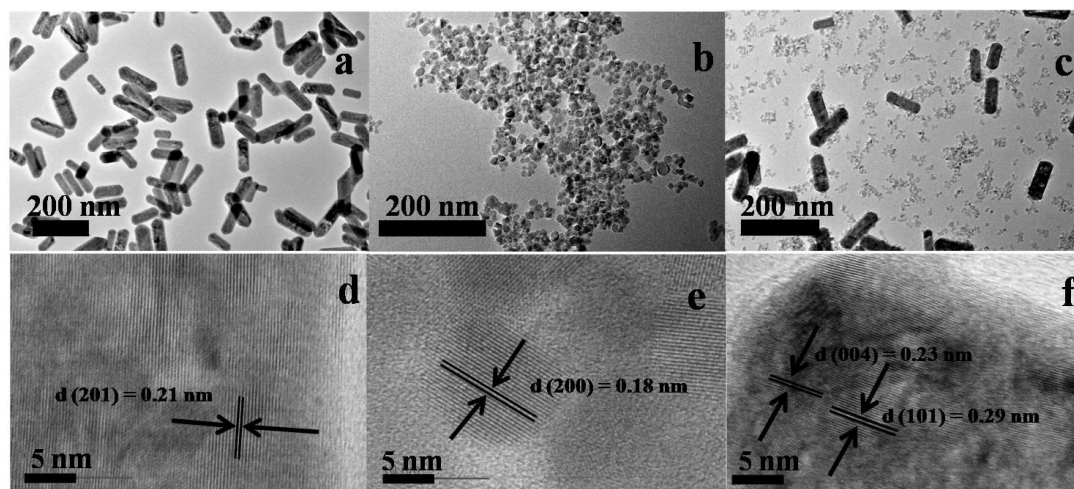


**Figure 3:** The TEM images of (a) Pure  $\beta$ -NaGdF<sub>4</sub>:Yb<sup>3+</sup>, Er<sup>3+</sup> (b) Pure *m*TiO<sub>2</sub>, (c)  $\beta$ -NaGdF<sub>4</sub>:Yb<sup>3+</sup>, Er<sup>3+</sup>/*m*TiO<sub>2</sub> nanocomposite. (d, e, f) are corresponding HRTEM images. The TEM image of nanocomposite clearly shows *m*TiO<sub>2</sub> nanoparticles distributed on and around  $\beta$ -NaGdF<sub>4</sub>:Yb<sup>3+</sup>, Er<sup>3+</sup> nanorods. The nanocomposite is highly crystalline and possesses fringes of both  $\beta$ -NaGdF<sub>4</sub>:Yb<sup>3+</sup>, Er<sup>3+</sup> nanorods and TiO<sub>2</sub> nanospheres.

The EDX elemental analysis of the  $\beta$ -NaGdF<sub>4</sub>: 18 % Yb<sup>3+</sup>, 2 % Er<sup>3+</sup>/*m*TiO<sub>2</sub> nanocomposite (Figure 4) shows that the Na, Gd, F, Yb, Er, Ti and O were detected in the nanocomposite.



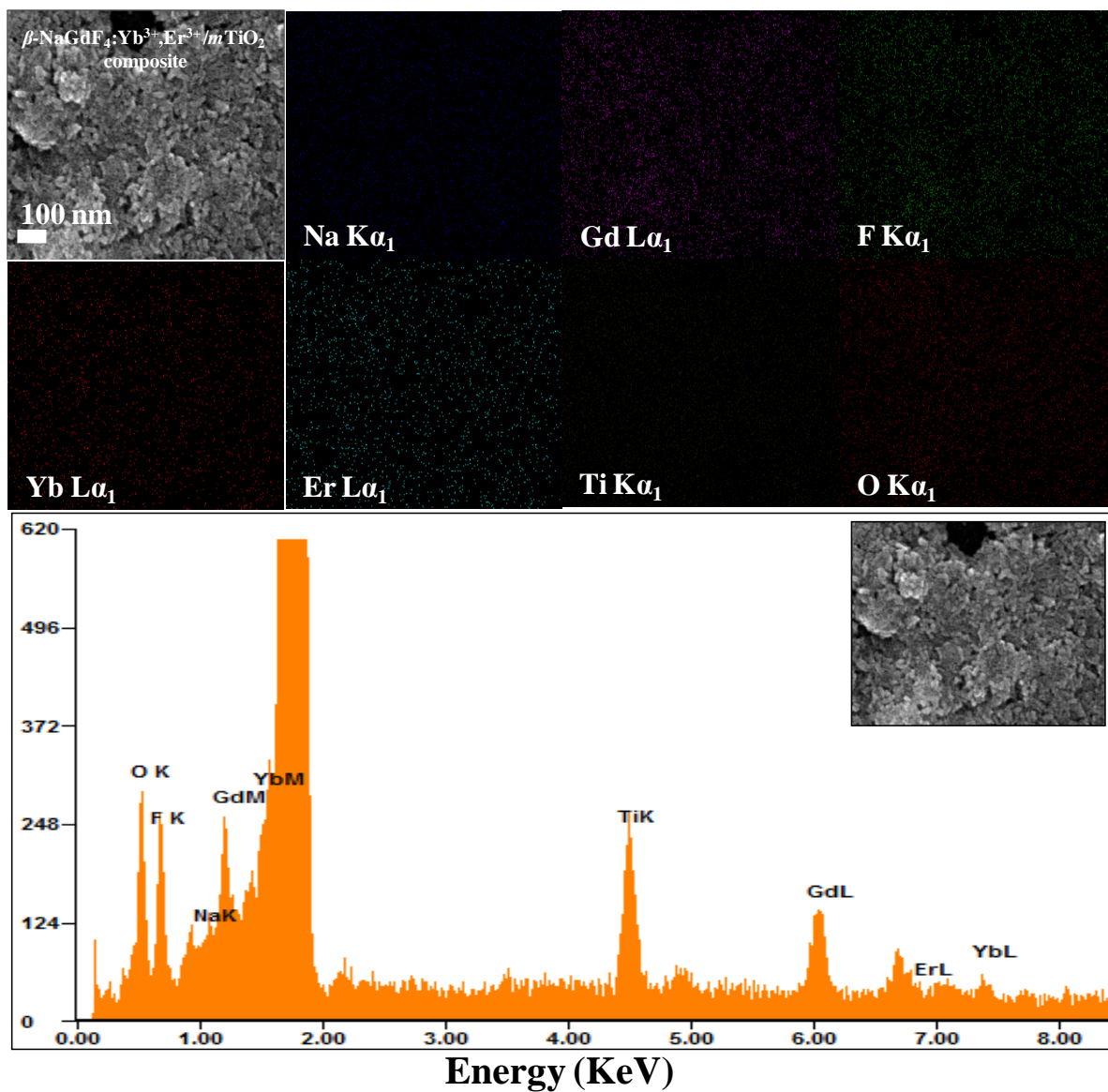


**Figure 4:** Element mapping and EDAX spectrum of the  $\beta$ -NaGdF<sub>4</sub>:Yb<sup>3+</sup>, Er<sup>3+</sup> /mTiO<sub>2</sub> nanocomposite.

### 4.3.2. Surface properties

#### 4.3.2.1. Surface functionalization

The surfaces-capping of upconverting  $\beta$ -NaGdF<sub>4</sub>: Yb<sup>3+</sup>, Er<sup>3+</sup> nanorods was done in situ (during the synthesis itself) by using a cationic polymer, polyethyleneimine (PEI). The polyethyleneimine is a stable, water dispersible and biocompatible polymer and thus considered as a versatile effective polymer for drug delivery applications.<sup>46, 47</sup> The surface properties of PEI-coated  $\beta$ -NaGdF<sub>4</sub>: Yb<sup>3+</sup>, Er<sup>3+</sup> samples were studied by Zeta potential and FTIR. The  $\zeta$ -potential of  $\beta$ -NaGdF<sub>4</sub>: Yb<sup>3+</sup>, Er<sup>3+</sup> nanorods in the aqueous medium (pH=7) was measured to be + 45 mV, indicating the successful capping of PEI. Owing to the presence of free amino group at the surface, the nanorods were readily dispersed in water to form a stable and visibly transparent suspension. The  $\zeta$ -potentials of as-prepared *m*TiO<sub>2</sub> and PEI-capped  $\beta$ -NaGdF<sub>4</sub>:Yb<sup>3+</sup>, Er<sup>3+</sup>/*m*TiO<sub>2</sub> nanocomposite were determined to be + 31 mV and + 24 mV respectively.

Figure 5 shows the FTIR spectrum of amine functionalized  $\beta$ -NaGdF<sub>4</sub>:Yb<sup>3+</sup>, Er<sup>3+</sup>, pristine *m*TiO<sub>2</sub> and PEI-capped  $\beta$ -NaGdF<sub>4</sub>:Yb<sup>3+</sup>, Er<sup>3+</sup>/*m*TiO<sub>2</sub> nanocomposite. The PEI capped  $\beta$ -NaGdF<sub>4</sub>:Yb<sup>3+</sup>, Er<sup>3+</sup> nanorods exhibited two weak absorption bands (Figure 5 (a)) at 2924 cm<sup>-1</sup> and 2857 cm<sup>-1</sup> corresponding to asymmetric and symmetric stretching vibrations of C-H bond respectively. The IR-bands centered at 1630 cm<sup>-1</sup> and 1382 cm<sup>-1</sup> were observed, which can be attributed to the N-H bending mode of amino group (-NH<sub>2</sub>) and N-H stretching vibration of amide bonds, thereby revealing the capping of PEI on the surface of nanorods.<sup>48</sup> Meanwhile, the sharp absorption bands centered at 1528 cm<sup>-1</sup> were attributed to the free amine groups present on the surface of nanorods.<sup>50</sup>

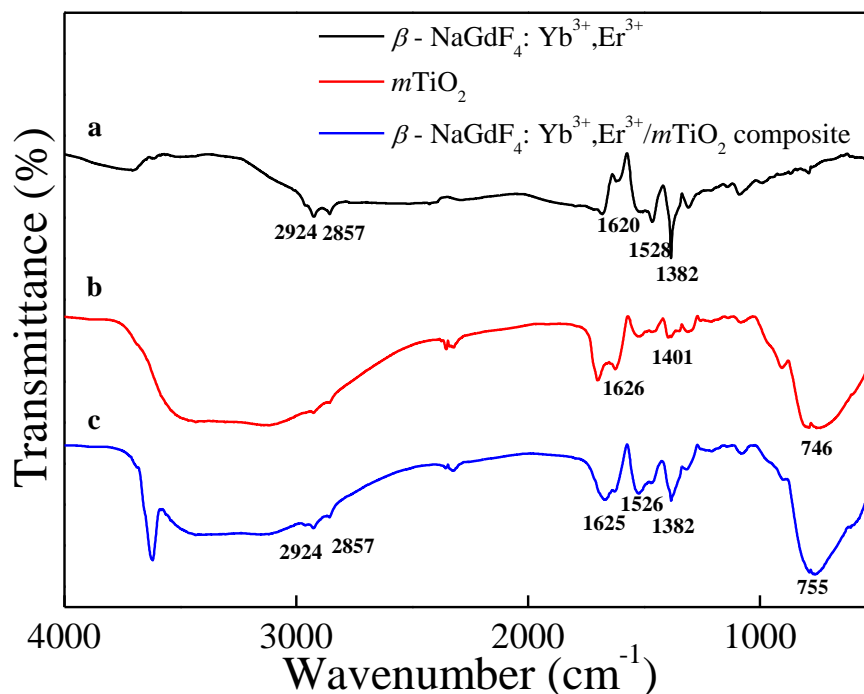


**Figure 5:** The comparative FT-IR spectra of (a)  $\beta$ -NaGdF<sub>4</sub>:Yb<sup>3+</sup>,Er<sup>3+</sup> (b)  $m$ TiO<sub>2</sub>, (c)  $\beta$ -NaGdF<sub>4</sub>:Yb<sup>3+</sup>,Er<sup>3+</sup> / $m$ TiO<sub>2</sub> nanocomposite. The FTIR spectrum of nanocomposite exhibits absorption bands of amine group vibrations as well as Ti-O-Ti vibrations.

The band located at 746 cm<sup>-1</sup> is due to titanium oxide (Figure 5 (b)) and is assigned to Ti-O-Ti stretching vibration. The absorption band at 1401 cm<sup>-1</sup> is attributed to the lattice vibrations of TiO<sub>2</sub>. The sharp absorption band centered at 1626 cm<sup>-1</sup> is due to bending vibration of Ti-OH.<sup>51</sup> Figure 5 (c), shows FTIR spectrum of  $\beta$ -NaGdF<sub>4</sub>: Yb<sup>3+</sup>, Er<sup>3+</sup>/  $m$ TiO<sub>2</sub> nanocomposite, which clearly exhibits the absorption band at 1382 cm<sup>-1</sup> for amide bond vibrations characteristic of amine functionalized  $\beta$ -NaGdF<sub>4</sub> and also the absorption band centered at 755 cm<sup>-1</sup> for Ti-O-Ti vibration characteristic of pristine TiO<sub>2</sub>.

#### 4.3.2.2. Surface area and porosity

The Brunauer–Emmett–Teller (BET) specific surface area and porosity of TiO<sub>2</sub> was investigated by using the N<sub>2</sub> adsorption–desorption isotherm analysis. As shown in Figure 6, the as-prepared TiO<sub>2</sub> exhibited a typical IV isotherm with H<sub>2</sub> type hysteresis loop and indicating the presence of mesoporous structure according to the IUPAC classification, generated from the capillary condensation in mesopores.<sup>52, 53</sup> Using multipoint BET method, the measured BET specific surface area values of TiO<sub>2</sub> found to be  $\sim 100 \text{ m}^2 \text{ g}^{-1}$ , and pore size  $\sim 3.8 \text{ nm}$ . Herein, we can therefore conclude that, the as-prepared TiO<sub>2</sub> is mesoporous in nature (*m*TiO<sub>2</sub>). The mesoporous materials are advantageous due to their distinctive properties such as high surface area and uniform pore size distribution, which is beneficial for applications in photocatalysis and solar cells.

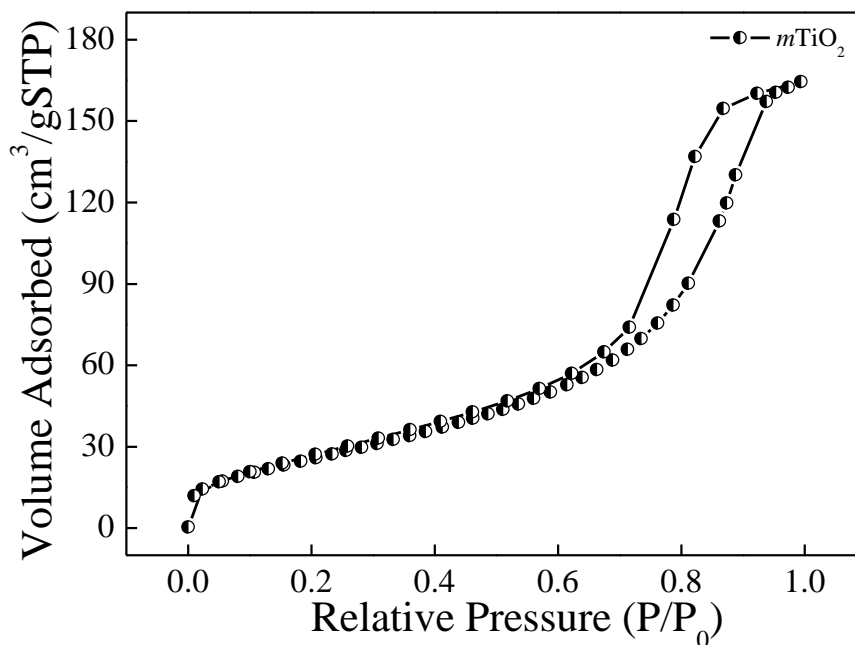


**Figure 6:** Nitrogen adsorption–desorption isotherms of as prepared TiO<sub>2</sub>.

### 4.3.2.3. Phonon modes

To further explore the local structure of  $\beta$ -NaGdF<sub>4</sub>: Yb<sup>3+</sup>, Er<sup>3+</sup>/mTiO<sub>2</sub> nanocomposite, Raman spectroscopy was used to analyze the vibrational properties of the sample. Figure 7 (A), shows the comparative Raman spectra of  $\beta$ -NaGdF<sub>4</sub>: Yb<sup>3+</sup>, Er<sup>3+</sup>, mTiO<sub>2</sub> and  $\beta$ -NaGdF<sub>4</sub>: Yb<sup>3+</sup>, Er<sup>3+</sup>/mTiO<sub>2</sub> nanocomposite. The Raman spectra of these samples have been recorded under two laser excitation lines; 633 nm and 325 nm. For pristine TiO<sub>2</sub>, 633 nm and for pristine  $\beta$ -NaGdF<sub>4</sub>: Yb<sup>3+</sup>, Er<sup>3+</sup> 325 nm excitation is used. Raman spectra of  $\beta$ -NaGdF<sub>4</sub>: Yb<sup>3+</sup>, Er<sup>3+</sup>/mTiO<sub>2</sub> nanocomposite was studied under both 633 nm and 325 nm excitations.

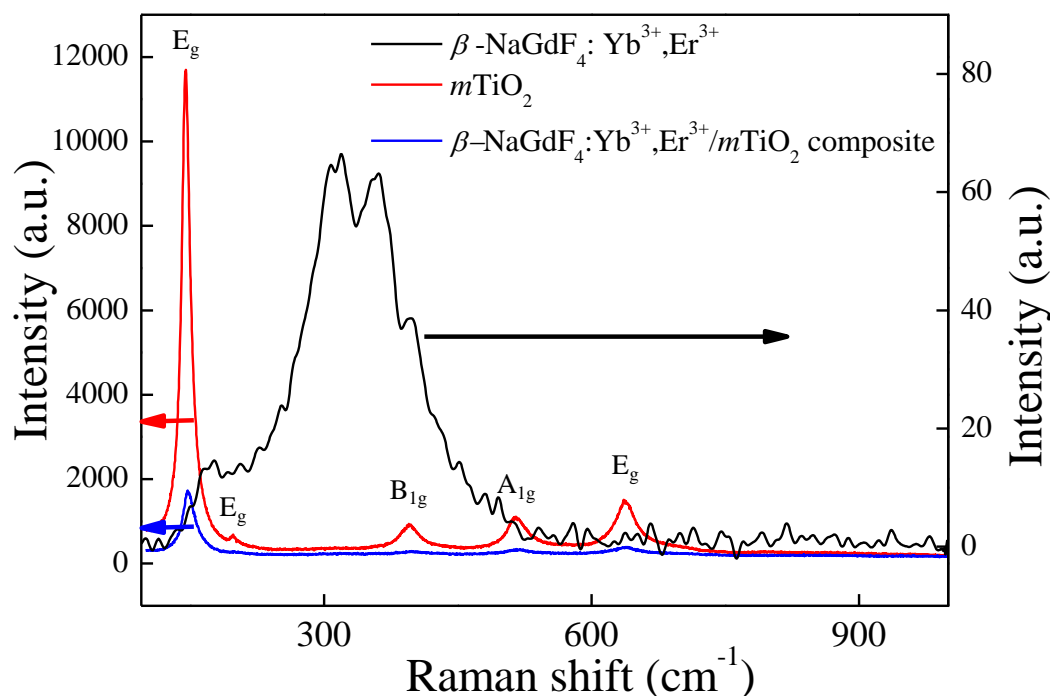


**Figure 7 (A):** The comparative Raman spectra of  $\beta$ -NaGdF<sub>4</sub>:Yb<sup>3+</sup>, Er<sup>3+</sup>, mTiO<sub>2</sub> and  $\beta$ -NaGdF<sub>4</sub>:Yb<sup>3+</sup>, Er<sup>3+</sup>/mTiO<sub>2</sub> nanocomposite.

The Raman spectra of TiO<sub>2</sub> clearly exhibit six Raman bands at 144 cm<sup>-1</sup> (E<sub>g</sub>), 197 cm<sup>-1</sup> (E<sub>g</sub>), 396 cm<sup>-1</sup> (B<sub>1g</sub>), 514 cm<sup>-1</sup> (A<sub>1g</sub>), 519 cm<sup>-1</sup> (B<sub>1g</sub>), and 638 cm<sup>-1</sup> (E<sub>g</sub>) characteristics of

pure anatase phase TiO<sub>2</sub>.<sup>13</sup> The Raman spectra of  $\beta$ -NaGdF<sub>4</sub>: Yb<sup>3+</sup>, Er<sup>3+</sup> revealed phonon bands of NaGdF<sub>4</sub>. The strongest phonon modes were observed at  $\sim 308$ ,  $\sim 319$ ,  $\sim 359$ ,  $\sim 400$  cm<sup>-1</sup>, which are in fair agreement with the reported values for NaLnF<sub>4</sub>.<sup>54, 43</sup> These Raman bands are attributed to the host lattice vibrations of Gd-F and Na-F distances, bond strength and vibration features.<sup>55</sup> The average weighted position of the band system was observed to be  $\sim 347$  cm<sup>-1</sup>. This corresponding phonon energy is low as compare to other fluoride host lattices such as LiYF<sub>4</sub> (570 cm<sup>-1</sup>)<sup>56</sup>, suggesting the fact that NaGdF<sub>4</sub> is an efficient host lattice for enhanced up-conversion luminescence. The Raman spectra of  $\beta$ -NaGdF<sub>4</sub>: Yb<sup>3+</sup>, Er<sup>3+</sup>/*m*TiO<sub>2</sub> nanocomposite at excitation wavelength line 633 nm, also exhibit characteristic Raman bands of anatase TiO<sub>2</sub>. At excitation wavelength line 325 nm as shown in Figure 7 (B), the characteristic Raman bands of NaGdF<sub>4</sub> and anatase TiO<sub>2</sub> overlapped rendering a broad band between 150 and 450 cm<sup>-1</sup>. The 519 cm<sup>-1</sup> (B<sub>1g</sub>), and 638 cm<sup>-1</sup> (E<sub>g</sub>) Raman bands of TiO<sub>2</sub> are slightly shifted to higher wavenumbers.

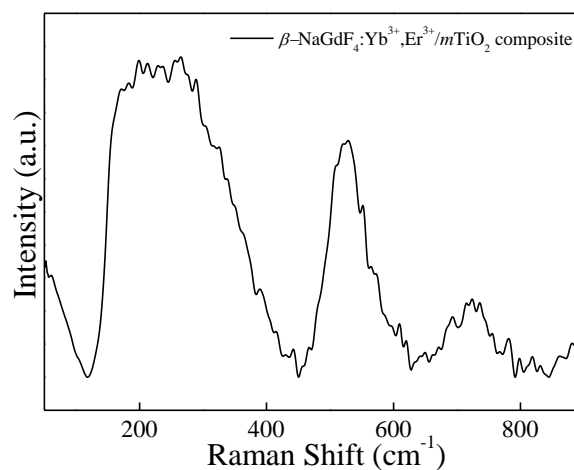


**Figure 7 (B):** The Raman spectra of  $\beta$ -NaGdF<sub>4</sub>:Yb<sup>3+</sup>, Er<sup>3+</sup> /*m*TiO<sub>2</sub> nanocomposite at excitation wavelength line 325 nm.

### 4.3.3. Optical properties

#### 4.3.3.1. UV-vis-NIR absorption spectra analysis

The typical UV-vis-NIR absorption spectra of  $\beta$ -NaGdF<sub>4</sub>: Yb<sup>3+</sup>, Er<sup>3+</sup>, *m*TiO<sub>2</sub> and  $\beta$ -NaGdF<sub>4</sub>: Yb<sup>3+</sup>, Er<sup>3+</sup>/*m*TiO<sub>2</sub> nanocomposite are compared in Figure 8. The absorption spectra of  $\beta$ -NaGdF<sub>4</sub>: Yb<sup>3+</sup>, Er<sup>3+</sup> show the relatively wide absorption range of ~ 100 nm at the NIR region ~ 980 nm, corresponds to the absorption of Yb<sup>3+</sup>. This large absorption cross section from about 900 to 1100 nm, overlaps one of the maximum NIR energy distribution ranges of sunlight. The pure *m*TiO<sub>2</sub> exhibits an absorption edge at ~ 400 nm corresponding to its bandgap and also exhibits weak absorption in visible region upto about 600 nm. This visible light absorption is due to the carbon doping into the TiO<sub>2</sub> lattice during calcinations; wherein the titanium butoxide precursor serves as a carbon source, which contributes to the mid-band gap electronic states in TiO<sub>2</sub>.<sup>57, 58</sup> When *m*TiO<sub>2</sub> was combined with  $\beta$ -NaGdF<sub>4</sub>: Yb<sup>3+</sup>, Er<sup>3+</sup>, the  $\beta$ -NaGdF<sub>4</sub>: Yb<sup>3+</sup>, Er<sup>3+</sup>/*m*TiO<sub>2</sub> nanocomposite represented a combination of strong UV absorption and weak visible absorption (due to TiO<sub>2</sub>) alongwith the NIR light absorption band (due to  $\beta$ -NaGdF<sub>4</sub>: Yb<sup>3+</sup>, Er<sup>3+</sup>) at ~ 980 nm.

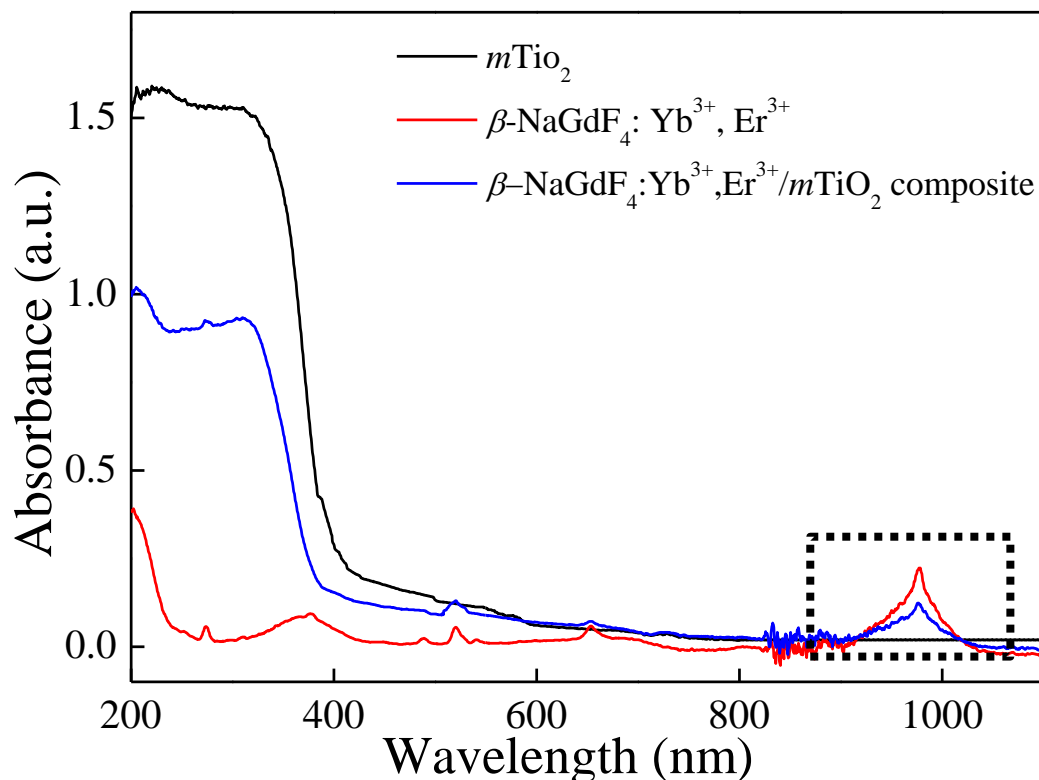


**Figure 8:** The UV-vis-NIR absorption spectra of  $\beta\text{-NaGdF}_4:\text{Yb}^{3+}, \text{Er}^{3+}$ ,  $m\text{TiO}_2$ , and  $\beta\text{-NaGdF}_4:\text{Yb}^{3+}, \text{Er}^{3+}/m\text{TiO}_2$  nanocomposite. Pure  $\beta\text{-NaGdF}_4:\text{Yb}^{3+}, \text{Er}^{3+}$  and  $\beta\text{-NaGdF}_4:\text{Yb}^{3+}, \text{Er}^{3+}/m\text{TiO}_2$  nanocomposite shows sharp absorption band at 980 nm.

Therefore, from the UV-vis-NIR absorption spectra it can be speculated that after absorbing the NIR photons,  $\beta\text{-NaGdF}_4:\text{Yb}^{3+}, \text{Er}^{3+}$  can emit UV and visible light via up-conversion process that can be absorbed by anatase  $\text{TiO}_2$  which are dispersed around  $\beta\text{-NaGdF}_4:\text{Yb}^{3+}, \text{Er}^{3+}$  via an energy transfer between them. These characters indicate that the material can definitely enhance the utilization rate of solar energy in photocatalysis as well as in solar cells.



#### 4.3.3.2. Up-conversion static luminescence properties of the nanocomposite

The Yb<sup>3+</sup>, Er<sup>3+</sup> co-doped phosphors based on hexagonal phase fluoride host matrix show most efficient green and blue up-conversion luminescence.<sup>37</sup> The up-conversion process involves conversion of low energy photons to higher energy photon through sequential absorption of two or more photons and energy transfer. The energy separation of the <sup>2</sup>F<sub>7/2</sub> ground state of Yb<sup>3+</sup> and its <sup>2</sup>F<sub>5/2</sub> excited state matches well the transition energy between the <sup>4</sup>I<sub>11/2</sub> and <sup>4</sup>I<sub>15/2</sub> states and also the <sup>4</sup>F<sub>7/2</sub> and <sup>4</sup>I<sub>11/2</sub> states of Er<sup>3+</sup>, thus allowing for efficient (quasi-) resonant energy transfer between the two ions.<sup>37</sup> The Figure 9 compares the up-conversion photoluminescence (PL) spectra of  $\beta$ -NaGdF<sub>4</sub>: 18 % Yb<sup>3+</sup>, 2 % Er<sup>3+</sup>, *m*TiO<sub>2</sub>, and  $\beta$ -NaGdF<sub>4</sub>: 18 % Yb<sup>3+</sup>, 2 % Er<sup>3+</sup>/ *m*TiO<sub>2</sub> nanocomposite under 980 nm laser excitation and fluorescence spectrum of *m*TiO<sub>2</sub> at 380 nm excitation. It can be evidently seen that, in  $\beta$ -NaGdF<sub>4</sub>: 18 % Yb<sup>3+</sup>, 2 % Er<sup>3+</sup> and NaGdF<sub>4</sub>: 18 % Yb<sup>3+</sup>, 2 % Er<sup>3+</sup>/ *m*TiO<sub>2</sub> nanocomposite samples, the peak-positions in the emission spectra remain similar, and the bands differ only in their relative intensities. The emission spectrum monitored under the excitation of 980 nm NIR laser,  $\beta$ -NaGdF<sub>4</sub>: 18 % Yb<sup>3+</sup>, 2 % Er<sup>3+</sup> emits intense green up-conversion luminescence. The spectra display four distinct Er<sup>3+</sup> emission bands. The weak violet emission peak at ~ 408 nm is assigned to electronic transition from <sup>2</sup>H<sub>9/2</sub> → <sup>4</sup>I<sub>15/2</sub>. The emission peaks at ~ 521 and ~ 540 nm in the green region are assigned to transitions from <sup>2</sup>H<sub>11/2</sub> and <sup>4</sup>S<sub>3/2</sub> to <sup>4</sup>I<sub>15/2</sub>. The red emission peak at ~ 655 nm, results from <sup>4</sup>F<sub>9/2</sub> → <sup>4</sup>I<sub>15/2</sub> transition.<sup>59</sup> Furthermore, both the samples exhibit a strong green-to-red emission ratio. The *m*TiO<sub>2</sub> rendered fluorescence emission band at ~ 532 nm and a small shoulder at ~ 445 nm respectively under 380 nm excitation, and when the emission spectrum of *m*TiO<sub>2</sub> was monitored under the excitation of 980 nm NIR laser, no emission band is observed. This means that, the up-conversion

luminescence in  $\beta$ -NaGdF<sub>4</sub>:Yb<sup>3+</sup>, Er<sup>3+</sup> /*m*TiO<sub>2</sub> nanocomposite under 980 nm excitation is truly from  $\beta$ -NaGdF<sub>4</sub>:Yb<sup>3+</sup>, Er<sup>3+</sup> component.

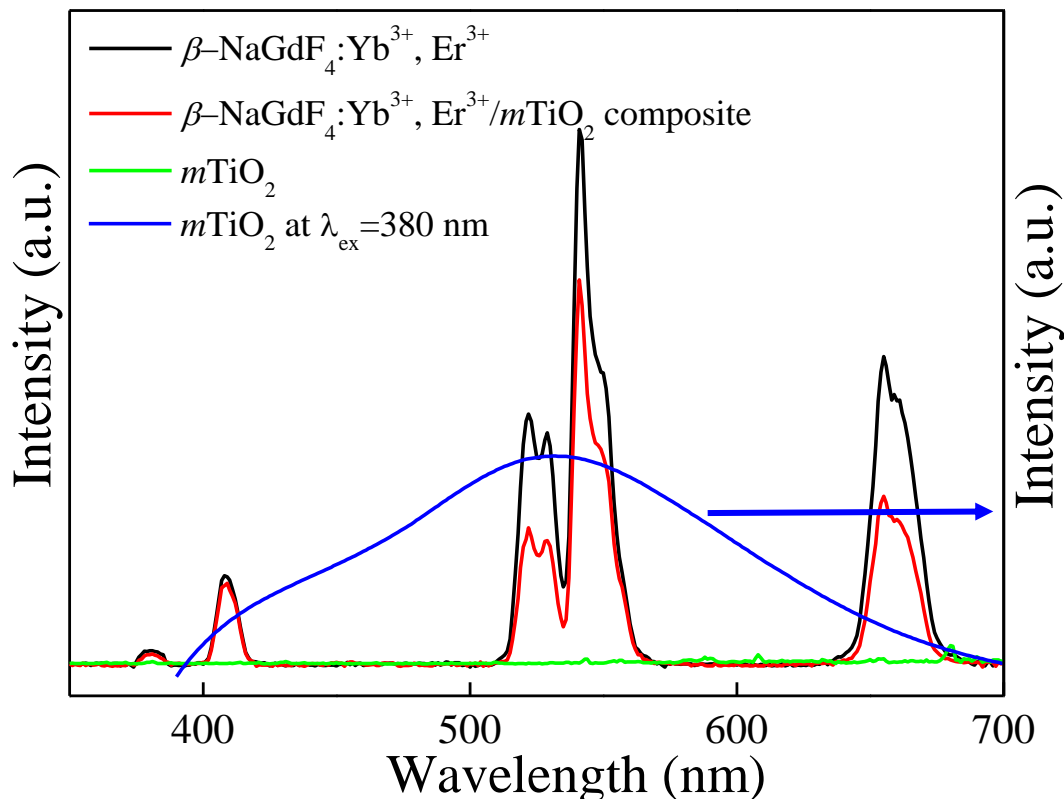


**Figure 9:** The comparison of static photoluminescence spectra of  $\beta$ -NaGdF<sub>4</sub>:Yb<sup>3+</sup>, Er<sup>3+</sup>, *m*TiO<sub>2</sub>, and  $\beta$ -NaGdF<sub>4</sub>:Yb<sup>3+</sup>, Er<sup>3+</sup> /*m*TiO<sub>2</sub> nanocomposite under  $\lambda_{\text{ex}} = 980$  nm laser excitation and fluorescence spectra of *m*TiO<sub>2</sub> under  $\lambda_{\text{ex}} = 380$  nm.

The emission intensities of the  $\beta$ -NaGdF<sub>4</sub>: 18 % Yb<sup>3+</sup>, 2 % Er<sup>3+</sup> / *m*TiO<sub>2</sub> nanocomposite decrease to certain degree in comparison with the pristine up-conversion spectrum of  $\beta$ -NaGdF<sub>4</sub>: 18 % Yb<sup>3+</sup>, 2 % Er<sup>3+</sup>. The calculated light emission intensity ratios of the emission peak at 521 nm, 540 nm, and 655 nm of pure  $\beta$ -NaGdF<sub>4</sub>: 18 % Yb<sup>3+</sup>, 2 % Er<sup>3+</sup> and  $\beta$ -NaGdF<sub>4</sub>: 18 % Yb<sup>3+</sup>, 2 % Er<sup>3+</sup> / *m*TiO<sub>2</sub> nanocomposite are ~ 1.80, ~ 1.38, and ~ 1.83, respectively. This spectral change should be due to the introduction of *m*TiO<sub>2</sub> nanoparticles

which may absorb the emitted light to some extent resulting in the diminution of emission light intensity.

#### 4.3.3.3. Time resolved luminescence properties

This conclusion is further supported by time-resolved dynamic curves of Er<sup>3+</sup> ions. The luminescence decay curves of Er<sup>3+</sup> ions for the  $^4S_{3/2} \rightarrow ^4I_{15/2}$  ( $\lambda_{\text{ex}} = 980$  nm,  $\lambda_{\text{em}} = 540$  nm; green) and  $^4F_{9/2} \rightarrow ^4I_{15/2}$  ( $\lambda_{\text{ex}} = 980$  nm,  $\lambda_{\text{em}} = 654$  nm; red) emission transition in  $\beta$ -NaGdF<sub>4</sub>:Yb<sup>3+</sup>, Er<sup>3+</sup> and  $\beta$ -NaGdF<sub>4</sub>:Yb<sup>3+</sup>, Er<sup>3+</sup> /*m*TiO<sub>2</sub> nanocomposite were recorded at 980 nm laser excitation, as shown in Figure 10. As can be seen from Table 1, the luminescence lifetime time of nanocomposite is decreased as compared to  $\beta$ -NaGdF<sub>4</sub>:Yb<sup>3+</sup>, Er<sup>3+</sup>. The decay times of the  $^4S_{3/2} \rightarrow ^4I_{15/2}$  ( $\lambda_{\text{ex}} = 980$  nm,  $\lambda_{\text{em}} = 540$  nm; green) and  $^4F_{9/2} \rightarrow ^4I_{15/2}$  ( $\lambda_{\text{ex}} = 980$  nm,  $\lambda_{\text{em}} = 654$  nm; red) emission transition decreased from 0.15, and 0.36 ms in pure  $\beta$ -NaGdF<sub>4</sub>:Yb<sup>3+</sup>, Er<sup>3+</sup> to 0.10, and 0.29 ms, respectively, in  $\beta$ -NaGdF<sub>4</sub>:Yb<sup>3+</sup>, Er<sup>3+</sup> /*m*TiO<sub>2</sub> nanocomposite. This occurs because, the lifetime of excited state,  $\tau$  depends of the radiative transition rate ( $W_R$ ), non-radiative transition rate ( $W_{NR}$ ) and energy transfer rate, which can be expressed as  $\tau = 1/(W_R + W_{NR} + W_{ET})$ . Thus, the presence of anatase *m*TiO<sub>2</sub> around  $\beta$ -NaGdF<sub>4</sub>:Yb<sup>3+</sup>, Er<sup>3+</sup>, creates non-radiative energy transfer from the excited state of Er<sup>3+</sup> ions to *m*TiO<sub>2</sub>. Such an additional energy transfer process accelerated the relaxation of the excited state of Er<sup>3+</sup>, leading to the reduction of the luminescence lifetime.<sup>60</sup>

Sample ( $\lambda_{\text{ex}} = 980 \text{ nm}$ )	Lifetime (ms)	
	$^4\text{S}_{3/2} \rightarrow ^4\text{I}_{15/2}$ ( $\lambda_{\text{em}} = 540 \text{ nm}$ )	$^4\text{F}_{9/2} \rightarrow ^4\text{I}_{15/2}$ ( $\lambda_{\text{em}} = 654 \text{ nm}$ )
$\beta$ -NaGdF <sub>4</sub> : Yb <sup>3+</sup> , Er <sup>3+</sup>	0.15	0.36
$\beta$ -NaGdF <sub>4</sub> : Yb <sup>3+</sup> , Er <sup>3+</sup> / mTiO <sub>2</sub> nanocomposite	0.10	0.29

**Table 1:** The luminescence lifetime values of Er<sup>3+</sup> ions for the  $^4\text{S}_{3/2} \rightarrow ^4\text{I}_{15/2}$  ( $\lambda_{\text{ex}} = 980 \text{ nm}$ ,  $\lambda_{\text{em}} = 540 \text{ nm}$ ; green) and  $^4\text{F}_{9/2} \rightarrow ^4\text{I}_{15/2}$  ( $\lambda_{\text{ex}} = 980 \text{ nm}$ ,  $\lambda_{\text{em}} = 654 \text{ nm}$ ; red) emission transition in  $\beta$ -NaGdF<sub>4</sub>:Yb<sup>3+</sup>, Er<sup>3+</sup> and  $\beta$ -NaGdF<sub>4</sub>:Yb<sup>3+</sup>, Er<sup>3+</sup> /mTiO<sub>2</sub> nanocomposite at 980 nm laser excitation.

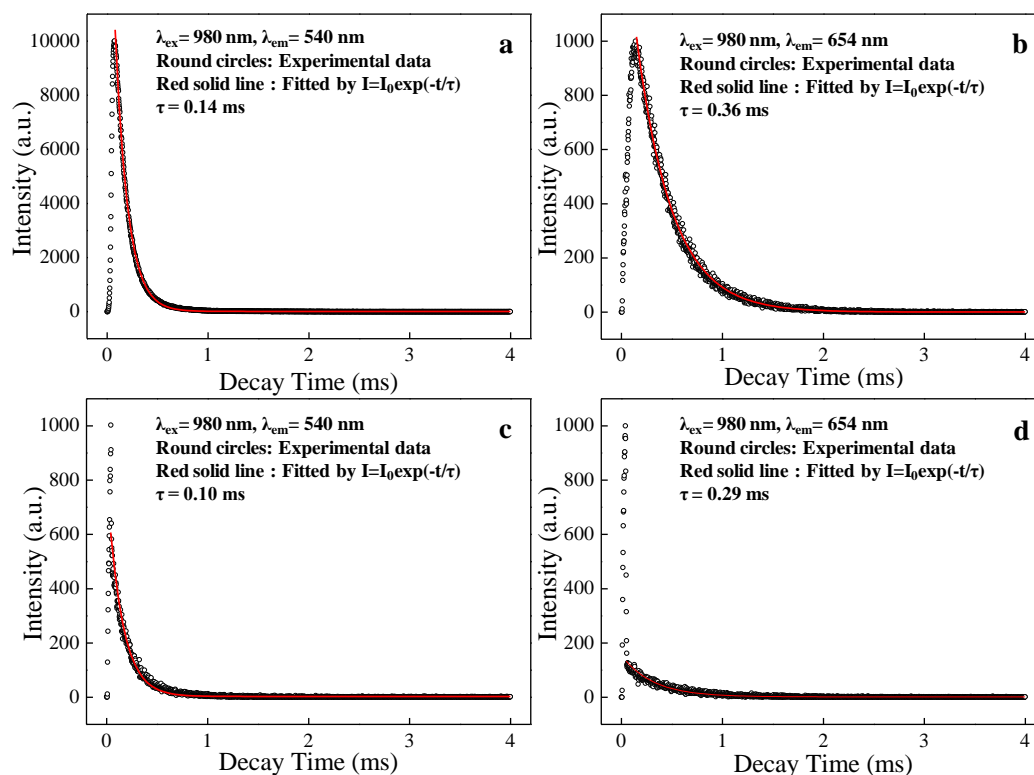


**Figure 10:** The Luminescence dynamic curves for the  $^4\text{S}_{3/2} \rightarrow ^4\text{I}_{15/2}$  ( $\lambda_{\text{ex}} = 980 \text{ nm}$ ,  $\lambda_{\text{em}} = 540 \text{ nm}$ ) and  $^4\text{F}_{9/2} \rightarrow ^4\text{I}_{15/2}$  ( $\lambda_{\text{ex}} = 980 \text{ nm}$ ,  $\lambda_{\text{em}} = 654 \text{ nm}$ ) emission of Er<sup>3+</sup> in (a, b)  $\beta$ -NaGdF<sub>4</sub>:Yb<sup>3+</sup>, Er<sup>3+</sup> and (c, d)  $\beta$ -NaGdF<sub>4</sub>:Yb<sup>3+</sup>, Er<sup>3+</sup> /mTiO<sub>2</sub> nanocomposite.

### 4.3.4. Photocatalysis properties

#### 4.3.4.1. Photocatalytic activity

The Photocatalytic measurements were performed by exposing the  $\beta$ -NaGdF<sub>4</sub>: 18 % Yb<sup>3+</sup>/ 2 % Er<sup>3+</sup> nanorods, *m*TiO<sub>2</sub> and  $\beta$ -NaGdF<sub>4</sub>: 18 % Yb<sup>3+</sup>, 2 % Er<sup>3+</sup>/ *m*TiO<sub>2</sub> nanocomposite to the direct sunlight irradiation to test the material in actual working conditions which cannot be truly simulated in the lab environment. For this purpose, we studied the degradation behavior of rhodamine B (RhB) and dye mixture containing equivalent rhodamine B (RhB), methylene blue (MB) and malachite green (MG). The study of degradation behavior of dye-mixture is significant because the industrial and textile wastewater consist of mixture of various dyes. The sample suspensions were kept in dark overnight for adsorption-desorption to reach the equilibrium. The photocatalytic experiments were performed on 14 April 2015 in Pune, India (latitude: 18°32'25.3"N & longitude: 73°48'42.3"E) from 11:00 AM (Sun's altitude: 51°, heading 149° SSE) to 12:00 PM (Sun's altitude: 55°, heading 172° S). The temperature was ~ 30 °C. The UV-visible absorbance spectra for the degradation of rhodamine B (RhB) and dye-mixture, catalyzed by  $\beta$ -NaGdF<sub>4</sub>: 18 % Yb<sup>3+</sup>, 2 % Er<sup>3+</sup>/ *m*TiO<sub>2</sub> nanocomposite, are compared in the Figure 11. The degradation of dyes was observed through the reduction in the absorbance peak intensity with an increase in the irradiation time. The kinetics of the reaction was plotted as  $(C/C_0)$  against time ( $t$ ), where  $C_0$  is the initial concentration and  $C$  is the final concentration of different dyes (Figure 12 (a)). The characteristic absorbance peaks of RhB ( $\lambda \sim 554$  nm) and dye mixture ( $\sim 617$  nm and  $\sim 554$  nm) were used as references for the photocatalytic degradation for respective dyes. The photocatalytic efficiency of the nanocomposite can be evaluated by calculating the time-dependent  $(C/C_0)$  ratio of the dye and compared with the blank sample (as control), *m*TiO<sub>2</sub>,

and  $\beta$ -NaGdF<sub>4</sub>: 18 % Yb<sup>3+</sup>, 2 % Er<sup>3+</sup> nanorods. It can be seen from Figure 12 (a) that the photocatalytic activity of the  $\beta$ -NaGdF<sub>4</sub>: 18 % Yb<sup>3+</sup>, 2 % Er<sup>3+</sup>/ *m*TiO<sub>2</sub> nanocomposite is higher than that of the other samples. The blank test confirms that RhB and dye mixture is quite stable. In the absence of the catalyst, no obvious change in the concentration of RhB and dye mixture concentration is observed after the irradiation for 50 min.

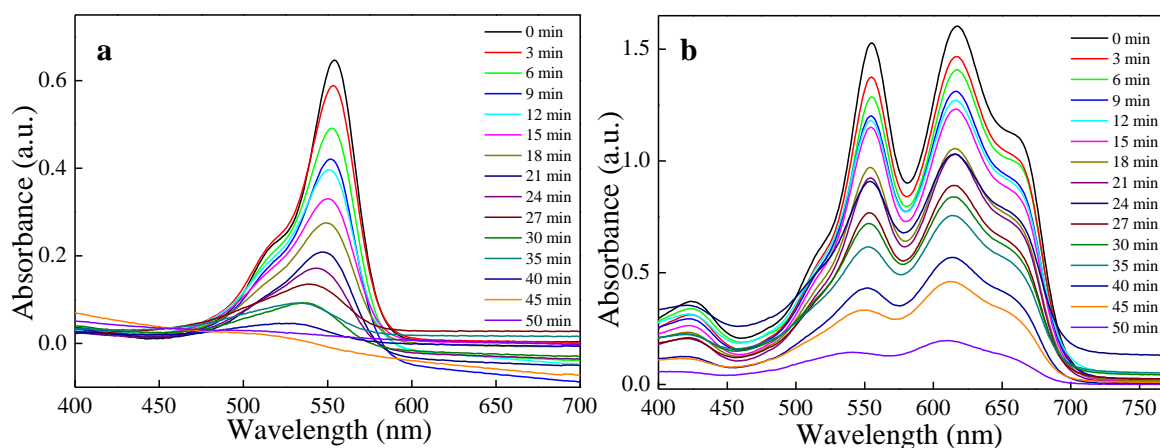


**Figure 11:** Photocatalytic activity of  $\beta$ -NaGdF<sub>4</sub>:Yb<sup>3+</sup>, Er<sup>3+</sup> /*m*TiO<sub>2</sub> nanocomposite for (a) rhodamine-B and (b) dye mixture, under solar light irradiation for 50 min.

The chromophore of the RhB gets almost completely degraded (~ 99 %) in presence of the  $\beta$ -NaGdF<sub>4</sub>: 18 % Yb<sup>3+</sup>, 2 % Er<sup>3+</sup>/ *m*TiO<sub>2</sub> nanocomposite under the sunlight irradiation for 50 min whereas,  $\beta$ -NaGdF<sub>4</sub>: 18 % Yb<sup>3+</sup>, 2 % Er<sup>3+</sup> and *m*TiO<sub>2</sub> degraded ~ 25 % and ~ 88 % respectively under similar condition. The nanocomposite also efficiently degraded dye-mixture down to ~ 89 % in 50 min. In comparison with the carbon doped mesoporous TiO<sub>2</sub>, which is a well-known benchmark catalyst, the photocatalytic activity of the  $\beta$ -NaGdF<sub>4</sub>: 18 % Yb<sup>3+</sup>, 2 % Er<sup>3+</sup>/ *m*TiO<sub>2</sub> nanocomposite is higher (~ 20 %). It is worth noting that the

photocatalytic efficiency of the nanocomposite is comparable and higher than the reported values for composites.<sup>2, 61, 62</sup>

The photocatalytic degradation kinetics was studied; the degradation of dyes follows apparent first order kinetics according to Langmuir-Hinshelwood (L-H) model, which is well-established for heterogeneous photocatalyst at low dye concentration.<sup>63</sup> The relevant equation is

$$\ln\left(\frac{C_0}{C}\right) = kt$$

where  $C_0$  is the initial concentration of the dye,  $C$  is the concentration of the dye after illumination time  $t$  and  $k$  is the apparent rate constant.

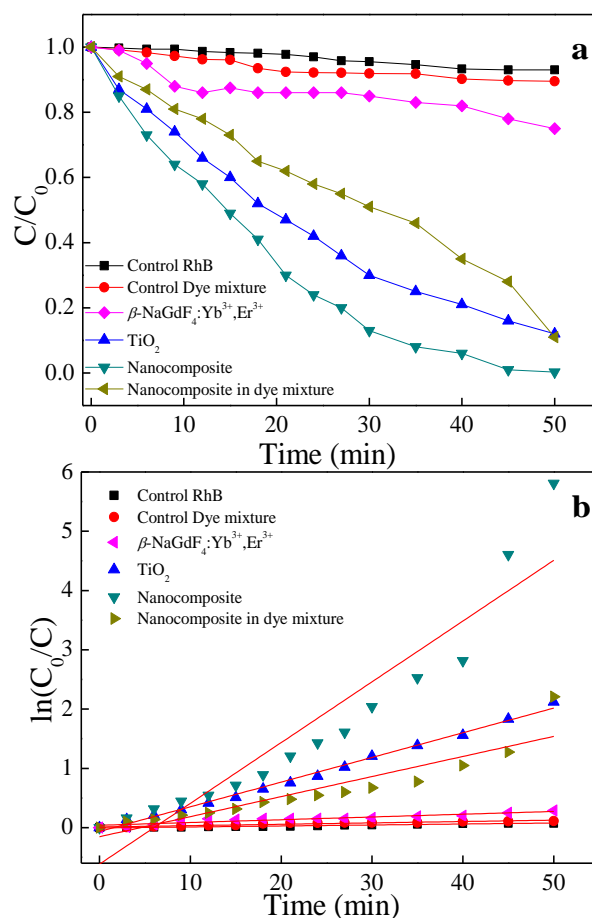


**Figure 12:** Plots of (a) dye concentrations ( $C/C_0$ ) vs. time and, (b) plot of  $\ln(C_0/C)$  vs. time first order reaction kinetics graph showing photodegradation of rhodamine B by  $\beta$ -

NaGdF<sub>4</sub>:Yb<sup>3+</sup>, Er<sup>3+</sup>, *m*TiO<sub>2</sub>, and  $\beta$ -NaGdF<sub>4</sub>:Yb<sup>3+</sup>, Er<sup>3+</sup>/*m*TiO<sub>2</sub> nanocomposite and photodegradation of dye mixture by  $\beta$ -NaGdF<sub>4</sub>:Yb<sup>3+</sup>, Er<sup>3+</sup>/*m*TiO<sub>2</sub> nanocomposite under solar light irradiation for 50 min.

As shown in the Figure 12 (b), the photocatalytic degradation of RhB catalyzed by the as-prepared samples fits well a first order reaction kinetics. A plot of  $\ln(C_0/C)$  vs. *t* provides a slope value, which is the rate constant (*k*) of the dye degradation by the samples. The *k*-value of RhB degradation by  $\beta$ -NaGdF<sub>4</sub>: 18 % Yb<sup>3+</sup>, 2 % Er<sup>3+</sup>, *m*TiO<sub>2</sub>, and  $\beta$ -NaGdF<sub>4</sub>: 18 % Yb<sup>3+</sup>, 2 % Er<sup>3+</sup>/*m*TiO<sub>2</sub> nanocomposite was  $\sim 4.66 \times 10^{-3} \text{ min}^{-1}$ ,  $\sim 4.16 \times 10^{-2} \text{ min}^{-1}$  and  $\sim 1.02 \times 10^{-1} \text{ min}^{-1}$  respectively. The *k* value for the degradation of dye mixture by the nanocomposite was  $\sim 3.38 \times 10^{-2} \text{ min}^{-2}$ . The high rate constant of the  $\beta$ -NaGdF<sub>4</sub>: 18 % Yb<sup>3+</sup>, 2 % Er<sup>3+</sup>/*m*TiO<sub>2</sub> nanocomposite further suggest its high photocatalytic activity.

#### 4.3.4.2. Photocatalytic mineralization of dye by nanocomposite

In order to assess the degree of mineralization reached during the photocatalytic treatment the formation of CO<sub>2</sub> and inorganic ions is generally determined. The determination of total organic carbon (TOC) of the irradiated solution is generally used for monitoring the mineralization of the dye. Changes in the TOC values reflect the degree of degradation or mineralization of nanocomposite-sample dye suspension during the irradiation period. The TOC analysis of the RhB dye solution in presence of  $\beta$ -NaGdF<sub>4</sub>:Yb<sup>3+</sup>, Er<sup>3+</sup>/*m*TiO<sub>2</sub> nanocomposite was performed using TOC analyzer. Total Organic Carbon (TOC) removal for the irradiated nanocomposite/RhB suspension is  $\sim 50 \%$ , *i.e.* decreased indicating that the mineralization of RhB occurs during the decomposition of the chromophore of RhB. This is due to the fact that, in general TOC values decrease with increase in irradiation time whereas the amount of NH<sub>4</sub><sup>+</sup> and NO<sub>3</sub><sup>-</sup> ions increase with increase in irradiation time.



#### 4.3.4.3. Mechanism of photocatalysis by nanocomposite

The mechanism of NIR driven photocatalysis of the  $\beta$ -NaGdF<sub>4</sub>: 18 % Yb<sup>3+</sup>, 2 % Er<sup>3+</sup>/*m*TiO<sub>2</sub> nanocomposite is described in the Figure 13. The up-conversion phosphor  $\beta$ -NaGdF<sub>4</sub>: 18 % Yb<sup>3+</sup>, 2 % Er<sup>3+</sup> absorbs photons in NIR and upconverts to UV and visible photons, which are reabsorbed by *m*TiO<sub>2</sub>. The Yb<sup>3+</sup> acts as a sensitizer in the  $\beta$ -NaGdF<sub>4</sub>: Yb<sup>3+</sup>, Er<sup>3+</sup> phosphor and it could absorb 980 nm NIR radiations, which results in populating the <sup>2</sup>F<sub>5/2</sub> level. After that, the excited electron would transfer back to the <sup>2</sup>F<sub>7/2</sub> ground state and the released energy is non-radiatively transferred to activator ions Er<sup>3+</sup>, resulting in the population of the higher <sup>4</sup>F<sub>9/2</sub>, <sup>4</sup>S<sub>3/2</sub>, <sup>2</sup>H<sub>11/2</sub> and <sup>2</sup>H<sub>9/2</sub> energy levels of Er<sup>3+</sup> via successive energy transfer process from Yb<sup>3+</sup> ions. Finally, these excited electrons would transfer to the <sup>4</sup>I<sub>15/2</sub> ground state of Er<sup>3+</sup> and radiatively emit in the UV and visible region.<sup>37</sup> The as-emitted photons could be reabsorbed by the *m*TiO<sub>2</sub> nanoparticles, which have photon absorption bands in the UV and visible regions due to small amount of carbon doping in *m*TiO<sub>2</sub> during the synthesis. The *m*TiO<sub>2</sub> nanoparticles are excited by the energy transfer from up-conversion phosphors and generate high energy electrons (e<sup>-</sup>) and holes (h<sup>+</sup>) in the conduction band (CB) and valence band (VB). The photogenerated holes oxidize water molecules present on the surface of the catalyst and produce hydroxyl ·OH radicals. The electrons in the conduction band react with O<sub>2</sub> molecules to form reactive ·O<sub>2</sub><sup>-</sup> radicals. The reactive radical species ·OH and ·O<sub>2</sub><sup>-</sup> degrade the dye molecules by forming by-products such as CO<sub>2</sub>, ammonia etc.<sup>64</sup>

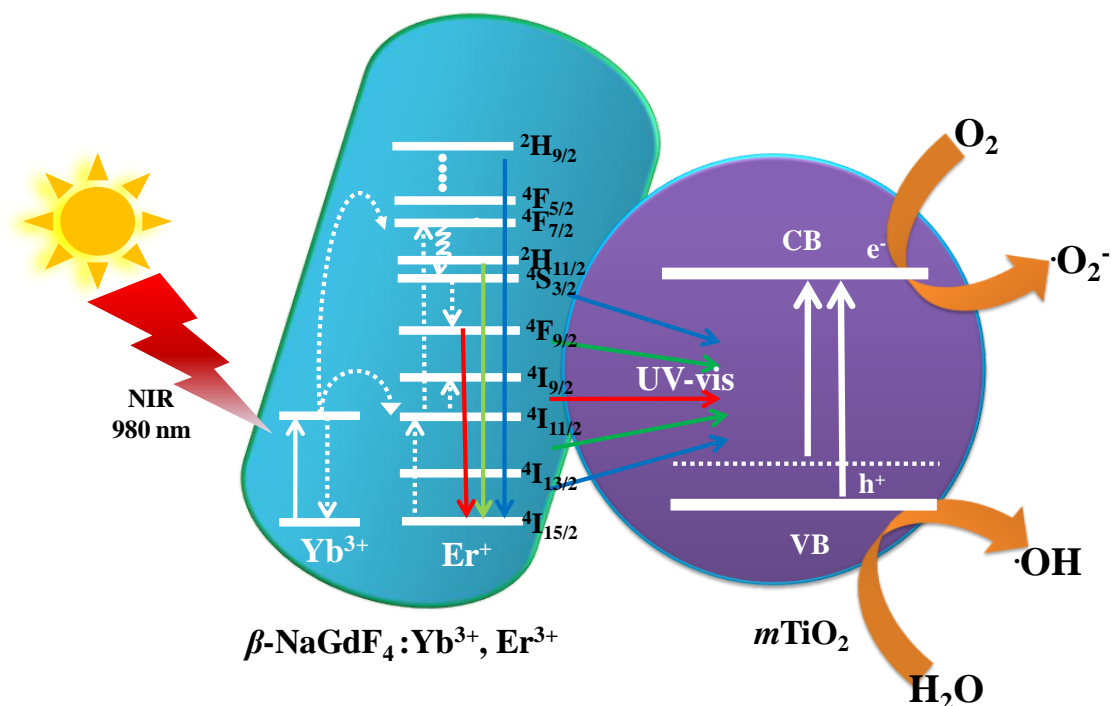


**Figure 13:** Schematic representation of the near-infra red driven photocatalytic mechanism of  $\beta$ -NaGdF<sub>4</sub>:Yb<sup>3+</sup>, Er<sup>3+</sup>/mTiO<sub>2</sub> nanocomposite showing energy level diagram and up-conversion luminescence process of Yb<sup>3+</sup>, Er<sup>3+</sup> co-doped  $\beta$ -NaGdF<sub>4</sub> under 980 nm excitation and the energy transfer process between  $\beta$ -NaGdF<sub>4</sub>:Yb<sup>3+</sup>, Er<sup>3+</sup> and TiO<sub>2</sub>, and the generation of ·OH and ·O<sub>2</sub><sup>-</sup> radicals.

#### 4.3.5. Photovoltaic characteristics

##### 4.3.5.1. Photovoltaic measurements

The photovoltaic properties of DSSCs fabricated with the mTiO<sub>2</sub> and  $\beta$ -NaGdF<sub>4</sub>: 18 % Yb<sup>3+</sup>, 2 % Er<sup>3+</sup>/ mTiO<sub>2</sub> nanocomposite were measured and compared in the Figure 14. The light harvesting property of the as-synthesized  $\beta$ -NaGdF<sub>4</sub>: 18 % Yb<sup>3+</sup>, 2 % Er<sup>3+</sup>/ mTiO<sub>2</sub> nanocomposite was investigated by preparing a film of the material (sensitized with the N719

dye) on FTO substrate, followed by the photoelectric conversion measurements by fabricating a DSSC. Due to the incorporation of the up-conversion phosphor material into the  $m\text{TiO}_2$ , there will be an increase in the photon scattering as well as their absorption as, in addition to the visible region photons, the photons in the IR-region of the spectrum are also utilized.

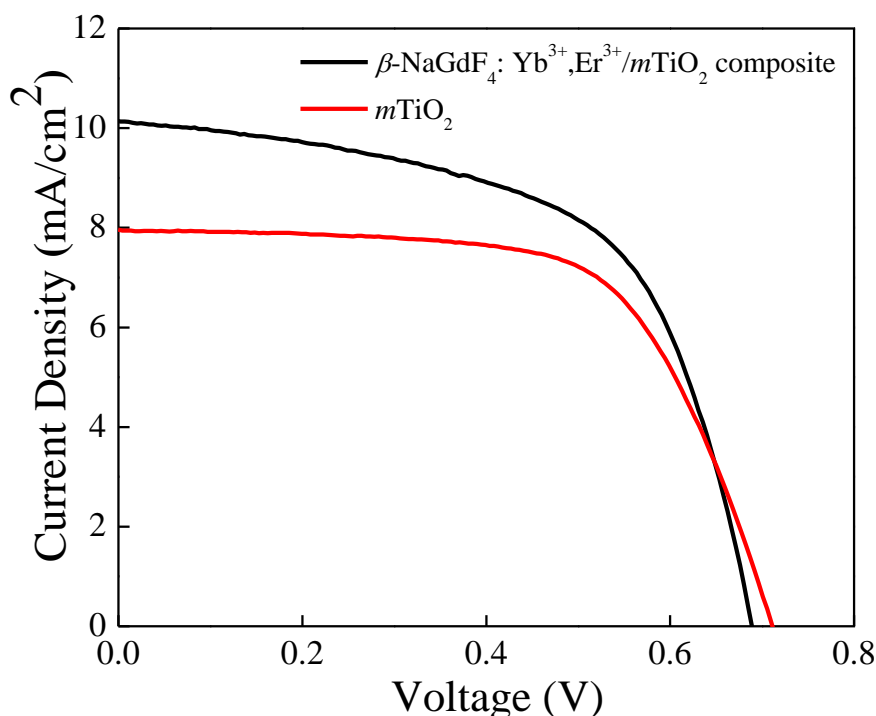


**Figure 14:** Current density vs potential curves for dye-sensitized solar cell fabricated from  $m\text{TiO}_2$ , and  $\beta$ -NaGdF<sub>4</sub>: Yb<sup>3+</sup>, Er<sup>3+</sup>/mTiO<sub>2</sub> nanocomposite.

In this system, the upconverting nanorods harvest NIR sunlight and transform into visible *via* anti-Stokes emission, which is directly reabsorbed by photoactive TiO<sub>2</sub>, thereby improving power conversion efficiency (PCE) in DSSC's. The Figure 14 shows the current density-voltage curves of the assembled solar cell under 100 mW/cm<sup>2</sup> illumination using dye-adsorbed  $m\text{TiO}_2$  and  $\beta$ -NaGdF<sub>4</sub>: 18 % Yb<sup>3+</sup>, 2 % Er<sup>3+</sup>/  $m\text{TiO}_2$  nanocomposite as photoanode and their photovoltaic parameters are summarized in Table 2. The overall performance of the

above described solar cell can be evaluated in terms of cell efficiency ( $\eta$ ) and fill factor (FF) expressed as:

$$FF = \frac{V_{max}J_{max}}{V_{oc}J_{sc}}$$

$$\eta = \frac{V_{oc}J_{sc}FF}{P_{in}} \times 100\%$$

Samples	$J_{SC}$ (mAcm <sup>-2</sup> )	$V_{OC}$ (V)	FF (%)	$\eta$ (%)
<i>m</i> TiO <sub>2</sub>	7.9	0.71	64	3.6
$\beta$ -NaGdF <sub>4</sub> , Yb <sup>3+</sup> , Er <sup>3+</sup> / <i>m</i> TiO <sub>2</sub> composite	10.5	0.68	59	4.3

**Table 2:** Photovoltaic characteristics of DSSCs with *m*TiO<sub>2</sub> and *m*TiO<sub>2</sub> combined with NIR active upconverting  $\beta$ -NaGdF<sub>4</sub>: Yb<sup>3+</sup>, Er<sup>3+</sup> nanocomposite.

It was found that in the composite material, the photocurrent density ( $J_{SC}$ ) increased from 7.9 to 10.5 mA cm<sup>-2</sup>, and the open-circuit voltage ( $V_{OC}$ ), decreased from 0.71 to 0.68 V. The fill-factor of nanocomposite decreased from 64 to 59 % and the photon to electron conversion efficiency of the nanocomposite increased from 3.6 to 4.3 %. The  $\beta$ -NaGdF<sub>4</sub>: 18 % Yb<sup>3+</sup>, 2 % Er<sup>3+</sup>/*m*TiO<sub>2</sub> nanocomposite film effectively pass and scatter the incident photons through the backside of the photoelectrode and thus, able to generate more photoelectrons to enhance the power conversion efficiency of the cell. Moreover, it should be noted that, in comparison to the DSSC made with *m*TiO<sub>2</sub> film, the  $\beta$ -NaGdF<sub>4</sub>: 18 % Yb<sup>3+</sup>, 2 % Er<sup>3+</sup>/*m*TiO<sub>2</sub> nanocomposite film DSSC system resulted in increased photocurrent density by

~ 24 %. This enhancement is attributed to the enhanced light harvesting of dye molecule, which is due to presence of up-conversion phosphor that enhances harvesting by utilizing NIR photons as well. The overall efficiency of the DSSC increased by 17 % in the composite material compared to only  $m\text{TiO}_2$  which support the advantageous effect of the synthesis of  $\beta$ -NaGdF<sub>4</sub>: 18 % Yb<sup>3+</sup>, 2 % Er<sup>3+</sup>/  $m\text{TiO}_2$  nanocomposite material and benefit of employ it as photoanode in liquid junction solar cell.

#### 4.3.5.2. Mechanism of the DSSC performance based on the nanocomposite

The Figures 15 and 16 illustrate the configuration and the response mechanism of the DSSC based on the  $\beta$ -NaGdF<sub>4</sub>: Yb<sup>3+</sup>, Er<sup>3+</sup>/ $m\text{TiO}_2$  nanocomposite. A typical DSSC consists of a dye-sensitized nanocrystalline TiO<sub>2</sub> semiconductor film on a conductive glass, an electrolyte solution containing an I<sup>-</sup>/I<sup>3-</sup> redox couple, and a platinum film as a counter electrode.<sup>65</sup> Upon excitation, the dye molecules absorb photons and inject electrons into the conduction band of TiO<sub>2</sub> from the excited state of the dye.<sup>65</sup> A major factor limiting the performance of DSSCs is the inability of utilizing near-infrared (NIR) photons. The most commonly used photosensitizers such as N3, N719, and N749 dyes can absorb UV and visible light.<sup>66</sup> Here, in this system with the aid of up-conversion  $\beta$ -NaGdF<sub>4</sub>: Yb<sup>3+</sup>, Er<sup>3+</sup> phosphor, the NIR light is utilized from broad solar spectrum. The  $\beta$ -NaGdF<sub>4</sub>: Yb<sup>3+</sup>, Er<sup>3+</sup> phosphor is excited by NIR energy and emits intense green visible light, which is reabsorbed by photosensitizer N719 dye.

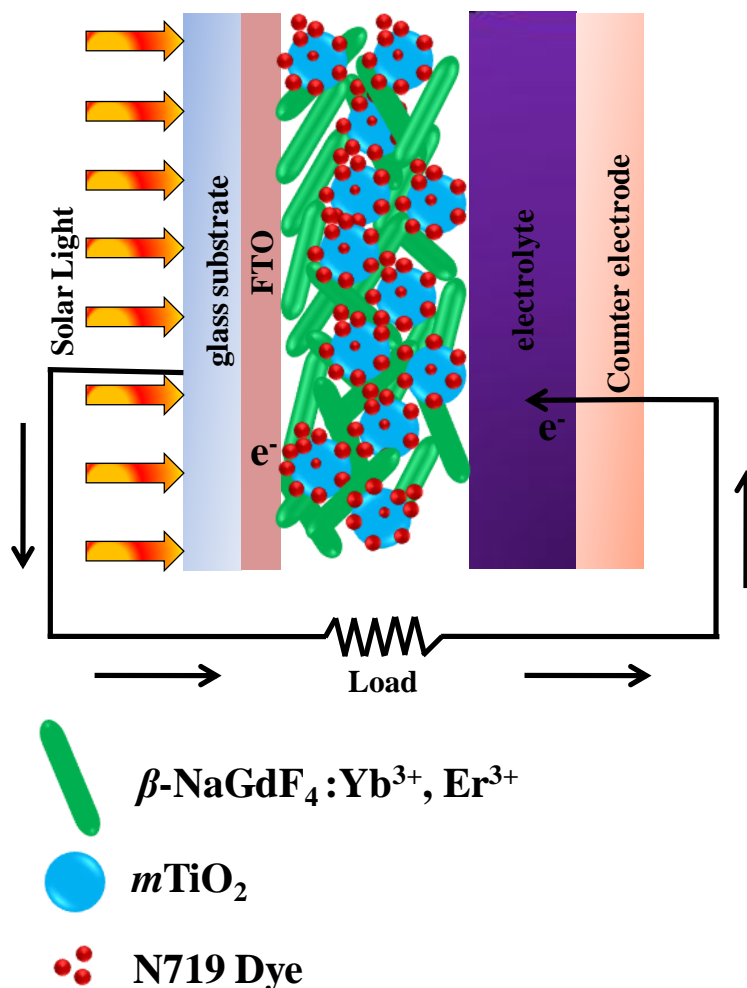


**Figure 15:** The configuration of the  $\beta$ -NaGdF<sub>4</sub>: Yb<sup>3+</sup>, Er<sup>3+</sup>/ $m$ TiO<sub>2</sub> nanocomposite modified DSSC.

Figure 16 (a) shows the absorption spectrum of the N719 dye and the UC emission spectrum of  $\beta$ -NaGdF<sub>4</sub>: Yb<sup>3+</sup>, Er<sup>3+</sup> nanorods. It can be clearly seen that the absorption band of the N719 dye is resonant with the green emission (540 nm) of the  $\beta$ -NaGdF<sub>4</sub>: Yb<sup>3+</sup>, Er<sup>3+</sup> phosphor, thus the N719 dye is able to efficiently absorb the green emitted light. Consequently, the NIR light absorbed by the up-conversion phosphor can be effectively used to excite the dye molecules, which further injects electrons to  $m$ TiO<sub>2</sub>, finally which in turn

will help increase the performance of DSSCs in the NIR region (Figure 16 (b)). Similar kind of systems have been studied, where the semiconductor (TiO<sub>2</sub>) based DSSC's are modified with upconverting nanoparticles and thus, up-conversion phosphors are utilized to improve the photovoltaic performance.<sup>67,68,69</sup>

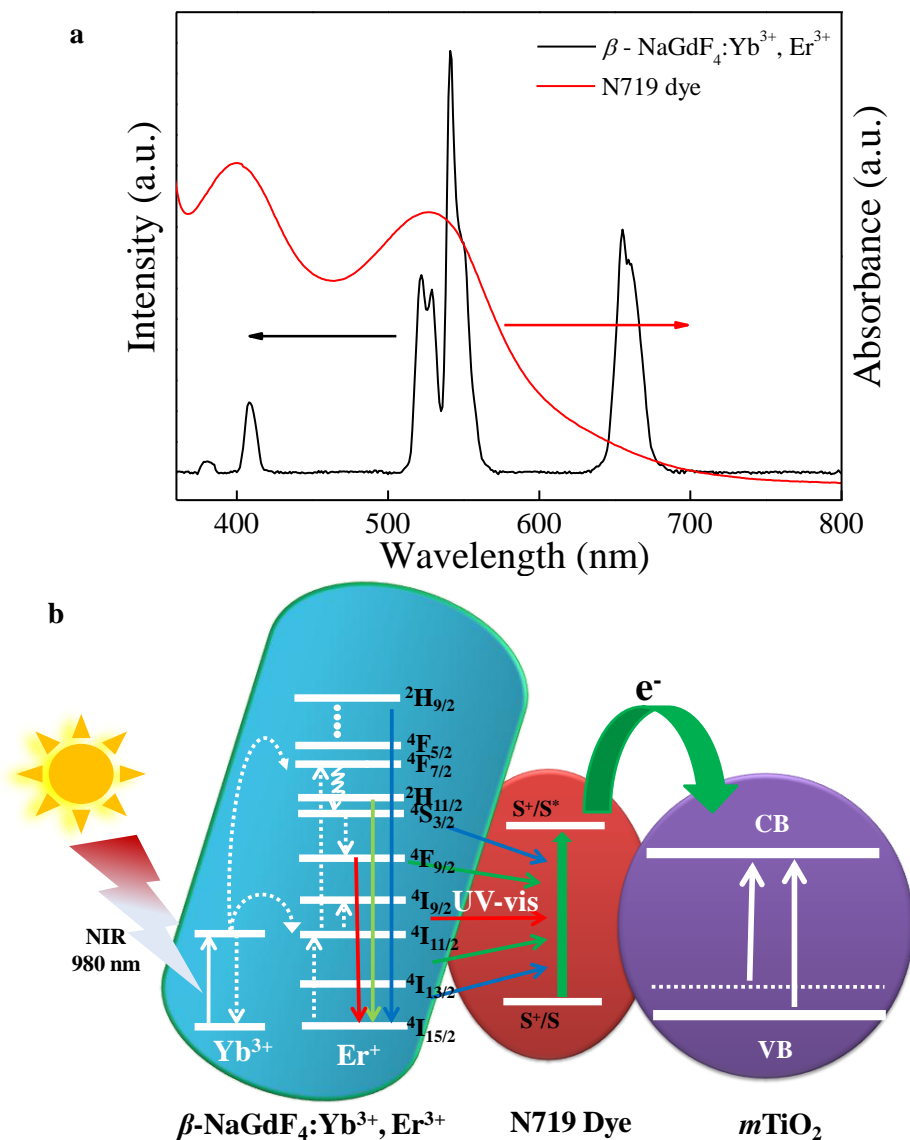


**Figure 16:** (a) The absorption spectrum of N719 dye and UC photoluminescence spectrum of  $\beta$ -NaGdF<sub>4</sub>: Yb<sup>3+</sup>, Er<sup>3+</sup> nanorods showing a strong spectral overlap around multiple absorption peaks of dye, and (b) response mechanism of the  $\beta$ -NaGdF<sub>4</sub>: Yb<sup>3+</sup>, Er<sup>3+</sup>/mTiO<sub>2</sub>

nanocomposite modified DSSC showing the energy transfer from the UC nanocrystals to the N719 dye.

### 4.3.6. Magnetic properties

#### 4.3.6.1. Magnetic mass susceptibility

In addition to the excellent up-conversion luminescence property, the amine functionalized  $\beta$ -NaGdF<sub>4</sub>: 18 % Yb<sup>3+</sup>/ 2 % Er<sup>3+</sup> nanorods as well as  $\beta$ -NaGdF<sub>4</sub>: 18 % Yb<sup>3+</sup>, 2 % Er<sup>3+</sup>/ *m*TiO<sub>2</sub> nanocomposite exhibited paramagnetism (Figure 17), which makes these nanorods suitable as a MRI contrast agent. The Figures 17 (a) and (b), show the room temperature (RT) magnetization (M) as a function of the applied magnetic field (H) for the amine functionalized  $\beta$ -NaGdF<sub>4</sub>: 18 % Yb<sup>3+</sup>/ 2 % Er<sup>3+</sup> nanorods and the  $\beta$ -NaGdF<sub>4</sub>: 18 % Yb<sup>3+</sup>, 2 % Er<sup>3+</sup>/ *m*TiO<sub>2</sub> nanocomposite respectively. These nanorods exhibit typical paramagnetic behavior at 300 K and applied field in range from - 40 to + 40 kOe. The paramagnetic properties of the Gd<sup>3+</sup> ions arise from seven unpaired inner 4*f* electrons, which are closely bound to the nucleus and effectively shielded from crystal field by the outer filled 5*s*<sup>2</sup> 5*p*<sup>6</sup> shell electrons. Thus, it prohibits sufficient overlap of the orbitals associated with the partially filled 4*f* electrons shells of the Gd<sup>3+</sup> ions necessary for ferromagnetism. It turns out that the magnetic moments associated with the Gd<sup>3+</sup> ions are all localized and non-interacting thereby giving rise to paramagnetism.<sup>70</sup> The magnetic mass susceptibility of  $\beta$ -NaGdF<sub>4</sub>: 18 % Yb<sup>3+</sup>/ 2 % Er<sup>3+</sup> nanorods and  $\beta$ -NaGdF<sub>4</sub>: 18 % Yb<sup>3+</sup>, 2 % Er<sup>3+</sup>/ *m*TiO<sub>2</sub> nanocomposite are ~ 1.36 X 10<sup>-4</sup> emu g<sup>-1</sup> Oe<sup>-1</sup> and ~ 6.45 X 10<sup>-5</sup> emu g<sup>-1</sup> Oe<sup>-1</sup> respectively. Furthermore, the magnetization of  $\beta$ -NaGdF<sub>4</sub>: 18 % Yb<sup>3+</sup>/ 2 % Er<sup>3+</sup> nanorods and  $\beta$ -NaGdF<sub>4</sub>: 18 % Yb<sup>3+</sup>, 2 % Er<sup>3+</sup>/ *m*TiO<sub>2</sub> nanocomposite is ~ 2.75 emu g<sup>-1</sup> and ~ 1.30 emu g<sup>-1</sup> respectively at 20 kOe.



These values are close to the reported values of nanoparticles, which are used very frequently for bioseparation and are also successfully used as T<sub>1</sub>-MRI contrast agent.<sup>71</sup>

#### 4.3.6.2. Longitudinal relaxivity and magnetic resonance imaging

To further demonstrate the potential application of the  $\beta$ -NaGdF<sub>4</sub>: 18 % Yb<sup>3+</sup>/ 2 % Er<sup>3+</sup> nanorods as a MRI contrast agent, a series of  $\beta$ -NaGdF<sub>4</sub>: 18 % Yb<sup>3+</sup>/ 2 % Er<sup>3+</sup> nanorods and  $\beta$ -NaGdF<sub>4</sub>: 18 % Yb<sup>3+</sup>, 2 % Er<sup>3+</sup>/ mTiO<sub>2</sub> nanocomposites with different molar concentrations were used for the ionic longitudinal relaxivity ( $r_1$ ) study using the NMR spectrometer. From the slope of plot of  $1/T_1$  versus Gd<sup>3+</sup> concentration (Figure 17 (c) and (d)), the relaxation rate  $1/T_1$  ( $r_1$ ) value for the of  $\beta$ -NaGdF<sub>4</sub>: 18 % Yb<sup>3+</sup>/ 2 % Er<sup>3+</sup> nanorods and  $\beta$ -NaGdF<sub>4</sub>: 18 % Yb<sup>3+</sup>, 2 % Er<sup>3+</sup>/ mTiO<sub>2</sub> nanocomposites were determined to be 7.81 s<sup>-1</sup> mM<sup>-1</sup> and 7.09 s<sup>-1</sup> mM<sup>-1</sup> respectively.

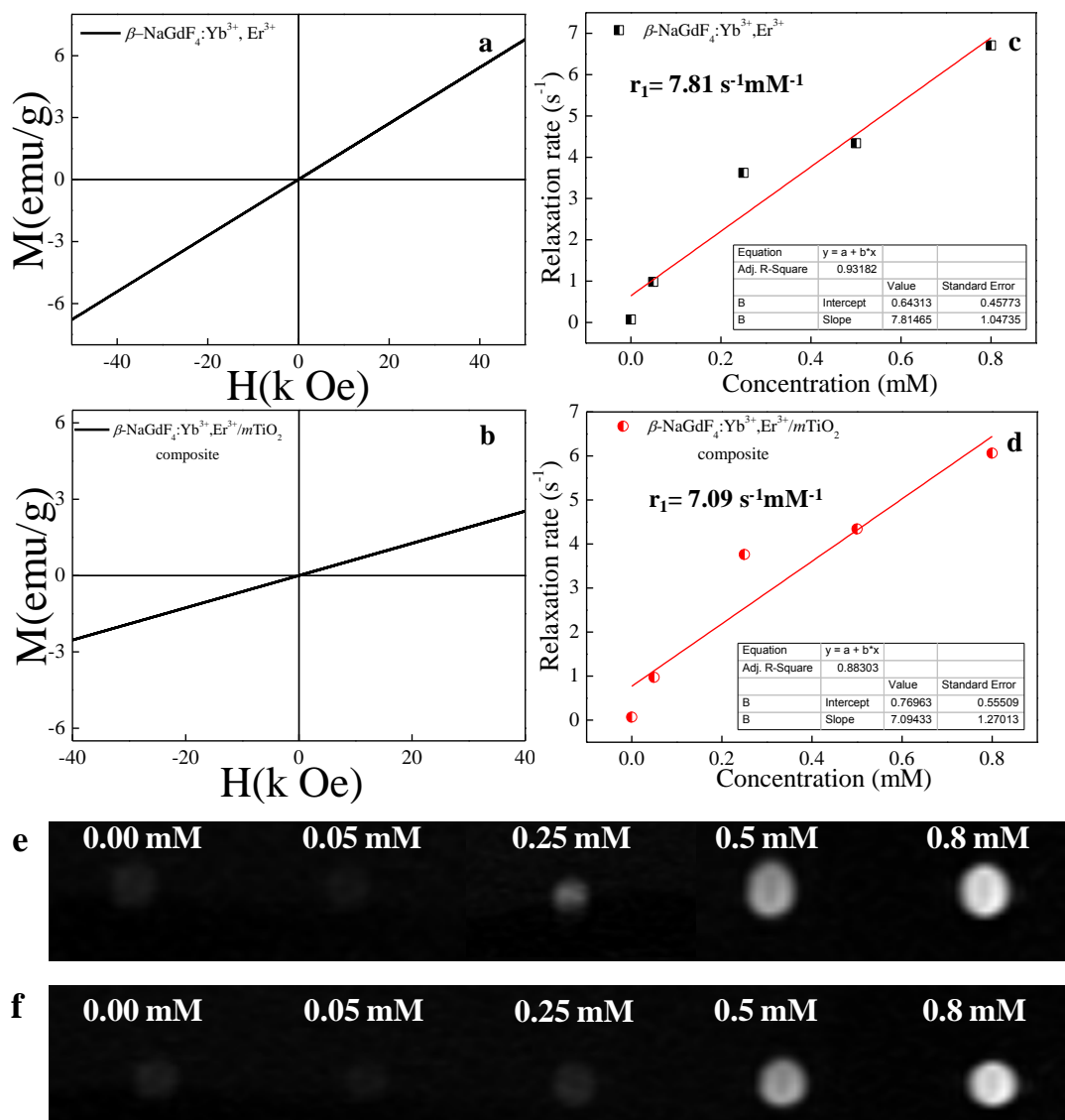


**Figure 17:** Magnetization as a function of applied field for (a)  $\beta$ -NaGdF<sub>4</sub>:Yb<sup>3+</sup>, Er<sup>3+</sup> and (b)  $\beta$ -NaGdF<sub>4</sub>:Yb<sup>3+</sup>, Er<sup>3+</sup>/mTiO<sub>2</sub> nanocomposite at room temperature showing paramagnetic behavior. The plot of <sup>1</sup>H spin-lattice relaxation rate (1/T<sub>1</sub>) as a function of molar concentration (mM) of (c)  $\beta$ -NaGdF<sub>4</sub>:Yb<sup>3+</sup>, Er<sup>3+</sup> nanorods and (d)  $\beta$ -NaGdF<sub>4</sub>:Yb<sup>3+</sup>, Er<sup>3+</sup>/mTiO<sub>2</sub> nanocomposite at RT and 9.4 T. The T<sub>1</sub> weighted MRI images of (e)  $\beta$ -

NaGdF<sub>4</sub>:Yb<sup>3+</sup>, Er<sup>3+</sup> nanorods and (f)  $\beta$ -NaGdF<sub>4</sub>:Yb<sup>3+</sup>, Er<sup>3+</sup>/mTiO<sub>2</sub> nanocomposite at various molar concentrations in water. Deionised water (0.00 mM) was taken as reference.

The obtained longitudinal relaxivity values are higher than that of the commercially used Gd-based MRI contrast agent such as Gd-DTPA/Magnevist ( $r_1 \sim 3.8 \text{ s}^{-1} \text{ mM}^{-1}$ ), Gd-DOTA/Dotarem ( $r_1 \sim 3.2 \text{ s}^{-1} \text{ mM}^{-1}$ )<sup>72, 73</sup> and other reported potential inorganic nanoparticles as KGdF<sub>4</sub> ( $r_1 \sim 5.8 \text{ s}^{-1} \text{ mM}^{-1}$ )<sup>45</sup>, GdF<sub>3</sub> ( $r_1 \sim 1.4 \text{ s}^{-1} \text{ mM}^{-1}$ )<sup>74</sup>, Gd<sub>2</sub>O<sub>3</sub> ( $r_1 \sim 5.1 \text{ s}^{-1} \text{ mM}^{-1}$ )<sup>75</sup>, NaGdF<sub>4</sub> ( $r_1 \sim 7.2 \text{ s}^{-1} \text{ mM}^{-1}$ )<sup>76</sup>, NaGdF<sub>4</sub>:Yb/Er (20/2)@NaGdF<sub>4</sub> ( $r_1 \sim 1.05 \text{ s}^{-1} \text{ mM}^{-1}$ )<sup>77</sup> etc. Thus, we believe the as prepared  $\beta$ -NaGdF<sub>4</sub>:Yb,Er (UCNPs) can be a potential MRI contrast agent.

In general, the longitudinal T<sub>1</sub> relaxivity value increases for smaller size nanoparticles, due to larger surface to volume (S/V) ratio, consequently large number of surface Gd<sup>3+</sup> ion interacting with water protons. This results due to  $1/r^6$  dependence of water proton relaxation on distance between Gd<sup>3+</sup> ions and water protons.<sup>78</sup> The high S/V ratio wherein the distance between Gd<sup>3+</sup> ions and water protons decreases, results in higher relaxivity. However, various number of anomalies of this inference has been reported so far in different literature which can be seen from the table below:

Nanoparticles (contrast agent)	Size (nm)	Longitudinal Relaxivity (s <sup>-1</sup> mM <sup>-1</sup> )	Ref.
<b>Gd<sub>2</sub>O<sub>3</sub>:Eu</b>	7.4	34.26	78
<b>Gd<sub>2</sub>O<sub>3</sub></b>	5.2	5.15	75
<b>Gd<sub>2</sub>O<sub>3</sub></b>	2.5 x 18	1.5	79
<b>GdF<sub>3</sub></b>	129.3	1.95	80
<b>Gd<sub>2</sub>O(CO<sub>3</sub>)<sub>2</sub> .H<sub>2</sub>O</b>	478	16.5	80
<b>NaGdF<sub>4</sub>:Nd<sup>3+</sup>, Yb<sup>3+</sup>, Tm<sup>3+</sup></b>	21	1.25	81
<b>NaGdF<sub>4</sub>:Yb/Er/Tm</b>	25–60	5.6	82
<b>NaGdF<sub>4</sub>:Yb/Er</b>	100 x 300	7.8	This work

According to the given examples, many larger particles possess larger longitudinal relaxivity ( $r_1$ ) value as compare to the smaller particles. Thus, inverse relation of size and  $r_1$  values is not always true. There are many other factors influencing longitudinal relaxivity ( $r_1$ ) value, such as Gd<sup>3+</sup> concentration, distribution of Gd<sup>3+</sup> ions in crystal in outer and inner sphere<sup>83, 76</sup>, molecular tumbling time effect<sup>84</sup>, presence of ligands affecting interaction with water protons<sup>84, 85</sup> etc.

Considering Gd<sup>3+</sup> ion concentration constant and gradient distribution of Gd<sup>3+</sup> ion unknown, we believe in this paper the higher relaxivity of as-prepared PEI capped  $\beta$ -NaGdF<sub>4</sub>:

Yb/Er, in spite of its quite larger size is evidently due to longer tumbling time owing to larger size and large coordinated number of water molecule due to increased water dispersibility by PEI capping of  $\beta$ -NaGdF<sub>4</sub>: Yb/Er nanorods. It is reported that, the bigger nanoparticles (NPs) have longer tumbling times ( $\tau_R$ ), i.e., surface ions on bigger NPs tumble more slowly than on the smaller NPs. This fact accounts for the increase in  $r_1/SA$  values with increase in NP size, which is in counteract to the effect of the S/V ratio and making the surface Gd<sup>3+</sup> ions on a larger NP affect the relaxivity more strongly than the ions on a smaller NPs.<sup>76</sup>

Similar was reported by Hou *et al.*, where relaxivity of large size (20 nm) NaGdF<sub>4</sub> was greater ( $r_1=8.78 \text{ s}^{-1}\text{mM}^{-1}$ ) than smaller NaGdF<sub>4</sub> (15 nm size;  $r_1=5.7 \text{ s}^{-1}\text{mM}^{-1}$ ).<sup>85</sup> Similarly, relaxivity of Gd<sub>2</sub>O<sub>3</sub>@MSN composite (size=25 nm;  $r_1=45.08 \text{ s}^{-1}\text{mM}^{-1}$ ) was greater than pure Gd<sub>2</sub>O<sub>3</sub> nanoparticles (size=2.5 nm;  $r_1=14.93 \text{ s}^{-1}\text{mM}^{-1}$ ).<sup>84</sup>

Figure 17 (e) and (f) shows typical T<sub>1</sub>-weighted MRI images of  $\beta$ -NaGdF<sub>4</sub>: 18 % Yb<sup>3+</sup>/ 2 % Er<sup>3+</sup> nanorods and  $\beta$ -NaGdF<sub>4</sub>: 18 % Yb<sup>3+</sup>, 2 % Er<sup>3+</sup>/ mTiO<sub>2</sub> nanocomposite. The T<sub>1</sub>-weighted imaging for the samples was performed for 4 different concentrations varying from 0.05 to 0.8 mM (water for the reference signal) on a 3T MR scanner. With the increasing concentration, the T<sub>1</sub>-weighted MRI signal intensity was clearly enhanced, thus showed positive enhancement effect, demonstrating that the of  $\beta$ -NaGdF<sub>4</sub>: 18 % Yb<sup>3+</sup>/ 2 % Er<sup>3+</sup> nanorods and  $\beta$ -NaGdF<sub>4</sub>: 18 % Yb<sup>3+</sup>, 2 % Er<sup>3+</sup>/ mTiO<sub>2</sub> nanocomposite might be an effective T<sub>1</sub>-MRI contrast agent.

#### 4.4. Conclusion

In summary, the multifunctional NIR light active  $\beta$ -NaGdF<sub>4</sub>: 18 % Yb<sup>3+</sup>, 2 % Er<sup>3+</sup>/mTiO<sub>2</sub> nanocomposites were designed for its applications in photocatalysis,

photovoltaics and biomedical sciences etc. The up-conversion phosphor  $\beta$ -NaGdF<sub>4</sub>: 18 % Yb<sup>3+</sup>, 2 % Er<sup>3+</sup> utilizes the NIR light and the mesoporous TiO<sub>2</sub> (*m*TiO<sub>2</sub>) utilizes the UV and weak visible which improves the photon harvesting across the solar spectrum (UV, visible and NIR region). Moreover, the mesoporosity of TiO<sub>2</sub> is expected to increase the active sites for an efficient photocatalysis and enhance the dye adsorption in the DSSCs. The photocatalytic activity of the nanocomposite was investigated via the decoloration of RhB and dye mixture (RhB, MB, MO and MG) under the direct solar light irradiation. In comparison to pure- *m*TiO<sub>2</sub>, the photocatalytic activity of nanocomposite is fairly improved, which presents a unified approach to enhance the solar energy harvesting ability of TiO<sub>2</sub> based catalytic materials. The efficiency of the DSSC increased by 17 % in the nanocomposite as compared to only *m*TiO<sub>2</sub>, by an increment in the photocurrent density which indicates that the improvement in the light harvesting capability of dye-molecules is achieved by the presence of phosphor particles. The longitudinal relaxivity ( $r_1$ ) value of  $\beta$ -NaGdF<sub>4</sub>: 18 % Yb<sup>3+</sup>, 2 % Er<sup>3+</sup>/*m*TiO<sub>2</sub> nanocomposite were close to those of materials reported for MRI and bio-separation. The proposed and designed a multifunctional  $\beta$ -NaGdF<sub>4</sub>: 18 % Yb<sup>3+</sup>, 2 % Er<sup>3+</sup>/*m*TiO<sub>2</sub> nanocomposite system act as a single platform with simultaneous multiple discrete functionalities of excellent luminescence properties, intrinsic paramagnetism and relaxivity, biocompatibility, photocatalytic activity, and solar cell efficiency, thus these may find other promising applications in bio-imaging, magnetic resonance imaging, water-splitting, photodynamic therapy, NIR triggered anticancer drug delivery and cancer therapy.

---

## 4.5. References

- 1 I. K. Konstantinou and T. A. Albanis, *Appl. Catal. B Environ.*, 2004, **49**, 1–14.
- 2 C. Wang, K. Song, Y. Feng, D. Yin, J. Ouyang, B. Liu, X. Cao, L. Zhang, Y. Han and M. Wu, *RSC Adv.*, 2014, **4**, 39118-39125.
- 3 B. O'Regan and M. Grätzel, *Nature*, 1991, **353**, 737–740.
- 4 X. Guo, W. Di, C. Chen, C. Liu, X. Wang and W. Qin, *Dalt. Trans.*, 2014, **43**, 1048–1054.
- 5 I.-C. Kang, Q. Zhang, S. Yin, T. Sato and F. Saito, *Environ. Sci. Technol.*, 2008, **42**, 3622–3626.
- 6 P. Roy, S. Berger and P. Schmuki, *Angew. Chemie Int. Ed.*, 2011, **50**, 2904–2939.
- 7 J. Liu, Q. Zhang, J. Yang, H. Ma, M. O. Tade, S. Wang and J. Liu, *Chem. Commun.*, 2014, **50**, 13971–13974.
- 8 Y. Zhang and Z. Hong, *Nanoscale*, 2013, **5**, 8930-8933.
- 9 W. Wang, M. Ding, C. Lu, Y. Ni and Z. Xu, *Appl. Catal. B Environ.*, 2014, **144**, 379–385.
- 10 W. Qin, D. Zhang, D. Zhao, L. Wang and K. Zheng, *Chem. Commun.*, 2010, **46**, 2304–2306.
- 11 P. Goswami and J. N. Ganguli, *Dalt. Trans.*, 2013, **42**, 14480-14490.
- 12 G. Liu, Y. Zhao, C. Sun, F. Li, G. Q. Lu and H.-M. Cheng, *Angew. Chemie Int. Ed.*,

- 2008, **47**, 4516–4520.
- 13 G. Yang, Z. Jiang, H. Shi, T. Xiao and Z. Yan, *J. Mater. Chem.*, 2010, **20**, 5301-5309.
- 14 X. Wu, S. Yin, Q. Dong, C. Guo, T. Kimura, J. Matsushita and T. Sato, *J. Phys. Chem. C*, 2013, **117**, 8345–8352.
- 15 J. Yu, T. Ma and S. Liu, *Phys. Chem. Chem. Phys.*, 2011, **13**, 3491–3501.
- 16 J. Tang, Z. Zou and J. Ye, *Angew. Chemie Int. Ed.*, 2004, **43**, 4463–4466.
- 17 M. C. Pereira, E. M. Garcia, A. Cândido da Silva, E. Lorençon, J. D. Ardisson, E. Murad, J. D. Fabris, T. Matencio, T. de Castro Ramalho and M. V. J. Rocha, *J. Mater. Chem.*, 2011, **21**, 10280-10282.
- 18 P. Padhye and P. Poddar, *J. Mater. Chem. A*, 2014, **2**, 19189–19200.
- 19 A. Biswas, R. Das, C. Dey, R. Banerjee and P. Poddar, *Cryst. Growth Des.*, 2014, **14**, 236–239.
- 20 P. Gupta and P. Poddar, *RSC Adv.*, 2015, **5**, 10094–10101.
- 21 S.-L. Li, K.-J. Jiang, K.-F. Shao and L.-M. Yang, *Chem. Commun.*, 2006, **2**, 2792-2794.
- 22 A. Burke, L. Schmidt-Mende, S. Ito and M. Grätzel, *Chem. Commun.*, 2007, 234–236.
- 23 G.B. Shan and G. P. Demopoulos, *Adv. Mater.*, 2010, **22**, 4373–4377.
- 24 S. Sadhu and P. Poddar, *J. Phys. Chem. C*, 2014, **118**, 19363–19373.
- 25 H.Q. Wang, M. Batentschuk, A. Osvet, L. Pinna and C. J. Brabec, *Adv. Mater.*, 2011,



- 23**, 2675–2680.
- 26 Q. C. Xu, Y. Zhang, M. J. Tan, Y. Liu, S. Yuan, C. Choong, N. S. Tan and T. T. Y. Tan, *Adv. Healthc. Mater.*, 2012, **1**, 470–474.
- 27 C. Wang, L. Cheng and Z. Liu, *Theranostics*, 2013, **3**, 317–330.
- 28 L. Zeng, Y. Pan, Y. Tian, X. Wang, W. Ren, S. Wang, G. Lu and A. Wu, *Biomaterials*, 2015, **57**, 93–106.
- 29 L. Cheng, K. Yang, Y. Li, J. Chen, C. Wang, M. Shao, S.T. Lee and Z. Liu, *Angew. Chemie Int. Ed.*, 2011, **50**, 7385–7390.
- 30 J. Kim, Y. Piao and T. Hyeon, *Chem. Soc. Rev.*, 2009, **38**, 372–390.
- 31 T. V. Gavrilović, D. J. Jovanović, V. Lojpur and M. D. Dramićanin, *Sci. Rep.*, 2014, **4**, 1–9.
- 32 C. Li and J. Lin, *J. Mater. Chem.*, 2010, **20**, 6831–6847.
- 33 J.-C. G. Bünzli and C. Piguet, *Chem. Soc. Rev.*, 2005, **34**, 1048–1077.
- 34 Z. Cheng and J. Lin, *Macromol. Rapid Commun.*, 2015, **36**, 790–827.
- 35 W. Zheng, D. Tu, P. Huang, S. Zhou, Z. Chen and X. Chen, *Chem. Commun.*, 2015, **51**, 4129–4143.
- 36 L. D. Carlos, R. A. S. Ferreira, V. de Zea Bermudez, B. Julián-López and P. Escribano, *Chem. Soc. Rev.*, 2011, **40**, 536–549.
- 37 M. Haase and H. Schäfer, *Angew. Chemie Int. Ed.*, 2011, **50**, 5808–5829.

- 
- 38 F. Wang and X. Liu, *Chem. Soc. Rev.*, 2009, **38**, 976-989.
- 39 R. X. Yan and Y. D. Li, *Adv. Funct. Mater.*, 2005, **15**, 763-770.
- 40 C. Li, C. Zhang, Z. Hou, L. Wang, Z. Quan, H. Lian and J. Lin, *J. Phys. Chem. C*, 2009, **113**, 2332-2339.
- 41 M. Banski, M. Afzaal, A. Podhorodecki, J. Misiewicz, a L. Abdelhady and P. O'Brien, *J. Nanoparticle Res.*, 2012, **14**, 1228.
- 42 Y. Liu, D. Tu, H. Zhu, R. Li, W. Luo and X. Chen, *Adv. Mater.*, 2010, **22**, 3266-3271.
- 43 M. Banski, A. Podhorodecki, J. Misiewicz, M. Afzaal, A. L. Abdelhady and P. O'Brien, *J. Mater. Chem. C*, 2013, **1**, 801-807.
- 44 S. Ito, P. Chen, P. Comte, M. K. Nazeeruddin, P. Liska, P. Péchy and M. Grätzel, *Prog. Photovoltaics Res. Appl.*, 2007, **15**, 603-612.
- 45 Q. Ju, D. Tu, Y. Liu, R. Li, H. Zhu, J. Chen, Z. Chen, M. Huang and X. Chen, *J. Am. Chem. Soc.*, 2012, **134**, 1323-1330.
- 46 T. Xia, M. Kovoichich, M. Liong, H. Meng, S. Kabehie, S. George, J. I. Zink and A. E. Nel, *ACS Nano*, 2009, **3**, 3273-3286.
- 47 O. Boussif, F. Lezoualc'h, M. a Zanta, M. D. Mergny, D. Scherman, B. Demeneix and J. P. Behr, *Proc. Natl. Acad. Sci. U. S. A.*, 1995, **92**, 7297-7301.
- 48 L.Q. Xiong, Z.G. Chen, M.X. Yu, F.Y. Li, C. Liu and C.H. Huang, *Biomaterials*, 2009, **30**, 5592-5600.

- 
- 49 Z. Yi, S. Zeng, W. Lu, H. Wang, L. Rao, H. Liu and J. Hao, *ACS Appl. Mater. Interfaces*, 2014, **6**, 3839–3846.
- 50 F. Wang, D. K. Chatterjee, Z. Li, Y. Zhang, X. Fan and M. Wang, *Nanotechnology*, 2006, **17**, 5786–5791.
- 51 S. S. Mali, C. A. Betty, P. N. Bhosale and P. S. Patil, *ECS J. Solid State Sci. Technol.*, 2012, **1**, M15–M23.
- 52 X. W. Lou and L. A. Archer, *Adv. Mater.*, 2008, **20**, 1853–1858.
- 53 J. Chen, Z. Hua, Y. Yan, A. A. Zakhidov, R. H. Baughman and L. Xu, *Chem. Commun.*, 2010, **46**, 1872–1874.
- 54 M. M. Lage, R. L. Moreira, F. M. Matinaga and J. Gesland, *Chem. Mater.*, 2005, **17**, 4523–4529.
- 55 D. Yuan, M. C. Tan, R. E. Riman and G. M. Chow, *J. Phys. Chem. C*, 2013, **117**, 13297–13304.
- 56 J. F. Suyver, J. Grimm, M. K. van Veen, D. Biner, K. W. Krämer and H. U. Güdel, *J. Lumin.*, 2006, **117**, 1–12.
- 57 Y. Park, W. Kim, H. Park, T. Tachikawa, T. Majima and W. Choi, *Appl. Catal. B Environ.*, 2009, **91**, 355–361.
- 58 X. Wu, S. Yin, Q. Dong, B. Liu, Y. Wang, T. Sekino, S. W. Lee and T. Sato, *Sci. Rep.*, 2013, **3**, 1–8.
- 59 C. Li, Z. Quan, J. Yang, P. Yang and J. Lin, *Inorg. Chem.*, 2007, **46**, 6329–6337.
-

- 60 X. Guo, W. Song, C. Chen, W. Di and W. Qin, *Phys. Chem. Chem. Phys.*, 2013, **15**, 14681–14688.
- 61 K. Zhou, Y. Zhu, X. Yang, X. Jiang and C. Li, *New J. Chem.*, 2011, **35**, 353–359.
- 62 L. Ren, X. Qi, Y. Liu, Z. Huang, X. Wei, J. Li, L. Yang and J. Zhong, *J. Mater. Chem.*, 2012, **22**, 11765–11771.
- 63 K. Lee and S. Hamid, *Materials (Basel)*, 2015, **8**, 339–354.
- 64 A. S. Bhadwal, R. M. Tripathi, R. K. Gupta, N. Kumar, R. P. Singh and A. Shrivastav, *RSC Adv.*, 2014, **4**, 9484–9490.
- 65 J. Gong, J. Liang and K. Sumathy, *Renew. Sustain. Energy Rev.*, 2012, **16**, 5848–5860.
- 66 C. Yuan, G. Chen, L. Li, J. a Damasco, Z. Ning, H. Xing, T. Zhang, L. Sun, H. Zeng, A. N. Cartwright, P. N. Prasad and H. Ågren, *ACS Appl. Mater. Interfaces*, 2014, **6**, 18018–18025.
- 67 L. Liang, Y. Liu and X.-Z. Zhao, *Chem. Commun.*, 2013, **49**, 3958–3960.
- 68 C. H. Han, H. S. Lee, K. won Lee, S. Do Han and I. Singh, *Bull. Korean Chem. Soc.*, 2009, **30**, 219–223.
- 69 G.-B. Shan, H. Assaoudi and G. P. Demopoulos, *ACS Appl. Mater. Interfaces*, 2011, **3**, 3239–3243.
- 70 H.-T. Wong, H. L. W. Chan and J. H. Hao, *Appl. Phys. Lett.*, 2009, **95**, 022512.
- 71 S. Zeng, M.-K. Tsang, C.-F. Chan, K.-L. Wong, B. Fei and J. Hao, *Nanoscale*, 2012,

- 4, 5118-5124.
- 72 M. Rohrer, H. Bauer, J. Mintorovitch, M. Requardt and H.-J. Weinmann, *Invest. Radiol.*, 2005, **40**, 715–724.
- 73 C. Dong, A. Korinek, B. Blasiak, B. Tomanek and F. C. J. M. van Veggel, *Chem. Mater.*, 2012, **24**, 1297–1305.
- 74 Q. Ju, Y. Liu, D. Tu, H. Zhu, R. Li and X. Chen, *Chem. - A Eur. J.*, 2011, **17**, 8549–8554.
- 75 S. Majeed and S. A. Shivashankar, *J. Mater. Chem. B*, 2014, **2**, 5585-5593.
- 76 N. J. J. Johnson, W. Oakden, G. J. Stanisz, R. Scott Prosser and F. C. J. M. van Veggel, *Chem. Mater.*, 2011, **23**, 3714–3722.
- 77 Y. I Park, J. H. Kim, K. T. Lee, K. Jeon, H. Bin Na, J. H. Yu, H. M. Kim, N. Lee, S. H. Choi, S. Baik, H. Kim, S. P. Park, B. Park, Y. W. Kim, S. H. Lee, S. Yoon, I. C. Song, W. K. Moon, Y. D. Suh and T. Hyeon, *Adv. Mater.*, 2009, **21**, 4467–4471.
- 78 V. A. Online, N. Luo, C. Yang, X. Tian, J. Xiao, J. Liu, F. Chen, D. Zhang, D. Xu, Y. Zhang, G. Yang, D. Chen and L. Li, 2014, 5891–5897.
- 79 G. K. Das, B. C. Heng, S. Ng, T. White, J. S. C. Loo, L. D’Silva, P. Padmanabhan, K. K. Bhakoo, S. T. Selvan and T. T. Y. Tan, *Langmuir*, 2010, **26**, 8959–8965.
- 80 I.-F. Li, C. Su, H. Sheu, H. Chiu, Y. Lo, W. Lin, J. Chen and C. Yeh, *Adv. Funct. Mater.*, 2008, **18**, 766–776.
- 81 X. Zhang, Z. Zhao, X. Zhang, D. B. Cordes, B. Weeks, B. Qiu, K. Madanan, D. Sardar

- and J. Chaudhuri, *Nano Res.*, 2015, **8**, 636–648.
- 82 J. Zhou, Y. Sun, X. Du, L. Xiong, H. Hu and F. Li, *Biomaterials*, 2010, **31**, 3287–3295.
- 83 C. Dong, J. Pichaandi, T. Regier and F. C. J. M. van Veggel, *J. Phys. Chem. C*, 2011, **115**, 15950–15958.
- 84 K. Ni, Z. Zhao, Z. Zhang, Z. Zhou, L. Yang, L. Wang, H. Ai and J. Gao, *Nanoscale*, 2016, **8**, 3768–3774.
- 85 Y. Hou, R. Qiao, F. Fang, X. Wang, C. Dong, K. Liu, C. Liu, Z. Liu, H. Lei, F. Wang and M. Gao, *ACS Nano*, 2013, **7**, 330–338.

## **Chapter 5**

### **Conclusion and future scope**

#### **Outline**

---

This chapter presents the summary of the research work depicted in this thesis and briefly present the future scope of research in this field.

## 5.1. Summary

Lanthanide ion-doped up-/down-converting phosphors are giving an edge over conventional organic fluorescent dyes or quantum dots due to their unique and beneficial tunable electronic, optical and magnetic properties that enable potential wide ranging applications in optoelectronics, solid state lasers, security printing, biomedical diagnostics, sensors, solar cells, catalysis and biological imaging. In the present research work we have studied the tunable optical properties of trivalent lanthanide ion-doped rare earth fluoride phosphors and have investigated their applications. We have deliberated the rare earth fluoride, specifically NaREF<sub>4</sub> system and understand the effect of different dopants and dopant combinations, surface cappings, functionalization and their structural and optical properties and explored various applications. We have also modified the system by conjugation of drug molecules and other entities to make them suitable and efficient for and according to the need of targeted application. The present thesis mainly describes a detailed work on hexagonal phase Ln<sup>3+</sup>-doped rare earth fluoride systems;  $\beta$ -NaREF<sub>4</sub>: Ln<sup>3+</sup>;  $\beta$ -NaYF<sub>4</sub>:Tb<sup>3+</sup>,  $\beta$ -NaYF<sub>4</sub>:Gd<sup>3+</sup>,Tb<sup>3+</sup> and  $\beta$ -NaGdF<sub>4</sub>:Yb<sup>3+</sup>,Er<sup>3+</sup>.

Firstly, we synthesized uniform  $\beta$ -NaYF<sub>4</sub>:5% Tb<sup>3+</sup> crystals and studied the effect of synthesis parameters and their optical properties. The hexagonal phase of NaYF<sub>4</sub>:Ln<sup>3+</sup> (Ln=Tb, Yb/Er and Yb/Tm) microcrystals with multiform morphologies; hexagonal prisms, microrods and spindle like structures was synthesized via a cationic/anionic binary capping agent system: CTAB and a trisodium citrate-assisted hydrothermal route. Under UV excitation, the as-prepared  $\beta$ -NaYF<sub>4</sub>:5% Tb<sup>3+</sup> crystals emit strong green emission (down-conversion luminescence) and possess long luminescence lifetime in milliseconds. In contrast, under 980 nm NIR excitation, the Yb/Er- and Yb/Tm-co-doped NaYF<sub>4</sub> samples exhibited strong green and blue up-conversion luminescence, respectively. The influence of capping agents, synthesis temperature, pH, and their growth



mechanisms was studied in detail, which showed strong dependence of reaction parameters on the morphology. The static and dynamic photoluminescence studies indicated that the luminescence properties of the  $\beta$ -NaYF<sub>4</sub>:5% Tb<sup>3+</sup> phosphors are strongly dependent on their crystalline size and shape. The optical studies on  $\beta$ -NaYF<sub>4</sub>:5% Tb<sup>3+</sup> crystals provided the surprising insight on the band gap and revealed the appearance of new energy level (inter-band energy level), which enthuse us to check out their photocatalytic properties. The photocatalytic studies showed that  $\beta$ -NaYF<sub>4</sub>:5% Tb<sup>3+</sup> phosphors are highly selective for methylene blue. In addition, we have also discussed the correlation between the morphologies and photocatalytic activities. To the best of our knowledge, for the first time, we have explored the photocatalytic selectivity and morphology dependent effects in catalytic activity of  $\beta$ -NaYF<sub>4</sub>:5% Tb<sup>3+</sup> phosphors. Apart from their photocatalytic properties, the unique luminescence properties and controlled morphologies of these phosphors may endow potential applications in the field of light emitting diodes (LEDs), solid state lasers, and biological sciences.

Although, the as-prepared  $\beta$ -NaYF<sub>4</sub>:5% Tb<sup>3+</sup> crystals were highly luminescent, with long luminescent lifetimes, but were not suitable for bio-applications as limited by size and biocompatibility. In this viewpoint, we have developed a multi-modal probe based on PEI functionalized, highly crystalline  $\beta$ -NaYF<sub>4</sub>:Gd<sup>3+</sup>/Tb<sup>3+</sup> nanorods system, which possesses excellent photoluminescence as well as paramagnetic properties, making them suitable for optical bioimaging and MRI applications. This system can also be used as drug delivery nanovehicle. A well established chemotherapeutic, doxorubicin (DOX) which is a weakly- basic drug suffers reduced internalization by tumor cells due to their acidic microenvironment and cause serious undesirable side effects on normal cells. This drawback can be overcome by enabling targeted drug delivery system. In light of these consequences, we conjugated doxorubicin to PEI capped  $\beta$ -NaYF<sub>4</sub>:Gd<sup>3+</sup>/Tb<sup>3+</sup> via pH-

sensitive hydrazone bond linkages. This system acted as a pH-triggered drug delivery system, where the doxorubicin is released by the cleavage of hydrazone bonds in the acidic microenvironment of tumors, which enhances cellular uptake and reduces the side-effects of chemotherapeutics. The pH dependent *in vitro* DOX release studies have shown that DOX release at acidic pH is significantly faster than at pH 7.4. Furthermore, the luminescence quenching of  $\beta$ -NaYF<sub>4</sub>: Gd<sup>3+</sup>/Tb<sup>3+</sup> by DOX due to a FRET mechanism can be applied as an optical probe to confirm the DOX conjugation and monitor the DOX release. Cell toxicity assays revealed that PEI capped  $\beta$ -NaYF<sub>4</sub>:Gd<sup>3+</sup>/Tb<sup>3+</sup> possesses very low toxicity to the normal cells and interestingly and advantageously the DOX-conjugated- $\beta$ -NaYF<sub>4</sub>:Gd<sup>3+</sup>/Tb<sup>3+</sup> showed a potential decrease in the cytotoxicity than free DOX, indicating that toxic effects of DOX are reduced when conjugated with the  $\beta$ -NaYF<sub>4</sub>:Gd<sup>3+</sup>/Tb<sup>3+</sup> nanorods. Meanwhile, the *in vitro* cytotoxicity of DOX-conjugated  $\beta$ -NaYF<sub>4</sub>:Gd<sup>3+</sup>/Tb<sup>3+</sup> on MCF-7 cancer cells exhibited comparable cellular toxicity with respect to free DOX. The cellular uptake of DOX-conjugated  $\beta$ -NaYF<sub>4</sub>:Gd<sup>3+</sup>/Tb<sup>3+</sup> by MCF-7 cells was established from a confocal laser scanning microscopy and flow cytometry studies. The cellular uptake of DOX-conjugated  $\beta$ -NaYF<sub>4</sub>:Gd<sup>3+</sup>/Tb<sup>3+</sup> by MCF-7 cells was enhanced compared to that of free DOX at pH 6.5, that mimics a tumor microenvironment, which establish the benefit of DOX-conjugated  $\beta$ -NaYF<sub>4</sub>:Gd<sup>3+</sup>/Tb<sup>3+</sup> nanorods system in targeting cancer cells. Along with high luminescence efficiency, the magnetic mass susceptibility and longitudinal relaxivity ( $r_1$ ) of  $\beta$ -NaYF<sub>4</sub>:Gd<sup>3+</sup>/Tb<sup>3+</sup> were observed to be  $\chi \sim 3.8 \times 10^{-5}$  emu g<sup>-1</sup> Oe<sup>-1</sup> and  $r_1 \sim 1.14$  s<sup>-1</sup> mM<sup>-1</sup>, respectively which are close to those of materials reported for MRI and bioseparation. Furthermore, magnetic resonance imaging gave enhanced T<sub>1</sub>-weighted MRI images with increased concentrations of  $\beta$ -NaYF<sub>4</sub>:Gd<sup>3+</sup>/Tb<sup>3+</sup> making them suitable for simultaneous magnetic resonance imaging. It is expected that DOX-conjugated  $\beta$ -NaYF<sub>4</sub>:Gd<sup>3+</sup>/Tb<sup>3+</sup> combining

pH-triggered drug delivery, efficient luminescence and paramagnetic properties promises to be a potential multifunctional platform for cancer theranostics, biodetection and imaging.

Further, the development of multifunctional platforms for broad range of applications has geared tremendous progress towards the design and engineering of various functional materials with multiple discrete functions as nanostructured composites. In this perspective, we designed a single multifunctional platform for broad range of applications; energy and biomedical, by judiciously integrating upconverting luminescent and magnetic  $\beta$ - NaGdF<sub>4</sub>:Yb<sup>3+</sup>,Er<sup>3+</sup> phosphor and photoactive semiconductor anatase TiO<sub>2</sub>. The multifunctional broad-spectrum photoactive  $\beta$ - NaGdF<sub>4</sub>:Yb<sup>3+</sup>,Er<sup>3+</sup>/mTiO<sub>2</sub> nanocomposites were developed for its enhanced applications in photocatalysis, photovoltaics and biomedical sciences. Currently, the photoactive materials for solar energy harvesting applications have limitations in their efficiency due to their narrow photon absorption spectrum. The upconversion phosphor  $\beta$ - NaGdF<sub>4</sub>:Yb<sup>3+</sup>,Er<sup>3+</sup> utilizes the NIR light and the mesoporous anatase TiO<sub>2</sub> (mTiO<sub>2</sub>) utilizes the UV and weak visible, thus the composite forms a broad spectrum photon-capture system across the solar spectrum (UV, visible and NIR region) and improved power conversion efficiency for enhanced applications in photocatalysis, and dye sensitized solar cells (DSSCs). Moreover, the mesoporosity of TiO<sub>2</sub> is expected to increase the active sites for an efficient photocatalysis and enhance the dye adsorption in the DSSCs. The photocatalytic activity of the nanocomposite was investigated via the degradation of RhB and dye mixture (RhB, MB, MO and MG) under the direct solar light irradiation. In comparison to pure-mTiO<sub>2</sub>, the photocatalytic activity of nanocomposite is fairly improved, which presents a unified approach to enhance the solar energy harvesting ability of TiO<sub>2</sub> based catalytic materials. The efficiency of the DSSC increased by ~ 17 %

in the nanocomposite as compared to only  $m\text{TiO}_2$ , by an increment in the photocurrent density ( $\sim 24\%$ ) which indicates that the improvement in the light harvesting capability of dye-molecules is achieved by the presence of phosphor particles. The nuclear magnetic resonance (NMR) measurements showed large longitudinal  $T_1$  relaxivity ( $r_1=7.09\text{ s}^{-1}\text{mM}^{-1}$ ) and magnetic resonance imaging showed an enhanced  $T_1$ -weighted MRI images with increased concentrations of  $\beta\text{-NaGdF}_4:\text{Yb}^{3+}, \text{Er}^{3+}/m\text{TiO}_2$  nanocomposite making them suitable for simultaneous magnetoresonance imaging. To the best of our knowledge, for the first time we have proposed and designed a multifunctional  $\beta\text{-NaGdF}_4:\text{Yb}^{3+}, \text{Er}^{3+}/m\text{TiO}_2$  nanocomposite as a single platform with simultaneous multiple discrete functionalities of excellent luminescence properties, intrinsic paramagnetism and relaxivity, biocompatibility, photocatalytic activity, and solar cell efficiency, thus these may find other promising applications in bio-imaging, magnetic resonance imaging, water-splitting, photodynamic therapy, NIR triggered anticancer drug delivery and cancer therapy.

## 5.2. Scope of future work

The studies on lanthanide ion-doped phosphor crystals drive importance and interest in both the fundamentals and enhanced applications. While the research work was being performed presented in this thesis, several advances have been taking place on the international front in the field of lanthanide ion-doped phosphors. At the fundamental front, spectroscopic information related to local symmetry of lanthanide ion in an inorganic host is crucial for optimizing their optical performance for technological applications. Although hexagonal phase  $\beta\text{-NaYF}_4$ , disordered structure is regarded to be the most efficient host for  $\text{Ln}^{3+}$  luminescence, but the spectroscopic or crystallographic site of  $\text{Ln}^{3+}$  in  $\text{NaYF}_4$ , has received much debate. Since the optical transitions of  $\text{Ln}^{3+}$  are sensitive to their local coordination, and the emission intensity of  $\text{Ln}^{3+}$ -doped crystals

strongly depends on the crystal structure and crystal-field (CF) surroundings around  $\text{Ln}^{3+}$ , it is of utmost importance to know the local symmetry around the lanthanide ions. In the present thesis although, the crystal structure of  $\beta\text{-NaYF}_4$  have been confirmed by XRD, but the actual site symmetry of a dopant in a cationic site cannot be revealed from the XRD data. Moreover, the incorporation of  $\text{Ln}^{3+}$  ions at a particular site leads to changes in the local surrounding environment in the doped host. Thus, the understanding these changes in the local environment is very important to study in future. To get a complete picture, experimental and theoretical studies can be done further using time correlated single photon counting (TCSPC), extended X-ray absorption fine structure (EXAFS) measurements *etc* to understand the local structure and site symmetry of  $\text{Ln}^{3+}$  ions. Also, the influence of local structure and site symmetry, correlation between structural and various properties, viz. optical, magnetic, and catalytic can be established by these studies.

Architectural manipulation and morphology tuning is also important to study as various properties are dependent on morphology. Thus, apart from effect capping agent, temperature, time and pH, the effect of other parameters such as Na:F ratio, RE:F ratio, concentration of precursors on the morphology of  $\beta\text{-NaYF}_4$  crystals can also be studied in future. Moreover, the synergistic effect of binary capping agents and selective binding affinity of these capping agents on the particular planes of the uniform and well defined facets of hexagonal prismatic  $\beta\text{-NaYF}_4$  crystal have not been proved in this research work. Thus, advanced experimental techniques and theoretical studies will help to prove the binding affinity of respective capping agents selectively on top/bottom and side planes in future. Till now, the band edge shift or inter-band energy levels picture of lanthanide ion-doped inorganic nanostructures with doping of  $\text{Ln}^{3+}$  is not cleared completely. It is also required to know how the shifting of band edge takes place with interstitial and

substitution doping, which is important to further study for their photocatalytic properties. Further, detailed photocatalytic studies including photodegradation kinetics and morphology dependence on photocatalytic activity and efficiency of  $\beta$ -NaYF<sub>4</sub>:Tb<sup>3+</sup> can be studied. Attempts to enhance the photocatalytic activity of  $\beta$ -NaYF<sub>4</sub>:Tb<sup>3+</sup> by modifying its properties via formation of composites can be performed. For instance, Graphene oxide (GO) possess excellent conduction properties, thus preparation of NaYF<sub>4</sub>:Tb<sup>3+</sup>-GO composite and their study of the photocatalytic activity can be done to check whether the photocatalysis efficiency increases.

In regard of biological applications, many approaches have been reported to enhance cellular uptake of doxorubicin, consequent site specific drug delivery and minimizing the risk-to-benefit ratio, including cancer receptor targeted nanocarrier system, pH-triggered drug delivery systems *etc.* However, in pH triggered drug delivery system negligible DOX release at physiological pH is not attained yet. Thus, such compact conjugated systems involving pH sensitive linkages should be developed further to minimize the DOX release at neutral pH to negligible. The *in vivo* and biodistribution studies of the DOX-conjugated- $\beta$ -NaYF<sub>4</sub>:Gd<sup>3+</sup>, Tb<sup>3+</sup> can be performed further.

The  $\beta$ -NaGdF<sub>4</sub>:Yb<sup>3+</sup>, Er<sup>3+</sup>/mTiO<sub>2</sub> composite in the present research work showed improved photocatalysis and solar cell performance by broad photon capture system. However, the catalysis and solar cell efficiency can be further enhanced by choosing modified TiO<sub>2</sub>, or modifying cell fabrication, or by preparing core-shell structures. Importantly, this composite system can be potentially used in drug delivery and cancer theranostics applications owing to high penetration depth of the NIR radiation. Titania gives an edge in drug delivery and cancer therapy by reactive oxygen species (ROS) production due to its high activity, stability, non-toxicity, however, low tissue penetration and UV photodamage limits its use. To overcome these issues, such composites of TiO<sub>2</sub>

with upconverting phosphor can be promising for NIR-triggered drug release and targeted cancer cell ablation. Since, under NIR light excitation, UCNPs are capable of emitting high-energy UV/visible light, UCNPs can activate surrounding photosensitizer (PS) molecules to produce singlet oxygen to kill cancer cells. Owing to the high tissue penetration depth of NIR light, NIR-excited UCNPs can be used to activate PS molecules in much deeper tissues compared to traditional PDT induced by visible or ultraviolet (UV) light. Thus, in the presented composite system, anatase  $m\text{TiO}_2$  act as a photosensitizer molecule which can trigger the production of ROS by formation of electron-hole pair, upon activation by safe and deeper NIR excitation for PDT, as a future application.

Despite the considerable progress made in the past decade, the field of lanthanide ion-doped phosphors has been hindered by significant experimental challenges associated with weak luminescence efficiencies, which limits further applications. Extensive work has been carried out to enhance emission intensity, such as modulating host materials and dopant concentrations, different dopant combinations, coating protective shells, and coupling with noble metals. Though in the present research work, the incorporation of sensitizer  $\text{Gd}^{3+}$  dopant ion in  $\beta\text{-NaYF}_4\text{:Tb}^{3+}$  in the  $\beta\text{-NaYF}_4\text{:Gd}^{3+},\text{Tb}^{3+}$  system rendered enhanced luminescence intensity. However, another approach to further enhance the luminescence efficiency of the same system can be performed by integration of Ag or Au nanoparticles. The presence of noble metallic nanostructures can either have beneficial or deleterious effect depending on the position of the Surface Plasmon Resonance (SPR) peak and the distance of the lanthanide ion from the metal surface. The SPR of metal should be resonant to excitation/emission wavelength of  $\text{Ln}^{3+}$ -doped phosphor, which in turn substantially increases the excitation flux via local field enhancement (LFE) effect, consequent radiative transition rate. Thus, the luminescence efficiency of  $\beta\text{-NaYF}_4\text{:Tb}^{3+}$  phosphors can be further enhanced by introducing protective coating such as optically

inactive, biocompatible nanocellulose and coupling it with noble metal (Ag/Au). The enhancement is expected due to the surface protective effect, presence of spacer, and Localized Surface Plasmon Resonance (LSPR), to be used for potential applications.

Furthermore, mesoporous NaYF<sub>4</sub> structures can also be beneficial and promising for various applications such as photocatalysis, solar cells, drug delivery *etc.* However due to high crystallinity, the preparation of mesoporous structure are challenging and are not developed yet. Thus, this problem is also left open to study and to be addressed in the near future and efforts can be put on for the same in the future for further applications.

The lanthanide ion-doped rare earth fluorides have potential for huge advanced applications in optoelectronics, security printing, abuse drug sensing, anti-drug/currency counterfeiting, which further needs to be explored.



---

---

## **List of publications**

1. “Static and dynamic photoluminescence and photocatalytic properties of uniform, monodispersed up/down-converting, highly luminescent, lanthanide-ion-doped  $\beta$ -NaYF<sub>4</sub> phosphor microcrystals with controlled multiform morphologies”, **P. Padhye** and P. Poddar, *J. Mater. Chem. A*, 2014, 2, 19189–19200.
2. “Doxorubicin-conjugated  $\beta$ -NaYF<sub>4</sub>:Gd<sup>3+</sup>/Tb<sup>3+</sup> multifunctional, phosphor nanorods: a multimodal, luminescent, magnetic probe for simultaneous optical and magnetic resonance imaging and an excellent pH-triggered anti-cancer drug delivery nanovehicle”, **Preeti Padhye**, Aftab Alam, Suvankar Ghorai, Samit Chattopadhyay and Pankaj Poddar, *Nanoscale*, 2015, 7, 19501–19518.
3. “A broad spectrum photon responsive, paramagnetic  $\beta$ -NaGdF<sub>4</sub>:Yb<sup>3+</sup>,Er<sup>3+</sup>–mesoporous anatase titania nanocomposite”, **Preeti Padhye**, Subha Sadhu, Monika Malik and Pankaj Poddar, *RSC Adv.*, 2016, 6, 53504–53518.
4. “Plasmonic modulation of luminescence in NaYF<sub>4</sub>:Tb phosphor *via* using silver nanoparticles and nanorods”, Preeti Padhye, Monika Malik and Pankaj Poddar,(manuscript under preparation).
5. “GQD mediated morphology manipulation of  $\beta$ -NaYF<sub>4</sub>:Gd<sup>3+</sup>/Tb<sup>3+</sup> phosphor, Monika Malik, Preeti Padhye, and Pankaj Poddar,(manuscript under preparation).

**Addendum:**

The term down-conversion in the present thesis can also be alternatively termed as down-shifting. Down-conversion (DC) and down-shifting (DS) are the technical terms. Theoretically, the conversion of one high energy photon into two or more low energy photon is known as down-conversion. This process is also called as quantum cutting (QC). Therefore, the quantum efficiency (QE) of down-converting phosphors could be close to or larger than unity. Down-shifting is similar to down-conversion whereby only one low energy photon is emitted from absorption of one high energy photon and the quantum efficiency is lower than unity. Down-shifting can be considered as a subcategory of down-conversion and although both processes are *similar*, their quantum efficiencies *differ*. In literature, the Ln<sup>3+</sup>-doped phosphors are often termed as down-converting materials. DC or QC exists in Tb<sup>3+</sup> ions and can be realized by cross-relaxation energy transfer (CRET) processes between Tb<sup>3+</sup> ions. Also, DC is always realized by constructing the Gd<sup>3+</sup>→Eu<sup>3+</sup> or Gd<sup>3+</sup>→Tb<sup>3+</sup> energy transfers. Since, the evaluation of the total QE that contains the DC processes is ideal and theoretical, because it ignores the absorption of incident light and energy losses at defects and impurities. Thus, the term down-conversion in the present thesis can be termed as down-shifting as and wherever applicable.

**References:**

1. X. Huang, S. Han, W. Huang and X. Liu, *Chem. Soc. Rev.*, 2013, **42**, 173-201.
2. Y. Liu, J. Zhang, C. Zhang, J. Jiang, and H. Jiang, *J. Phys. Chem. C.*, 2016, **120**, 2362-2370.
3. M. B. de la Mora, O. Amelines-Sarria, B. M. Monroy, C. D. Hernández-Pérez, J. E. Lugo, *Solar Energy Materials & Solar Cells.*, 2017, **165**, 59-71.